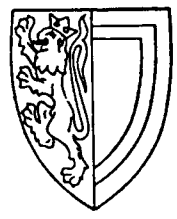
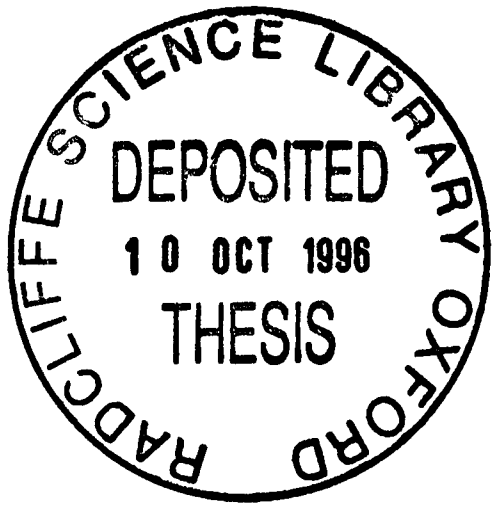
The ZEUS First Level Tracking Trigger and Studies of Supersymmetry at HERA

Peter Paul Otto Morawitz
Balliol College, Oxford

Submitted for the degree of Doctor of Philosophy
Michaelmas Term 1993





The ZEUS First Level Tracking Trigger and Studies of Supersymmetry at HERA

Peter Paul Otto Morawitz
Balliol College, Oxford

Submitted for the degree of Doctor of Philosophy
Michaelmas Term 1993

Abstract

The HERA accelerator, an electron-proton collider facility based at the DESY laboratory in Hamburg, started delivering luminosity to the ZEUS experiment in May 1992. The short time of 96ns between bunch crossings and the fact that the primary source of detector activity in ZEUS does not come from the e-p interactions of interest but rather from other sources makes a high performance three level trigger system essential to data-taking. We present one part of the ZEUS trigger system, the Central Tracking Detector First Level Trigger (CTD-FLT). The principle of operation and the hardware implementation are discussed at length. A prototype system which was used during the early stages of ZEUS data-taking is described. We detail the principles of the CTD-FLT hardware testing and discuss aspects of the First Level Trigger data from the 1993 running period. During this time the CTD trigger has proved to be an invaluable part of the overall system.

The high energies accessible at HERA make it possible to probe a variety of new physics models. The second part of this thesis focuses on one such model - Supersymmetry (SUSY). After an introduction to the model, a search for R-parity violating SUSY in the ZEUS data from the 1992 running period is described. No evidence for such signals has been found and hence we set upper limits on the mass scale of the theory. Finally we present a Monte Carlo study of the potential discovery reach of HERA for R-parity violating SUSY models, and come to the conclusion that HERA is an ideal place to look for such phenomena.

Acknowledgements

It was my mum, who gave me all the necessary encouragement and the inspiration to move to England and to pursue these studies. She - who I can no longer thank in person - deserves the real credits. Thank you mum.

Thanks to ...

My grandmother, for her endless moral and financial support throughout my six years at University. This thesis would not have been possible without her. My father, who has too helped me financially and prevented my bank manager from getting epileptic fits, and who has always given me lifts to Vienna Airport. To my brother Stefan, who had to put up with my moodiness, especially over the past months of my thesis writing. To Christine, for her emotional and physical support, for being there when I most needed her, for pretending to be my secretary (and in the process adding exotic twelve digit phone numbers to my phone bill), and for not knowing or wanting to know what the difference between a proton and a packet of crisps is. To Hansi Hummel, who has always been my best friend, and has made me understand that the problems encountered in physics are minor compared to the problems of the people from Cafe Alt. To Lars Donath, who had to take a lot of abuse from me because my work was not going anywhere, but always managed to distract me from work over a drink down the pub. To all my other friends, who I have not mentioned, and who have helped me over the past three years.

To Neville Harnew, my supervisor, for a lot of long-winded but often fruitful discussions; for finding the time in between meetings in Didcot, Hamburg, Liverpool and Oxford to correct my thesis over and over again; for pointing out various flaws in my analysis, and for providing me with a lot of inspiration. To Fergus Wilson, for introducing me to the First Level Trigger, for giving me help in my first year at Oxford and for correcting my FLT chapter. To Herbi Dreiner, for teaching me all I know about supersymmetry, for always answering my often frantic e-mail messages, for making physics sound so easy, and for proving that theorists are not necessarily 26 dimensions above inflated universes. To Grahame Blair, for exquisite night tours around Hamburg, for showing me the Insbeth, the Madhouse, the Frank and Frei, the Shamrock, the ... ; for never talking physics in his private life; and for collaborating on supersymmetric matters and generators. To Roman Walczak, for correcting a chapter of this thesis and spotting problems in my SUSY analysis.

To Roger Cashmore, for persuading me to join ZEUS, for finding the time to solve my most trivial (and yet vital) bureaucratic problems, and for managing to organise large sums of cash from various funds, committees and colleges and thus rescuing my existence from sure bankruptcy. To the Overseas Research Award, for

paying my 'alien' university fees. To the Rutherford Appleton Labs, for financing my numerous trips to Hamburg. To the Hardship-fund of Balliol College and to the Nuclear Physics Lab, for lending me various amounts of cash. And to the Ministry of Higher Education in Vienna, for no support whatsoever! Thanks.

To Helmut Harfman and Alois Hickersberger, who have helped my scientific perception of things to develop, and taught me that sailing, philosophising and drinking is just as important as science is. To Robin Devenish, for an exquisite Relativistic Quantum Mechanics course in my first year.

To Jon and Susana Butterworth, for sharing a house with me, being good friends and visiting me in Vienna. To Jon especially, for working together with me on SUSANA matters, and not mentioning in his thesis that I did the dishes (occasionally) too! To Thariq Khatri, for games of tennis and pool, coming out for drinks, and not minding being dragged to Cafe Alt every evening when he stayed in Vienna. To Mark Lancaster, for not taking various Tequilla attacks too personal (but nevertheless attempting to drown me in large amounts of alcoholic 'Zombie'-fluid), and for making people laugh when they most needed it. To Tim(bo) Short, for providing the major source of numerous and humorous UK-gossip, always being cheerful and easygoing, and letting me stay in his flat. To Alex Byrne, for proudly ringing bells all over Europe, singing in choirs and always liking a chat. To Dave (Bangkok) Bailey, for always being good for a 'swift one' and for compiling alpha software. To all the new and still enthusiastic first years at the Nuclear Physics Lab, namely Jason Mcfall, Arnulf Quadt, Dave Daniels, Chandy Nath, for sharing an office with me. To Patrick Luffman, for finding various K_S s and J/ψ s, and thus taking science beyond the boundaries of the 2GigaByte disk facilities at the Nuclear Physics Lab. To Ken Long, for never getting tired of answering the most trivial of questions on tracking, computers and life in general. To Nick Brook, for always being helpfull with ZEUS offline software matters, and for explaining to me how to 'f...ing use the f...ing IBf...ingM'. To Nigel Roocroft, John Nash, Tim Yip, Dave Cussans, and all the other people who had to work together with me over the years.

To Pete Gronbech, for running a very efficient UNIX system. To Ian Mcarthur and Stig Topp-Jorgensen, for explaining how transputers and DAQ systems work (or should work in an ideal world of computer experts). To all the engineers I have worked with over the years, namely Pete Shield, Saeed Madani, Rob Hasall, Martin Postraneky, Martin Morrisey, and to John Lane, for forgiving me for shouting at them in the process of heated discussions about hardware. To Brain Foster, for his chaotic and very interesting way of organising things, and for always having the guts to stand up in meetings to proclaim new deadlines for the CTD hardware installation.

And to all the other people who I have worked together with and who have helped me over the past three years.
Thanks.

To my Mum.

Contents

1 Introduction **5**

1.1 The HERA machine 6

1.2 HERA Kinematics 7

1.3 Physics at HERA 11

1.3.1 Deep Inelastic Scattering 11

1.3.2 Low-x Physics 13

1.3.3 Photoproduction 13

1.3.4 Physics beyond the SM - Exotic Physics 14

1.4 Overview 14

2 The ZEUS Detector **17**

2.1 Overview 17

2.2 The ZEUS Components 19

2.3 The Central Tracking Detector 22

2.3.1 The r-ϕ System 25

2.3.2 The z-by-timing System 26

2.4 The ZEUS DAQ and Trigger System 27

3 The CTD First Level Trigger **33**

3.1 Introduction and Overview 33

3.1.1 Introduction 33

3.1.2 Overview 34
3.2 System Layout 41
3.2.1 The z-by-timing Crate 42
3.2.2 The Readout Controller 44
3.2.3 The Timing Controller 48
3.2.4 Communication with the GFLT 52
3.3 The Trigger Processors 53
3.3.1 The Cell Processors 53
3.3.2 The r-ϕ Cell Processor 54
3.3.3 The r-z Cell Processor 55
3.3.4 The Sector Processors 58
3.3.5 The r-ϕ Sector Processor 60
3.3.6 The r-z Sector Processor 60
3.3.7 The Regional FLT 61
3.4 A Prototype System 66
3.4.1 The Prototype LTC 66
3.4.2 The GFLT Test Module 68
3.4.3 Performance on Data from Cosmic Muons 70
3.5 Processor Board Testing 74
3.6 Performance of the FLT on Data 77
3.7 Status and Conclusions 85

4 Supersymmetry **87**
4.1 Beyond the Standard Model 87
4.1.1 Unification of Coupling Constants 87
4.1.2 The Naturalness Problem 88
4.2 Theoretical Motivations for Supersymmetry 91
4.3 Minimal SUSY 93

4.3.1 The Particle Content of the MSSM 93
4.3.2 The Interactions of the MSSM 96
4.3.3 Minimal SUSY Production at HERA 97
4.4 R-parity Violating SUSY Models 100
4.4.1 The Origin of R_p 100
4.4.2 Consequences of R_pViolation 101
4.4.3 $\not{R}_p$ Squark Production at HERA 104
4.5 Existing Limits on Supersymmetry 105
4.5.1 MSSM Limits 105
4.5.2 $\not{R}_p$ Limits 106

5 A Search for s-channel Squark Production at HERA 110
5.1 Introduction 110
5.2 Jet Finding and Reconstruction 112
5.2.1 Jet Multiplicities 113
5.2.2 Jet Algorithms 113
5.2.3 Proton Remnant Treatment 116
5.3 Data Taking and Simulation 117
5.4 Event Reconstruction and Detection Efficiencies 119
5.5 Results and Conclusions 121

6 Tau-Signals for Supersymmetry at HERA 133
6.1 Overview 133
6.2 Introduction 134
6.3 Production Mechanism 137
6.4 LSP Decays 139
6.5 Signals and Backgrounds 144
6.5.1 SUSY Signals 144

6.5.2 Backgrounds 150
6.6 Analysis 152
6.6.1 Positron and Muon Identification 152
6.6.2 Cuts 154
6.6.3 Signal Extraction 155
6.6.4 Discovery Reaches 162
6.7 Summary of Results 169
6.8 Conclusions 170

A Glossary **172**

B MSSM 1.0: A MC Generator for SUSY at HERA **177**
B.1 Abstract 177
B.2 Introduction and Overview 177
B.3 Physics Processes 178
B.4 Gaugino Mixing 179
B.5 R-parity Violating Decays 180
B.6 Assumptions on the SUSY Model 181
B.7 The MSSM Generator - Program Usage and Availability 182
B.7.1 Availability 182
B.7.2 Program Input, The Cards File 183
B.7.3 Program Output Listing 185
B.8 Future Plans 190
B.9 Subroutines and Functions 190

Chapter 1

Introduction

HERA, the Hadron-Electron Ring Accelerator, is the world's first machine to collide electrons head-on with protons (at energies of 30GeV and 820GeV respectively). Previously, fixed target experiments were able to probe nucleonic structure up to a four-momentum transfer squared of $Q^2 \sim 300\text{GeV}^2$. HERA extends this range up to $Q^2 \sim 10^5\text{GeV}^2$. Thus the structure of the proton can be probed at distance scales down to 10^{-18}m.

At HERA electron and proton beams cross every 96ns. However the primary source of detector activity in ZEUS does not come from the e-p interactions of interest, but from other sources. The ZEUS First Level Trigger has the difficult task of rejecting most of these backgrounds, while retaining a high efficiency for the e-p interactions. The first part of this thesis is concerned with the First Level Trigger of the Central Tracking Detector, which was installed at the ZEUS experiment in the first half of 1993, and has since then proven invaluable to the experiment.

The high (design) centre of mass energy of 314GeV at HERA makes it possible to probe a variety of new physics beyond the Standard Model. The large discovery potential for new particles predicted by novel physics theories makes HERA a very promising facility, and an ideal place to look for such 'exotic' phenomena. It is the subject of the second part of this thesis to focus on one such model - Supersymmetry at HERA.

The remainder of this chapter gives a short introduction to the HERA machine, the kinematics at HERA, the deep inelastic scattering formalism and some aspects of the physics at HERA relevant to this thesis.

1.1 The HERA machine

HERA, an electron proton accelerator and the first one of its kind, is situated at the DESY (Deutsches Elektron Synchrotron) laboratory in Hamburg. The HERA machine accelerates electrons and protons in two separate underground tunnels of 6.3km circumference. Collisions are possible in four regions, of which three are currently occupied by experiments: the ZEUS experiment [1] in the south hall, the H1 experiment [2] in the north hall, and the HERMES experiment [3] in the east hall. A layout of the HERA collider is shown in Figure 1.1.

HERA started operation in May 1992 when it collided 26.6GeV electrons on 820GeV protons. During the 1992 and 1993 running periods, HERA provided 29nb^{-1} and 650nb^{-1} of integrated luminosity respectively to the ZEUS experiment.

Eventually the electron beam energy will be raised to 30GeV, and electrons and protons will be accelerated in 210 bunches around the HERA ring, plus a further 10 bunches left empty (the 'pilot' bunches). Pilot bunches consist of full proton bunches but empty electron bunches and vice versa. The crossings of these bunches, during which no e-p collisions occur, can be used by the experiments for measurements of backgrounds. The time between bunch crossings at the interaction point is 96ns. This very short time, together with the high design luminosity, is made necessary by the low (high Q^2) electron-proton cross-sections at HERA energies.

HERA provides a facility to polarise the electron beams: spin rotators just before the interaction regions of the experiments can use the natural transverse polarisation of the electron beam caused by synchrotron radiation to provide longitudinal polarisation up to 80%. Furthermore, by reversing the polarity of the electron ring magnets,

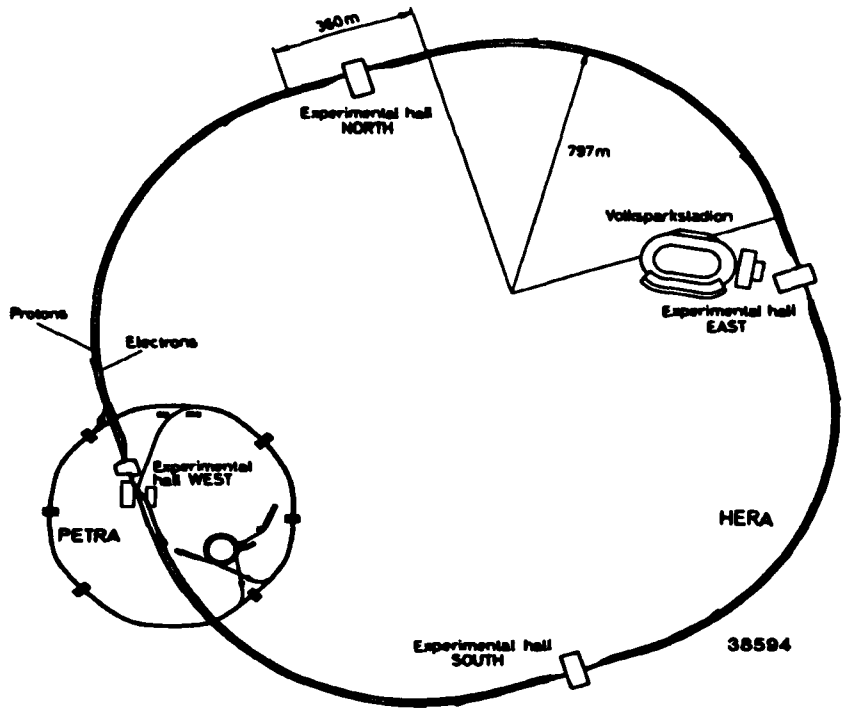


Figure 1.1: Layout of the HERA collider.

it will also be possible to accelerate positrons in place of the electrons. These features of machine operation were not utilised during the 1992/93 running periods.

Table 1.1 summarises the main parameters of HERA.

1.2 HERA Kinematics

HERA is able to investigate the proton structure at much higher energies than previous experiments. Information about the structure of the proton can be obtained by Deep Inelastic ep Scattering (DIS)[1], where the electron scatters elastically from the quarks of the proton. A generic diagram for the inelastic scattering process $e + p \rightarrow l + X$ at HERA is shown in Figure 1.2. Here e, l, P and X denote the initial and final state leptons, the proton and the final hadronic state respectively. The symbols in brackets $(k), (k'), (p), (p')$, are the four-momenta of the respective particles. The exchange vector boson, γ/Z^0 for neutral current (NC) interactions and $W^{\pm}$ for

[1]We refer the reader to the Glossary section at the end of this thesis for a listing of the numerous abbreviations and symbols.

	proton ring		electron ring
Nominal beam energies	820GeV		30GeV
Centre of mass energy		314GeV	
Maximum Q^2		98400GeV^2	
Design Luminosity		$1.5 \cdot 10^{31}$cm^{-2}s^{-1}	
Polarisation time			28min
Number of interaction points		4	
Crossing angle		0°	
Circumference		6.3km	
Length of straight section		360m	
Bending radius	588m		608m
Magnetic field	4.65T		0.16T
Energy range	300-820GeV		10-33GeV
Injection energy	40GeV		14GeV
Total number of particles	$2.1 \cdot 10^{13}$		$0.8 \cdot 10^{13}$
Number of bunches	210		210
Number of bunch buckets	220		220
Time between crossings		96ns	

Table 1.1: HERA design parameters.

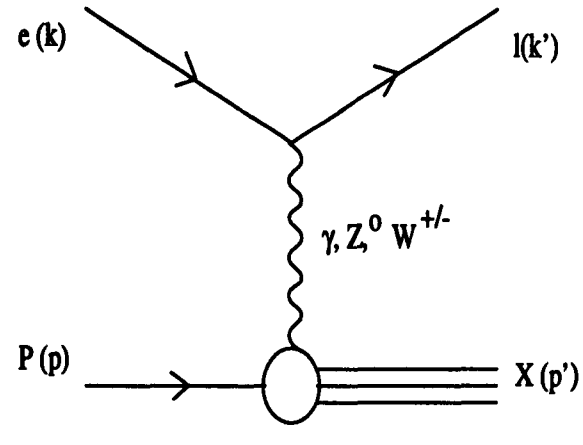


Figure 1.2: A generic diagram of deep inelastic ep scattering.

charged current interactions, has a four-vector $q = k - k'$ which is spacelike.

The overall event kinematics can be fully described by any two independent variables. For example, by measuring the energy and angle of the scattered lepton, one can determine all other variables. In neutral current interactions (see Figure 1.3a) the observed final state in the detector consists of an electron and the final hadronic state, the 'current jet'. The remains of the proton, the diquark jet or 'proton remnant', generally moves very close to the proton direction, and only deposits energy in the calorimeter close to the beam pipe. The kinematics of NC events can thus be determined by a measurement of the electron energy(E_e) and angle(θ_e), or the current jet energy and angle, or a combination of the two measurements. In CC events, the final state lepton is a neutrino (see Figure 1.3b) and only the current jet is visible and hence measurable.

The HERA kinematics is conventionally specified by two out of the three Lorentz scalars Q^2, x and y, where

$$Q^2 = -q^2 = -(k - k')^2 \tag{1.1}$$

is the four momentum transfer squared, and can range from $0 < Q^2 < s$. Here s is the total invariant mass squared $s = (k + p)^2$. In some sense the variable Q^2 defines the resolution with which the proton is probed. A higher value of Q^2 defines

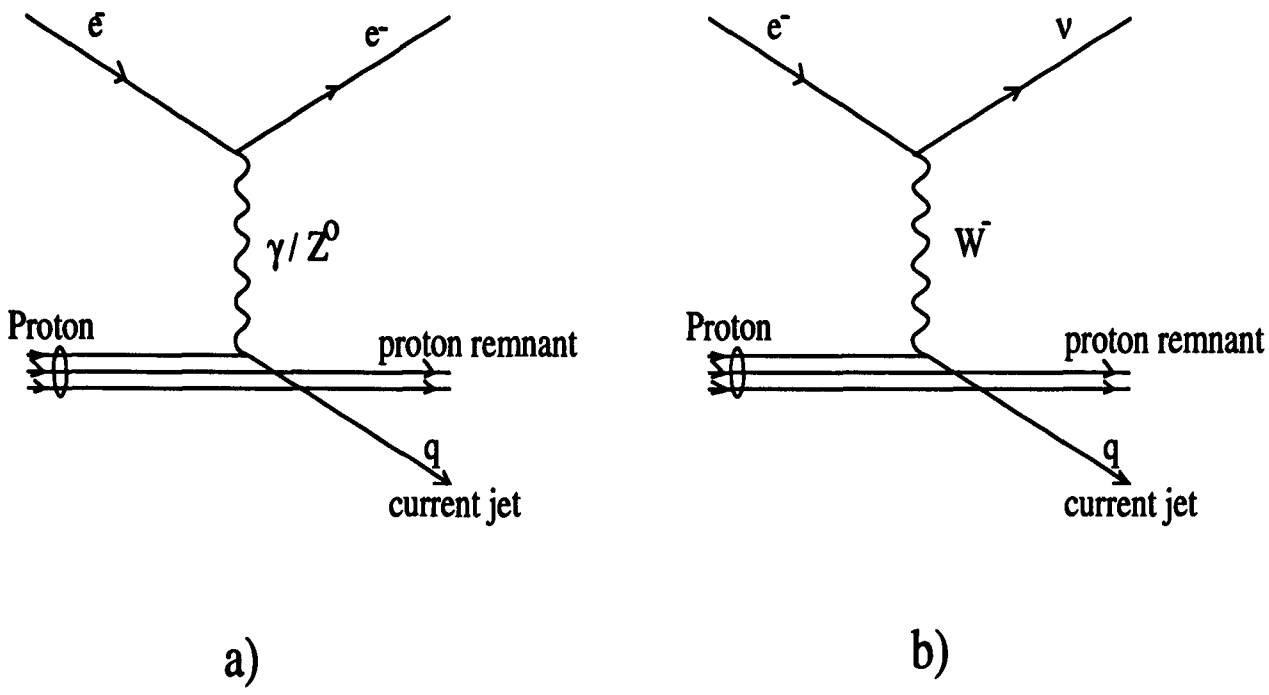


Figure 1.3: Deep inelastic ep scattering at HERA in the quark-parton model. Figure a) shows a neutral current (NC) interaction, and Figure b) shows a charged current (CC) interaction.

a correspondingly smaller distance scale, and hence more and more detail of the structure of the proton is revealed. The dimensionless scaling variables, Bjorken-x and y, are given by

$$x = \frac{Q^2}{2p.q} \tag{1.2}$$

$$y = \frac{p.q}{p.k} \tag{1.3}$$

and are always in the range $0 < x < 1$ and $0 < y < 1$. The inelasticity parameter, y, is commonly used in fixed target experiments, since it is the fractional energy loss of the electron in the proton rest frame. Assuming the quark-parton model (QPM) in which the proton is assumed to consist of individual partons, the Bjorken-x variable corresponds in the infinite momentum frame to the fraction of the proton momentum carried by the struck quark. The three variables x, y and Q^2 are simply related by

$$Q^2 = xys. \tag{1.4}$$

Another kinematical variable of interest at HERA is W, the invariant mass of the

hadronic system, defined as

$$W^2 = (p+q)^2 = Q^2\frac{1-x}{x} + {m_p}^2, \tag{1.5}$$

where m_p is the proton mass. W can also be thought of as the centre of mass energy of the (virtual) γ-p system.

Finally we introduce a variable of experimental interest, the $E - p_z$ quantity. E is the sum of the total energies of the final state particles in the detector, and p_z is the sum of the z component of momentum [2] of all particles measured in the detector. Since it is a conserved quantity, if all final state particles are detected, it is easy to see that $E - p_z = 2A$ (where A is the initial electron energy). However, if for example the final state electron were not detected, it would not be included in the $E - p_z$ sum, and hence $E - p_z < 2A$. Therefore $E - p_z$ is a good variable to identify events where low angle electrons escape detection down the beam pipe. Note that since $E \approx p_z$ for proton remnants close to the beam pipe, low angle diquark fragments do not contribute to the $E - p_z$ sum. $E - p_z$ is also a good variable for discriminating against proton beam-gas events (see Chapter 2). Here an electron does not participate in the collision process, hence $E - p_z < 2A$ always.

1.3 Physics at HERA

1.3.1 Deep Inelastic Scattering

Let us now turn to the deep inelastic scattering formalism and cross-sections at HERA. Without making any assumptions on the proton structure, the e-p cross-section can be written in terms of the leptonic and hadronic tensors $L^{\mu\nu}, W_{\mu\nu}$ as [4]

$$\frac{d^2\sigma}{dQ^2dW^2} = \frac{2\pi m_p \alpha^2}{Q^4} L^{\mu\nu} W_{\mu\nu}. \tag{1.6}$$

[2] The z-axis is defined to point along the proton direction. For a description of the ZEUS coordinate system see chapter 2.

Here $W^{\mu\nu}$ parameterises the hadronic current as resolved by the exchanged electroweak bosons, m_p is the proton mass and α is the fine structure constant. Writing $W^{\mu\nu}$ in its most general Lorentz invariant form and applying current conservation at the hadronic vertex, it can be written as :

$$\begin{aligned} W^{\mu\nu} &= -W_1(g^{\mu\nu} + \frac{q^\mu q^\nu}{Q^2}) \\ &\quad + W_2\frac{1}{m_p^2}(p^\mu + \frac{p\cdot q}{Q^2}q^\mu)(p^\nu + \frac{p\cdot q}{Q^2}q^\nu) \\ &\quad - W_3\frac{i}{m_p}\epsilon_{\mu\nu\rho\sigma}p^\rho q^\sigma. \end{aligned} \tag{1.7}$$

Here the W_i are the 'structure functions', and are (in general) functions of x and Q^2. The structure functions express in some sense our ignorance of the details of the hadron-electroweak boson interaction vertex.

Under the assumption of the naive quark-parton model (i.e. the interacting quark is massless, and does not interact with other quarks) the structure functions *scale*, that is, the structure functions only depend on the scaling variable x, so that $W_i(x, Q^2) \longrightarrow F_i(x)$. One can then construct sum rules relating the structure functions to the distribution of quarks inside the proton by [4]

$$F_2(x) = x\sum_i e_i^2 q_i(x) \tag{1.8}$$

and thus give the structure function a physical interpretation. Here the function $q_i(x)$ is the probabilities that a struck quark of flavour i carries a fraction x of the proton momentum, and e_i^2 is the electric charge of the quark.

In Quantum Chromo Dynamics (QCD), the strong forces are mediated by colour fields, the gluons. The assumption that partons cannot interact with each other is no longer valid, as quarks can now interact via gluons. Consequently the structure functions will become Q^2 dependent, i.e. $F_i(x, Q^2)$. Thus QCD predicts that the structure functions do not scale, but evolve in Q^2.

Comparing the structure functions measured at previous fixed target experiments [5] with the corresponding structure functions measured at HERA will thus provide an important test of QCD. The large gap between previously measured Q^2 s of $\sim$ 300GeV^2 and the maximum Q^2 accessible at HERA of 98400GeV^2 makes this machine particularly sensitive to scaling effects, and thus to quantitative tests of QCD.

1.3.2 Low-x Physics

In the low-x region ($x < 10^{-3}$) QCD evolutions predict a strong rise in the structure functions as x decreases. When x becomes sufficiently small, the structure functions eventually violate unitarity bounds. In this region, perturbative QCD begins to break down. Measurements of the low-x regime will therefore allow investigations of non-perturbative QCD dynamics.

Furthermore, as can be seen from equation (1.4), at fixed values of Q^2 the variable x can become small for large s. Due to the high centre of mass energy accessible at HERA a completely new domain at low-x can be measured and compared with perturbative QCD predictions.

1.3.3 Photoproduction

In photoproduction (i.e. γ-p scattering) processes, the interacting photon radiated by the electron is almost real, i.e. $Q^2 \sim 0$. In this class of event, the electron is hardly scattered at all, and its direction only changed by a small amount. Thus the electron generally escapes detection by the central ZEUS detectors (such as the calorimeter), and only the resulting hadronic system is seen by the detectors. Photoproduction processes constitute the bulk of 'physics' cross-sections at HERA, and have been measured to be $(153 \pm 16(stat.) \pm 36(syst.))\mu b$ at $\sqrt{s} = 210GeV$ [6, 7].

Photoproduction processes are of particular interest at HERA, as they will provide measurements of the parton distributions within the photon (the 'photon structure

function'), as well as measurements of the gluon density inside the proton.

1.3.4 Physics beyond the SM - Exotic Physics

The high centre of mass energy of 314GeV at HERA makes it possible to test the ideas of a variety of proposed new physics models beyond the Standard Model (SM). Several theories based on the ideas of Grand Unification predict the existence of so-called 'leptoquarks' and 'leptogluons'. New lepton-quark and lepton-gluon forces can result in leptoquark and leptogluon states, which (depending on the model) are either pointlike or have a spatial extend. The leptoquarks (leptogluons) are produced as s-channel resonances of the electron and the quark (gluon) of the proton. Such s-channel processes are characterised by a peak in the kinematical variable x, which if seen in the DIS cross-section measurements would imply the existence of such particles.

Furthermore, electrons and quarks can be probed for substructure. The idea of compositeness leads to excited states of electrons and quarks. Such states can give rise to exotic signatures in the ZEUS detector.

The existence of new heavy electroweak bosons is predicted by a number of extensions to the Standard Model. Such heavy bosons would cause changes in the predicted deep inelastic scattering cross-sections of the SM.

Supersymmetry predicts the existence of a large spectrum of new particles. The search for supersymmetry at HERA is the particular interest of this thesis, and we refer to chapters 4,5 and 6 for further discussions of the subject.

1.4 Overview

This thesis can be outlined as follows. The first part of the thesis is concerned with the First Level Trigger (FLT) of the Central Tracking Detector (CTD). Chapter 2 describes the individual components of the ZEUS detector. Particular emphasis is placed on the Central Tracking Detector and its readout hardware. Furthermore,

the reader is introduced to the ideas of a 'pipelined' system. This is necessary in the ZEUS environment for triggering and detector readout because of the very short beam crossing time of 96ns. Chapter 3 discusses the CTD First Level Trigger in detail. We introduce the principles of the First Level Trigger tracking algorithms, and discuss the hardware implementation. A prototype system which was used during the early stages of the ZEUS experiment is presented. We comment on the testing of the trigger hardware, and discuss some aspects of the CTD first level trigger data from the 1993 running period.

The second part of the thesis investigates models of supersymmetry at HERA. Chapter 4 gives an introduction to supersymmetry (SUSY), discusses notations and parameter space, and lists previous limits on SUSY from other experiments. Chapter 5 presents a search for s-channel squark production in the 1992 ZEUS data. We have found no evidence for supersymmetry in the data, and thus can set discovery limits. Chapter 6 investigates the future potential of HERA for producing SUSY via pair-production mechanisms. This is achieved by running detailed Monte Carlo simulations of the processes. We show that for certain SUSY models the potential discovery reach of supersymmetry at HERA is large, and the sum of the combined squark and selectron mass reach can be as high as 205GeV. This makes HERA a unique place to look for supersymmetry.

Part One

The ZEUS First Level Tracking Trigger

Chapter 2

The ZEUS Detector

2.1 Overview

The ZEUS detector, a multipurpose detector designed to measure a variety of physics processes, is shown in figure 2.1. Its asymmetric shape in the forward direction[1] is designed for the imbalance of the beam energies, resulting in a boost of the interaction products along the proton direction.

The essential elements of the detector are a vertex detector (VXD); a tracking system consisting of Central Tracking Detector (CTD), forward and rear planar drift chambers (F/RTD), and a transition radiation detector (TRD); an electromagnetic (EMC) and a hadron calorimeter (HAC); a backing calorimeter (BAC); a barrel and rear muon detector (B/RMUON) and a forward muon spectrometer (FMUON). The individual components are discussed in section 2.2, and section 2.3 concentrates on the Central Tracking Detector and its readout. The final section (2.4) places particular emphasis on the ZEUS data aquisition (DAQ) and trigger system in preparation for chapter 3, which treats the CTD first level trigger and the CTD DAQ system in more detail.

[1]The ZEUS coordinate system is defined such that the z-axis points along the proton beam direction, the x-axis points horizontally towards the centre of HERA, and the y-axis completes a right-handed coordinate system. The polar angle θ is measured from the positive z-axis, such that the proton beam (or forward) direction is at $\theta = 0°$, and the (backward or rear) electron direction is along $\theta = 180°$.

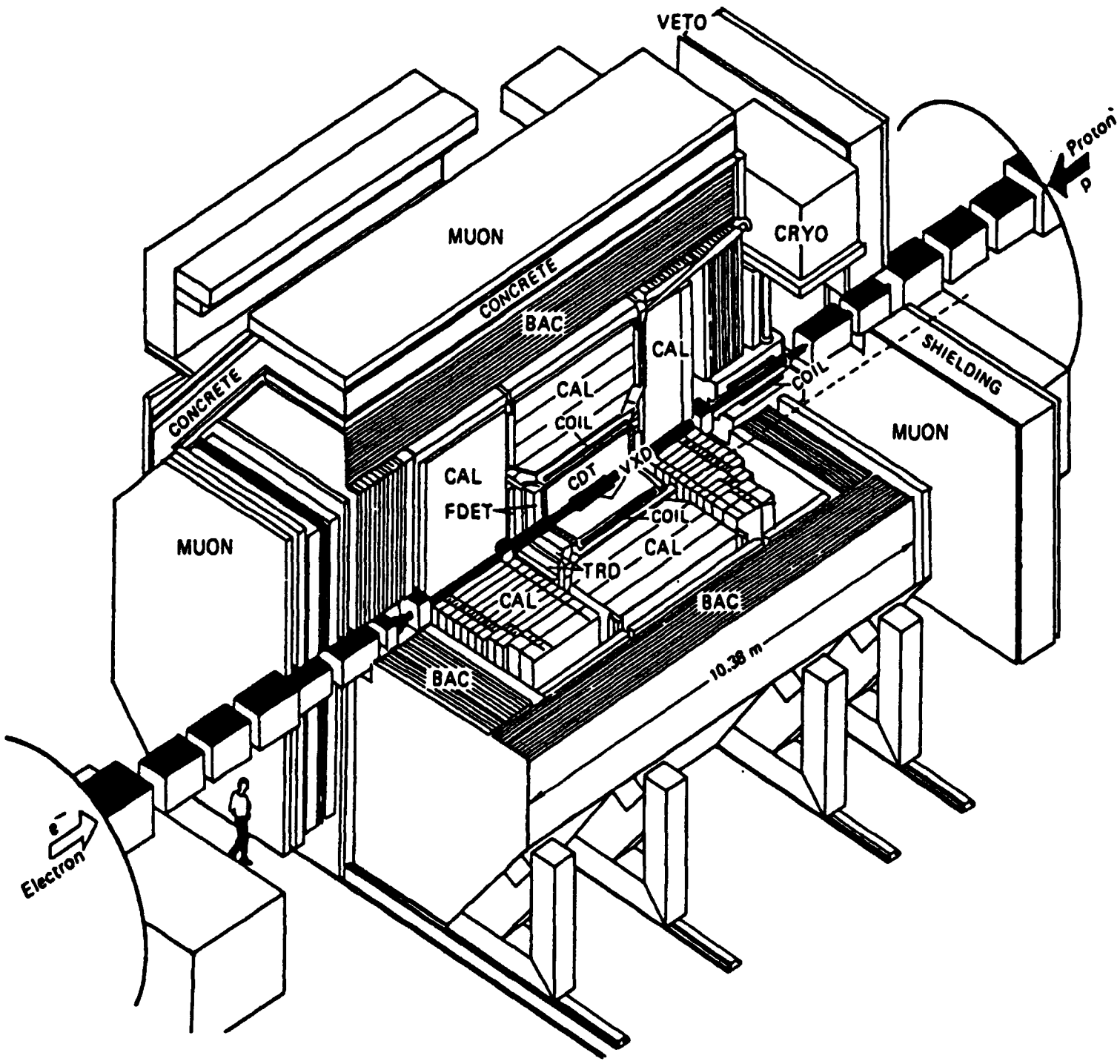


Figure 2.1: The ZEUS detector

A superconducting solenoid, located between the Central Tracking Detector (CTD) and the uranium calorimeter (UCAL) produces a magnetic field of 1.43 Tesla. It enables charged particle momentum measurements in the CTD. Conducting coils and the return flux of the solenoid induce a further toroidal magnetic field of 1.6Tesla (nominal) in the iron yoke, which consists of large iron modules placed around the ZEUS detector. Together with the muon detectors, located in front and behind the iron modules, they form the muon detection system.

2.2 The ZEUS Components

There follows below a brief description of the individual components of the ZEUS detector [1], starting from the innermost detector:

- The Vertex Detector (VXD): The VXD, a multiwire drift chamber, uses a slow gas (dimethyl ether) to increase drift times to obtain a high spatial resolution. Its purpose is to measure the vertex position of the interaction in r-ϕ with an intrinsic spatial resolution of $30\mu m$, and to enable detection of secondary vertices of short-lived particles.

- The Central Tracking Detector (CTD) is described in section 2.3.

- The Forward and Rear Tracking Detectors (FTD and RTD): The F/RTD are designed to increase the polar angle, θ, coverage of the tracking system. The RTD in particular plays an important role in the measurement of scattered primary electrons in low Q^2 events at backward angles.

  The FTD (RTD) consists of three (one) sets of planar drift chambers. Each chamber set is a sandwich of three layers of drift cells, inclined with respect to each other at angles of 0°, +60° and −60°. A momentum measurement of the charged particles is only possible together with the CTD. The angular coverages are:

	polar angular coverage
FTD	$7.5° \rightarrow 28°$
RTD	$159° \rightarrow 170°$

- The Transition Radiation Detector (TRD): The TRD consists of four modules, each 1cm deep, containing a polypropylene fibre radiator stack followed by a xenon filled drift chamber. Two packages of two modules are sandwiched between the three FTD chambers. The purpose of the TRD is to allow electron identification within the momentum range 1 to 30GeV with a hadron/electron rejection ratio of about 10^{-2}.

- The Uranium Calorimeter (UCAL) is divided into Forward, Barrel and Rear (F/B/RCAL) depleted uranium-scintillator calorimeters. The self-compensating nature of the depleted uranium (DU) ensures that the electromagnetic(e) to hadronic(h) energy response is e/h $\sim$ 1, which helps to minimise errors in the hadronic energy measurement since $\pi^{\pm}$ and π^0 s give approximately equal response. Self-compensation is achieved by a judicious choice of relative thickness of the layered depleted uranium and scintillators. Fission and spallation processes in the uranium nucleus will result in the creation of low energy neutrons, which give rise to further detectable showers in the scintillator, and hence compensation.

DU plates and plastic scintillators are interleaved in multiple layers, and wavelength shifter bars and lightguides transport the signals to the photomultiplier readout. Each calorimeter tower is divided up into sections of one EMC and one (or two) HAC modules (RCAL or FCAL,BCAL), which are stacked above each other. There are four (two) EMC cells per module in the F/BCAL (RCAL), but only one HAC cell per module, and their cell dimensions are given below.

	FCAL	BCAL	RCAL
EMC cell dimension	$20 \times 5cm^2$	$24 \times 5cm^2$	$20 \times 10cm^2$
HAC cell dimension	$20 \times 20cm^2$	$24 \times 20cm^2$	$20 \times 20cm^2$

The UCAL is 99.7% hermetic in the 4π solid angle , has a high energy resolution of $\sigma(E)/E = 35\%\sqrt{E}\oplus 2\%$ for hadrons [2] (where E is measured in units of GeV), and a medium energy resolution of $\sigma(E)/E = 18\%\sqrt{E} \oplus 1\%$ for electrons. Its angular resolution for jets is better than $10mrad$.

- The Hadron Electron Separator (FHES and RHES) consists of a series of silicon pads, installed at a three radiation length depth in the F and RCALS. The HES is designed to identify electrons within dense jets.

- The Backing Calorimeter (BAC) is part of the iron yoke absorber with aluminium proportional tubes, and surrounds the uranium calorimeter. It measures late showering particles not fully contained inside the main calorimeter with an energy resolution of $\sigma(E)/E \sim 100\%/\sqrt{E}$.

- The Muon Detectors (F/B/RMUON) are planar drift chambers and streamer tubes. Together with the iron yoke they enable muon detection and independent momentum measurements , with design resolutions given below.

$$\begin{array}{ll} \text{FMUON} & \frac{\sigma(p)}{p} = 23\% \text{ at } p_\mu = 100 \text{ GeV/c} \\ \text{B/RMUON} & \frac{\sigma(p)}{p} = 30\% \text{ at } p_\mu = 20 \text{ GeV/c} \end{array}$$

- The Leading Proton Spectrometer (LPS): The LPS consists of six miniature silicon detectors in Roman pots positioned between 20-90m downstream in the proton beam direction. The LPS measures the momentum of low angle debris of the protons or leading protons in elastic and diffractive photoproduced γ-p events.

- The Luminosity Monitor (LUMI): The LUMI consists of two Pb/scintillator calorimeters divided up into electron and photon detectors distanced 36m and 108m away respectively from the interaction point in the electron beam direction. The LUMI allows not only a luminosity measurement via the high energy

[2] where $\oplus$ means added in quadrature.

bremsstrahlung process ep $\rightarrow$ epγ, but also small angle electron tagging in photoproduction events.

- The VETO wall (VETO): A scintillator hodoscope placed either side of an iron wall 7m upstream of the proton beam rejects very upstream beam-gas interactions produced outside the detector.

- The C5 counter: The C5 consists of silicon counters placed around the beam pipe just behind the RCAL. The C5 can be used to veto events produced outside the interaction region or beam halo travelling close to the beam line.

2.3 The Central Tracking Detector

The CTD is a cylindrical drift chamber of 2m length and 1.9m diameter. Situated in the centre of the ZEUS detector it provides the principal 3D tracking information of charged particles, and enables particle identification through a measurement of the ionisation energy loss $\frac{dE}{dx}$ as the particle traverses the tracking chamber.

The chamber is organised in nine radial superlayers (SLs), each further subdivided into 8 sense layers (see Figure 2.2). The odd numbered SLs are axial layers, whereas the even numbered SLs are 'stereo' layers, inclined to the z-axis by stereo angles of approximately $\pm 5°$. The basic geometrical unit of a superlayer is a drift cell (Figure 2.3), consisting of a plane of eight sense wires with ground wires interleaved, and a field wire plane to either side of it. The sense wire plane is inclined to a radial line from the chamber axis by 45°. Given a specific magnetic field, the chamber gas and drift field can be chosen to give a Lorentz angle of 45°, and hence an azimuthal electron drift [8].

A positional r-ϕ measurement is achieved by determining the drift time of the ionisation of the chamber-gas (induced by a charged particle) to the nearest sense wire. This will yield two possible reconstructed points either side of the sense wire -

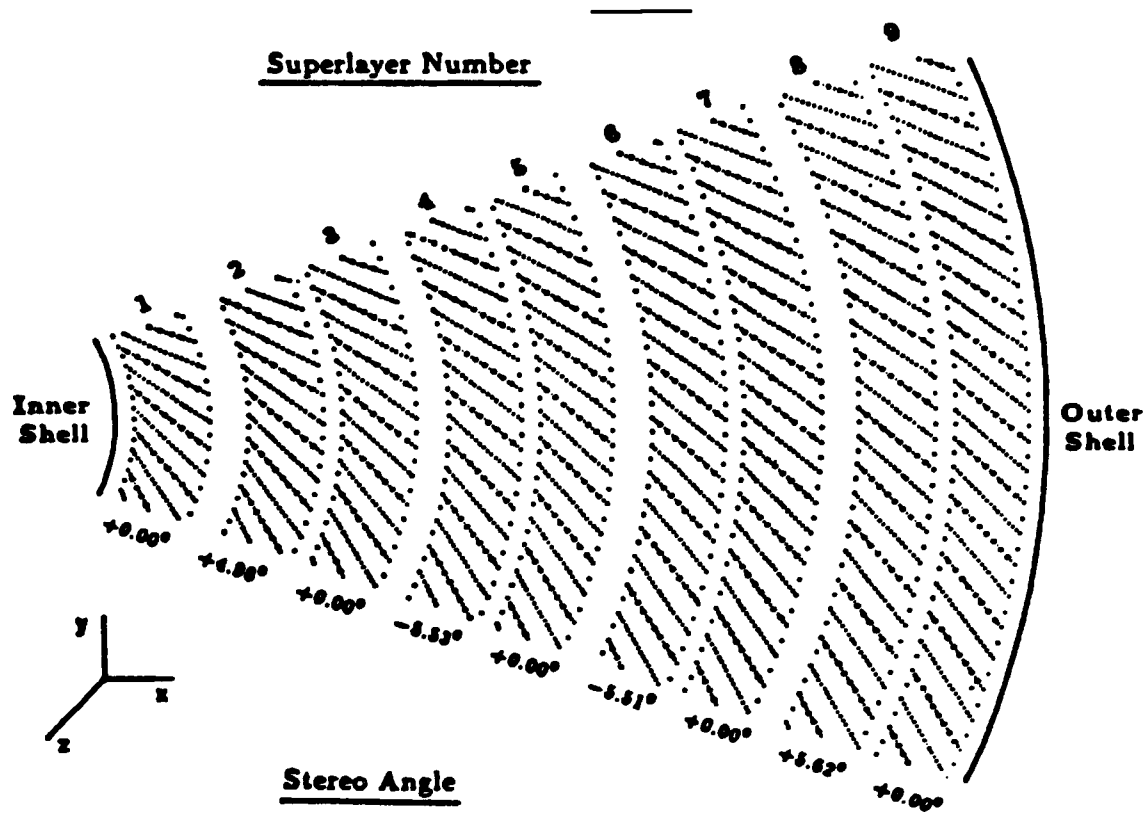


Figure 2.2: A sector of the CTD, showing superlayer, layer and drift cell structure.

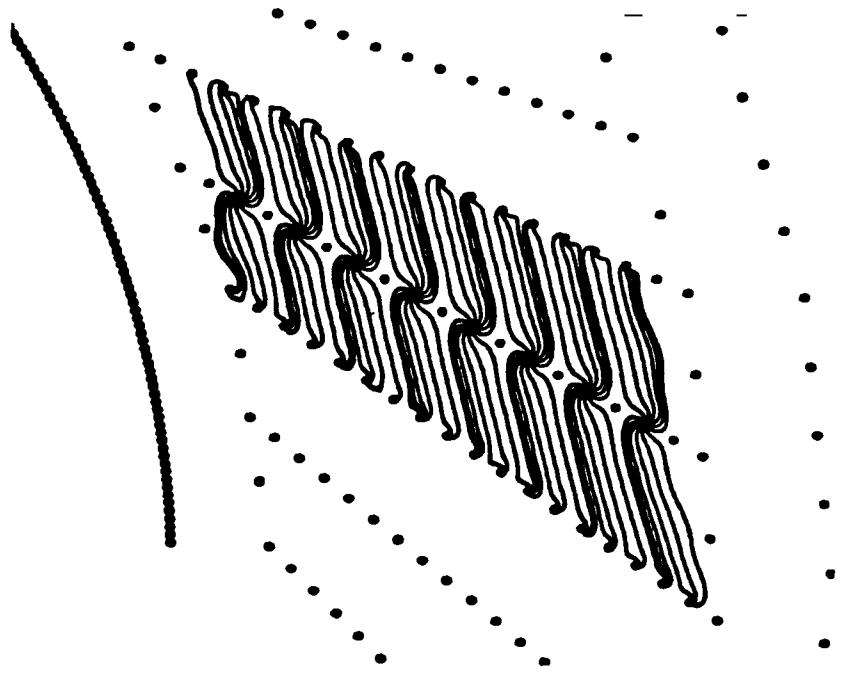


Figure 2.3: CTD drift cell, showing the electron drift lines to the sense wires.

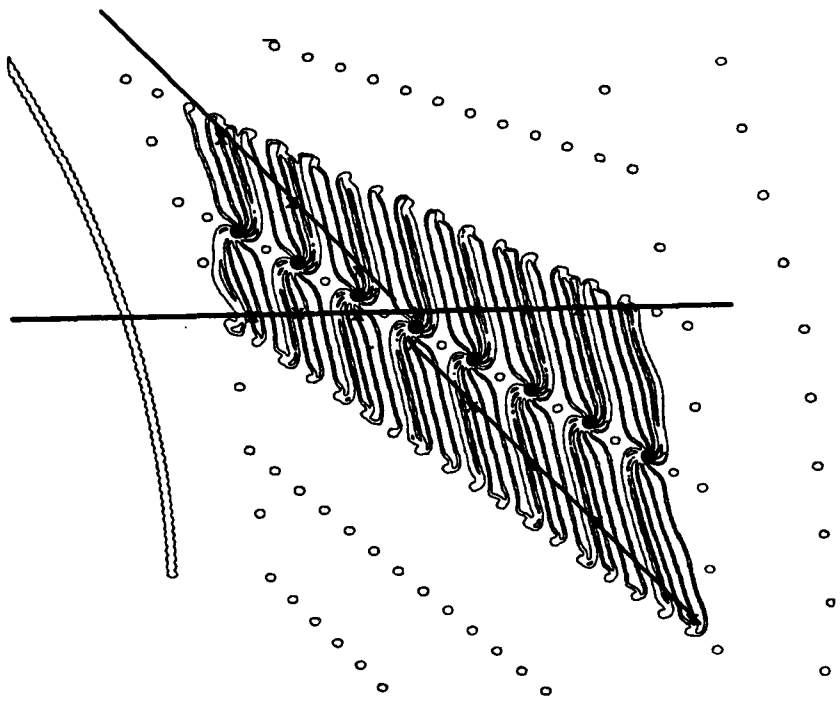


Figure 2.4: A reconstructed track crossing a sense wire plane. Ghost hit (or left-right) ambiguities can be resolved by demanding a continuous track at the geometric interface.

only one lies on the particle trajectory, the other point is called a 'ghost'. Furthermore the maximum drift time of approximately 500ns (which is almost equivalent to five bunch-crossings of HERA) means that hits from different crossings can also contribute to hit misidentification. Figure 2.4 shows how these ambiguities can be resolved when the particle track crosses a geometric interface (a sense or a field wire plane) by demanding continuity of the track. In this way one can determine the bunch crossing of the event from which the track originated. Note that the 45° tilt of the sense wire plane ensures that essentially all particles cross one such interface within each superlayer [9].

The z-coordinate of a hit can be obtained from a full 3D offline '$r-\phi$' reconstruction of both axial and stereo superlayers. This method, although accurate, is far too slow compared to the total processing time available to the First Level Trigger, which in principle has to make a decision every 96ns[3]. Therefore the CTD employs

[3]The ZEUS First Level Trigger has to arrive at a trigger decision after 52 bunch crossings, but

Total number of wires	24192
Number of sense wires	4608
Magnetic field (Nominal)	1.43T (1.8T)
Gas mix (Nominal)	90:8:2 Ar:CO_2:Ethane bubbled through ethanol (50:50 Ar:Ethane bubbled through ethanol)
Drift velocity	52μm/ns
Maximum drift time	500ns
Momentum resolution	$\frac{\sigma(p)}{p} = 0.0021p \oplus 0.0029(GeV/c)$ at 90°
$\frac{dE}{dx}$ resolution	< 6% for electrons
Polar angle coverage	15°-164°
r-ϕ position resolution	120-130μm
z resolution (stereo)	1-1.4mm
z-by-timing resolution (nominal)	4cm (3cm)

Table 2.1: Properties and Parameters of the CTD

two distinctly different readout systems: a slow and accurate r-ϕ system [10], and a fast z-by-timing system [11]. The later is used as input to the CTD trigger. Table 2.1 summarises the properties and parameters of the CTD.

2.3.1 The r-ϕ System

All of the 4608 sense wires are read out by the r-ϕ system. Preamplifiers directly mounted on one endplate of the CTD (or both endplates if the superlayer is also equipped with z-by-timing readout) amplify the signals before they are sent down 42m halogen-free coaxial cables to the 'rucksack', which houses all the ZEUS readout and trigger electronics. Postamplifiers further amplify the signals and then send them to 104MHz Flash Analogue-to-Digital Converter (FADC) cards, which digitise the pulses into 8-bit words every 9.6ns. Each card services two cells, i.e. 16 channels. The

individual decisions have to be segmented into 96ns time intervals in order to 'keep up' with the input data. The ZEUS trigger and the principle of pipelining are described in section 2.4.

outputs of the 16 FADC channels are fed into an on-board Digital Signal Processor (DSP) which then zero-suppresses the data and improves the drift time resolution to approximately 2.4ns by fitting the leading edge of the signal to a pulse-shape parameterisation [12]. In addition the pulse heights are computed by this algorithm for subsequent use in dE/dx analysis.

2.3.2 The z-by-timing System

The z-by-timing method uses the time difference in the arrival times of the pulses (Δt) at either end of the axial sense wires to determine the z-position of the hit. The measured time difference is converted to a voltage proportional to Δt by a Time-to-Amplitude Converter (TAC), and is finally digitised by an 8bit FADC into a 7+1 bit word (the 8^{th} bit corresponds to a hit flag). The processing and digitisation occurs every 48ns, and this allows a coarse r-ϕ measurement to be made. The drift time resolution is approximately $48/\sqrt{12} \sim 14ns$, which results in a nominal spatial resolution of 750μm [1] in r-ϕ. A design resolution in Δt of 200ps corresponds to a z-resolution of 3cm for a single hit [11].

The z-by-timing readout is used by the CTD First Level Trigger (FLT). In order to reduce costs only SL1 is fully equipped with z-readout. The larger lever arm in higher superlayers (and hence the better effectiveness in multi-track resolution) means that only alternate sense wires in SL3 and SL5 are equipped with z-readout. Before the 7 bit z-value is transferred to the FLT-processors, it is corrected for small non-linearities in the time difference to position relationship [13], and is then converted into a z/r-value (i.e. equivalent to cot(θ)). Both correction and conversion are implemented using an on-board look-up table in the form of a PROM [4].

[4]Programmable Read Only Memory

2.4 The ZEUS DAQ and Trigger System

The short time of 96ns between bunch crossings at HERA and the high rates of background processes to the interesting physics interactions place stringent requirements on the ZEUS DAQ and trigger system. The design is therefore in many ways different to that of other HEP experiments today in that it employs pipelined, asynchronous and parallel processing methods throughout [14].

Turning to the background processes, the main sources are:

- Collisions between beams and residual gas in the beam pipe. This type of background is commonly referred to as a beam-gas (electron or proton beam-gas) interaction.
- Beam-scraping halo, produced by dispersed particles colliding with beam pipe walls, magnets and collimators.
- Synchrotron radiation from the electron beam as it is bent towards the interaction region.
- Cosmic ray muons.

Of these, beam-gas and beam-scraping events are by far the dominant background, and their rates are 20-80kHz and 20-450kHz [19] respectively. On the other hand, the rate of interesting DIS ($Q^2 > 10GeV^2$) physics processes is of the order of 1Hz. A data volume of $\sim$ 100 kB/event dictates the maximum rate at which events can be written to magnetic storage to be within 3-5Hz, and therefore a high performance trigger system is needed to reject 99.999% of the backgrounds while retaining most of the physics events.

The ZEUS three level trigger system is shown schematically in Figure 2.5. The first level is a component-based hardware trigger. It is required to make a decision $52\times$96ns$\sim 5\mu s$ after the start of the processing of an event, and to reduce the maximum

input rate of 10MHz to an average of 1kHz. Hence the First Level Trigger (FLT) must be deadtime free; it has to be able to continuously accept data for input, process it and in principle make an FLT decision every 96ns. This can only be achieved by breaking up the complicated tasks into smaller steps. Each step must be simple enough such that it can be executed within 96ns; output from one step is pipelined into the next step. Figure 2.6 shows the data flow in such a system. The data is stored in pipelines in the form of circular buffers. Only in the case of a positive FLT-accept decision is the data transferred from the front-end pipelines to the second level trigger (SLT) buffers (Figure 2.6). It is the maximum speed of the transfer to the SLT buffers that determines the maximum FLT output rate of 1kHz. For some components like the CTD the information has already been digitised and is therefore stored in digital pipelines; other components like the calorimeter store their information in analogue pipelines in the form of a switched capacitor array.

After each component's FLT has made a decision, which happens a fixed time between $1\mu s$ and $2.5\mu s$ (depending on the component) after the crossing occurred, it sends its recommendation for accepting or rejecting an event together with additional trigger information to the Global First Level Trigger (GFLT). The GFLT spends a large fraction of its time synchronising the components' data. It then combines the various subtriggers, and in case of a positive GFLT decision it sends the beam crossing number of the event that caused the trigger to all components. This occurs exactly 52 bunch crossings (i.e. $5\mu s$) after the interaction, and hence the components can determine the offset in the pipelines to find the data from the relevant event.

The Fast Clear (FC) is designed to abort an event after a trigger accept has already been issued by the GFLT, but before the transfer of the data to the SLT has been completed. Its purpose is to reduce deadtime incurred from the large readout and FADC processing time of the UCAL information. The FC only starts processing calorimeter data if a GFLT accept decision has already been issued, and the decision

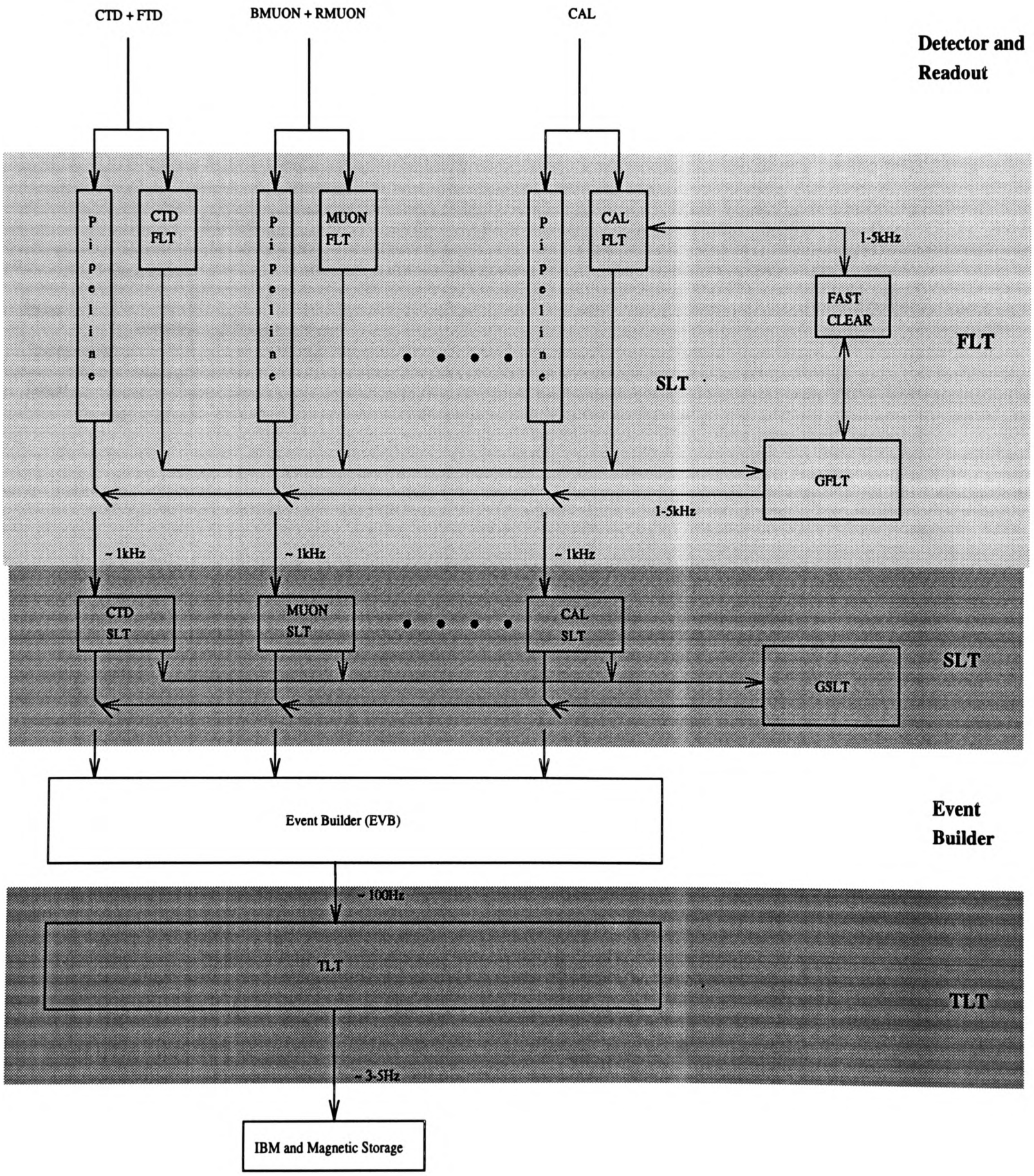


Figure 2.5: The ZEUS trigger system

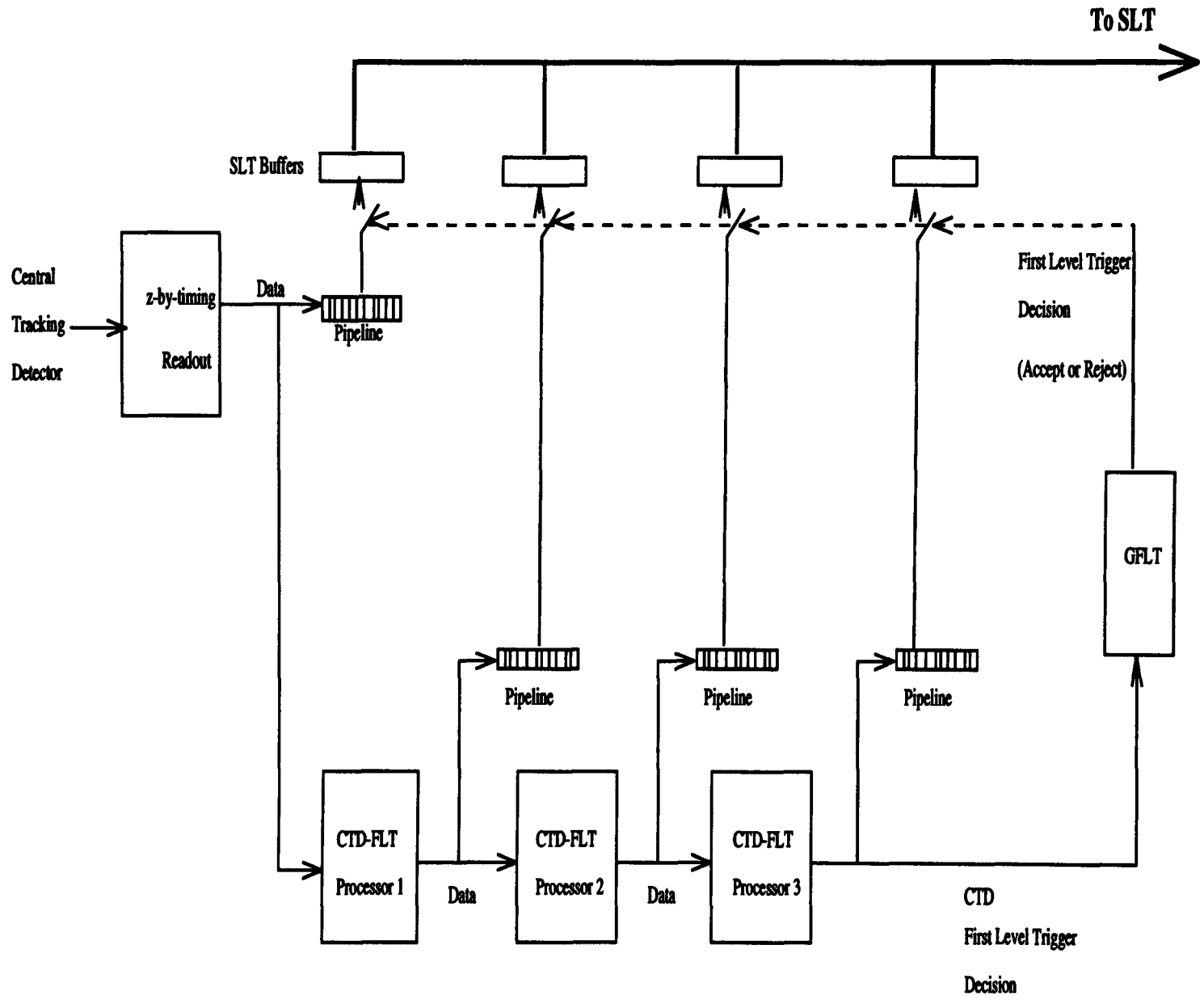


Figure 2.6: A typical processing cycle in the ZEUS pipelined trigger environment. The data is read out, digitised, stored in pipelines, processed by the FLT, and in the case of a positive trigger decision finally transferred to the SLT buffers.

was partly based on the CAL-FLT. It uses more sophisticated algorithms not possible in the CAL-FLT to decide whether the event was a background event. If it decides to clear (i.e. veto) an event, the transfer of data from the front-end pipelines to the SLT buffers (which started when the GFLT issued an accept) is immediately aborted, and the event is discarded. Should another GFLT accept decision arrive within the FC processing time, then the FC stops processing and moves on to the next event, losing the option to clear the current event. Given an average processing time of $20\mu s$ this mechanism can reduce a 5kHz GFLT output rate to 1kHz [15]. However it does become a lot less efficient when the GFLT rate exceeds 5kHz.

Like the FLT, the Second Level Trigger (SLT) is component-based. The average event processing time of $1ms$ enables the use of more elaborate software algorithms like pattern matching, track finding, cluster finding and electron identification to make a trigger decision. The SLT has access to the full digitised event data. Algorithms are run on transputer networks [5], allowing for both more flexibility in the algorithms and a higher degree of asynchronisation between components. All the components' SLT information is fed into the Global Second Level Trigger (GSLT), which has to reduce the average input rate of 1kHz to an average output of 100Hz or less.

If the event survives the SLT, all the components' data are collected and synchronised to form a consistent event record by the Event Builder (EVB), an array of transputers. The event is then passed on to the Third Level Trigger (TLT) where the final accept decision is made.

The TLT utilises a network of Silicon Graphics workstations to run global reconstruction code on the entire event. Whereas the FLT and SLT strategy is based on rejecting backgrounds such as beam-gas and beam-scraping events , the TLT also has to reduce some of the high rate physics processes (such as photoproduction) to produce a net output rate of 3-5Hz. The data is then sent to the IBM mainframe,

[5] A transputer is a single chip microcomputer, with on board microprocessor, memory and communication interface.

which writes it onto magnetic cartridges.

We now proceed in chapter 3 to discuss the CTD First Level Trigger at length.

Chapter 3

The CTD First Level Trigger

3.1 Introduction and Overview

3.1.1 Introduction

This chapter describes the hardware aspects and functionality of the CTD First Level Trigger (CTD-FLT) in some detail. The author was personally involved in work on the prototype Local Timing Controller (section 3.4.1) and the Global First Level Trigger test module (section 3.4.2). The modules were used during the run-up and cosmic ray data-taking periods with the ZEUS detector, which took place in late 1991/92 before the start-up of HERA. In order to introduce the reader to the details of the functionality and implementation of both modules, we have preceded section 3.4 ('A Prototype System') with an introductory section (section 3.2, 'System Layout') on communication and timing aspects of the FLT-system.

The author was furthermore involved with work on the CTD-FLT test software and FLT-processor board testing both at the Rutherford Appleton Laboratory and at DESY. The author worked on data aquisition (DAQ) aspects of the FLT, and contributed to work on the integration of the FLT with other ZEUS components before the startup of HERA in June 1992. In order to make this a self contained chapter on a wide range of aspects of the CTD-FLT, a short description of the functionality of the trigger processors is given in section 3.3. Complete accounts on the design

and implementation of the FLT logic can be found in [16, 19]. Section 3.5 comments on the processor board testing and verification of their functionality, and section 3.6 discusses some aspects of the online performance of the CTD-FLT on data from the 1993 running period. Section 3.7 offers preliminary conclusions on the first level tracking trigger and lists future plans for next year's running period (1994).

3.1.2 Overview

Most components' FLTs are able to base their decisions mainly on global detector activity - the Calorimeter for example uses energy sums, E_T and missing p_T triggers. Unfortunately any simple CTD activity criteria such as *number of hits* is not a good discriminator between physics processes and backgrounds (such as beam-gas interactions) and cannot be used as a trigger. Proton beam-gas interactions and beam-scraping halo from upstream of the proton beam often produce a large number of tracks (and a large number of hits) in the CTD, however all pointing to an interaction vertex outside the ZEUS detector, upstream of the proton direction. On the other hand, interesting physics events (such as high Q^2 DIS) can also have high hit multiplicities, but with vertices originating from around the nominal e-p interaction point. It is therefore much more useful to determine whether an event has originated from a vertex inside the interaction region, and to count the track multiplicity of an event rather than discriminating against the number of hits. However such criteria entail the need for fast 3D track reconstruction. As a result the CTD-FLT [16, 17, 18, 19] is the most complex and sophisticated hardware trigger employed in the ZEUS experiment.

The Tracking Algorithm - Principles

The CTD-FLT algorithm must be sufficiently simple such that it can be implemented in hardware, but sophisticated enough to identify event vertices originating

from the interaction region and to determine track multiplicities. We now describe such an algorithm:

A track is made from individual segments, the track segments. Because only superlayers one, three and five (SL1, SL3 and SL5) are equipped with z-by-timing readout, the tracks are naturally made up of SL1, SL3 and SL5 track segments. A segment consists of a pair of adjacent cells, referred to below as 'cellpairs'. It is necessary to consider two adjacent cells since, because of the 45° inclination of the cell, a straight (or curved) track from the origin will generally cross a cell boundary. There are 32 overlapping cellpairs, corresponding to the 32 cells in SL1. Cellpair 1 contains cells (32,1), cellpair 2 cells (1,2) and so forth. Overlapping cellpairs have the advantage that most of the tracks are contained within one cellpair. In order to simplify the track segment- finding algorithm further, the trigger processor does not consider a full 3D segment in a given cellpair, but considers two 2D projections of that cellpair independently from each other:

- An r-ϕ projection. The radius r is measured from the centre of the CTD cylinder and perpendicular to the cylinder axis, while ϕ is the azimuthal angle defined with respect to the ZEUS coordinate system (see chapter 2).

- An r-z projection. The z-axis here is the z-axis of the CTD coordinate system, which is the same as the ZEUS coordinate system, but offset by 2.5cm in z in the direction of the proton beam.

The criteria for a good track segment in the r-ϕ projection will typically demand a minimum number of hits in a cellpair. The two adjacent wires in a sense-layer in a given cellpair are ORed together. Hence an ideal track segment will have eight (four[1]) hits in a SL1(SL3,SL5) cellpair. In the r-z projection, the z-values of the eight SL1 hits have to lie on a coarse straight line pointing towards the interaction region to

[1]Only four sense wires are equipped with z-by-timing readout in SL3 and SL5.

constitute a good r-z track segment.

Only if both 2D projections identify a good track segment in a given cellpair will the segment be used in the next stage of track reconstruction. This stage tries to match the individual track segments from SL1, SL3 and SL5 to form a complete track. Again two 2D projections in r-ϕ and r-z are considered separately. The algorithm considers 32 regions, the so-called sectors, in turn. Each sector contains one SL1, four SL3 and six SL5 cellpairs (see Figure 3.1). This is necessary because tracks are curved, and the sectors are designed such that all tracks with sufficient p_T (curved in both the positive and negative direction) lie within a given sector. Consequently the 32 sectors partially overlap, ensuring that no tracks are lost due to insufficient geometrical mapping of the chamber. A good track in r-ϕ requires a SL1 track segment and a matching SL3 and SL5 track segment if the track went through SL3 and SL5 [2]. The r-z algorithm tries to match track-segments in the three superlayers in r-z. Three segments have to lie on a coarse straight line (within a certain 'window') pointing towards the centre of the CTD to be classified as a good r-z track. A 'window' in the r-z track matching is necessary because the e-p interaction vertex is spread around the centre of the ZEUS detector by $\pm$20cm.

In the final stage of track reconstruction, the information from the 32 sectors (the r-ϕ and r-z tracks) is combined together. Ratios of $\frac{\textit{pointing (r-z) tracks}}{\textit{potential (r-}\phi\textit{) tracks}}$ are formed in various regions of the detector (forward, barrel and rear), and are used to determine whether an event had a sufficient number of tracks originating from within the e-p interaction region. A *potential (r-ϕ) track* is a valid track in r-ϕ, but it does not necessarily have to come from the interaction vertex, while a *pointing (r-z) track* is a track (in the r-z projection) which does come from the interaction vertex. Because the algorithm works on *overlapping* geometrical areas of the chamber[3], some tracks or

[2]Note that forward or rear tracks might for example go only through SL1 and SL3 before they exit the chamber.

[3]The algorithm considers overlapping cellpairs, and combines the cellpairs to overlapping sectors.

track segments are double-counted. By considering the ratio of $\frac{pointing\ (r\text{-}z)\ tracks}{potential\ (r\text{-}\phi)\ tracks}$ the effect of double-counting is somewhat reduced. The final decision on whether the event is a 'good physics event' is made from:

- A combination of cuts on the ratios of $\frac{pointing\ (r\text{-}z)\ tracks}{potential\ (r\text{-}\phi)\ tracks}$ in the various regions. The actual choice of the cut values and regions is complicated and not intuitive, and has to be determined from MC studies.

- Dedicated subtriggers. An example is the two-track trigger, i.e. back-to-back tracks from the interaction vertex.

In the above description we have attempted to outline the principles of the CTD-FLT tracking algorithm. We shall now concentrate on how the various stages of the algorithm and the geometrical subdivision of the chamber into cellpairs and sectors corresponds to segmentations of the hardware into individual modules and logic stages.

Implementation of the Tracking Algorithm in Hardware

The overall aim of the CTD-FLT hardware can be summarised as follows:

- To determine the start and the end of an event[4], accumulate data over that time, and assign it either to a unique bunch crossing or to an ambiguous range of bunch crossings.

- To perform track reconstruction on the z-by-timing data (see chapter 2) from SL1,SL3 and SL5. This is for simplicity split into r-z and r-ϕ reconstruction. The r-z part is responsible for finding out whether the track originated from the interaction region (a *pointing (r-z) track*), whereas the r-ϕ part finds *potential*

[4]This is necessary because the maximum drift time in the CTD is ~500ns (equivalent to 5 bunch crossings at HERA).

(r-ϕ) tracks. The ratio of $\frac{pointing\ (r\text{-}z)\ tracks}{potential\ (r\text{-}\phi)\ tracks}$ then allows for a classification of the event into one of the following groups: events with good vertices, events produced upstream (beam-gas events), and events where no decision could be formed due to no track segments being found.

- To estimate the track multiplicity.

- To output an 8×8 bit map of pointing tracks in θ and ϕ , which is sent to the GFLT and eventually will allow for CTD track-matching with calorimeter clusters.

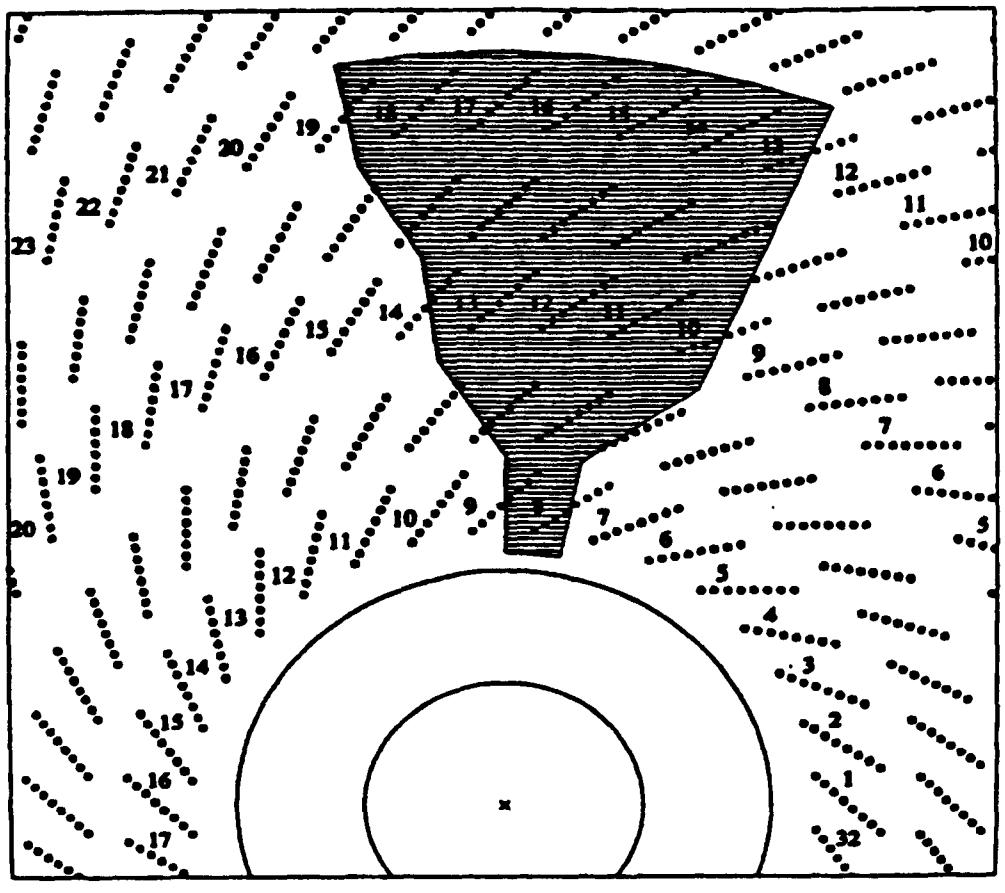
Such a complicated task cannot be performed in a single processing step of 96ns. The CTD-FLT is therefore split into individual modules, and the modular structure of the CTD First Level Trigger is summarised in Figure 3.2. The CTD-FLT is *functionally* broken down into the following units:

- Cell Processors (CP), which process separate pairs of cells, cellpairs, in a given superlayer (CP1, CP3 and CP5 in SL1, SL3 and SL5 respectively). The CPs perform the task of track segment-finding.

- Sector Processors (SP), which combine the CP1, CP3 and CP5 results of a given sector to form complete tracks out of the track-segments found by the Cell Processors. The SPs perform the task of track finding.

- The Regional Box (RBOX), which combines all the SP information and produces the final CTD-FLT decision.

The FLT is also *geometrically* divided into units of cellpairs and sectors. There are 32 cellpairs in SL1 comprising of cells (32,1), (1,2), ..., (31,32). There are also 32 sectors, and each consists of one SL1, four SL3 and six SL5 cellpairs (Figure 3.1).



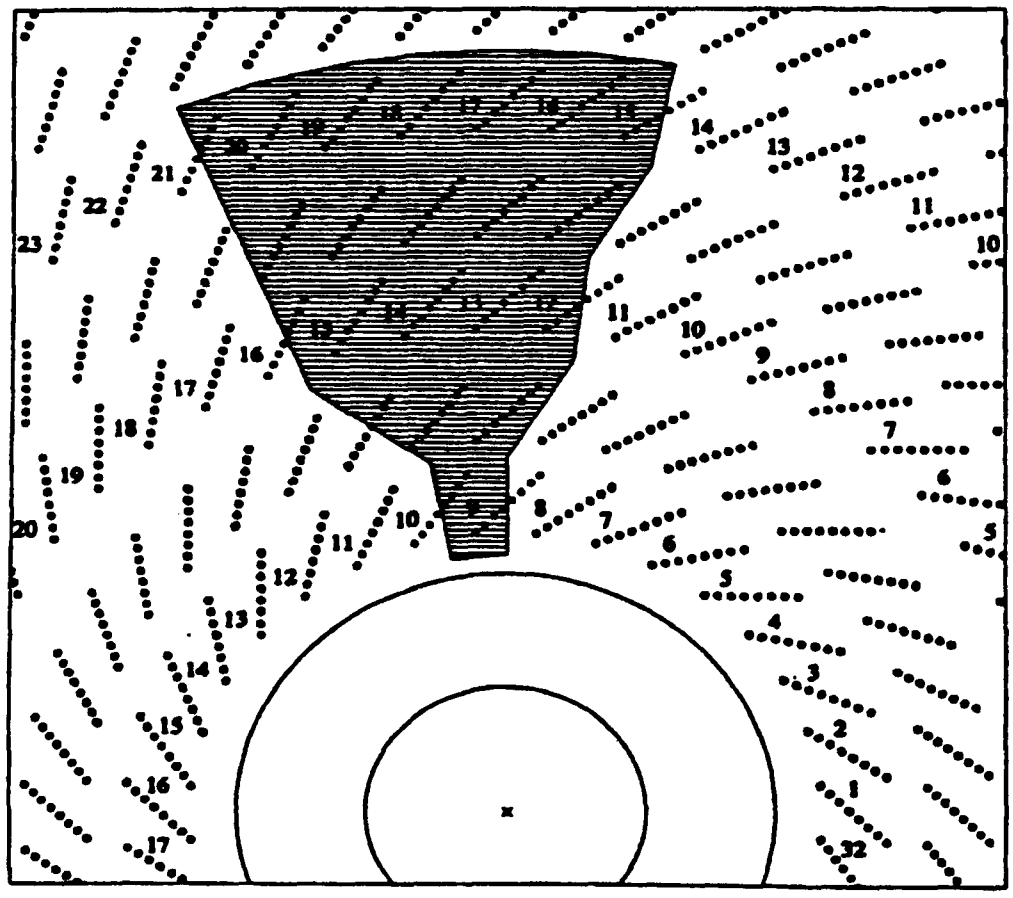


Figure 3.1: Examples of the even and odd azimuthal sectors (in the r-ϕ projection of the CTD chamber) used in the Sector Processors. The cells in SL1, SL3 and SL5 which are equipped with z-by-timing readout are numbered. Cellpairs consist of pairs of cells. In SL1 the cellpairs consist of cells (32,1), (1,2), ... (31,32).

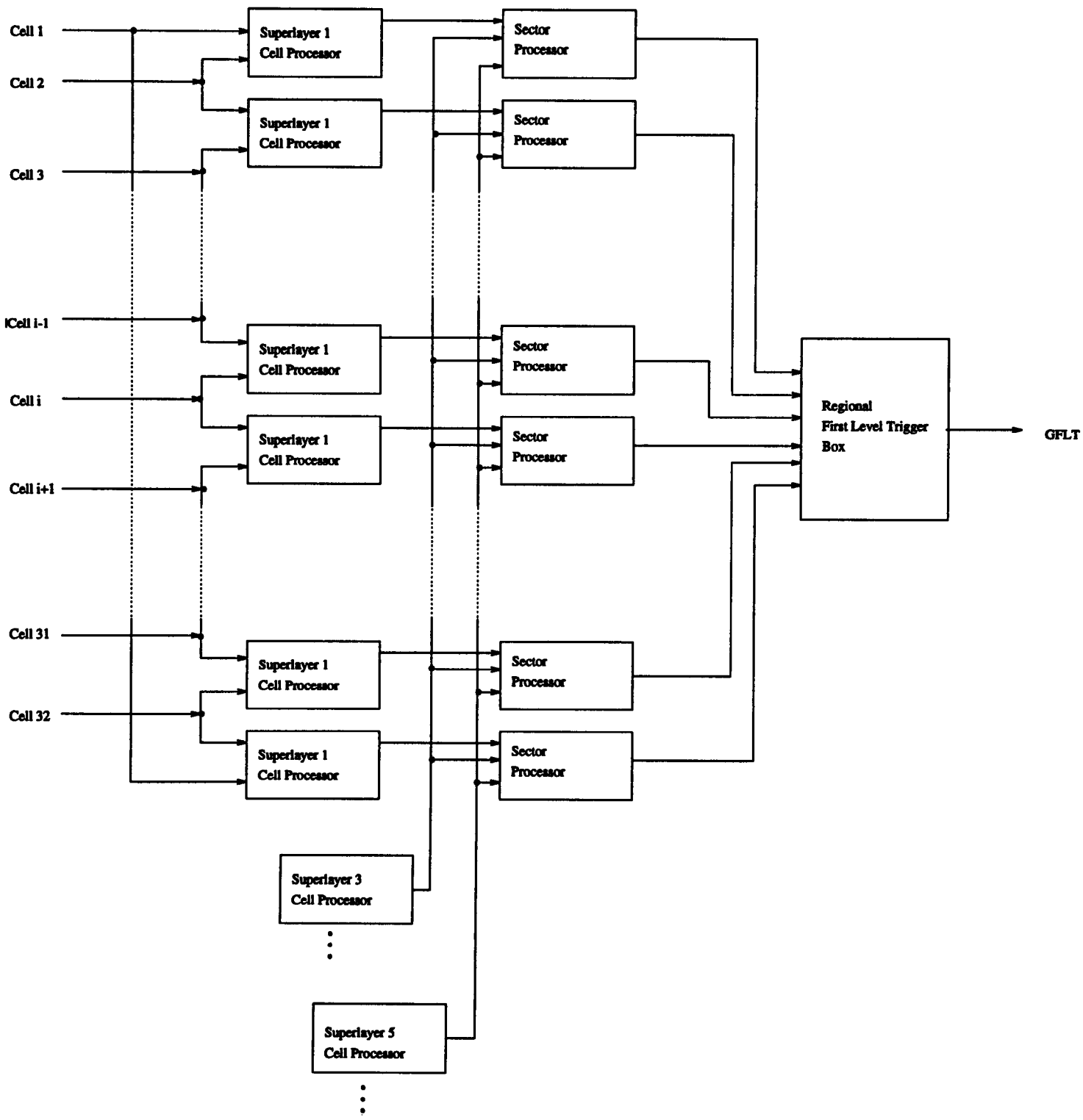


Figure 3.2: The CTD-FLT architecture.

3.2 System Layout

We now proceed to discuss the CTD-FLT system: the timing aspects, interconnections, data transfer within the system and communications between various parts of the system and the 'outside world', e.g. the other ZEUS components. The CTD hardware is housed in the 'rucksack', a three story building positioned next to the ZEUS detector. The hardware occupies two adjacent rows of racks in the rucksack. Each rack, servicing 1/16th of the chamber, has three crates, making 48 crates in all. In addition there is a rack which holds the two Regional First Level Trigger crates. Each rack of three crates has a postamplifier crate in the middle, which distributes the amplified chamber pulses to the 'FADC crate' and the 'z-by-timing crate'. The FADC crate contains 18 FADC cards, where each FADC card processes 16 channels. One Readout Controller card (ROC) and one Local Timing Controller (LTC) per crate are responsible for transferring and reading out the data. The z-by-timing crate contains z-by-timing cards (z-cards), a ROC and an LTC, as well as the CTD-FLT processors.

The CTD-FLT tracking algorithm considers *overlapping* cellpairs and *overlapping* sectors. The Cell Processors and Sector Processors therefore have to receive input from their own crate and from adjacent crates. Because of the inter-crate connections between the trigger processors and the short time of 48ns between clock cycles, timing aspects are particularly crucial in such a system. The z-cards and FLT-cards have thus been positioned within the system in such a way, that no card has to receive data signals from more than one crate away (except the Regional Box (RBOX), which has to access FLT-data from the whole chamber).

Another complicating matter in the system is the amount of data which has to be transferred between the z-cards and the trigger processors. The z-by-timing data input to the Cell Processors alone requires 8448 individual transfer lines between z-

cards and CP-cards over the whole system. The Cell Processors then have to transfer data to the Sector Processors, which in turn transfer data to the 'Hit Count Modules' (see section 3.3.7), which in turn transfer data to the 'Final Decision Module' (section 3.3.7). The final CTD-FLT trigger decision is packed into a mere 2-bit word. The CTD-FLT system has to provide enough interconnections to accomplish such transfers, while the trigger processors are faced with the task of reducing the data between the stages without loosing any information vital to the trigger decision. On top of this, the above tasks have to be performed in parallel in a pipelined environment. The resulting system is very complex, and we shall try to introduce the system by explaining each of its components in detail.

3.2.1 The z-by-timing Crate

This crate has 19 slots available to z-cards and trigger processors. It also houses two controller cards: a Local Timing Controller (LTC) in slot 1 and a Readout Controller (ROC) in slot 21. The task of the ROC, a programmable device, is to firstly address registers on the readout, trigger and LTC cards and hence define their mode of operation prior to data-taking; and secondly to access memory on the cards during data-taking. The timing controller distributes clocks and pipeline addresses, and controls the transfer of pipeline data into buffer memory on the z-by-timing and FLT-cards (the SLT buffers of Figure 2.6). Once the mode of operation of the LTC has been programmed by the ROC, the two controllers can work concurrently and completely independently of each other via two separate backplane buses.

The custom-made 12 layer backplane links cards via two types of interconnections:

- A 120 line bussed interconnection (table 3.1) - the ROC-bus. This allows the ROC to address individual cards via 'Geographic address lines' (the 'N'-line, 'N1'..'N20'). Once a single card has been selected by the ROC, it uses a bidirectional 16-bit data bus (D0..D15) and a unidirectional 14-bit address bus

PIN NUMBER	Col (a)	Col (b)	Col (c)	Col (d)
1 –	n/c	n/c	n/c	n/c
2 –	Notintrpt	Scrn b2	Notwrite	Scrn d2
3 –	Scrn a3	Notmemen	Scrn c3	'N1'
4 –	Notrst	Scrn b4	Notwait	Scrn d3
5 –	Scrn a5	Reserved	Scrn c5	Nothalt
6 –	Reserved	Reserved	Reserved	Reserved
7 –	PB1	PB1	PB1	PB1
8 –	D 0	A 1	A 8	D 8
9 –	D 1	A 2	A 9	D 9
10 –	D 2	A 3	A10	D10
11 –	D 3	A 4	A11	D11
12 –	D 4	A 5	A12	D12
13 –	D 5	A 6	A13	D13
14 –	D 6	A 7	A14	D14
15 –	D 7	Spare	Spare	D15
16 –	PB2	PB2	PB2	PB2
17 –	*	*	*	*
18 –	*	*	*	*
19 –	*	*	*	*
20 –	RA 0	RA 1	RA 2	RA 3
21 –	RA 4	RA 5	RA 6	RA 7
22 –	RA 8	RA 9	DA 0	DA 1
23 –	DA 2	DA 3	DA 4	DA 5
24 –	DA 6	DA 7	DA 8	DA 9
25 –	DA10	Reset	Transfer	Clk2
26 –	*	*	*	*
27 –	Vth1	Vth2	Vth3	Vth4
28 –	AutoCal En	*	*	*
29 –	AutoCal Strb	*	*	*
30 –	Clk 1 +	Clk 1 –	n/c	'N0'

NOTE :-
(1) ... n/c - Not connected, free pins
(2) ... * Unused bussed pins between Slot 1 and Slot 21
(3) ... ROC control lines [Rows 2 - 15] to be terminated on LTC module, Slot 1
(4) ... LTC control lines [Rows 17 - 29] to be terminated on ROC module, Slot 21
(5) ... PB 1 & PB 2 available for POWER BUSES or CLEAN GRND if required
(6) ... Scrn These pins to be connected to GRND on all modules
(7) ... 'N0' to 'N20' Geographic address lines ('N0'= CAL) - ('N1'= LTC)
(8) ... All pins in this slot will be 2 level wire wrap

Table 3.1: The Readout Controller (ROC) Bus.

(A1..A14) to transfer information between the ROC and the card.

The LTC uses its own two address buses: One to assert the 10-bit pipeline address (RA0..RA9), and one for the 11-bit buffer memory (DA0..DA10). Furthermore it provides a 'Transfer' signal and a 48ns clock to all modules. When the 'Transfer' signal is high, all the modules in the crate are put into transfer mode, and data from the pipelines is transferred into the SLT buffers(the buffer memory).

- A 360 line auxiliary bus, connecting z-cards to Cell Processors, and Cell Proces-

sors to Sector Processors. This bus is not present in the FADC crates. Figure 3.3 shows the interconnections of z-cards and trigger processors in even-sector and odd-sector crates. Inter-crate links are implemented using ECL signals transmitted via ribbon cables.

The ROC-bus signals are transmitted by open collector drivers from either ROC or LTC cards (depending on the signal), and are terminated at the opposite end of the crate by resistors on the LTC or ROC card. Alternate column pins in the first rows of the ROC bus are connected to ground (scrn a3, scrn b2, ... in table 3.1) and act as shielding wires to minimise cross-talk between the control signals.

The timing of the system is designed such that each crate processes data from the same 48ns cycle. This is achieved by keeping cable lengths small (signals travel 8.6m in 48ns), and by optimal impedance matching of transfer lines in order to maintain a good signal quality throughout the backplane. There are two types of cables in the system: daisy chain cables, carrying control signals between LTCs, and inter-crate cables between trigger modules. The two types of interconnections are described below. Figure 3.4 shows the 16 z-crates, grouped into quadrants of four crates each. The 48ns clock is supplied to each crate's LTC. Control signals (which are issued and received in 96ns cycles) are daisy-chained from the first LTC of each quadrant to the three other LTCs. The maximum cable length of 4.5m×2 (bidirectional) is within a single 96ns clock-cycle. The maximum length of any interconnection between z-by-timing cards and Cell Processor cards is kept blow 2.6m. This again ensures that data from two z-cards of different crates can be latched in by one CP in the same 48ns cycle. This is demonstrated in Figure 3.5.

3.2.2 The Readout Controller

Each Readout Controller card (ROC) has one readout transputer (ROT), several SLT transputers, additional external memory and a Direct Memory Access (DMA)-

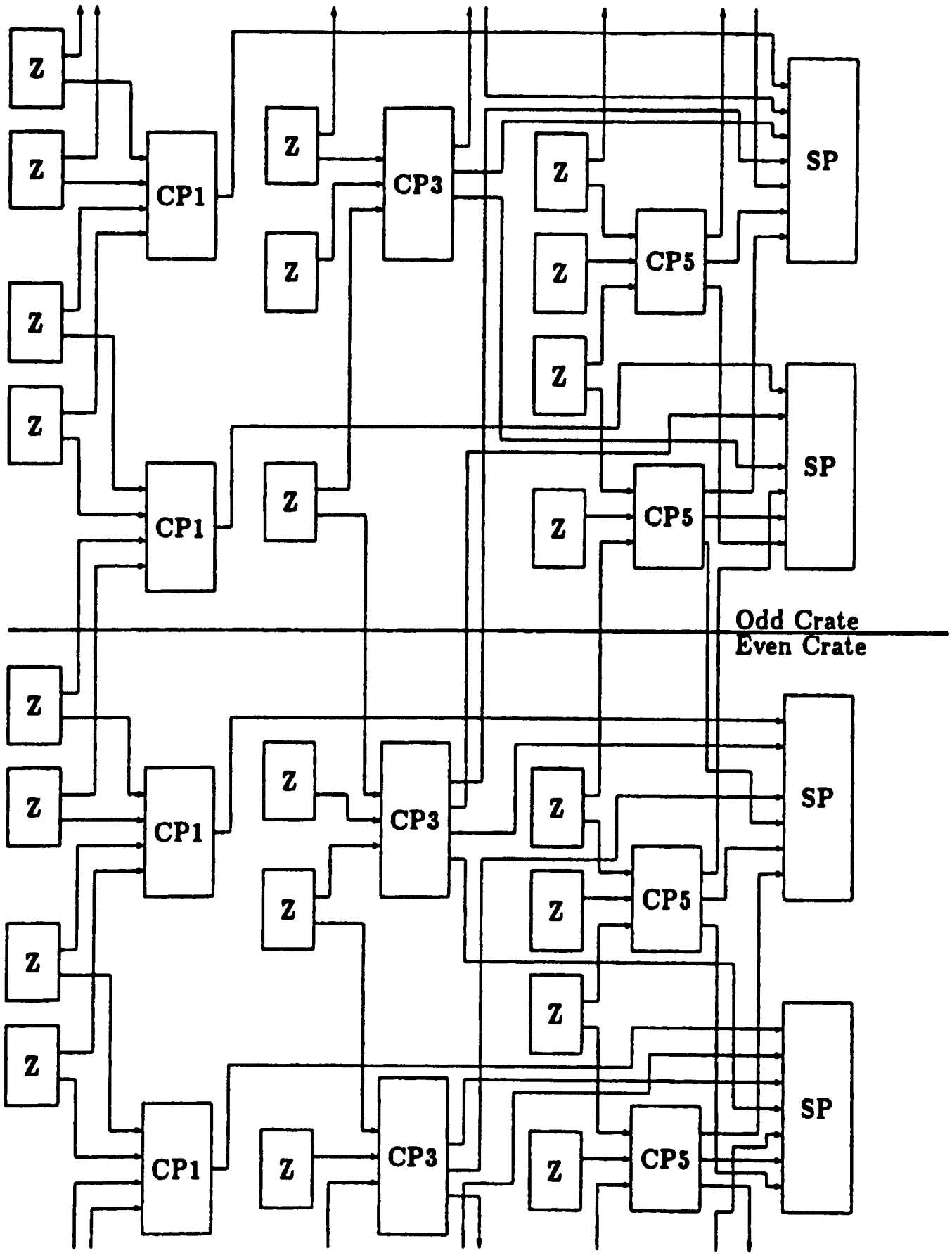


Figure 3.3: Interconnections of trigger processors in even and odd sector crates

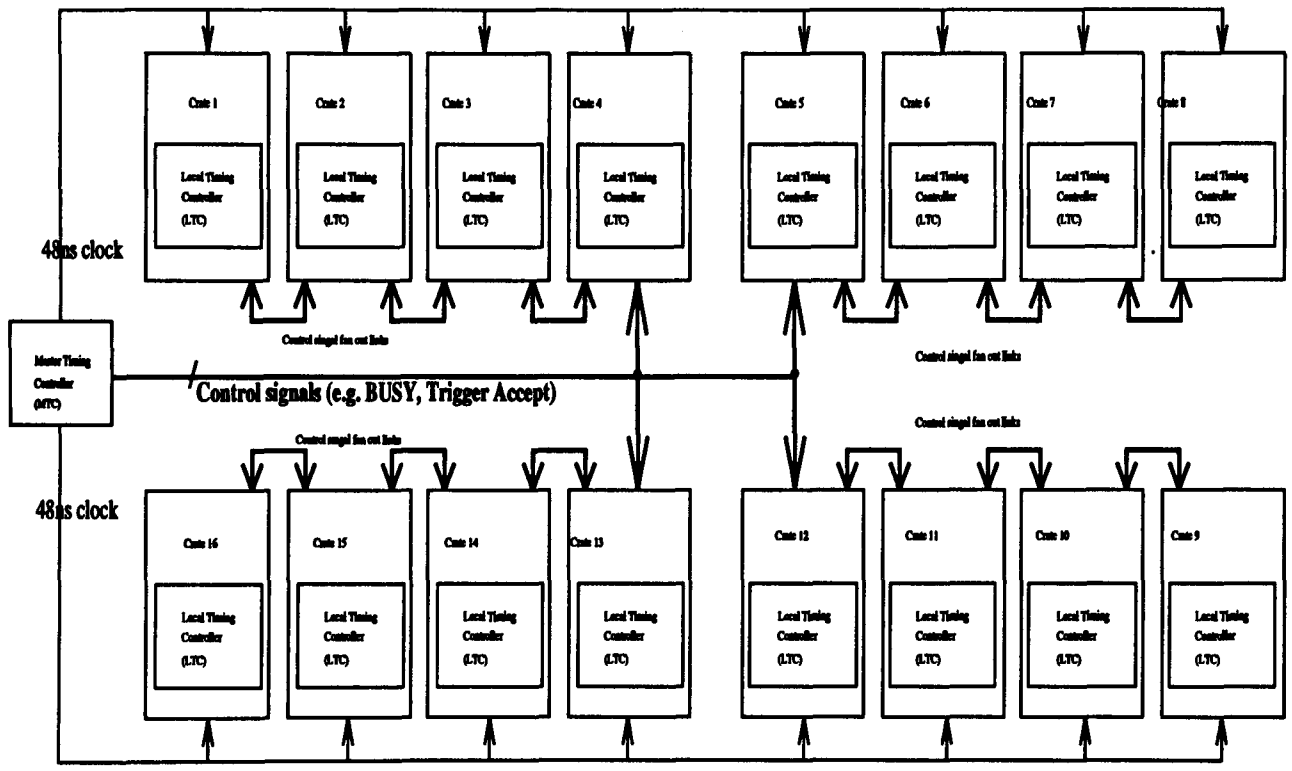
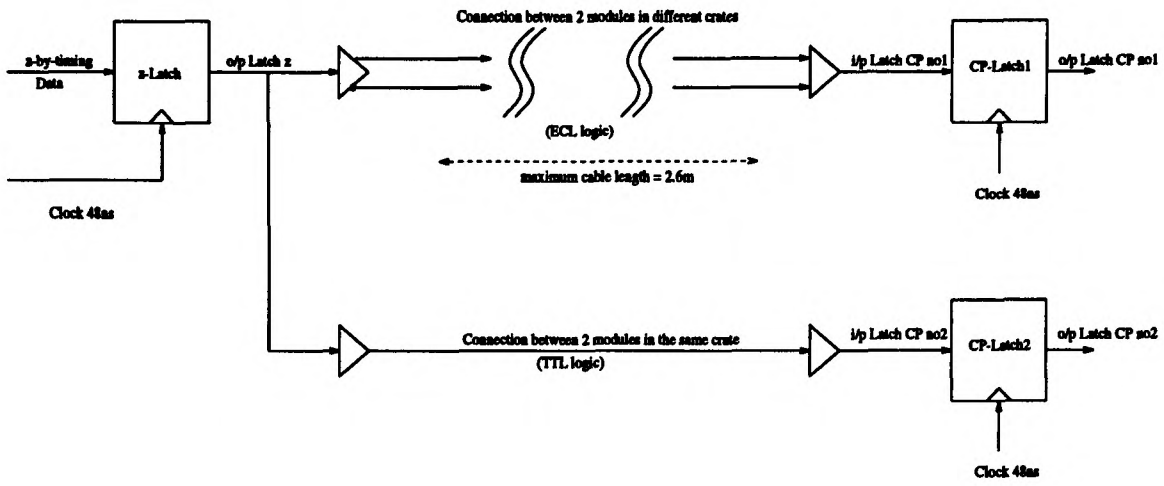


Figure 3.4: The 16 crate z-FLT system. All crates receive the same 48ns clock. Control signals are daisy-chained from the first LTC in each quadrant to the other three LTCs.



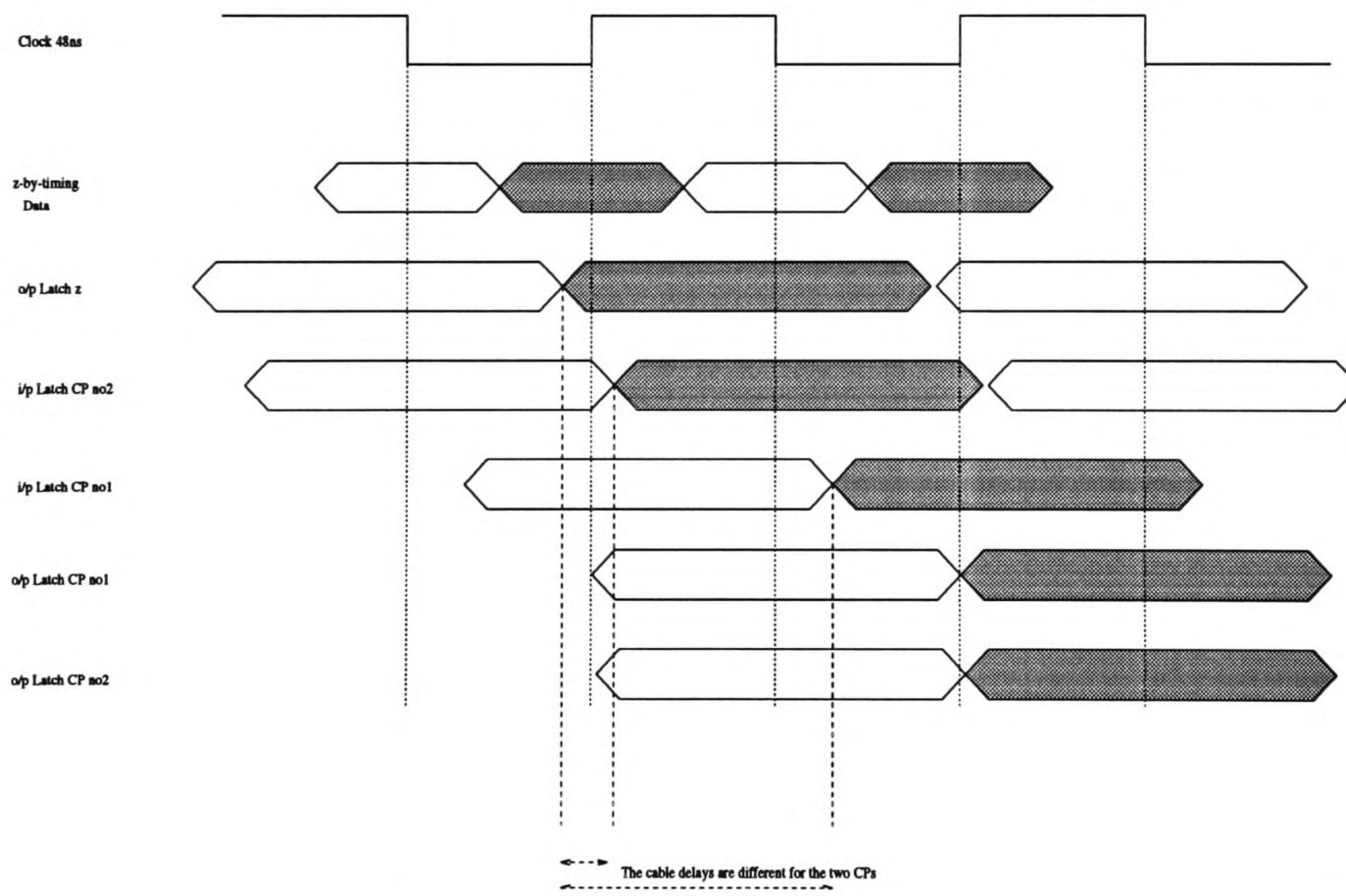


Figure 3.5: The timing of data which is input to a Cell Processor from z-cards in 1) a different crate, and 2) the same crate as the CP-card is in. The shaded areas in the timing diagrams represent valid data. Data to the i/p latch of CP card number 1 (which is in a different crate than the z-card) is offset with respect to the data of CP card number 2. However, after being latched in by the rising edge of the 48ns clock, the data of the Cell Processors in both crates is again in synchronisation.

interface to the ROC-bus backplane. A readout transputer can access a card within a crate by specifying a certain address range. The task of the DMA-interface is to carry out the communication with that card and read or write to its specified memory location.

The ROC utilises a single transputer to facilitate the readout of the z-cards and trigger-cards. Transputers [20, 21], single chip microprocessors, have four serial bidirectional links for communication with the 'outside world'. The links of the Readout Transputer (ROT) are connected to the SLT transputer and to ROTs of adjacent crates to either side. A 'Caplin' link at the end of that 16 z-crate transputer network provides the connection to the DAQ VAX computer (Figure 3.6). Thus if for example a readout transputer is instructed to read out memory of one of its cards, the card's location and memory address must be specified to the DMA interface via the ROC, which will then access it. The ROT formats the data, and sends it to its adjacent crate ROT. This again forwards the data - and this procedure continues until the data reaches the last transputer in the chain. The data is then transferred to the DAQ computer via the Caplin link.

3.2.3 The Timing Controller

Every time a trigger is issued by the Global First Level Trigger, data in the pipelines (the pipelines of the z-cards and the trigger processors) have to be transferred to the Second Level Trigger buffers. It is the task of the Local Timing Controllers in the z-crates to initiate such a transfer.

The timing controller provides the pipeline buffer addresses and clock and transfer signals to the z-cards and trigger cards. The buffers are implemented using Dual Port Memories (DPM) (which are located on the readout and trigger cards). This has the advantage that the ROC can read out the DPM buffer through one port while the LTC is transferring data into it through the other port (Figure 3.7). The LTC is

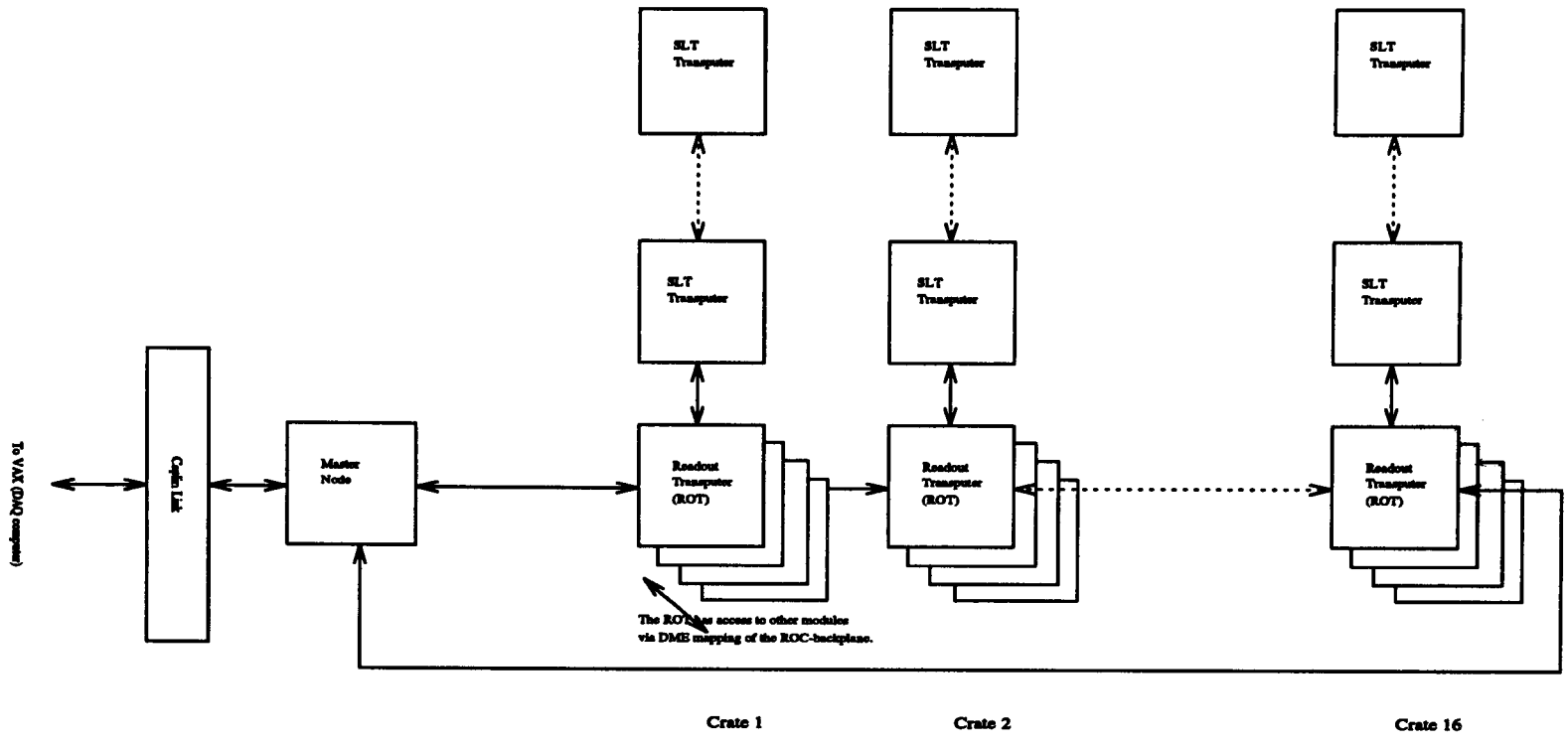


Figure 3.6: The 16 crate z-FLT transputer network. Adjacent Readout Transputers are connected together to form a circular network.

designed to keep track of and transfer up to 10 'pipeline windows' from different triggers into the DPM buffer. One can think of the DPM as being partitioned into 10 equal sized windows (the 'pipeline windows'). A counter keeps track of the current window to be filled. Every time a transfer occurs, the counter is incremented. The buffers are filled in a circular order until all 10 windows are full, and the LTC then has to wait until a buffer is released by the ROC - after the ROC has read out the buffer, the corresponding buffer bit in the LTC control register is cleared.

The buffer mechanism can reduce the deadtime of the system substantially from $\sim 100\mu s$ to $\sim 5\mu s$ per trigger. This is because the time it takes the ROC to complete a software transfer from the Dual Port Memory Buffers (on the front end cards) to its internal SLT Buffers is rather large, and of the order of $\sim 100\mu s$; on the other hand the time for the transfer of the pipelines to the Dual Port Memory (which is controlled by the LTC hardware) is much shorter, and of the order of $5\mu s$. Intermediate buffering

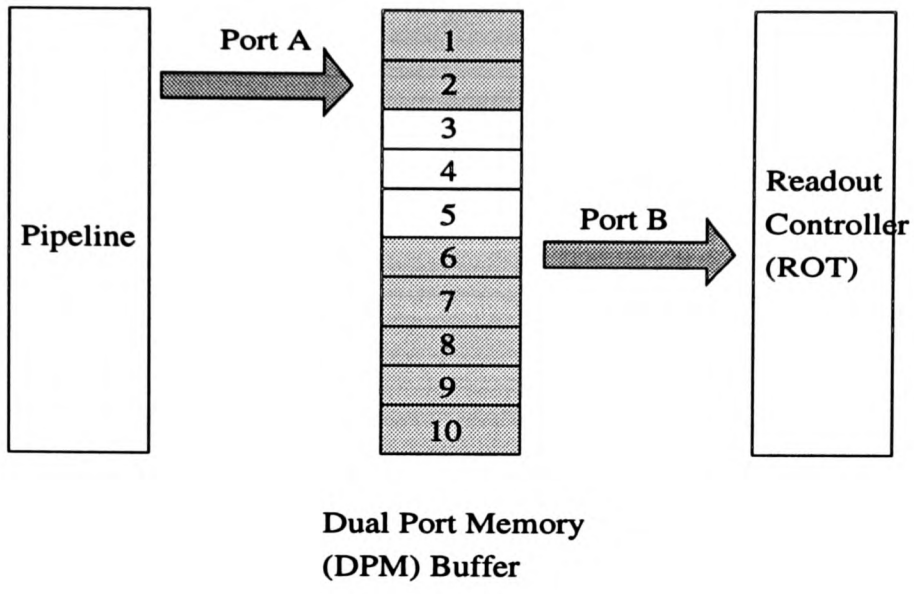


Figure 3.7: An example of a pipeline to Dual Port Memory transfer. Here the LTC transfers data from the pipeline into the second DPM buffer, while the ROC is concurrently reading out data from buffer number 6. Buffers 3 to 5 contain data from many past beam crossings, and are now being overwritten.

between the pipelines and the SLT buffers ensures that as long as the average FLT-trigger rate does not exceed 1kHz, the average deadtime of the system will be $\sim 5\mu s$ per trigger.

After the GFLT has issued an accept signal, each component of ZEUS responds by setting a BUSY signal. The BUSY condition tells the GFLT that the components are transferring data from the pipelines into their DPMs, and are not ready to receive another accept until the BUSY has been cleared (Figure 3.8). The LTC sets it's BUSY bit during the transfer, but does not clear the bit if it has just filled the 10^{th} buffer, since it would not be able to deal with another GFLT. Instead it waits until a buffer has been released (via transfer to the ROC) before it clears the BUSY again.

The task of the Master Timing Controller (MTC) is to coordinate all 16 LTCs. It resides in one of the RBOX crates and converts the 96ns HERA clock signal from the GFLT to its internal 48ns clock, which is then distributed to the individual LTCs. Upon receipt of a GFLT accept it also distributes the Bunch Crossing Number (BCN)

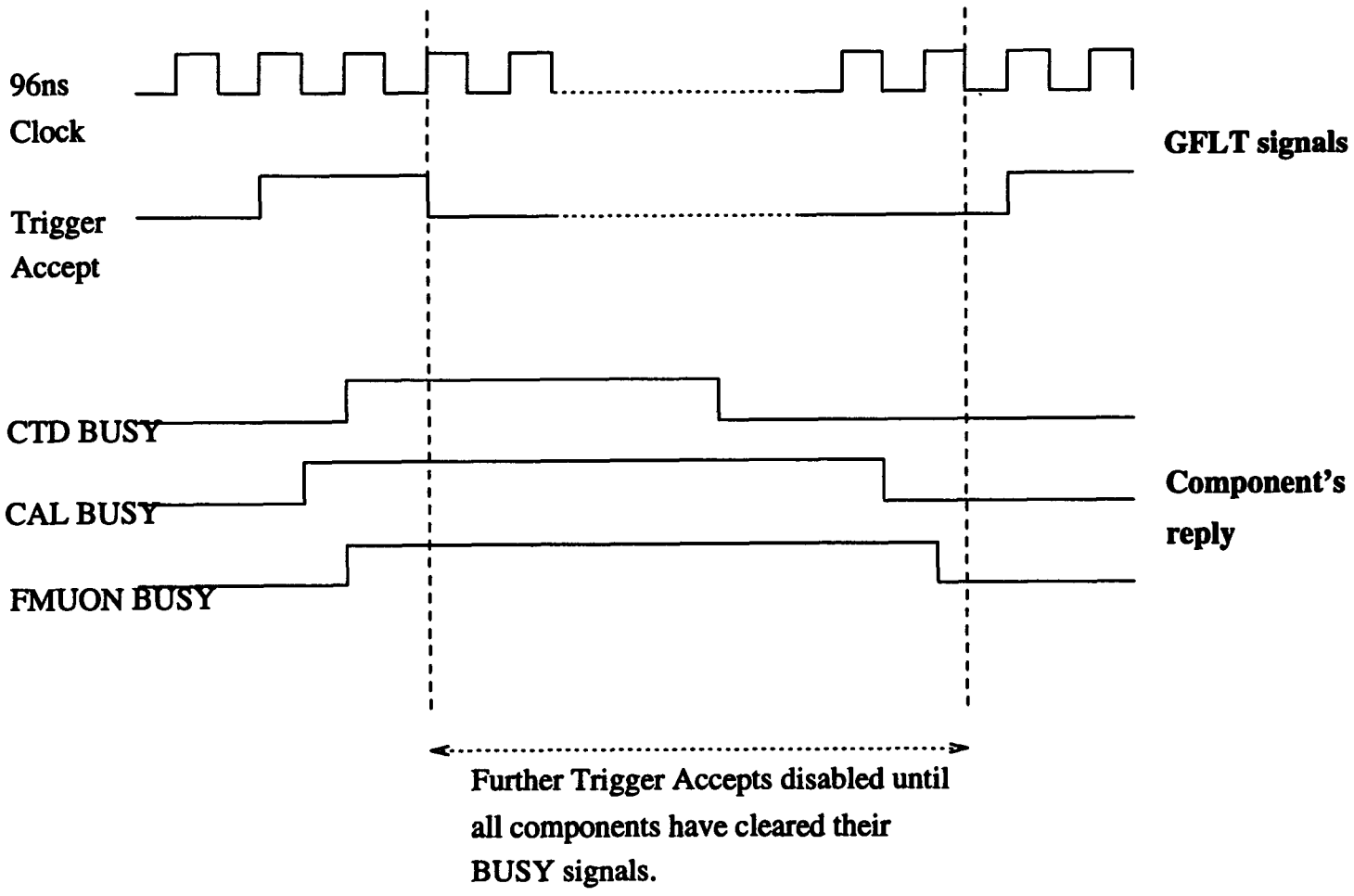


Figure 3.8: ACCEPT and BUSY handshake with the GFLT. After a Trigger Accept, components reply by setting their BUSY bits. The GFLT will not issue another Trigger Accept until all components are ready to receive one, and have cleared their BUSY bits.

and the FLT event number. This is necessary because the readout of individual crates can be up to 10 events out of synchronisation with respect to each other. Therefore the BCN and FLT number have to be stored locally on each LTC in order to identify an event in a given buffer. Special triggers such as 'Begin of Run', 'End of Run' and 'Test Trigger' are decoded in the MTC, and the 16 BUSY signals from each crate are ORed together by the MTC before they are sent to the GFLT [5]. Only when all LTCs are ready is the MTC ready to accept another trigger. Only when all components are ready is the detector ready to accept a new event.

3.2.4 Communication with the GFLT

As already mentioned above, the basic handshake mechanism between the GFLT and the CTD is the ACCEPT and BUSY sequence of Figure 3.8. The signals are transmitted in ECL logic via 30m 34-way twisted pair cables. Timing markers are sent with the output of the RBOX (which includes the BUSY signal) to enable the GFLT to resynchronise the CTD data with its internal timing. Among the signals from the GFLT are a 96ns clock[6] synchronised with the HERA machine, trigger ACCEPT, BCN and FLT numbers, Readout Type ('Begin of Run', etc...), ABORT, empty bunch and a Bunch Crossing 0 indicator (BCN0). The signals are fanned out to both the FADC and the z-trigger system via the distribution modules in one of the RBOX crates. The BCN0 indicator allows the RBOX to calculate the offset of the event data to the 0^{th} bunch crossing, and hence to determine the bunch crossing number of the event. The BCN is then sent to the GFLT, which distributes it to all ZEUS components.

[5] In fact the BUSY of the z-by-timing MTC is ORed together with the BUSY from the FADC system in the RBOX before it is sent to the GFLT.

[6] The 96ns clock acts as the timing marker for data sent from the GFLT.

3.3 The Trigger Processors

The tracking algorithm of the CTD-FLT has been discussed in section 3.1.2. The algorithm is implemented in hardware by the trigger processors. The Cell Processors perform the track segment-finding in cellpairs. The Sector Processors form complete tracks out of the SL1, SL3 and SL5 track segments. The Regional Box (RBOX) finally combines all the FLT data, and calculates the trigger decision. The only difference between the tracking algorithm description of section 3.1.2 and the functionality of the trigger hardware is that the processors also have to assign the event to a unique bunch-crossing, and to determine over which time data from a single event have to be accumulated. This is because the maximum CTD drift time is 500ns, i.e. ~5 beam crossings, and hence hits in a cellpair are spread out over that time. These tasks are performed by the CPs, which are the first part of the trigger processor chain, and therefore have to know which data belong to the same event. The RBOX has access to all FLT data, and can thus resolve any remaining bunch crossing ambiguities.

Although the First Level Trigger is a hardware trigger, the use of Look Up Tables (LUTs) in form of static Random Access Memories (SRAMs), field programmable gate arrays and registers storing cut values preserves a high degree of flexibility wherever possible, so that the details of the track reconstruction algorithm can be varied and adjusted to the HERA machine and the background conditions. In order to aid the reader through the following sections on the detailed functionality of the trigger processors, we have summarised the data-flow between the modules in Figure 3.9. The nature of the individual signals between the processors are explained in the relevant sections below.

3.3.1 The Cell Processors

Processing is split into independent r-z and r-ϕ segment- finders[25], both for simplicity and speed. The two tasks are performed in parallel. The output of the r-z

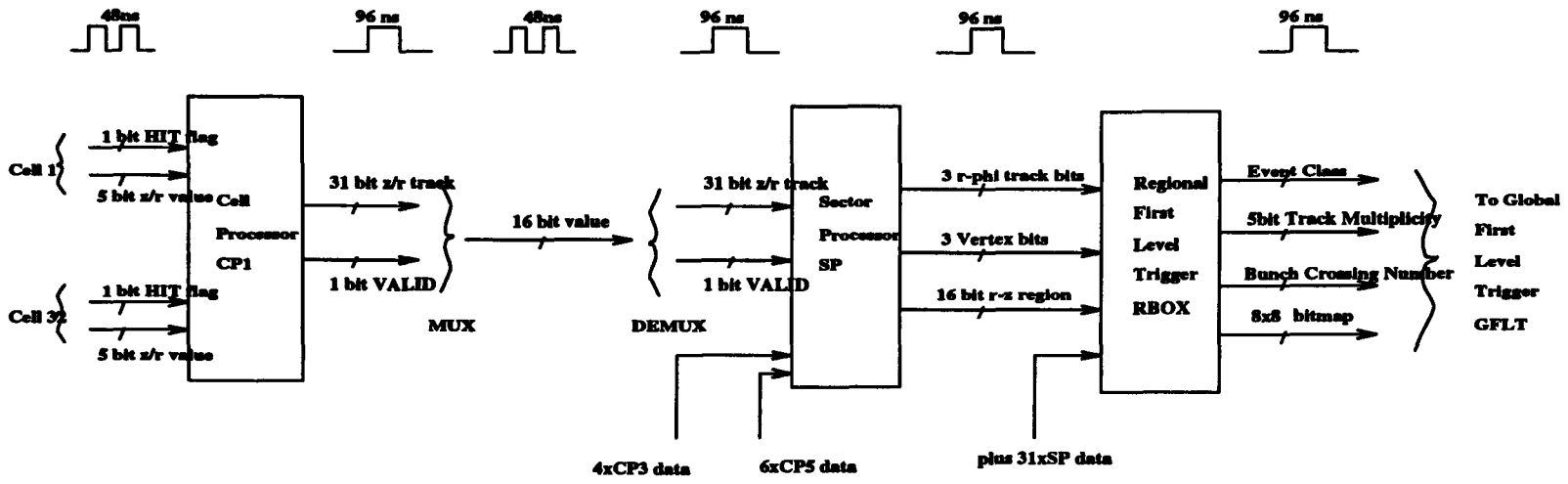


Figure 3.9: Data flow between the CTD-FLT trigger processors.

algorithm, the *pointing (r-z) tracks*, are only validated if the r-ϕ processor has found a corresponding *potential (r-ϕ) track.*

3.3.2 The r-ϕ Cell Processor

This module uses the hit-flags of the z-output (a bit which is set if a sense wire has a hit) to perform two tasks:

- Assign a track segment to one or more crossings (Bunch Crossing Logic).
- Consider the number and patterns of hits accumulated over time to determine whether they were consistent with a valid track segment (Valid Pattern Logic).

The bunch crossing assignment is based on the time of the first hit in SL1, as this generally arrives within 96ns of the interaction. The logic considers an OR of all wires in a given cellpair over time. An event is characterised by a continuous train of hits (Figure 3.10a), but the logic is sophisticated enough to deal with chamber inefficiencies by allowing a predefined number of 48ns gaps to occur in the arrival pattern (Figure 3.10b). The train of hits over time thus defines the number of cycles over which the CPs have to accumulate data from a single event.

The Valid Pattern Logic accumulates an OR of hits on the same layered sense wires within a cellpair over a certain time and compares it with allowed patterns of hit layers. For example in SL1 this criteria might be to demand hits in layers (wires) 1, 2, 7 and 8. If the logic finds an allowed pattern, the cellpair is classified as a valid r-ϕ track segment. This corresponds to a *potential (r-ϕ) track.*

The output of the r-ϕ processor is the VALID bit, which is a combination of the result of the above two logic stages. It determines the time when all the data from the same event has been collected and processed, and the output result of the Cell Processor is valid - i.e. the cellpair constitutes a valid track segment.

3.3.3 The r-z Cell Processor

This processor accumulates the 5-bit $(\frac{z}{r})$ data from the z-by-timing system (see chapter 2) over a certain time in a $(\frac{z}{r})\times$ r table [7]. It then performs segment-finding in the $(\frac{z}{r})\times r$ plane. Since $(\frac{z}{r}) \equiv cot(\theta)$, a straight track coming from the origin will have the same $(\frac{z}{r})$ value in all eight sense layers. Segment-finding is therefore in principle a relatively simple task, and a segment can be crudely defined as a number of hits in the eight sense-layers with the same (or similar) $(\frac{z}{r})$-values.

Figure 3.11 shows tracks originating from z_0=0cm, z_0=10cm and $z_0 = -95$cm respectively. It is easy to see that only tracks from z_0=0cm are constant in $(\frac{z}{r})$. A pattern matching algorithm is employed to identify such straight or nearly straight $(\frac{z}{r})\times r$ lines. The details of the hardware implementation of the algorithm are complicated, because the $(\frac{z}{r})\times r$ plane has to be split up into smaller and smaller units, until only a 4×4 bit window remains, which is then small enough to implement the pattern matching via a look-up table in hardware. This is described below.

The entire plane of $32(\frac{z}{r})\times 8(r)$ pixels is split into smaller regions - one even- and

[7] This is a table which has a predefined number of 32 columns corresponding to 32 possible $(\frac{z}{r})$ values, and 8 rows corresponding to the 8 possible values of the radius r, the radius of the eight sense-layers in a given cellpair.

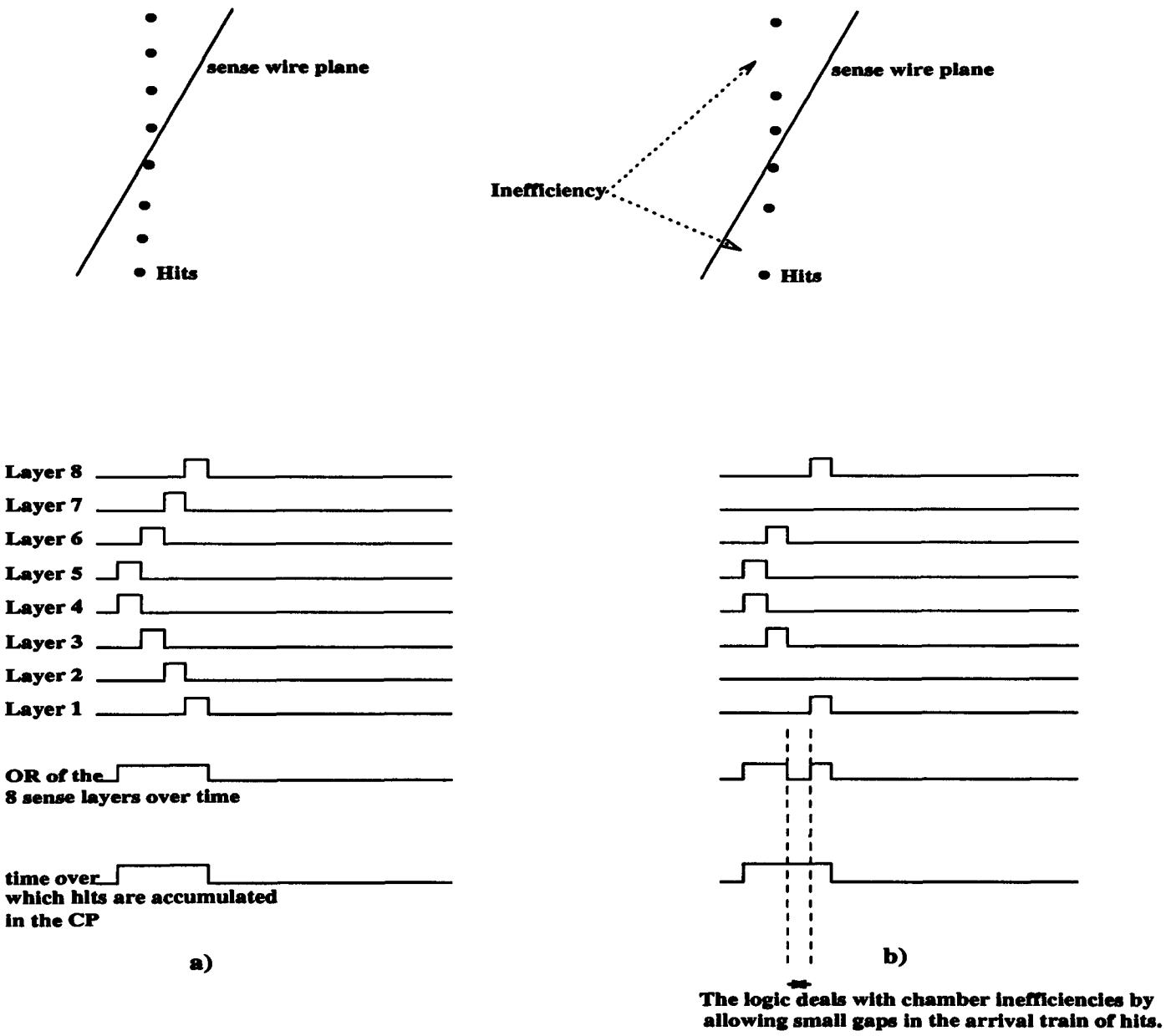


Figure 3.10: The Figure shows from top to bottom: a drift cell with hits from a track going through the cell and the corresponding timing of the signals caused by the hits in the sense layers. Figure a) shows an ideal event, in which all hits are present, while Figure b) shows the effect of missing hits due to chamber inefficiencies. The CP bunch crossing logic is sophisticated enough to deal with such small gaps in the arrival pattern.

one odd-layered wire plane of $32(\frac{z}{r})\times4(r)$ bits each[8]. This $32(\frac{z}{r})\times4(r)$ plane is further divided into 31 overlapping 4×4 bit windows as shown in Figure 3.12. Each of the 31 windows is compared with stored test patterns, and the result of the comparison is detailed by three values:

- A vertex bit, which is set if the pattern is consistent with a track originating from a z-vertex coordinate with its value (z_0) within a preprogrammed cut-value.
- A further bit (the 'centre' bit) is set if the mean ($\frac{z}{r}$) value lies within a certain distance of the window centre. This reduces double counting of adjacent overlapping windows.
- A 2-bit weight value, proportional to the accuracy of the z_0 estimate. Segments that have hits on the outer layers have a higher quality than inner-layer segments. The weight is defined to be (the Maximum Layer Hit minus the Minimum Layer Hit)/2 and is inversely proportional to the error on the least-squares fit of a straight line through the hits [16].

Finally for SL1 the two even- and odd-layered 4×4 windows have to be combined to form a one-bit result (a '$\frac{z}{r}$' bit). This can be accomplished for example by demanding that both vertex bits and centre bits are set, and that both weight values are above a minimum weight cut. The combination of the cuts is not fixed in hardware, but can be programmed in order to preserve greater flexibility in the algorithm.

The output of a CP1 board is the VALID bit together with the 31 ($\frac{z}{r}$) bits. A set ($\frac{z}{r}$) bit indicates a pointing track in that particular ($\frac{z}{r}$)-window. A ($\frac{z}{r}$) bit will only be set if the track is valid.

CP3 and CP5 are slightly different to the SL1 Cell Processors because they only consider the four odd-layered sense wires in a given cell. Hence some of the processing

[8]Only true for SL1, since only half of SL3 and SL5 is equipped with z-by-timing readout. The CP3 and CP5 windows therefore do not need to be split.

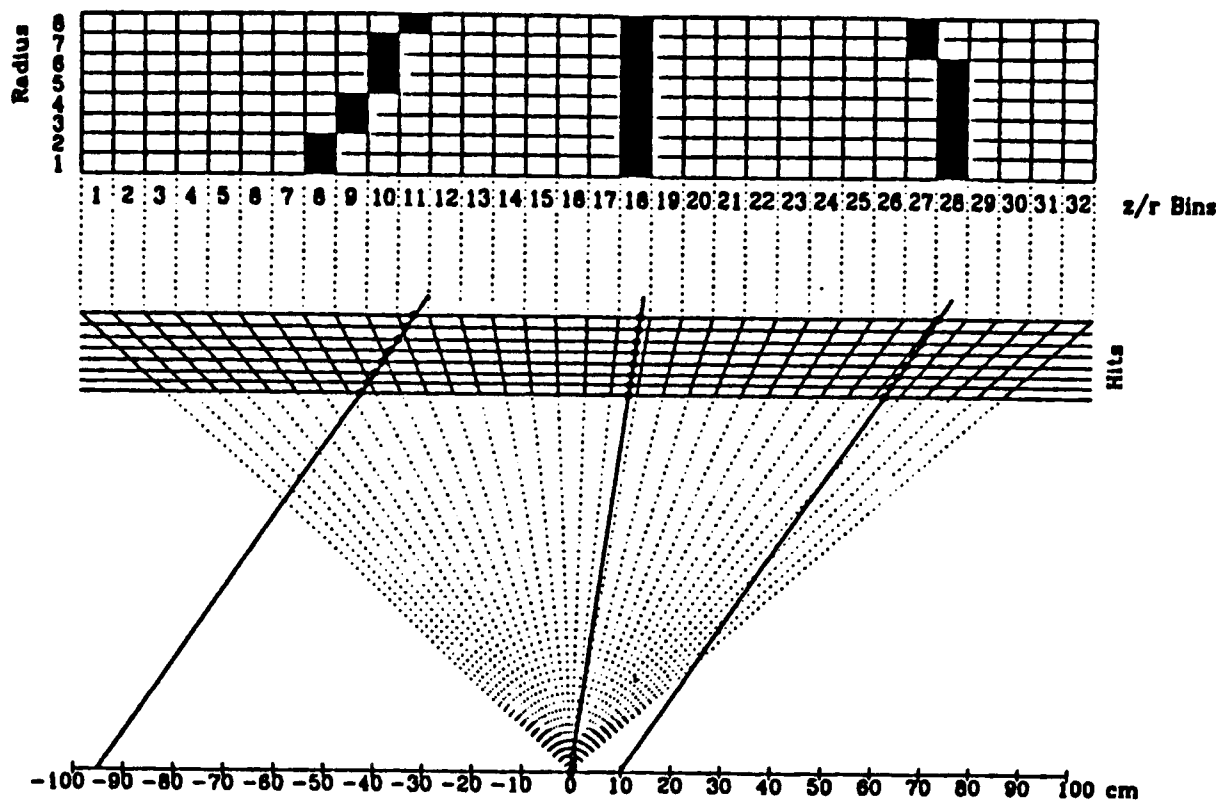


Figure 3.11: Tracks in the $(\frac{z}{r})\times$r plane.

is simplified. The number of $(\frac{z}{r})$ windows is different to CP1 and chosen such that a SL1 $(\frac{z}{r})$ bin corresponds to two $(\frac{z}{r})$ bins in SL3 and SL5 (Figure 3.13). Therefore CP3 and CP5 output 39 and 28 $(\frac{z}{r})$ bits respectively. Note that not all SL1 $(\frac{z}{r})$ bins have a corresponding $(\frac{z}{r})$ bin in higher superlayers.

3.3.4 The Sector Processors

The Sector Processors [26] make use of the long lever-arm provided by SL3 and SL5 track segments and the smaller size of $(\frac{z}{r})$ bins in superlayers 3 and 5 to give an accurate estimate of the track vertex. The vertex (z_0) resolution can in principle be calculated using a least square fit algorithm [16], and table 3.2 indicates the enormous improvement in $\sigma(z_0)$ when track segments from two or more superlayers are combined (assuming an intrinsic 3cm resolution of the z-system).

The Sector Processors find r-ϕ *potential tracks* and r-z *pointing tracks* in three superlayers. This is done in two stages, an r-ϕ and an r-z processing stage, both

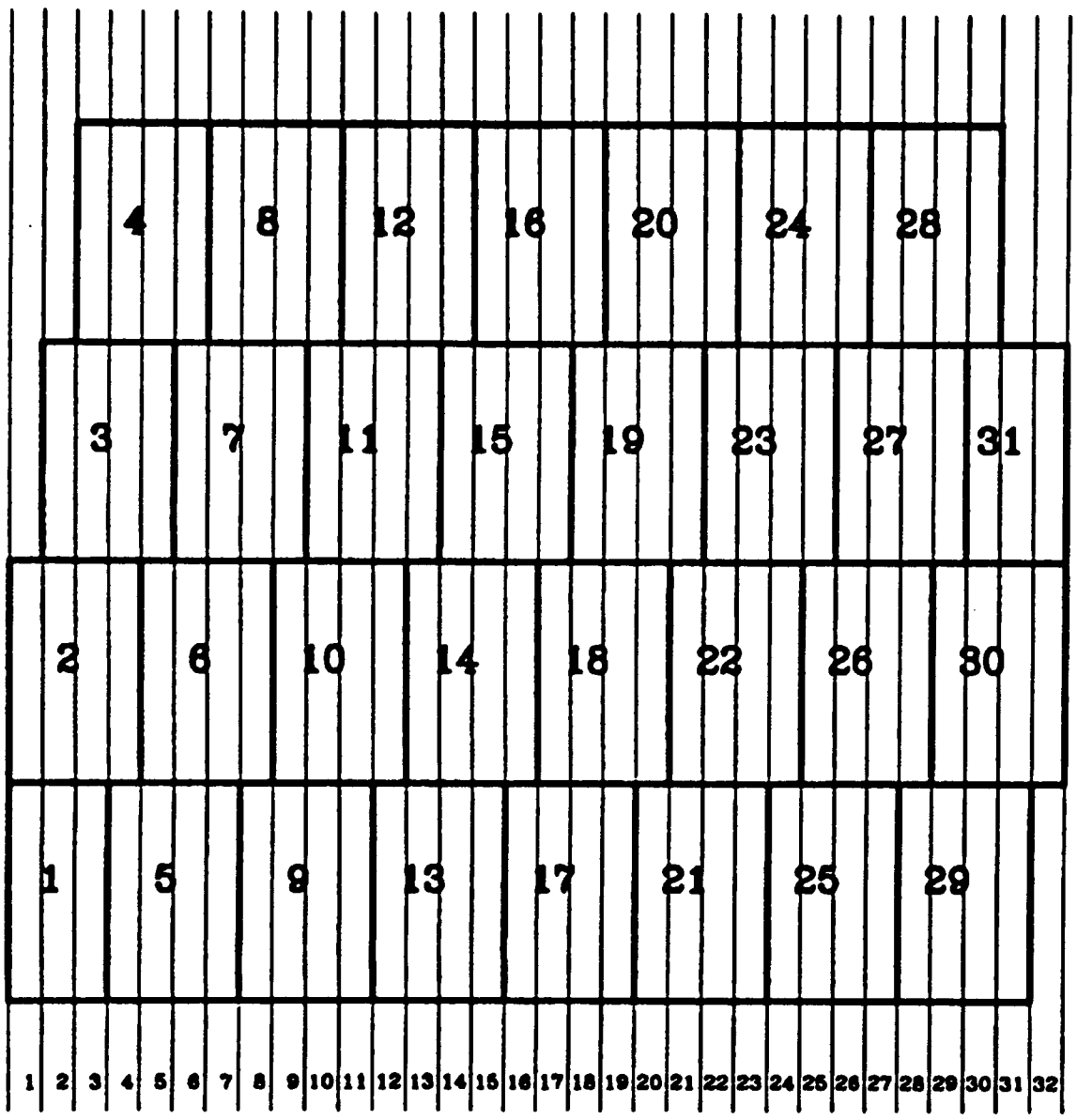


Figure 3.12: The entire $(\frac{z}{r})$-r plane is split into 31 overlapping 4×4 $(\frac{z}{r})$ windows.

Superlayers crossed	$\sigma(z_0)$
1	17.3cm
1, 3	3.5cm
1, 3, 5	2.2 cm

Table 3.2: Least squares fit z_0 resolutions for tracks crossing superlayers 1, 3 and 5.

working in parallel. The results of both stages are combined, and a pointing track is only considered valid if it has a corresponding potential track.

3.3.5 The r-ϕ Sector Processor

The SP accepts input from one SL1, four SL3 and six SL5 cellpairs (Figure 3.1) every 96ns. The produced r-ϕ pattern (Figure 3.14) is compared with test-patterns stored in a look-up table. This results in potential track candidates, and the track quality is determined by three bits:

- A **SL1 Track Bit**, which is set if a track segment is found in SL1.
- A **SL3 Track Bit**, which is set if a track segment is found in SL1 and in SL3.
- A **SL5 Track Bit**, which requires the track to go through all three superlayers and produce a valid pattern.

The patterns of the potential track candidates are not fixed in hardware, but are programmable.

3.3.6 The r-z Sector Processor

As pointed out in section 3.3.3, one SL1 $(\frac{z}{r})$ window has two corresponding $(\frac{z}{r})$ windows in each of SL3 and SL5. This improves the vertex resolution because it reduces the extrapolation uncertainty caused by the short lever-arm of SL1 alone. Figure 3.13a shows a track originating from z_0=13cm contained within a window of z_0=$\pm$25cm, whereas Figure 3.13b shows a track from z_0=-50cm not contained within the z_0=$\pm$25cm window.

The Track Segment Matching (TSM) algorithm is implemented by reprogrammable Gate Array Logics (GALs) and a 'z_0-cut' register. The z_0-cut specifies the TSM window size inside which tracks are still to be considered as coming from the interaction

region. The window is required because the e-p interaction vertex is not always centered in the middle of the CTD, but can vary by ±20cm. The algorithm produces two types of outputs:

- Three vertex bits: A **SL1 Vertex Bit**, a **SL3 Vertex Bit** and a **SL5 Vertex Bit** similar to the track bits of the r-ϕ processor.
- A 16 Z/R-bin output, detailing in which region a good z/r track has been found. Figure 3.15 shows the assignment of the 16 Z/R bits to ten 'Forward', five 'Barrel' and one 'Rear' region. For example for the first forward bit (F1) to be set a track has to go through both SL1 and SL3. The fine granularity in the forward region is designed to eventually enable track-matching of CTD and FTD segments.

The output of the SP is a combination of the r-ϕ and r-z output. The three vertex bits and the 16 Z/R bits are only considered at the next stage of processing if their corresponding track bits (section 3.3.5) have been set too.

3.3.7 The Regional FLT

The Regional First Level Trigger Box (RBOX) [28] receives its input from the 32 Sector Processors of the CTD and the sextant processors of the FTD. The RBOX has two main tasks: the more rudimentary task of distribution of timing and control signals to the z-trigger system and the FADC system [9] ; and the difficult task of forming a First Level Trigger decision. The RBOX is the first FLT stage which has full access to FLT data from the entire chamber.

Figure 3.16 shows the functional subdivision of the RBOX. The RBOX combines the information of the 32 Sector Processors. In the first stage of processing, the number of potential and pointing tracks (of the SPs) are summed together individually

[9]The signals are first fanned out by the RBOX to the z-trigger MTC, which subsequently distributes them to the 16 z-by-timing crates.

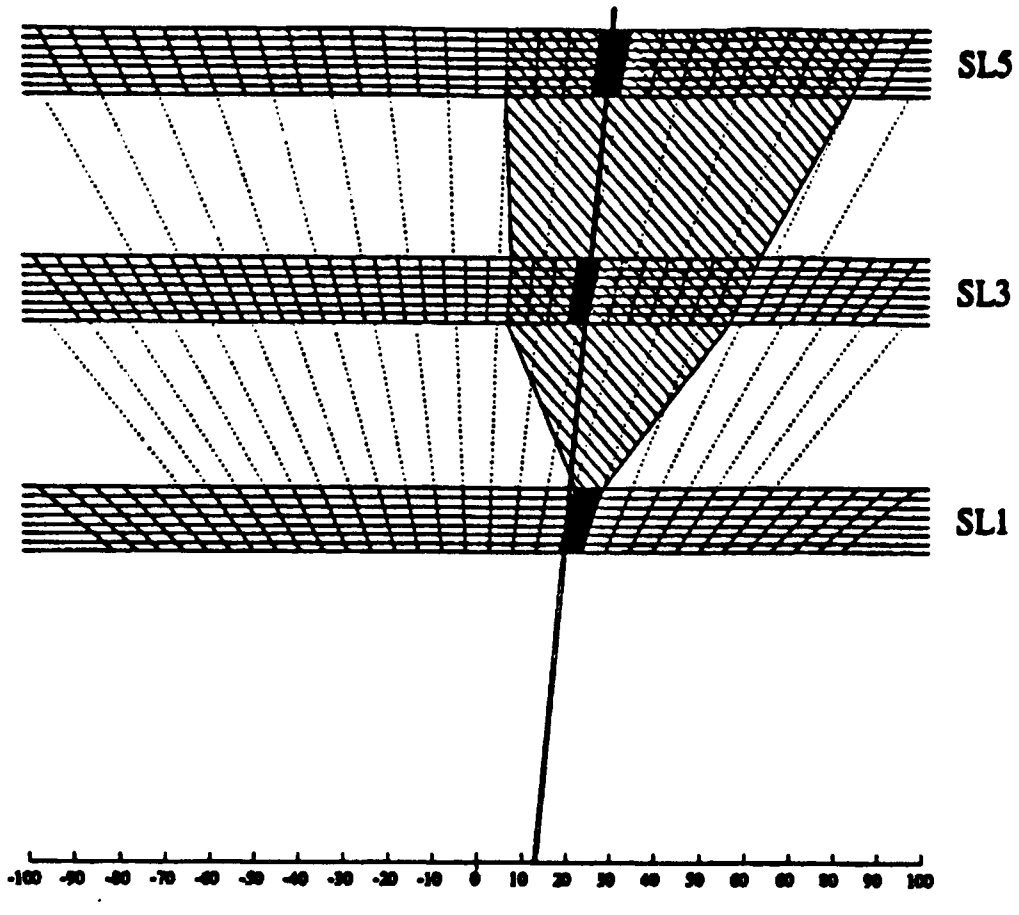


Figure 3.13: Tracks over three superlayers in the $(\frac{z}{r})\times$r plane as seen by the Sector Processors: (a) track coming from within $z_0=\pm 25$cm, and (b) track coming from outside the $z_0=\pm 25$cm region.

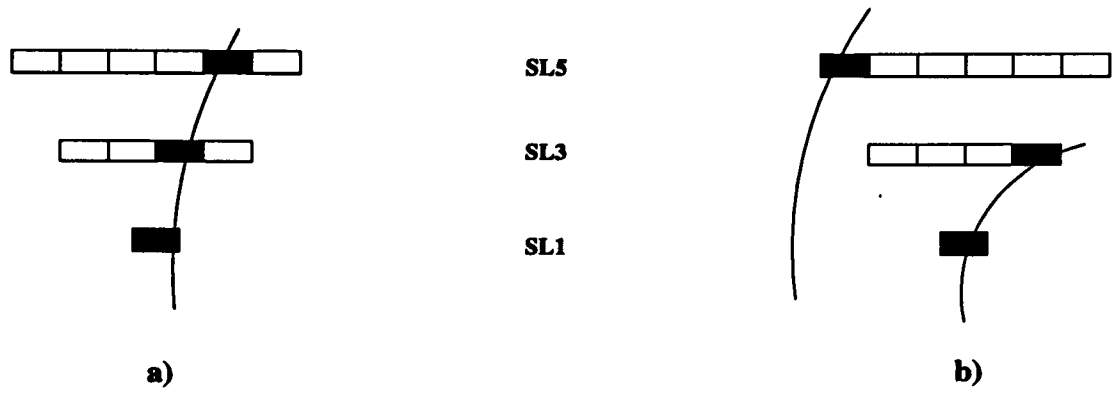
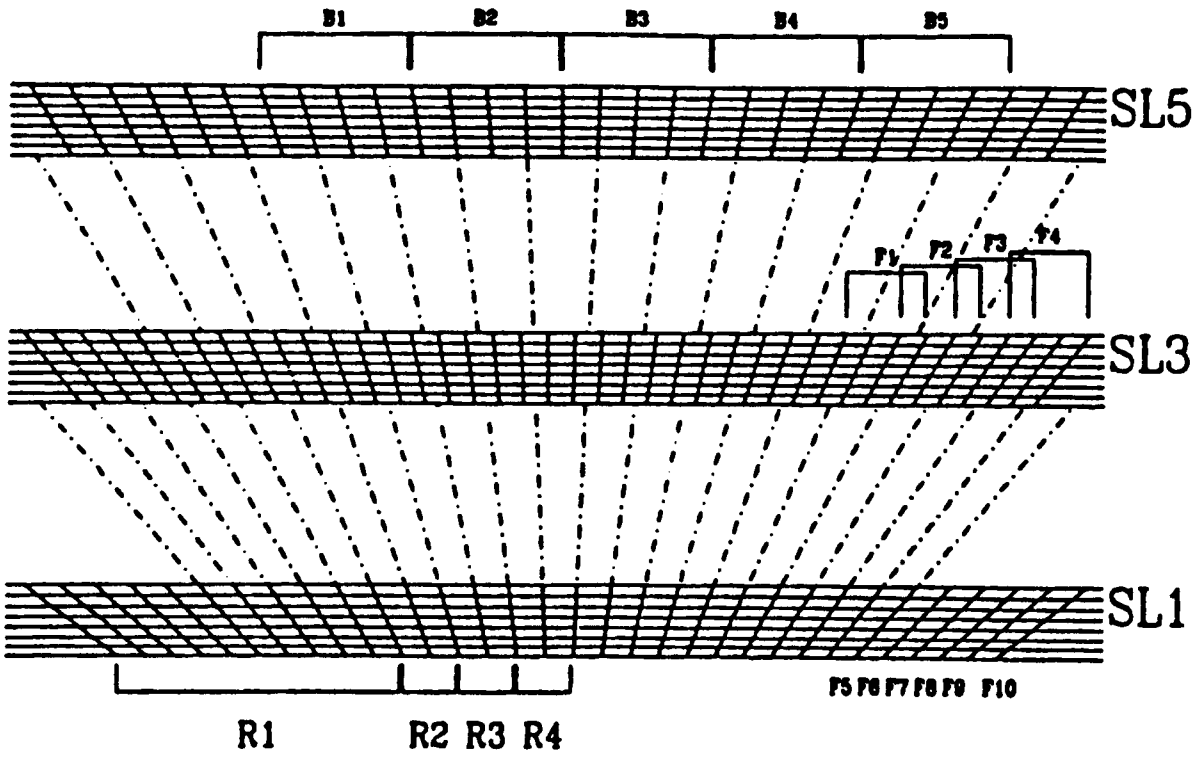


Figure 3.14: R-Phi bitmap of SL1, SL3 and SL5 bits as seen by the Sector Processor. Figure a) shows an example of a valid pattern, and Figure b) shows an example of an invalid pattern.



16 Z/R Bins :	One Rear	R1.OR.(R2.AND. .NOT.B1) .OR.(R3.AND. .NOT.B1 .AND. .NOT.B2) .OR.(R4.AND. .NOT.B1 .AND. .NOT.B2 .AND. .NOT.B3)
	Five Barrel	B1-B5
	Four Forward	F1-F4
	Six Very Forward	F5-F10

Figure 3.15: Division of the Z/R bitmap into 16 Regions.

Event Class	2 bit value
Tight Accept	3
Loose Accept	2
Reject Event	0
No decision because no tracks found	1

Table 3.3: RBOX event classification.

and the 16-bit Z/R outputs of the SPs are converted into a $4(\theta)\times32(\phi)$ bitmap for event classification. Furthermore an $8(\theta)\times8(\phi)$ bitmap is also formed and will eventually be used for CTD-CAL track-cluster matching. FTD diamonds[10] can also be matched with CTD tracks in the overlap region. This task is carried out by the Hit Count Modules (HCMs).

In the second stage of processing the bunch crossing number is determined and an event classification is formed. This is carried out by the Final Decision Module (FDM), which provides a 2-bit event class, defined in table 3.3.

The decision is formed from the sums of potential and pointing tracks in the $4(\theta)\times32(\phi)$ regions. The four polar regions are a Very Forward (VF), Forward (F), a Barrel (B) and a Rear (R) region. A total of ten combinations of these four regions can be formed, such as VF, VF+F, VF+B etc. of which four combinations are chosen to satisfy a minimum $\frac{pointing\ (r\text{-}z)\ tracks}{potential\ (r\text{-}\phi)\ tracks}$ cut. One of the combinations, VF+F+B+R, is always chosen as it covers the whole detector. Neither the choices of the three other regions, nor the precise cut values of the $\frac{pointing\ (r\text{-}z)\ tracks}{potential\ (r\text{-}\phi)\ tracks}$ cuts are intuitive. However, detailed studies[29] have shown that the method of Functional Discriminant Analysis (FDA) is well suited to devise choices of such cuts to provide good discrimination between physics and background.

In the 1993 trigger configuration for example, the $\frac{pointing\ (r\text{-}z)\ tracks}{potential\ (r\text{-}\phi)\ tracks}$ cut was

[10]FTD 'diamonds' are the geometric intersection of the three FTD layers, each offset by 60° with respect to each other (section 2.2). In the FTD-FLT, diamonds are found by the FTD sextant processors. They are the equivalent to the CTD track segments found by the CTD Cell Processors.

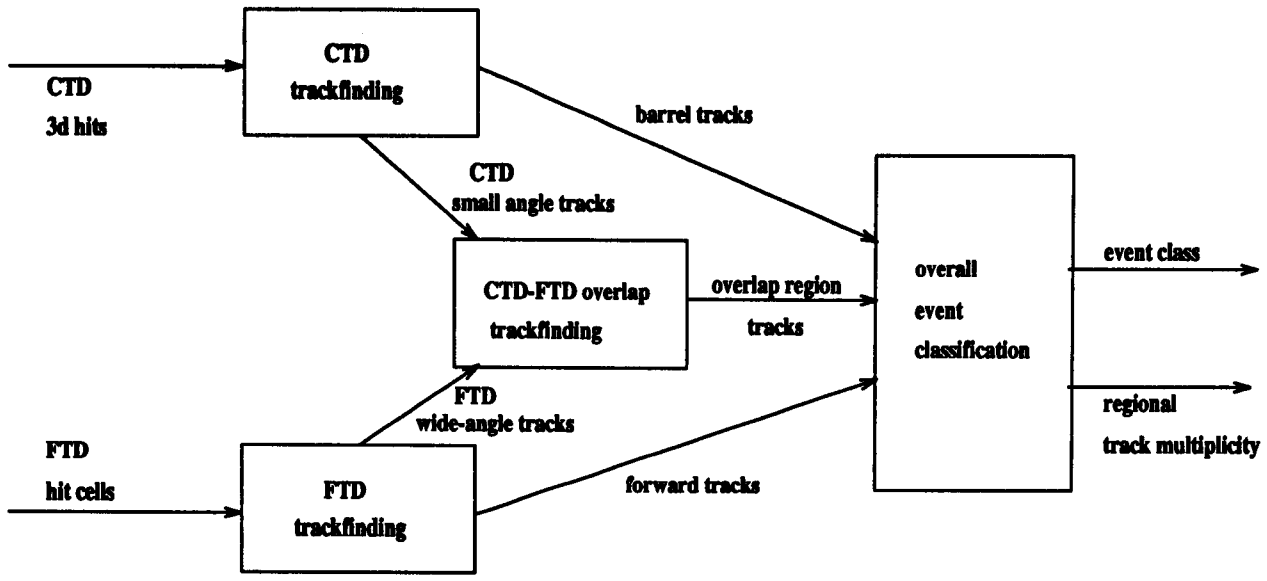


Figure 3.16: Functional subdivision of the RBOX.

chosen to be > 0.01 (e.g. 1%) for class 2 (Loose Accept) events, and > 0.5 (e.g. 50%) for class 3 (Tight Accept) events.

It should be pointed out that the RBOX trigger is designed to make a coarse decision on physics and backgrounds - dedicated triggers for particular physics subprocesses are best constructed by combining trigger information of detectors at the Global First Level Trigger.

3.4 A Prototype System

A prototype system was employed during the early cosmic ray runs of ZEUS in 1991. It was designed to allow readout of z-by-timing modules in a single crate and consisted of a trigger-crate, z-by-timing cards, a ROC and a prototype timing controller. The LTC had to be modified to correctly communicate with the GFLT (and hence with the rest of ZEUS) via the BUSY-ACCEPT handshake, which is normally handled by the RBOX and the MTC (neither were available in the early days of the experiment). Figure 3.17 shows the connections of the system to the GFLT. Upon receipt of a trigger[11] the LTC issued an interrupt request to the ROC. The readout transputer waited until the LTC had finished the pipeline to DPM transfer and then read out the DPM. The ROC only cleared the BUSY bit after it had finished reading the DPMs, because the prototype timing controller did not support the 10 buffer window transfer described in the previous section (rather the whole pipeline was transferred). As a consequence the deadtime of the system was large.

A prototype GFLT test module was also adapted to work with the above system. This allowed standalone testing of the LTC-GFLT communications. It was used later on for standalone system tests of the trigger processors, where a complete loop could be formed between LTC, z-cards, CP, SP and the prototype GFLT.

3.4.1 The Prototype LTC

A wire-wrap prototype LTC module [22] was modified to provide the minimum communication required by the GFLT to integrate the CTD system with the other ZEUS components. The following functions had to be implemented:

[11]The GFLT formed its trigger decision from CTD and calorimeter standalone trigger sources during Cosmic Run I. The CTD trigger simply consisted of NIM modules, ANDing and ORing together certain combinations of the sense wire signals. No CTD-FLT trigger processors were available at this time.

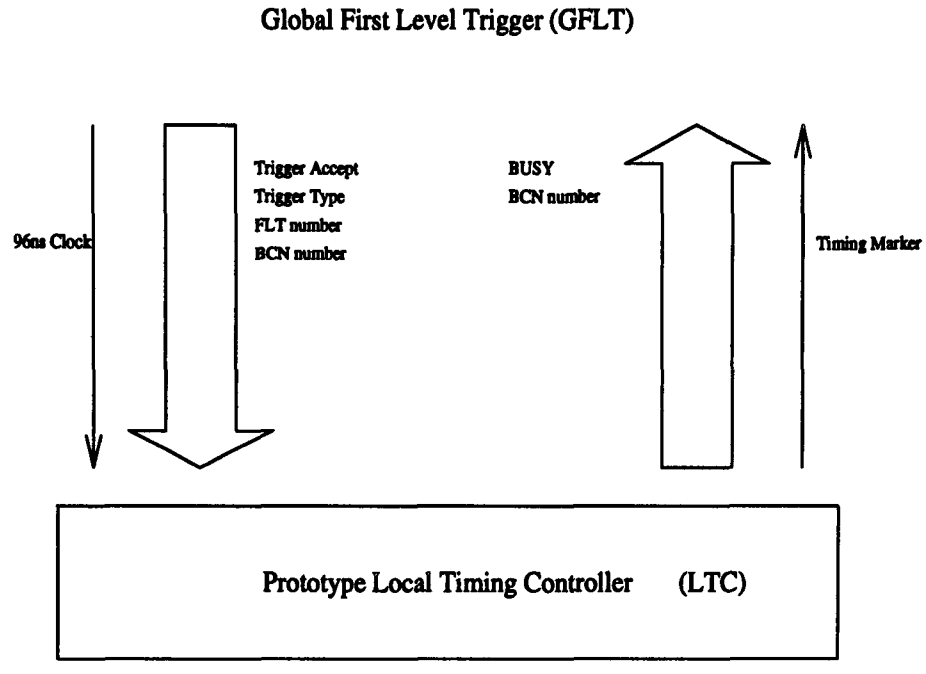


Figure 3.17: Connections of the prototype z-by-timing readout system with the GFLT during Cosmic Run I.

- Identification of the trigger type (or readout type). The 'Readout Type' (ROSYS0..1, ROUSR0..2) had to be stored in a register upon receipt of a trigger.
- A register holding the FLT number of the latest trigger.
- Generation of a BUSY signal after a trigger ACCEPT and a command to allow the ROC to clear this signal upon completion of readout.
- A timing marker to validate the BUSY signal.
- Generation of an interrupt signal to the ROC.
- A slow software clock for debugging purposes.

Table 3.4 summarises the commands of the LTC module which can be issued by reading from the corresponding 'ROC address'. Figure 3.18 shows the modification circuitry which implements the GFLT communications. Address lines A11..A14 and A8..A10 are used to decode the new functions ROT_register_read, FLT_number_read,

SEQ.	ROC ADDRESS A1 → A11	A12	A13	A14	FUNCTION	HEX VALUE
1	X	0	0	0	DUMMY TRIGGER PULSE	0
2	X	1	0	0	START ONE PIPELINE CYCLE	1000
3	END ADDRESS	0	1	0	LOAD PIPELINE LENGTH END ADDRESS	2370
4	END ADDRESS	1	1	0	LOAD PIPELINE WINDOW END ADDRESS	3370
5	START ADDRESS	0	0	1	LOAD PIPELINE WINDOW START ADDRESS	4000
6	START ADDRESS	1	0	1	LOAD DUAL-PORT RAM START ADDRESS	5000
7	X	0	1	1	TRIGGER ENABLE	6000
8	00000000000	1	1	1	RESET	7000
9	00000000001	1	1	1	READ ROT REGISTER	7800
10	00000000011	1	1	1	CLEAR BUSY	7C00
11	00000000101	1	1	1	READ FLT NUMBER	7A00
12	00000001001	1	1	1	SOFTWARE CLOCK	7900

Table 3.4: Prototype LTC commands. An 'X' in the ROC ADDRESS column means any combination.

ROC_BUSY_clear and Software_clk. The latches IC87, IC94 and IC90 store the Readout type, FLT number and BUSY bit respectively. Conversion of ECL signals to TTL is accomplished by the MC10125 tranceivers IC69, IC92 and IC93. The communication protocol with the ROC is set up via three types of lines: The 'N'-line geographically addresses the card; address lines, data lines and a write line specify the access request; the memory enable signal finally executes the request (Figure 3.20b).

3.4.2 The GFLT Test Module

The prototype GFLT [23, 24] is a relatively simple module to provide a subset of the functionality of the real GFLT for test purposes. It can be programmed to use internal or external trigger sources, issue different trigger types, measure the deadtime and detect errors in the communication protocol. The Tokyo group provided a PCB prototype GFLT module which can be controlled via two VME busses.

An interface board was designed to physically mount the GFLT module, and to interface the VME-bus of the GFLT prototype module to the custom-backplane TTL ROC-bus. Circuit diagram 3.19 shows an implementation of such an interface.

Figure 3.20a and 3.20b show timing diagrams of a VME and a ROC bus access

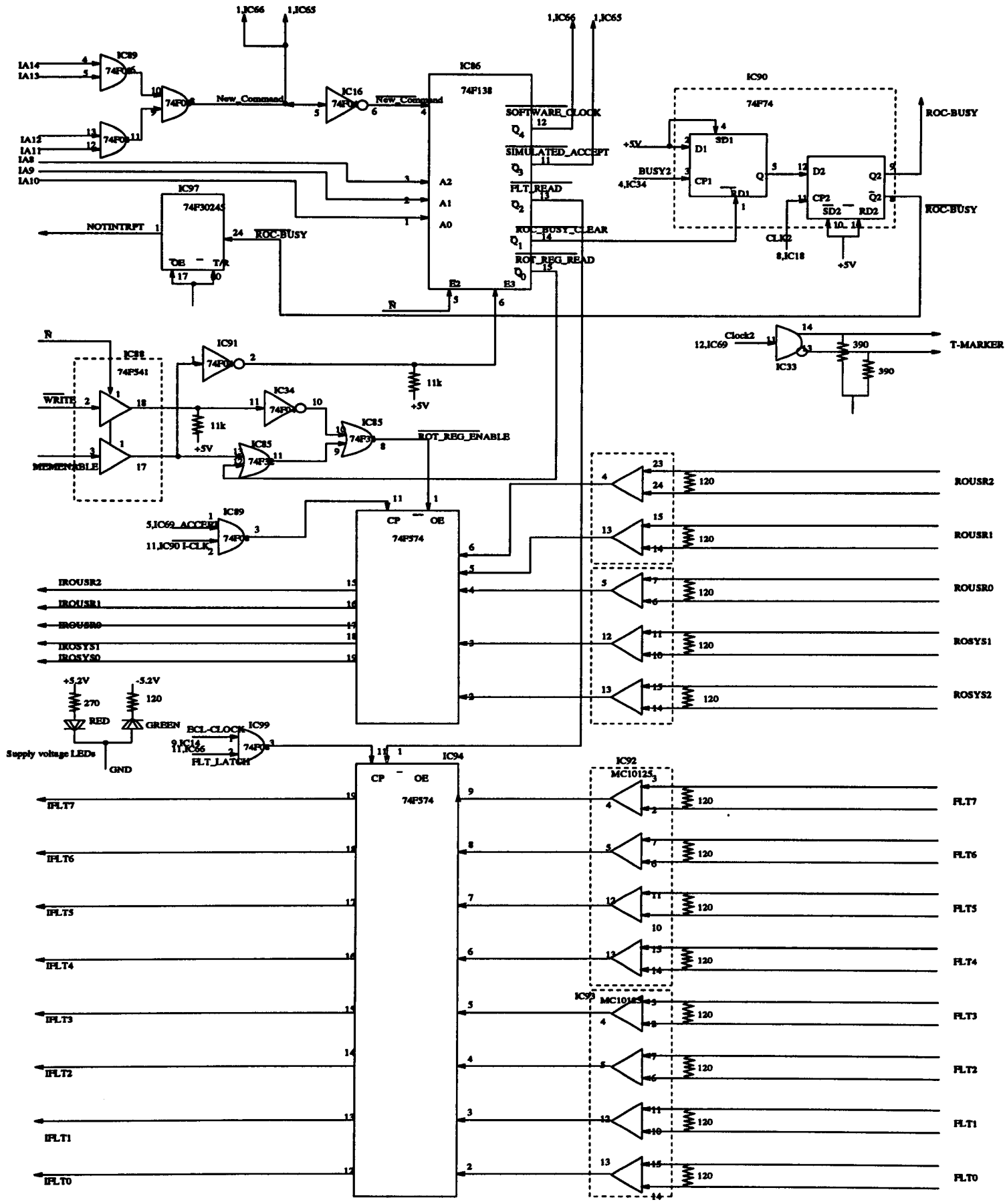


Figure 3.18: Prototype LTC circuit responsible for communications with the GFLT.

respectively. The VME bus allows asynchronous data transfer via the signals AS (Address Strobe), DS0 (Data Strobe) and DS1, and DTACK (Data Acknowledge). The MASTER (in this case the Readout Controller) drives the AS signal low to inform the SLAVE module that the address is stable. The DS signals perform a similar task for the data lines, only that they are driven low by the MASTER to indicate valid data during a write cycle, and high by the SLAVE to validate the data lines during a read cycle. DS0 and DS1 also specify the word width of the transfer. The SLAVE drives DTACK low to indicate that it has successfully received data on a write cycle. On a read cycle, the SLAVE drives DTACK low to indicate that it has placed data on the data bus.

The TTL ROC-bus is a synchronous bus, and hence its read/write access specifications are much simpler. A Read/Write line specifies the type of access, and the memory enable signal executes the request, once address (and data) lines are stable.

3.4.3 Performance on Data from Cosmic Muons

The system (consisting of a single crate of z-by-timing modules, the prototype LTC, and a prototype RBOX) was successfully integrated with the GFLT and other ZEUS components during Cosmic Run I. It read out part of the CTD chamber for the first time during October 1991. Figure 3.21 shows a reconstructed track originating from a cosmic muon traversing the CTD. Although only 72 sense wires were read out by z-by-timing modules during this period, this was sufficient to estimate resolutions of the z-by-timing system [13] and to prove that the system was working. The prototype GFLT was also employed during Cosmic Run II, where it assisted with debugging a more advanced version of the Local Timing Controller.

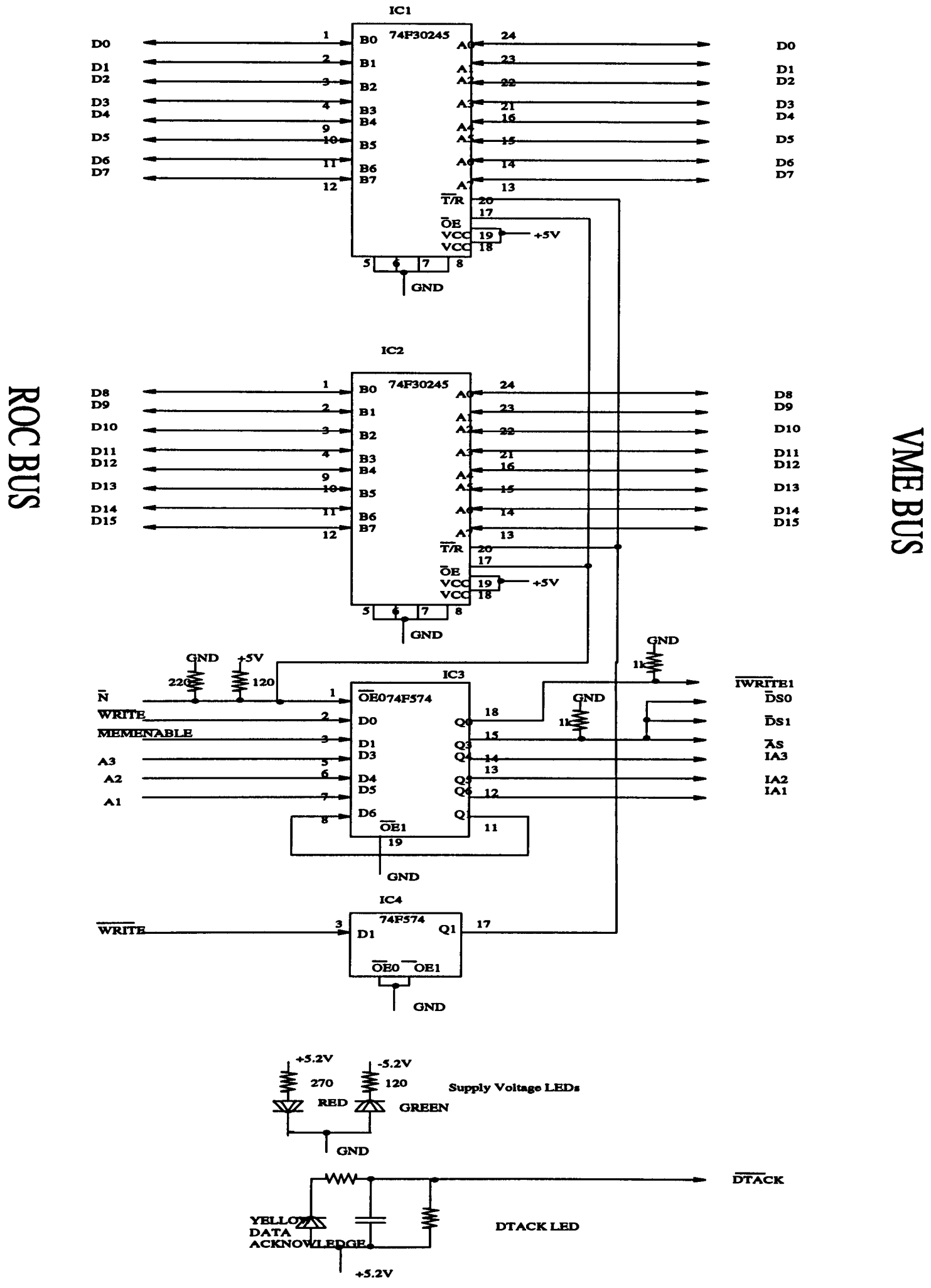


Figure 3.19: VME/ROC-bus interface circuitry for the GFLT test module.

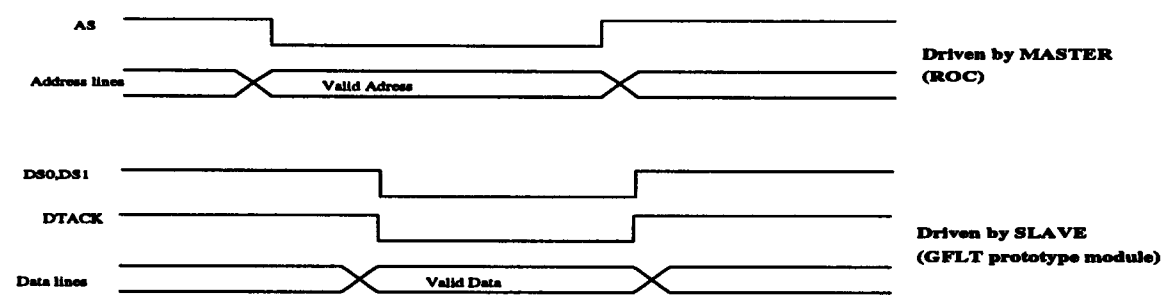


Figure 3.20: a) A VME bus read access cycle; b) a TTL ROC bus read access cycle.

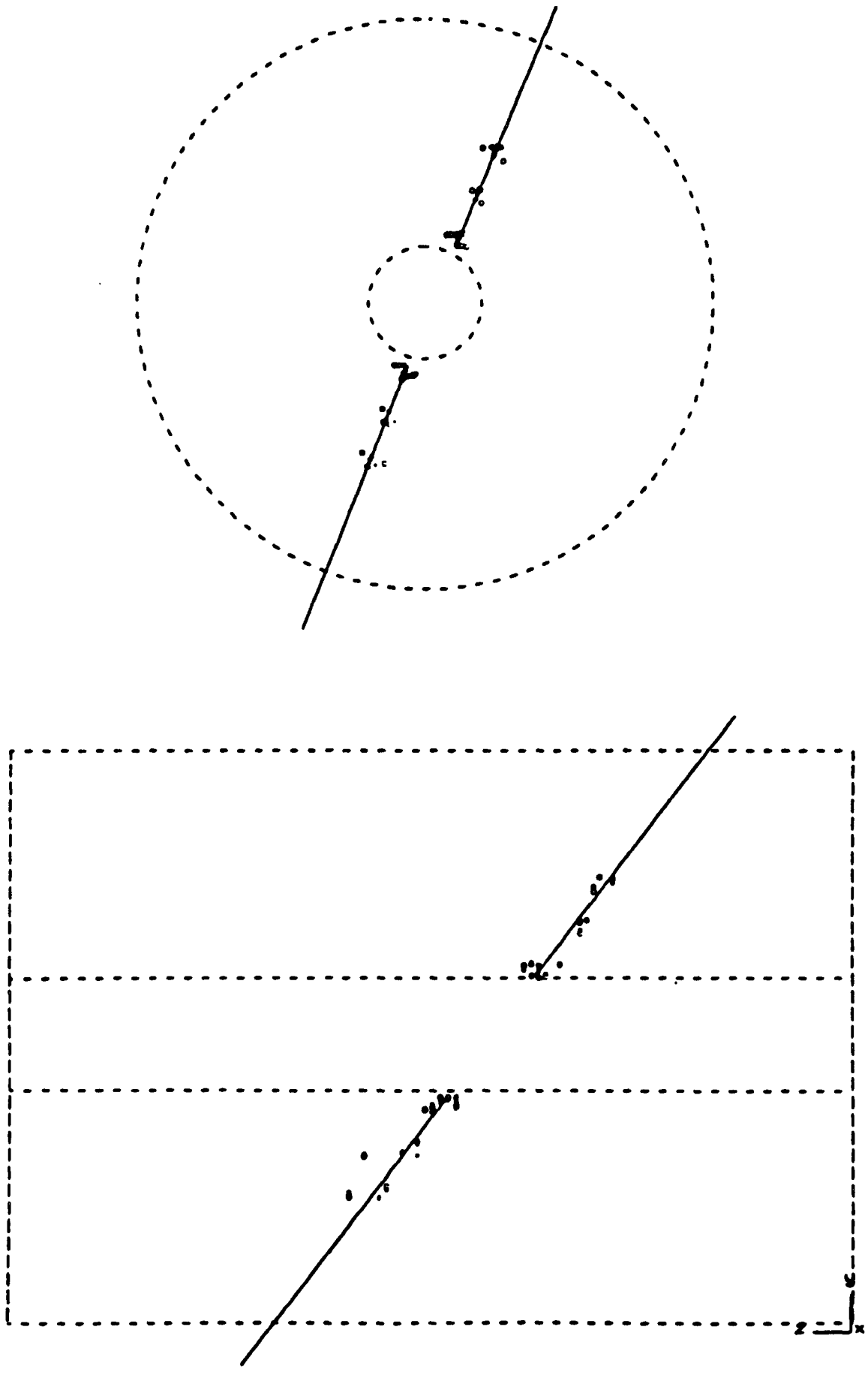


Figure 3.21: One of the first cosmic tracks seen in the CTD during the 1991 Cosmic Run I. The Chamber was only partially equipped with z-by-timing readout at that time.

3.5 Processor Board Testing

The complexity of the trigger boards makes testing and verification of their operation a difficult task. In general the testing can be broken down into three stages, according to the level of sophistication of the test:

- Simple memory checks will try to detect faults on memories and registers. Typically this stage of testing would find problems due to blown chips, stuck bits, grounded lines and cross-talk between address and data lines.

- Verification of the functionality of the boards is more complicated. All the boards have input and output registers, which allow the loading up of test-vectors. After one or more such vectors have been clocked through the processor logic [12], they can be read from the output registers and checked against a software simulation. Sometimes it is not possible on combinatorial grounds to test all possible input-vectors. In this case a subset of vectors has to be generated, which represents a fair sample of expected input from real data. A further complication of such functionality tests is that the timing is different under slow and fast clock cycles.

- High speed testing of the modules and testing the communication links between them. Unlike the other two stages of testing, the sources of test-failure are often difficult to locate. They include for example broken backplane connections, input or output driver problems, inferior signal quality, timing problems and many others.

A multi-purpose program, the CTDFLT test software, had to be designed to accomplish these tasks. In the beginning the single board tests were employed during

[12]This is done by asserting 'slow' clock signals under software control. After a specified number of cycles, the processed input will appear in the output latch.

the design phase of wire-wrap versions of the trigger boards at the Rutherford Appleton Laboratory. Later on they were used for production testing of the final PCB versions of the modules. The multi-board high speed tests were carried out at both RAL and DESY. The need for periodic checking of all parts of the CTD-FLT system meant that the test software had to be designed to run integrated with the 16-crate, 120 transputer CTD-DAQ system[13] , as well as stand-alone on a single crate single transputer laboratory system. The software needed to test 17 types of different cards, and yet had to be small enough in size to fit on the small 1Mb on-board transputer memories.

The high speed testing of modules is aided by a specially designed card, the Module Test Driver (MTD) [27]. The MTD behaves like a general purpose logic analyser, and is capable of driving and receiving signals to and from other modules residing on the MTC test-crate backplane. It does not require the presence of a LTC or a z-card[14]. A burst of test-vectors, stored in a block of Serial Protocol Channels (SPC) RAMs, is clocked through the trigger module at high speed, while a different block of SPC RAMs simultaneously receives the output of the processor. Serial Protocol Channels have to be used because data from the 360 line auxiliary ROC bus has to be accessed by the 16-bit ROC data bus. By serially multiplexing 16-bit groups into a single bit, the entire auxiliary ROC bus can be multiplexed into a 16-bit word. In this way the MTD is able to access the whole range of the 360 line auxiliary ROC bus via the SPC RAMs.

In a different test-setup, the z-by-timing cards can be put in a special test-mode, and their pipelines can be loaded up with test-vectors. The data are then clocked through the Cell Processors under LTC control. After a simulated software trigger, the LTC will transfer the CP's pipeline into the DPM buffer, where output is available

[13]In the CTD-DAQ system, the software performs checks on the trigger processors before the beginning of every data run.

[14]This reduces the number of sources for test failure, provided the MTD does not have a fault.

for comparison with a software simulation of the cell processor.

In integration test setups, the prototype GFLT of section 3.4.2 and one or more LTC modules were used to test the communication interface of the CTD trigger system with the GFLT. This setup also proved to be a good test bed for the CTD-DAQ readout code, because errors in the readout code invariably result in errors in the communication protocol which can be identified by the prototype GFLT.

3.6 Performance of the FLT on Data

During the 1993 run period, all the 32 SL1 Cell Processors (CP1), the 32 Sector Processors , the eight Hit Count Modules and the Final Decision Modules were installed. Only superlayer 1 was equipped with FLT electronics. The trigger cards were fully integrated with the DAQ, and their pipelines were read out every time an event was triggered. It was found that FLT hardware and offline simulation agreed well with each other [30, 31] [15]. The CTD-FLT actively contributed to trigger decisions. In particular, combinations of calorimeter threshold triggers ANDed with the CTD trigger reduced the trigger rates on beam-gas backgrounds substantially. This allowed calorimeter thresholds to be lowered, and hence increased the acceptance of physics processes over backgrounds [33]. Furthermore, two dedicated triggers for physics subprocesses were employed using the CTD-FLT information: an elastic J/ψ trigger, and an elastic rho trigger. For example the J/ψ trigger demanded the track multiplicity to be 1,2 or 3 (together with calorimeter subtriggers and C5 and VETO wall vetos) [32]. Figure 3.22 shows the effectiveness of the dedicated J/ψ trigger on the data from the 1993 running period. The solid line shows contributions of the dedicated J/ψ trigger to a selected J/ψ event sample as a function of the invariant mass of the e^+e^- tracks, while the hatched region shows contributions from all other trigger sources. Note that roughly one third of all J/ψ events in the sample were triggered by the dedicated J/ψ trigger, thus yielding the CTD-FLT an essential tool for such physics studies.

In the following paragraphs we show the online results of the trigger processors from data of the 1993 running period. We do not present trigger rate studies, nor discuss the impact of the CTD-FLT on the trigger rate, but refer to [34] for such studies.

[15] Because all the vital information of each trigger stage is stored in pipelines, each stage can be checked by running an offline simulation of the FLT on the output data of the previous stage.

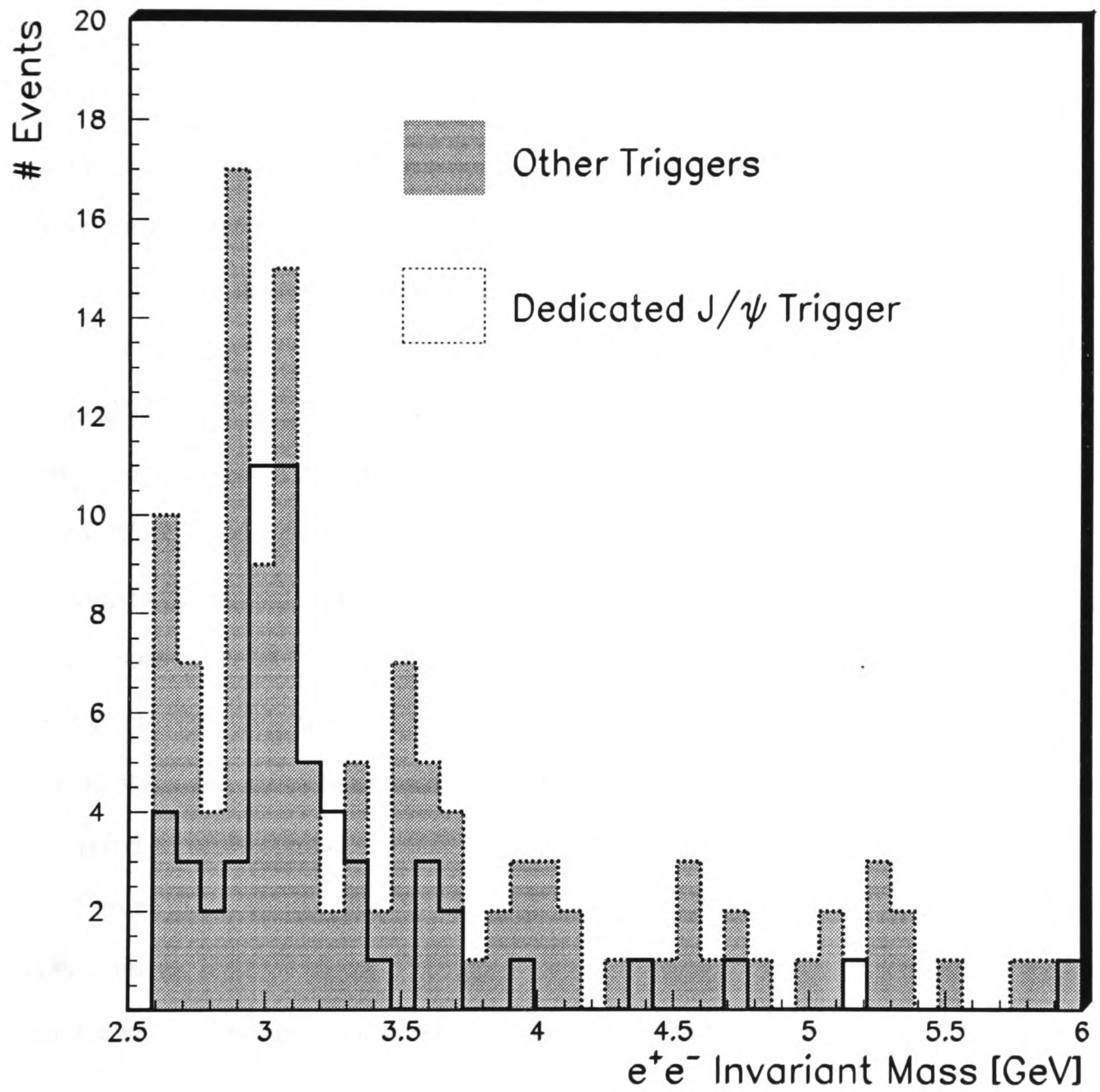


Figure 3.22: The effect of the dedicated CTD-FLT J/ψ trigger on the data. Roughly one third of all J/ψ events were selected by the dedicated J/ψ trigger.

Throughout we have used the same data sample of 20787 events of 'RAWDATA' - events which have triggered all three levels of the ZEUS trigger [16], and have been consequently written to tape. The sample corresponds to an integrated luminosity of L=2pb^{-1}. Figure 3.23 shows the time profiles of the CP1 and RBOX VALID bit outputs [17]. Time bin zero (t=0) corresponds to the time bin in which the interaction has occurred, as defined by the GFLT. Signals from the interaction at t=0 are subsequently digitised by the z-by-timing cards and processed by the Cell Processors. Data finally should arrive at the output latches of the Cell Processor 14×96ns cycles later, which is indeed observed. The VALID bit remains set for two 96ns time bins for ideal events[18] (time bins 14 and 15 in Figure 3.23) but can be spread out over several bins for non ideal events (up to time bin 17 in Figure 3.23). After the data has been processed by the Sector Processors [19] and the RBOX, it should arrive in the RBOX pipeline 24 cycles after t=0. Again this is observed. Because the RBOX combines the information of 32 cellpairs, it can reduce the ambiguity range of the Cell Processors (spread throughout time bins 14-17) considerably. As a result, most of the events can be assigned to a single time bin (time bin 24 in Figure 3.23), and hence the RBOX can usually identify the Bunch Crossing Number at which the collision occurred unambiguously.

Figure 3.24 shows the $(\frac{z}{r})$-output of the Cell Processors of events which were classified as RBOX 'class 3' (Tight Accept) events. The $(\frac{z}{r})$-bin 30 corresponds to the forward direction, and $(\frac{z}{r})$-bin 15 is centered in the middle of the CTD. The overall

[16]This includes events which were not triggered by the CTD-FLT, but by other components.

[17]Like the CP VALID bit discussed in section 3.3.2, the RBOX VALID bit is only set when all the data from the same event has been collected and processed. The RBOX trigger decision is only valid during the time the VALID bit is on.

[18]Ideal events are events which neither have missing hits due to chamber inefficiencies, nor have additional noise hits.

[19]Because only SL1 was equipped with trigger processors during 1993, the Sector Processors did not play an important role in the trigger, and they were configured to accept every event. We therefore omit distributions of the outputs of the SP, as they do not add anything new to the above discussion.

shape of the distribution is due to details of the applied calorimeter trigger at the third level: If there is no energy deposition in the rear calorimeter (RCAL), no calorimeter timing cut is applied and the event is allowed through. Because forward-distributed events are less likely to cause activity in the RCAL, they are more likely to pass the third level trigger. The small hump at bin 28 can be attributed to contributions from the proton remnant. The peak at $(\frac{z}{r})$-bin 12-13 contains contributions from physics interactions. In this run the vertex was shifted towards the electron direction, and hence this peak is not centered on $(\frac{z}{r})$-bin 15.

Finally Figure 3.25 shows comparisons of the online and offline track multiplicities. Note that the online track multiplicity is formed from the sum of the *pointing (r-z) tracks.* Only tracks from within the interaction region (z=±25cm) are considered to be pointing tracks. The offline track multiplicity on the other hand is defined as the number of tracks from within z=±25cm, and the tracks are the result of a full 3D track reconstruction. The difference between the two tracking methods can be summarised as follows:

- The offline reconstruction has access to data from all nine superlayers, while the CTD-FLT only has access to SL1, SL3 and SL5 (only SL1 for 1993).
- The offiine reconstruction program uses data from the much more accurate FADC readout, while the CTD-FLT uses data from the z-by-timing system.
- The CTD-FLT track multiplicity is based on the track segments of CP1, while the offline track multiplicity is based on full tracks.
- The CTD-FLT has to be able to process ~2 million events per second compared to the offline reconstruction of one event every two seconds.

It is important to note that the CTD-FLT generally overestimates the track multiplicity because of double-counting effects from overlapping cellpairs and sectors. This

in general is a safeguard as good physics events are less likely to be rejected by a multiplicity cut. However in comparison with the offline reconstruction, the CTD-FLT multiplicity undershoots the offline multiplicity because it only considers data from one superlayer, and hence is less efficient. On the whole, the online and offline multiplicities compare very well at low track multiplicities.

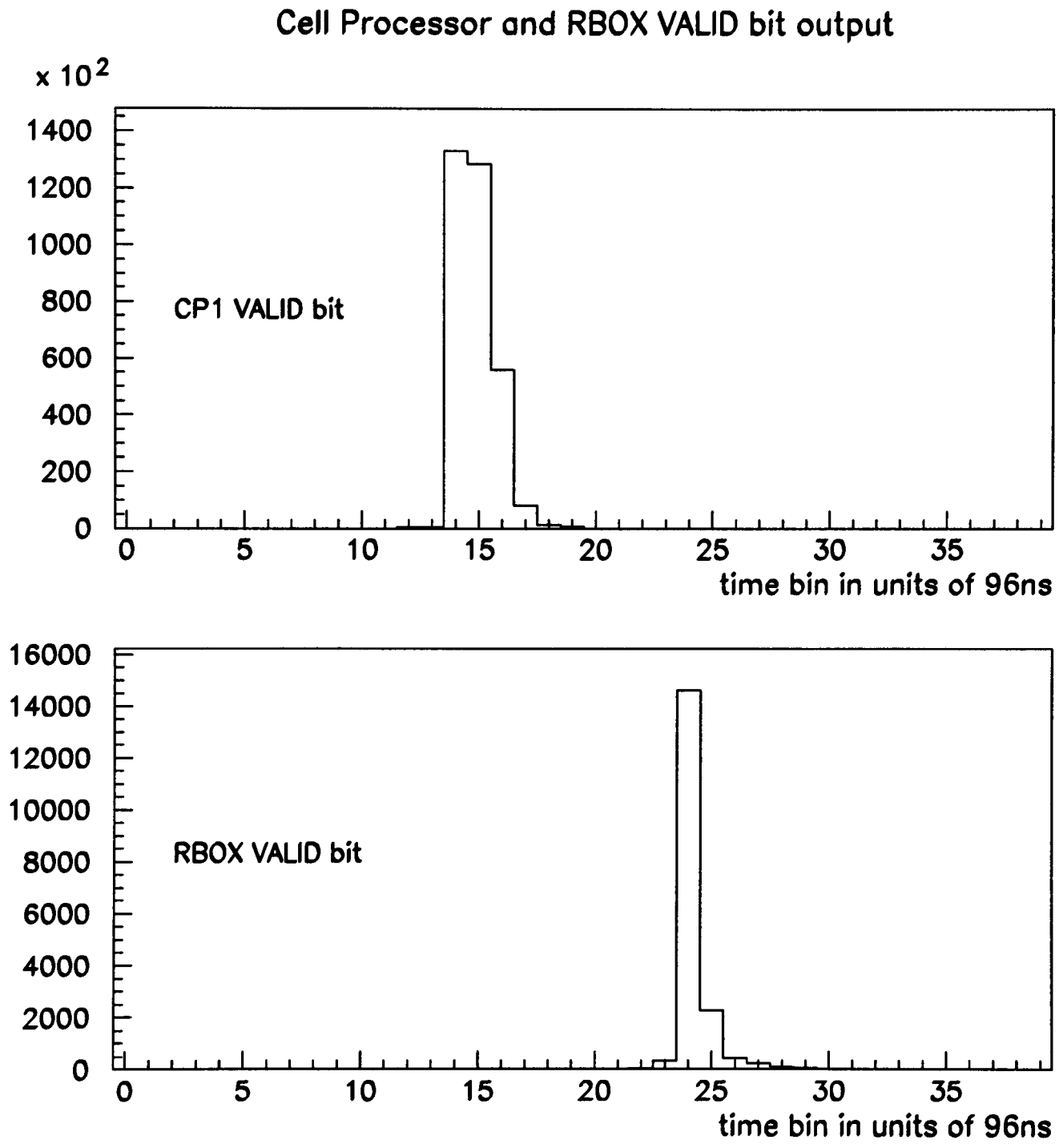


Figure 3.23: The VALID bit output from the Cell Processor 1 boards and the RBOX Final Decision Module.

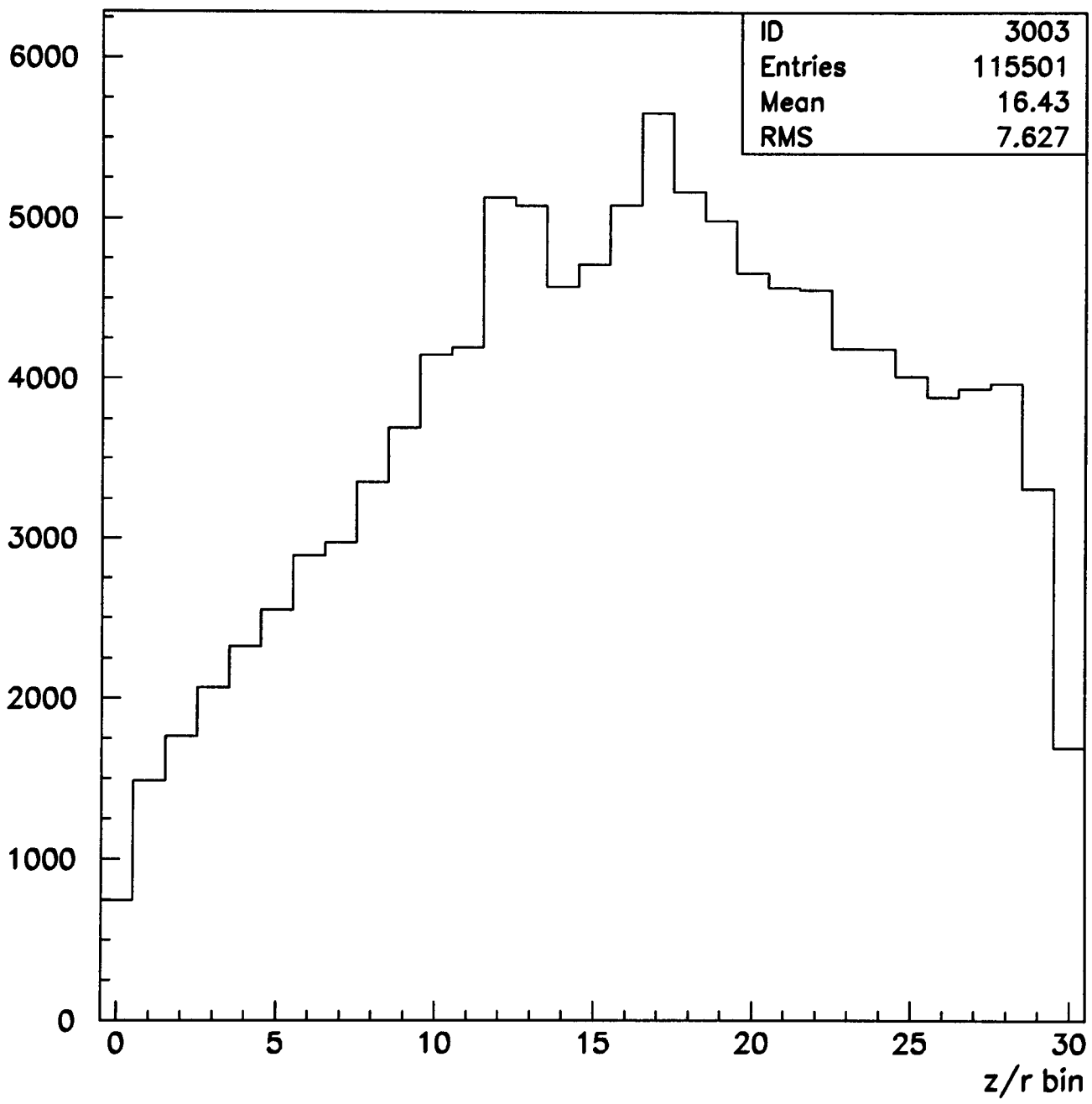


Figure 3.24: The Cell Processor 1 $(\frac{z}{r})$-output of events which were classified as 'ACCEPT' class 3 events by the RBOX.

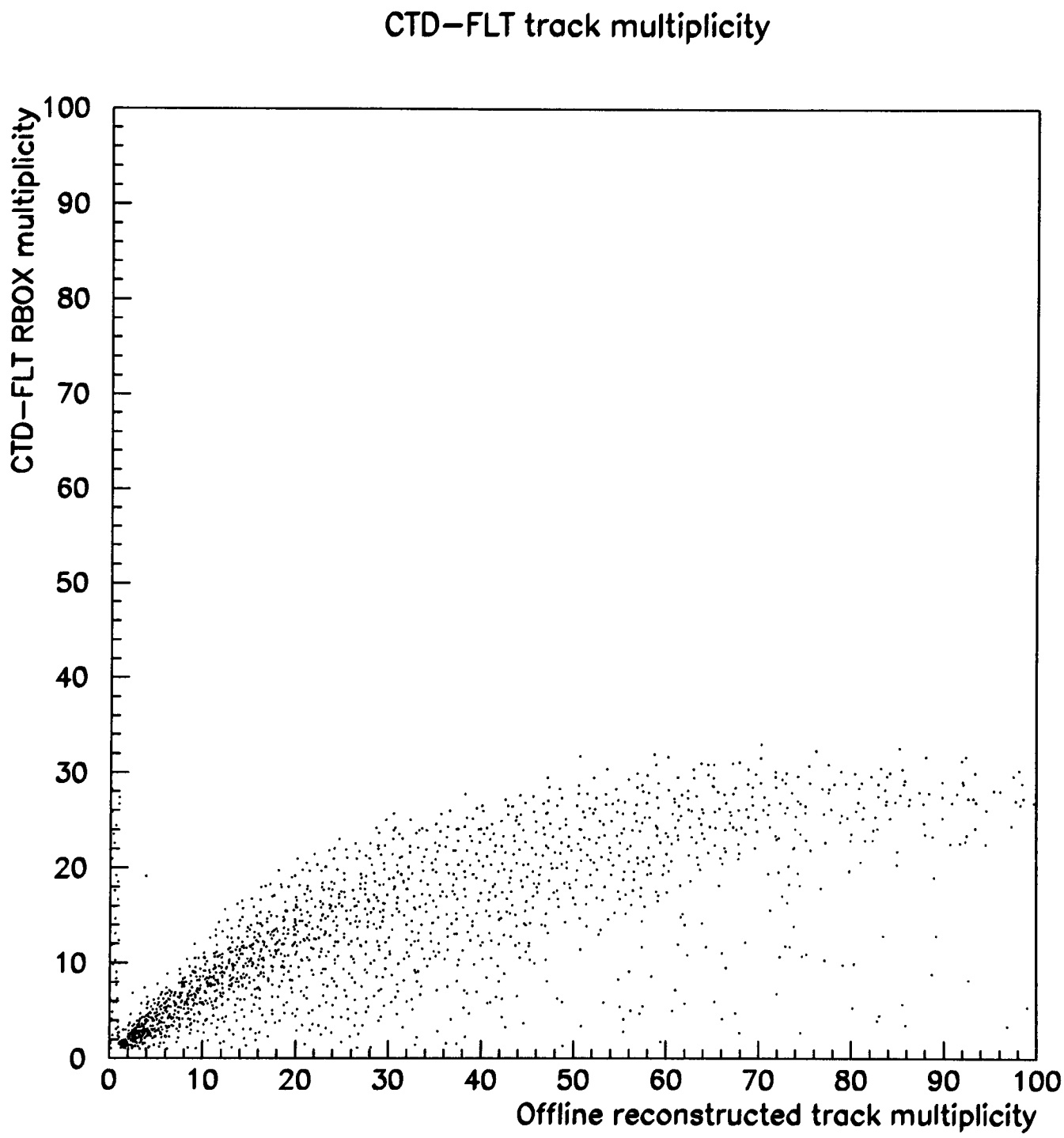


Figure 3.25: CTD-FLT online track multiplicity vs offline reconstructed multiplicity.

3.7 Status and Conclusions

During the 1993 running period, only superlayer 1 was equipped with trigger processors. During that period, the 32 Cell Processor (CP1) boards, the 32 Sector Processors, the eight Hit Count Modules of the Regional First Level Trigger box, and the Final Decision Module were fully integrated with the ZEUS DAQ environment and read out on every first level trigger.

The CTD-FLT system also contributed actively to first level trigger decisions. The track multiplicity and event classification results of the RBOX were combined with trigger information from other detectors by the Global First Level Trigger, and subsequently used to construct subtriggers for specific physics processes. The CTD-FLT trigger proved to be an invaluable part of the First Level Trigger system.

The design of the Cell Processor boards for superlayers 3 and 5 has already been completed, and the full number of boards is expected to arrive at DESY and to be installed before next year's running period, starting in May 1994. The design of the CTD-calorimeter track-cluster matching hardware is already under way, and is expected to be finished before the Summer 1994.

Part Two

Studies of Supersymmetry at HERA

Chapter 4

Supersymmetry

4.1 Beyond the Standard Model

The Standard Model (SM) has been tremendously successful in explaining phenomena at energy scales accessible by past and present experiments. However, due to the large number of free parameters, there is a consensus that a more fundamental theory will be needed to explain phenomena at higher energies. The idea of Grand Unification lends itself naturally as one possible principal for such a theory beyond the SM, as it reduces the number of parameters of the theory by unifying the three forces of the SM into one force. This section uses the idea of Grand Unification to investigate an experimental and a theoretical problem - both a consequence of Grand Unified Theories (GUTs). The problem can be cured by introducing a new theory, supersymmetry (SUSY) [35, 36, 37]. Although a number of other theories also satisfy this criteria, supersymmetry is the only *perturbative* such extension of the SM, and therefore is the only calculable theory beyond the SM.

4.1.1 Unification of Coupling Constants

Recently, evolutions of the electroweak and strong couplings from their measured values at M_Z to very high energies have shown [46] that a single unification point is excluded by more than eight standard deviations for SM physics alone. However, if

one includes minimal SUSY, with superparticle masses around M_{SUSY}, and performs a best χ^2 fit on the three couplings meeting at a single unification scale M_{GUT}, one finds that the fitted values for M_{SUSY} and M_{GUT} are [46]

$$M_{SUSY} = 10^{3\pm1} GeV, \tag{4.1}$$

$$M_{GUT} = 10^{16\pm0.5} GeV. \tag{4.2}$$

The proton lifetime at M_{GUT} is $\sim 10^{34}$ years, safely above the experimental limit. Although this can not be taken as direct evidence for the existence of supersymmetry, it illustrates that the minimal SUSY model is consistent with recent experimental data, a single unification point and a SUSY mass $O(TeV)$.

It should be pointed out that the result of the SUSY mass scale fit could in principle have been very different to the $1TeV$ scale, in which case SUSY would have had to be excluded as a candidate theory (due to reasons discussed in section 4.1.2). These results are the only 'experimental' results to date which might hint to supersymmetry as the theory beyond the Standard Model.

4.1.2 The Naturalness Problem

If one assumes a fundamental scalar particle, the Higgs particle, introduced to explain the mechanism by which the gauge bosons $W^{\pm}$, Z^0 and the fermions acquire mass in the Standard Model (SM), then this has two serious consequences. The first consequence is that the Higgs should be discovered in the near future, and that, one might argue, will only be a matter of time. The other consequence, the naturalness problem, is more fundamental and requires one to look for physics beyond the SM in order to explain it. What is the naturalness problem? Following the notation and argument of [37], the SM couplings and masses can be expressed as a function of a momentum cutoff scale Λ. Fermion masses have a logarithmic divergence in the scale Λ. If one wants to calculate the effective fermion mass at some higher energy scale Λ_2,

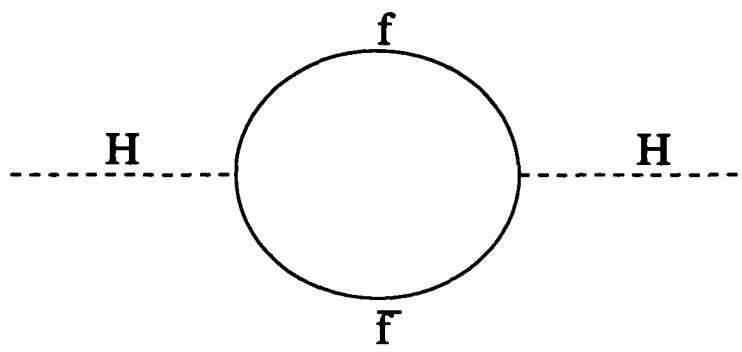


Figure 4.1: Fermionic loop correction to the Higgs mass.

given $m(\Lambda_1)$ at some lower scale Λ_1, then $m(\Lambda_2)$ can be written in the most general form as

$$m(\Lambda_2) = m(\Lambda_1) + \int_{\Lambda_1}^{\Lambda_2} const \times \frac{1}{\Lambda} d\Lambda. \tag{4.3}$$

However, a scalar particle, such as the SM Higgs, will pick up quadratic contributions from radiative corrections of fermionic loops, such as shown in Figure 4.1. Hence

$$m_{Higgs}(\Lambda_2) = m_{Higgs}(\Lambda_1) + \int_{\Lambda_1}^{\Lambda_2} const \times \Lambda d\Lambda, \tag{4.4}$$

i.e. m_{Higgs} has a quadratic divergence in Λ. Now let Λ_1 be $O(100\text{GeV})$, the electroweak scale, and let Λ_2 be a higher scale at which a more fundamental theory takes over. If that scale is the Grand Unification scale (GUT scale), M_{GUT} $O(10^{15}\text{GeV})$, or M_{Planck}, $O(10^{19}\text{GeV})$, then in order that $m_{Higgs}(\Lambda_1)$ is consistent with the SM [1], $m_{Higgs}(\Lambda_2)$ must be chosen to an accuracy of one part in $10^{27}...10^{35}$. This 'fine tuning' is unphysical [2], and is referred to as the naturalness problem.

The naturalness problem can be taken as a hint that the SM is only the lower energy effective part of a more fundamental theory, in which these facts are explained

[1] I.e. in order that $m_{Higgs}(\Lambda_1)$ is ~100GeV..1TeV .
[2] A natural value for $m_{Higgs}(\Lambda_2)$ is of the order of Λ_1.

naturally. If so, then we expect the new physics to enter at an energy scale of the order of m_{Higgs}, O(TeV) [35], such as to give a cutoff scale below a few TeV. The above arguments make no assumption on the nature of the new physics, except that it is required to deal with the fine tuning of the Higgs. As will be discussed in section 4.2, supersymmetry is such a theory which can deal with the naturalness problem.

Current experiments (at HERA, LEP and the Tevatron) have already started to probe this high energy region. It is therefore no longer a mere academic exercise to learn about various proposed new models for physics beyond the SM, but an experimental necessity to understand their phenomenological consequences in order to be able to investigate signals of such 'exotic' physics. The remainder of this chapter will focus on such a very attractive theory - supersymmetry.

Section 2.2 lists a number of theoretical motivations for SUSY; section 2.3 elaborates on a particular supersymmetric model, the Minimal Supersymmetric Standard Model (MSSM). Section 2.4 reviews a more general SUSY model, in which R-parity is relaxed; and section 2.5 finally sums up previous experimental limits on SUSY and the discovery potential at HERA.

4.2 Theoretical Motivations for Supersymmetry

Nature has shown that it likes gauge theories, and SUSY is the next logical extension to try [35]. In 1967 Coleman and Mandula [41] showed that it was impossible to 'combine space-time symmetries [i.e. the Poincare group] and internal symmetries in any but a trivial way.' In 1974 Wess and Zumino discovered a symmetry [42] that connected Bose(B) and Fermi(F) fields

$$Q|F>=|B>, Q|B>=|F> \tag{4.5}$$

and is generated by 'spinorial' charges Q_α which obey *anticommutation* relations

$$\{Q_\alpha, \bar{Q}^\beta\} = -2(\gamma^\mu)_{\alpha\beta} P_\mu \tag{4.6}$$

where α, β are spinor indices, σ^μ are the Pauli matrices and P_μ is the energy-momentum operator. Haag et al. [43] proved that this 'pseudo Lie algebra' is the *only possible extension* to the Poincare algebra, and allows mixing of an internal symmetry (the Boson-Fermion symmetry, or spin degree of freedom) and the space-time symmetry [3].

The reason why SUSY solves the naturalness problem can be easily seen from equation (4.5). Each fermion has a scalar supersymmetric partner, and each boson has a spin $\frac{1}{2}$ partner. Contributions to the amplitude from fermionic loops (such as Figure 4.1) carry a minus sign relative to those from bosonic loops, and thus the quadratic divergences are guaranteed to cancel. If supersymmetry was exact, the SM particles and their superpartners would have exactly the same mass. Unfortunately none of the known SM particles are SUSY partners of each other ($m_{\tilde{e}} >> m_e$), which means that supersymmetry (if it exists) must be broken. However as long as the level

[3] This can be seen from equation (4.6). The left-hand side only contains the spinorial indices α and β, while the right-hand side contains both the spinorial indices and the space-time index μ.

of symmetry breaking is small, i.e. the mass scale $M_{SUSY} \lesssim 0(1\text{TeV})$, SUSY can still solve the naturalness problem.

Yet another theoretical argument for SUSY is the following: If one argues that any unrenormalised theory must be free of quadratic divergences to all orders in perturbation theory, then this necessarily implies that the theory is supersymmetric, and all SUSY theories satisfy this requirement [44].

4.3 Minimal SUSY

Having argued the case for supersymmetry, we shall now employ the strongest point of such theories - the ability to construct a concrete gauge invariant model, enabling us to make definite theoretical predictions. The minimal supersymmetric extension of the Standard Model is called the Minimal Supersymmetric Standard Model (MSSM) [49].

4.3.1 The Particle Content of the MSSM

The MSSM has the particle content of the SM (but with two Higgs doublets) simply extended by global SUSY. The spinorial charges Q_α of (4.6) change the spin by half a unit, transforming bosons into fermions and vice versa. All the internal quantum numbers of the SM particles - except spin - remain the same. Furthermore the number of bosonic and fermionic degrees of freedom is equal. The SM electron (e_L^-, e_R^-) will transform into two scalar-electrons (selectrons [4]), $\tilde{e}_L^-$ and $\tilde{e}_R^-$, where the L, R subscripts of the scalar particles no longer denote handedness but two distinct states.

In general, the $\tilde{l_L}$ and $\tilde{l_R}$ (sleptons) are weak interaction eigenstates, and their physical mass eigenstates $(\tilde{l_1}, \tilde{l_2})$ will be a mixture of the two. The amount of mixing is not fixed by the MSSM, but is *a priori* unknown, and will have to be determined from experiments.

Quarks transform into scalar quarks in just the same way leptons transform, but additionally carry colour-charge. Thus the left-handed up quark will go to

$$u_{L_{Red}} \rightarrow \tilde{u}_{L_{Red}},$$

$$u_{L_{Green}} \rightarrow \tilde{u}_{L_{Green}},$$

$$u_{L_{Blue}} \rightarrow \tilde{u}_{L_{Blue}},$$

and again $\tilde{q}_L, \tilde{q}_R$ will mix to give physical eigenstates $\tilde{q}_1, \tilde{q}_2$.

[4] A tilde above a particle denotes its supersymmetric partner. The usual naming conventions for a SUSY particle is its name suffixed by 'ino' (e.g. photino, gluino etc.), or in the case of fermions prefixed by a 'scalar' (scalar-electrons, scalar-quarks or alternatively selectrons, squarks).

SM particles	Supersymmetric partners Weak interaction eigenstates	Mass eigenstates
$W^{\pm}$	$\tilde{W}^{\pm}$	$\tilde{\chi}^{\pm}_{1,2}$ "chargino"
H_1^+	$\tilde{H}_1^+$	
H_2^-	$\tilde{H}_2^-$	
γ	$\tilde{\gamma}$	$\tilde{\chi}^0_i$ (i=1..4) "neutralino"
Z^0	$\tilde{Z}^0$	
H_1^0	$\tilde{H}_1^0$	
H_2^0	$\tilde{H}_2^0$	
g	$\tilde{g}$	"gluino"

Table 4.1: The fermionic partners of the SM gauge bosons - the 'gauginos'.

For the partners of the electroweak bosons, mixing will also occur between the weak eigenstates (see table 4.1).

As before, only the coupling of the weak eigenstates is determined by the SM, but not the mixing between the states. Let us for example consider the mass matrix of the neutralinos. Following the conventions of [47], the mass terms of the Lagrangian can be expressed in terms of the mass matrix Y_{kl}

$$\mathcal{L}_M = -\frac{1}{2}\psi^0_k Y_{kl}\psi^0_l + \text{hermitian conjugate } (h.c.) \tag{4.7}$$

with

$$Y = \begin{pmatrix} M'\cos^2\theta_W + M\sin^2\theta_W & (M-M')\sin\theta_W\cos\theta_W & 0 & 0 \\ (M-M')\sin\theta_W\cos\theta_W & M'\sin^2\theta_W + M\cos^2\theta_W & -m_Z & 0 \\ 0 & -m_Z & \mu\sin 2\theta_v & \mu\cos 2\theta_v \\ 0 & 0 & \mu\cos 2\theta_v & -\mu\sin 2\theta_v \end{pmatrix} \tag{4.8}$$

and $\psi_l^0 = (-i\lambda_\gamma, -i\lambda_Z, \sin\theta_v\psi_{H1}^1 - \cos\theta_v\psi_{H2}^2, \cos\theta_v\psi_{H1}^1 + \sin\theta_v\psi_{H2}^2)$, with $\lambda_\gamma, \lambda_Z, \psi_{H1}^1, \psi_{H2}^2$ two component spinor fields of $\gamma, Z, H1, H2$, and $\tan\theta_v = (\tan\beta) = \frac{v_1}{v_2}$, the ratio of the vacuum expectation values of the neutral Higgs fields, and similar expressions for ψ_k^0. M and μ are free mass parameters of the theory, and specify the details of the neutralino mixing. M and M' are usually related by constraints from GUT models [52]

$$M' = \frac{5}{3}\frac{\sin^2\theta_W}{\cos^2\theta_W}M \simeq \frac{1}{2}M, \tag{4.9}$$

where θ_W is the electroweak mixing angle. The mass matrix Y can be diagonalised by a real matrix N, and denoting the mass eigenvalues and eigenstates by m_k and χ_k^0 we have

$$\mathrm{diag}(\eta_1 m_1, ..., \eta_4 m_4) = NYN^+ \tag{4.10}$$

where $\eta_k = \pm 1$, and is chosen such as to make m_k positive. Given the parameters $M, \mu, \tan\theta_v$, and the relation 4.9, we can obtain the mass eigenvalues m_k and the matrix N, and thus relate the mass eigenstates χ_k^0 to the weak interaction eigenstates ψ_l^0 by

$$\chi_k^0 = N_{kl}\psi_l^0. \tag{4.11}$$

Although in general N_{kl} will have off-diagonal elements, there are some simple cases. For example when $\mu = 0$ and $M = M'$ there will always be a pure massive photino state. Furthermore note that the neutralino coupling is only uniquely determined by the parameters M, μ and $\tan\theta_v$, and not just by the neutralino masses.

4.3.2 The Interactions of the MSSM

Supersymmetry is a renormalisable gauge theory, and we can construct SUSY Lagrangians and Feynman rules. However the only interaction terms of the MSSM Lagrangian - for reasons to be discussed below in section 4.4.1 - are the ones that conserve R-parity, a discrete multiplicative symmetry defined to be

$$R_p = (-1)^{2S+3B+L} \tag{4.12}$$

where S, L and B are spin, lepton and baryon number respectively. Thus, R_p is $+1$ for all SM particles, and -1 for their superpartners. The product of all R_p numbers at each vertex must be $+1$, and it is easy to see that the only allowed vertices joining both types of particles are the ones with an even number of sparticles. For example, the $ee\gamma$ vertex gives

$$e^+e^-\gamma \rightarrow \tilde{e}^+\tilde{e}^-\gamma \text{ or } \tilde{e}^+e^-\tilde{\gamma} \text{ or } e^+\tilde{e}^-\tilde{\gamma}. \tag{4.13}$$

Thus R_p-conservation has two far-reaching consequences. Firstly, sparticles must be produced in pairs. Secondly, the Lightest Supersymmetric Particle (LSP) must be stable. From the stability requirement and the following cosmological argument [53] we can also infer that the LSP must be neutral: In the early universe all particles were in thermal equilibrium. As the universe cooled down, heavier SUSY particles decayed into lighter ones, until the temperature of the universe dropped below a critical value, at which point the reaction *LSP* $\rightarrow$ *pairs of sparticles* 'froze out' - leaving behind a residual density of LSPs. If the LSP was a charged particle, it could easily be observed in our universe today, as its electromagnetic interactions would ensure that it did not separate from normal matter. In particular, results from terrestrial searches for anomalously heavy protons [54] exclude such particles.

Good candidates for the LSP are thus neutralinos and scalar-neutrinos. Since

R-parity is conserved, the neutral LSP will escape the detector without decaying, producing a signal of missing (or unbalanced) transverse momentum. In this sense the LSP will behave much like a neutrino, and cross-section measurements of $\not{p}_T$ events allow one to either discover supersymmetry, or to set limits on the sparticle masses involved. We shall throughout make the simplifying assumption that the lightest neutralino is the LSP. There are some differences in the scalar-neutrino case, however the basic missing p_T signatures are the same [35].

For completeness we shall mention one exception to the missing p_T signature of the LSP - the light gluino scenario. Although gluinos have been excluded as LSPs over a wide range of gluino masses from terrestrial heavy proton searches [54], there is a small gluino mass-window - $m_{\tilde{g}} \sim 2 - 4GeV$, - which has not yet been excluded by experiments. In this case the $g\tilde{g}\tilde{g}$ vertex would enable copious gluino production without intermediate heavy supersymmetric particle exchange. This would have possible implications on the scaling violations of the structure functions at HERA [55].

4.3.3 Minimal SUSY Production at HERA

At HERA the dominant contributions to the MSSM production of scalar fermions come from the neutralino current and chargino current pair production mechanisms of Figure 4.2a and 4.2b respectively.

The coupling at each vertex is determined by the SM, and is just the electroweak coupling. Cross-sections depend on the sparticle masses involved: $m_{\tilde{e},\tilde{\nu}}, m_{\tilde{q}}$ and $m_{\tilde{\chi}^0,\tilde{\chi}^\pm}$, and hence M, μ and $\tan\theta_v$. Furthermore the cross-section only depends on the sum of $(m_{\tilde{e},\tilde{\nu}} + m_{\tilde{q}})$, rather than the individual scalar masses. The produced sfermions (sleptons or squarks) decay into the corresponding fermions (leptons or quarks) and neutralinos or charginos:

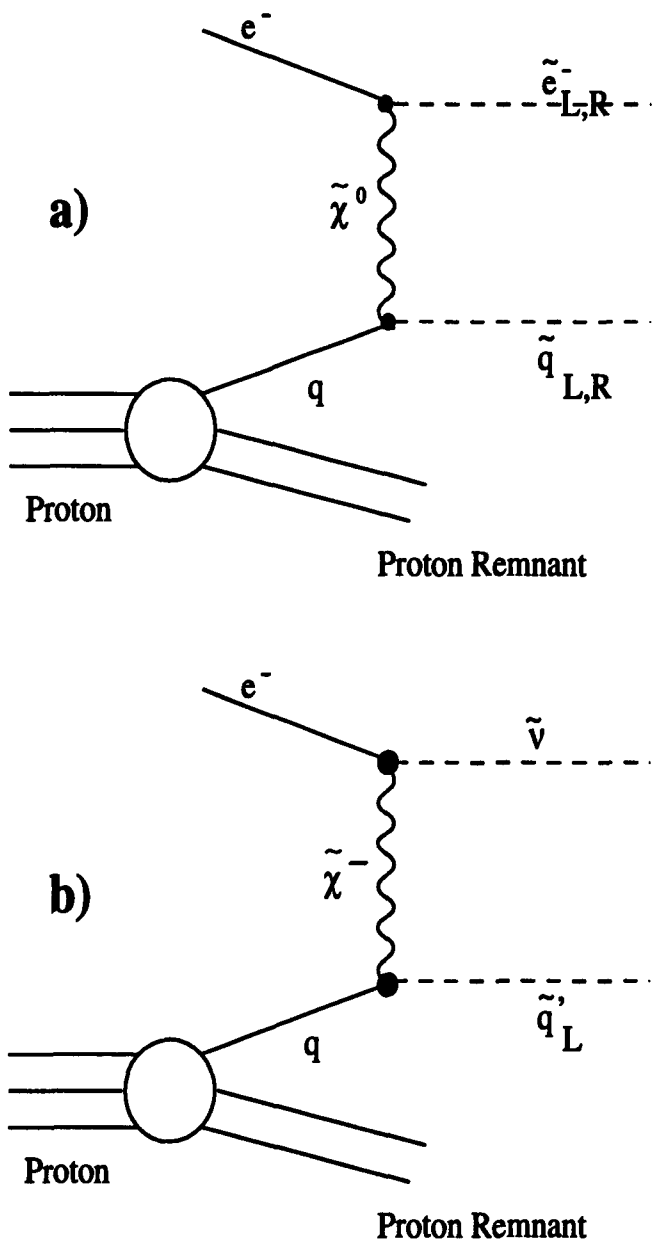


Figure 4.2: MSSM pair production at HERA.

$$\tilde{\mathbf{e}}^{-}_{\mathbf{L,R}} \rightarrow \mathbf{e}^{-} + \tilde{\chi}^{\mathbf{0}}_{\mathbf{i}} \tag{4.14}$$

$$\tilde{e}^{-}_{L} \rightarrow \nu + \tilde{\chi}^{-}_{i} \tag{4.15}$$

$$\tilde{\nu} \rightarrow \nu + \tilde{\chi}^{\mathbf{0}}_{\mathbf{i}} \tag{4.16}$$

$$\tilde{\nu} \rightarrow e^{-} + \tilde{\chi}^{+}_{i} \tag{4.17}$$

$$\tilde{\mathbf{q}}_{\mathbf{L,R}} \rightarrow \mathbf{q} + \tilde{\chi}^{\mathbf{0}}_{\mathbf{i}} \tag{4.18}$$

$$\tilde{q}_{L} \rightarrow q' + \tilde{\chi}^{\pm}_{i} \tag{4.19}$$

where the direct decays to the neutralino have been highlighted. Since we have assumed that the lightest neutralino is the LSP, the charginos of equations (4.15), (4.17) and (4.19) must also cascade-decay into the LSP $\tilde{\chi}^{0}_{1}$.

The cross-section $\sigma_{eq\rightarrow\tilde{\nu}+\tilde{q}}$ is typically 1.5 times larger than $\sigma_{eq\rightarrow\tilde{e}^{-}+\tilde{q}}$ [56]. However the experimental signature of the neutral current process is unique (e^{-}, $\not{p}_T$ and 1 jet), whereas process $eq \rightarrow \tilde{\nu} + \tilde{q}$ is indistinguishable from the conventional SM charged current process $eq \rightarrow \nu + q$ if the scalar neutrino decays via (4.16). Thus only decay (4.17) can be easily experimentally distinguished, as it will have the same signature as the neutralino current MSSM interaction. This is only possible if one restricts the parameter space to a certain range of values which make (4.17) the dominant sneutrino decay process.

4.4 R-parity Violating SUSY Models

Recently there has been much interest in the field of R-parity violating ($\not{R}_p$) models. The reader is referred to [57] for theoretical, [59] for cosmological and [60, 61, 62, 63, 64] for phenomenological work on R-parity violating SUSY.

4.4.1 The Origin of R_p

In its most general form, the construction of a supersymmetric version of the Standard Model immediately runs into difficulty for, unlike the Standard Model, there are terms of dimension-4 allowed by the SU(3)×SU(2)×U(1) gauge symmetry which violate baryon and lepton number [65]. These terms allow for unacceptable nucleon decay rates, and must therefore be suppressed in any such model. Introducing a discrete symmetry such as R-parity (defined in equation (4.12)) eliminates lepton and baryon number violation, and hence inhibits proton decay. However the origin of such a discrete matter parity is not clear at the level of the minimal supersymmetric extension of the SM; presumably it comes from the underlying grand unified theory.

Recent work [58] has shown that R-symmetry [5] belongs to a more general class of continuous gauge symmetries, and is by no means the only such symmetry. In particular the authors of [58] showed that after imposing the minimal light particle spectrum and after supersymmetry breaking, two preferred discrete gauge symmetries remain, the R-parity of the MSSM and a 'baryon parity', with baryon parity being preferred since it eliminates not only dimension-4 operators but also the potentially large dimension-5 contributions to nucleon decay.

It is worth remembering that R-parity is only one such symmetry that can deal with dimension-4 operators. Pending further understanding of the origin of this symmetry it is imperative to consider both, R-parity conserving and R-parity violating

[5] R-symmetry is a continuous symmetry - a generalisation of fermion number conservation. If the photino and the gluino are massive, this R-symmetry is broken, and what remains is a discrete R-parity [35].

models.

4.4.2 Consequences of R_p Violation

R-parity violation ($\not{R}_p$) has two important consequences on the phenomenology of the SUSY model. Firstly, as already pointed out in section 4.3.2, $\not{R}_p$ allows the Lightest Supersymmetric Particle to decay into SM particles. Hence SUSY events will no longer have the characteristic missing p_T signature of the MSSM [6], but the LSP decay can give rise to spectacular multileptonic and multijet final states. The second consequence is that sparticle pair production is not the only supersymmetric production mechanism. Sparticles can now also be produced singly via $\not{R}_p$ Yukawa couplings. Thus the phenomenological characteristics of $\not{R}_p$ SUSY are very different from the MSSM. Let us now study the additional R_p violating couplings in more detail.

Given the particle content of the SM, the most general gauge and supersymmetry invariant superpotential is given by [97]

$$W = W_{MSSM} + W_{\not{R}_p}, \tag{4.20}$$

where W_{MSSM} is the superpotential of the MSSM, and $W_{\not{R}_p}$ consists of the $\not{R}_p$ Yukawa couplings

$$W_{\not{R}_p} = [\lambda_{ijk} L_i L_j \bar{E}_k + \lambda'_{ijk} L_i Q_j \bar{D}_k + \lambda''_{ijk} \bar{U}_i \bar{D}_j \bar{D}_k]_F. \tag{4.21}$$

L is the left-handed lepton doublet, $\bar{E}$ is the antilepton singlet, Q is the (left-handed) quark doublet and $\bar{U}, \bar{D}$ are the u-type and d-type antiquark singlet chiral superfields respectively [61]. $\lambda, \lambda', \lambda''$ are dimensionless Yukawa couplings and i, j, k are generation indices (e.g. e, μ and τ for $\bar{E}_{i=1,2,3}$). As well as breaking R-parity, the first two sets of terms in equation (4.21) violate lepton number, and the last

[6] Note that there can be a diluted missing p_T signature. This arises from LSP decays to one or more neutrinos (and jets or leptons).

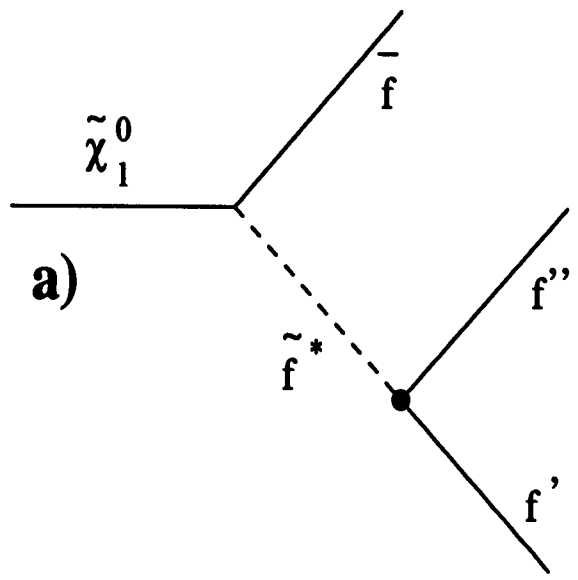
set violates baryon number (see Figure 4.3 for specific examples of these operators). Provided only one operator is dominant, and the last operator is absent the nucleon will be stable. Throughout we shall make the simplifying assumption that only one of the allowed couplings consistent with nucleon decay is dominant. This means that we will only allow one of the two operators $L_iL_j\bar{E}_k$ and $L_iQ_j\bar{D}_k$, and only consider one non-zero coupling λ_{ijk} (for fixed indices i,j,k). It was pointed out by [67] that this perhaps is the most likely circumstance as the new couplings are of the same character as the SM Yukawa couplings responsible for quark and lepton masses, which show a vast difference in magnitude ($\frac{h_e}{h_{top}} \sim 5 \times 10^{-6}$). In any case, this assumption is necessary to enable an easy interpretation of any experimental limits on the Yukawa coupling constants and/or sparticle masses.

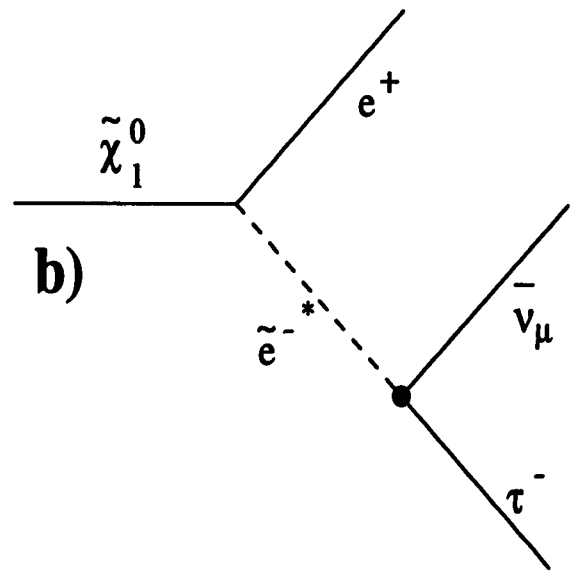
Again we shall make throughout the assumption that the lightest neutralino is the LSP. Note that the cosmological arguments for a neutral lightest supersymmetric particle (section 4.3.2) no longer hold, and therefore this assumption is no longer a trivial one.

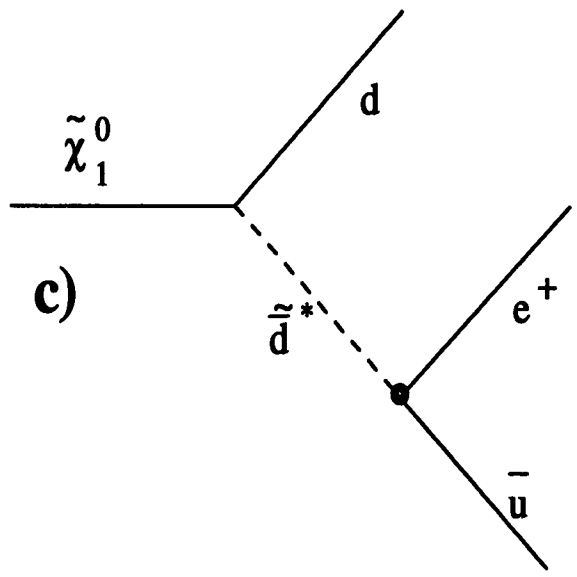
Any of the three operators in (4.21) will enable the LSP to decay, and Figure 4.3a shows the generic diagram for neutralino decay. Figures 4.3b-d show examples of specific decays via the $LL\bar{E}$ (b), $LQ\bar{D}$ (c) and $\bar{U}\bar{D}\bar{D}$ (d) operators. The $\not{R}_p$ vertices are marked. Note that the intermediate sparticles, superscribed by asterisks, are virtual. The LSP will always decay. If λ is too small, the LSP will decay outside the detector, and will again produce the missing p_T signature of the R_p conserving scheme.

The condition that the LSP (which for simplicity was assumed to be the photino in the calculation below) decays within the detector (say within 1 meter of the interaction point) translates into a lower bound on the coupling constant [68]

$$c\gamma\tau_{\tilde{\gamma}} \sim 3 \times 10^{-3}\gamma(M_{\tilde{f}}/100GeV)^4(1GeV/M_{\tilde{\gamma}})(1/\lambda)^2 < 1m \quad , \quad \text{or} \quad (4.22)$$







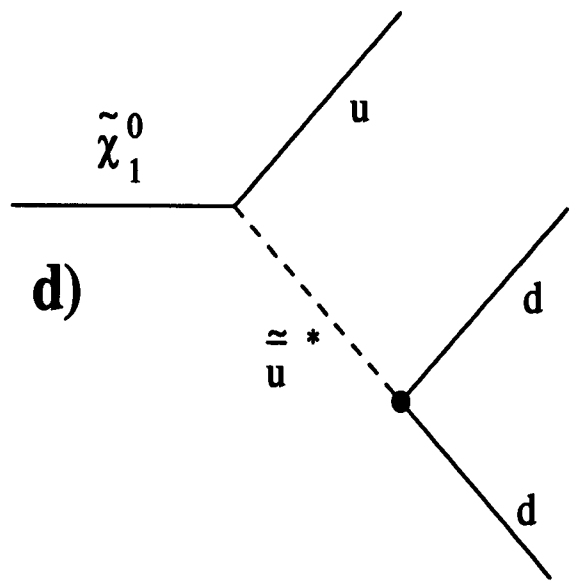


Figure 4.3: LSP-decays via $R\!\!\!/_p$ Yukawa couplings. Figure a) shows the generic diagram for LSP decays, and Figures b)-d) show examples of decays via $LL\bar{E}$, $LQ\bar{D}$ and $\bar{U}\bar{D}\bar{D}$ respectively.

$$\lambda \;>\; 1.6 \cdot 10^{-4}(M_{\tilde{f}}/100GeV)^2(10GeV/M_{\tilde{\gamma}})^{5/2} \tag{4.23}$$

where $\tau_{\tilde{\gamma}}$ is the photino lifetime, γ is the Lorentz boost in the lab-frame, and $M_{\tilde{f}}$ is the mass of the virtual scalar fermion.

4.4.3 $\not{R}_p$ Squark Production at HERA

At HERA the first generation coupling associated with the $L_1Q_j\bar{D}_k$ operator, λ'_{1jk}, is of particular interest. Expanding the $L_1Q_j\bar{D}_k$ operator explicitly in terms of the four-component Dirac states gives

$$\begin{aligned} L_1Q_j\bar{D}_k = \lambda'_{1jk}[&- \tilde{e}_L u^j_L \bar{d}^k_R - e_L \tilde{u}^j_L \bar{d}^k_R - (\bar{e}_L)^c u^j_L \tilde{d}^k_R \\ &+ \tilde{\nu}_L d^j_L \bar{d}^k_R + \nu_L \tilde{d}^j_L \bar{d}^k_R + (\bar{\nu}_L)^c d^j_L \tilde{d}^k_R] + \text{h.c.} \end{aligned} \tag{4.24}$$

where again i, j, k are generation indices, and the superscript c denotes the charge conjugated spinor. Terms 2 and 3 can give rise to direct s-channel resonant squark production at HERA [61], and Figure 4.4 shows the diagram for this process. In contrast to the MSSM pair production mechanism of 4.3.3, the size of the cross-section for single squark production will now also depend on an additional parameter, the Yukawa coupling strength λ'_{1jk}. Hence discovery limits on $L_1Q_j\bar{D}_k$ via this process can only be quoted within a certain λ-range, in which the cross-section for the s-channel process of Figure 4.4 is large enough.

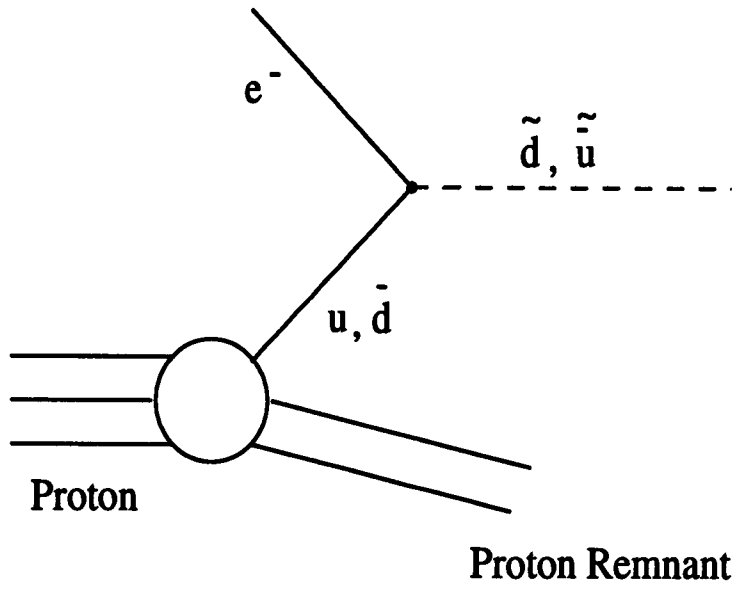


Figure 4.4: $R\!\!\!/_p$ s-channel $\tilde{q}$ production.

4.5 Existing Limits on Supersymmetry

4.5.1 MSSM Limits

LEP provides the model independent bound [69] on

$$m_{\tilde{e}^{\pm}}, m_{\tilde{q}} \geq 45GeV \tag{4.25}$$

from the measurement of the Z^0 width. The $\tilde{\nu}$ mass bounds from LEP are somewhat lower [70]

$$m_{\tilde{\nu}} > 32GeV \tag{4.26}$$

$$m_{\tilde{\nu}} > 39.4GeV \tag{4.27}$$

where (4.26) and (4.27) assume one and three $\tilde{\nu}$-flavours respectively to be degenerate in mass. CDF provides much stronger limits on the squark mass [71]

$$m_{\tilde{q}} > 150GeV \tag{4.28}$$

under the assumption that all five squarks are degenerate and that the branching fraction BF($\tilde{q} \rightarrow q + \tilde{\chi}_i^0$) is 100%. However, relaxing the model dependence somewhat

by making one squark substantially lighter than the others [72] results in

$$m_{\tilde{q}} > 64GeV. \tag{4.29}$$

Combining 4.25,4.27,4.28 and 4.29 we obtain limits to which HERA must aspire:

$$m_{\tilde{e}^-} + m_{\tilde{q}} > 195GeV \quad (109GeV) \tag{4.30}$$

$$m_{\tilde{\nu}} + m_{\tilde{q}} > 190GeV \quad (96GeV). \tag{4.31}$$

The numbers in brackets are the more conservative (i.e. less model dependent) limits. The discovery potentials at HERA for MSSM pair-produced SUSY and a typical two year running period with an integrated luminosity of $200pb^{-1}$ are $m_{\tilde{e}^-} + m_{\tilde{q}} < 200GeV$ [73] and $m_{\tilde{\nu}} + m_{\tilde{q}} < 185GeV$ [56], and hence there is hardly any discovery window at HERA for Minimal SUSY (assuming five degenerate squarks).

4.5.2 $\not{R}_p$ Limits

Limits (4.25) and (4.27) are still applicable to the $\not{R}_p$ case, since they are determined from the width of the Z^0. All other limits of interest come from low energy constraints or from direct searches for $\not{R}_p$ signals, and are of two forms: Either a limit is set on the Yukawa coupling λ, in which case the λ-limit is usually normalised to a SUSY mass, e.g. $(\frac{m_{\tilde{q}}}{100GeV})$. Alternatively a limit is given on the sensitive sparticle mass of the search, valid for all values of the coupling λ (down to the lower bound of equation (4.23)).

In the case of the low energy bounds, for example charged current universality constraints (Figure 4.5) imply upper limits on λ_{12k} and λ'_{11k}. Table 4.2 lists the existing bounds from reference [62] on the $LL\bar{E}$ and $LQ\bar{D}$ operators.

Using the CDF dilepton search data, stringent bounds on the squark masses for various types of couplings have been determined [63], and table 4.3 summarises them. The model assumes 5 degenerate squarks and the dominance of only one $\not{R}_p$ coupling.

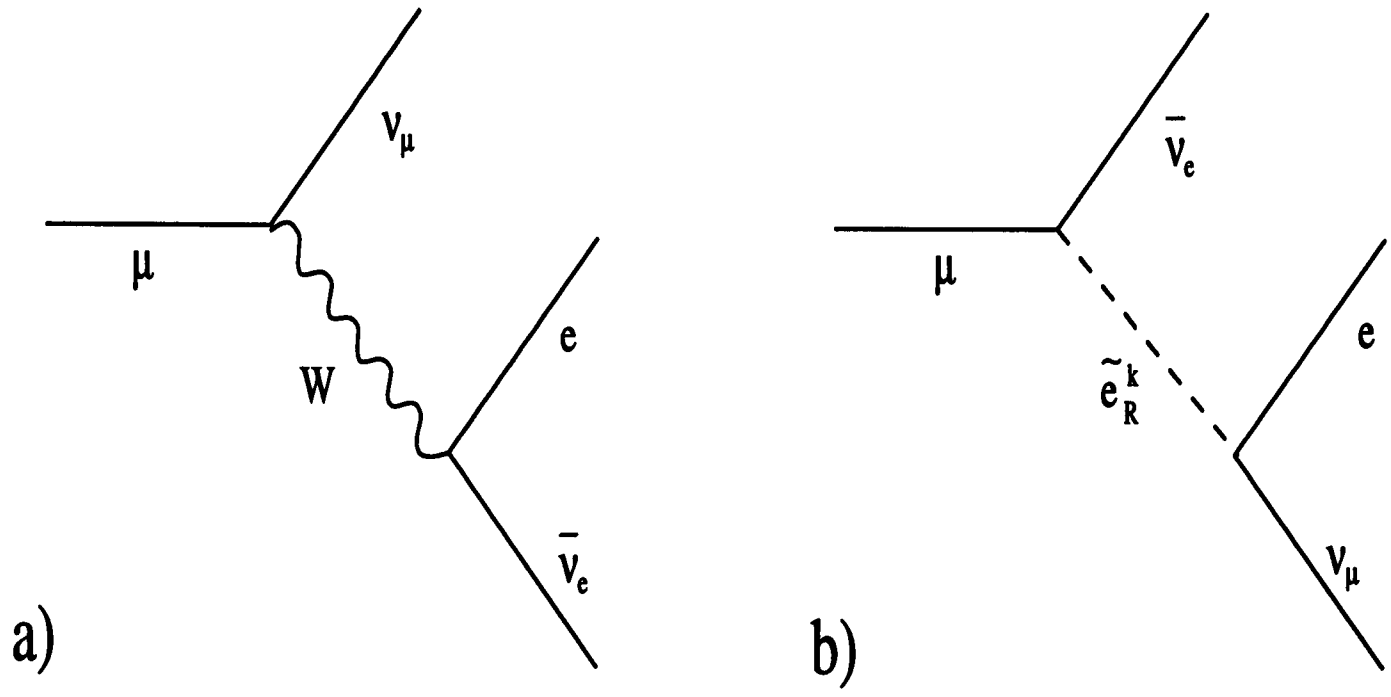


Figure 4.5: Diagrams for μ decay from (a) the standard model, and (b) the R_p breaking interaction.

ijk	$\lambda_{ijk} <$	ijk	$\lambda'_{ijk} <$
12k	0.04	11k	0.03
13k	0.10	21k	0.09
23k	0.09	121	0.26
		122	0.45
		123	0.26
		133	0.26
		221	0.22
		231	0.22
		131	0.25

Table 4.2: Upper limits at the 68% confidence level on the $R\!\!\!/_p$ couplings normalised to $(\frac{m_{\tilde{q}}}{100GeV})$ from low energy data.

Leading Yukawa coupling	Limit of $m_{\tilde{q}}$(GeV)
$\lambda'_{3jk,i3k}$	–
$\lambda'_{ijk}(i,j \neq 3)$	100
$\lambda_{133,233}$	100
λ_{123}	140
$\lambda_{331,322,312,321}$	160
$\lambda_{121,122}$	175

Table 4.3: CDF dilepton limits at the 95% confidence level on the squark masses.

However, it must be stressed that this search crucially depends on the second assumption, since the only signals considered were dielectrons and dimuons [7]. Hence the results are very model dependent. If, for example, two equal strength couplings are present, e.g. $\lambda'_{211} = \lambda'_{311} \neq 0$, then the decay to $\mu\mu$ would be suppressed by a factor 3 to the single μ signal.

Table 4.4 finally summarises all existing bounds on the $\not{R}_p$ couplings which are of interest to HERA, as they can potentially be improved after an integrated luminosity of 200pb^{-1}, two nominal years of HERA running. It is the subject of chapter 5 and chapter 6 to study direct squark production and $\not{R}_p$ LSP decay in detail in order to set limits using ZEUS data from the running period of 1992, and to present precise potential discovery limits for the future.

[7] The analysis assumed that *both* $\tilde{\gamma}$'s would decay via the same coupling to produce either $\mu\mu$ or *ee* signals.

$R\!\!\!/_p$ Couplings of interest to HERA	
LQD-coupling λ'	existing limits
11k	$m_{\tilde{q}} > 100GeV$, $\lambda' < 0.03$
121	$m_{\tilde{q}} > 100GeV$, $\lambda' < 0.26$
122	$m_{\tilde{q}} > 100GeV$, $\lambda' < 0.45$
123	$m_{\tilde{q}} > 100GeV$, $\lambda' < 0.26$
131	$\lambda' < 0.25$
132	–
133	$\lambda' < 0.26$
21k	$m_{\tilde{q}} > 100GeV$, $\lambda' < 0.09$
221	$m_{\tilde{q}} > 100GeV$, $\lambda' < 0.22$
222,223	$m_{\tilde{q}} > 100GeV$
231	$m_{\tilde{q}} > 100GeV$, $\lambda' < 0.22$
232,233	$m_{\tilde{q}} > 100GeV$
3jk	–

Table 4.4: World limits on $R\!\!\!/_p$ couplings of interest to HERA.

Chapter 5

A Search for s-channel Squark Production at HERA

5.1 Introduction

This chapter is based on reference [74] and investigates direct s-channel squark production via the R-parity violating coupling λ'_{1jk} of equation (4.21). We refer to [61] for a discussion of the production cross-section, details of the subsequent R-parity violating decay of the produced squark, and eventual discovery reaches of $\not{R}_p$SUSY via this process at HERA.

A search for R-parity violating SUSY production has been performed on the 1992 ZEUS autumn data sample with an integrated luminosity of 26 nb^{-1} and is described in this chapter. After all cuts, three candidates with $m_{SUSY} > 80\ GeV$ remained. The candidates were scanned by eye, and were found to be deep inelastic scattering neutral current events and therefore excluded from the search sample. We set a limit on the squark mass, $m_{\tilde{q}}$, as a function of the $\not{R}_p$coupling strength λ' at the 90% confidence level. This limit is inferior to the current CDF and Charged Current universality limits of table 4.4. However, scaling up to a luminosity of 10 pb^{-1}, the sensitivity can be substantially improved up to squark masses of 210 GeV.

In $\not{R}_p$models the 'Lightest Supersymmetric Particle' (LSP) - throughout assumed

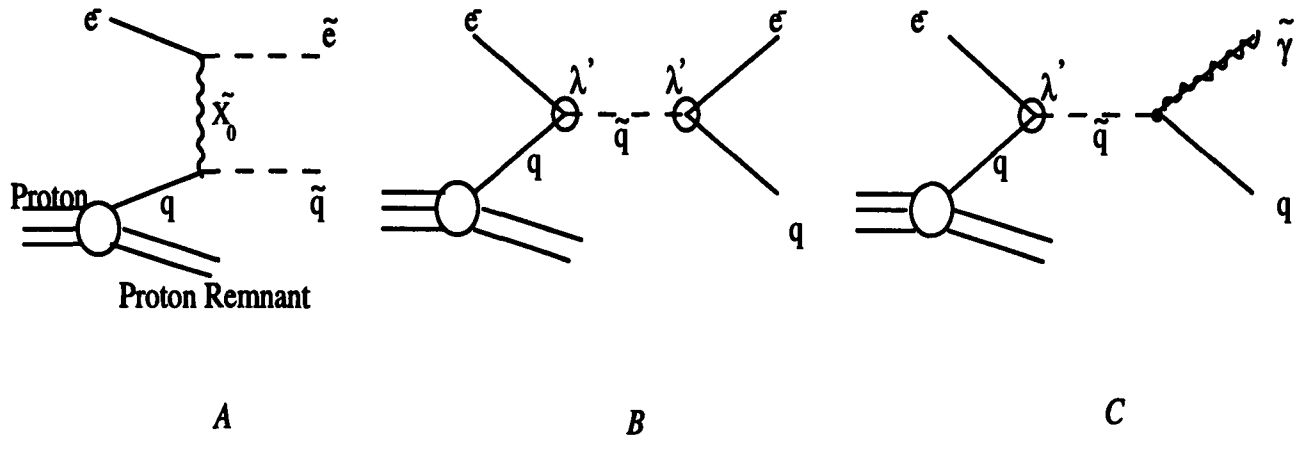


Figure 5.1: $R_p$and $\not{R}_p$ SUSY signals at HERA.

to be the photino ($\tilde{\gamma}$) [1] - is no longer protected by a symmetry, and can decay into Standard Model particles. For example, a typical decay via the LQD operator is

$$\tilde{\gamma} \rightarrow d(\tilde{\bar{d}})^* \rightarrow d\bar{u}e^+ \tag{5.1}$$

where the d-squark is virtual (denoted by an asterisk). A further consequence of $R_p$violation is that sparticles can be produced singly via $\not{R}_p$couplings. At HERA, s-channel squark production is possible in addition to the MSSM pair production mechanism.

Figure 5.1 summarises the most promising SUSY signals at HERA. Diagram 5.1A demonstrates the MSSM pair production mechanism. This process gives rise to either R_p-conserved missing p_T signals, described elsewhere [36, 73], or the $\tilde{e}+\tilde{q}$ decay $\not{R}_p$into multileptonic final states. The latter possibility is considered in chapter 6. Diagram 5.1B and Diagram 5.1C show the $\not{R}_p$s-channel production of a $\tilde{q}$. The amplitude for Process 5.1B is suppressed according to the value of λ' with respect to process 5.1C, and the analysis is similar to that of leptoquark production (see also [75, 76]). Process 5.1C is of great interest to HERA, as the cross-sections can be large for

[1]This assumption simplifies the model substantially. Subsequent studies of chapter 6 have considered possibilities other than the photino scenario. It was found that after extending the model to the more general case of neutralinos, the LSP will still behave like a photino in some parts of the SUSY parameter space, but more like a zino in other parts. The nature of the LSP subsequently changes the branching ratios of its decay products. We refer to chapter 6 for a further discussion on this matter.

sufficiently large values of λ', and the $\tilde{\gamma}$ can decay into an interesting signature of 2 jets + a charged lepton (c.f. Equation (5.1)). It is this process which should be dominant at HERA, and the rest of this chapter will concentrate on the detection and reconstruction of its signal.

The overall decay chain for process 5.1C is

$$e^- + q \rightarrow \tilde{q} \rightarrow q + \tilde{\gamma} \rightarrow e^{\pm} + 3 \text{ jets} \qquad \text{(BF 87\%)} \qquad (5.2)$$

$$e^- + q \rightarrow \tilde{q} \rightarrow q + \tilde{\gamma} \rightarrow \nu_{e^{\pm}} + 3 \text{ jets} \qquad \text{(BF 13\%)} \qquad (5.3)$$

and typical branching fractions (BF) (although depending on the photino mass) are shown in brackets [61]. Only the charged lepton channel of equation (5.2) will be used for the 1992 ZEUS autumn data analysis, and Figure 5.2 shows the expected number of events for the 1992 integrated luminosity of 26 nb^{-1}.

Because of hardware limitations of the readout of the Central Tracking Detector[2], no positron identification was possible for the 1992 data sample. The (detectable) event topology of process (5.2) therefore consisted of an 'electron' (an electron or a positron) plus some jet-activity. The main background to such a topology comes from deep inelastic scattering neutral current events, which also have an electron in the final state. The following sections show how a jet-finding algorithm can be used to reconstruct the three jets of process (5.2). We explain how the jet measurement can be used to calculate the mass of the photino and the mass of the squark ($m_{\tilde{\gamma}}$ and $m_{\tilde{q}}$ respectively). The two masses ($m_{\tilde{\gamma}}$ and $m_{\tilde{q}}$) can subsequently be used to distinguish between the $\not{R}_p$SUSY events of interest and the NC DIS events.

5.2 Jet Finding and Reconstruction

Following equations (5.2) and (5.3) we draw the reader's attention to the high jet multiplicities in the $\not{R}_p$decay processes. A large part of the following analysis is

[2]In the 1992 running period, the CTD was only equipped with z-by-timing readout.

therefore concerned with finding and reconstructing these jets. The intention of this chapter is to give a quick introduction to the problems and difficulties of jet finding at HERA. It describes

- the definition of jets and jet multiplicities
- various jet finding algorithms and their motivations
- how the proton remnant effects the jet analysis at HERA.

5.2.1 Jet Multiplicities

The first issue to address is how a jet is defined. Although it is very tempting to define a jet to be produced by hadronic cascades (or showers) originating from a single parton, it is often experimentally difficult to distinguish between showers originating from *one* or *more* jets. A jet therefore can only be defined by a particular jet-algorithm and its parameters, and will only asymptotically (at high energies, for example) resolve the underlying parton level process. Because of this, jet multiplicities are often plotted as a function of the cut-off parameters of the jet-algorithm, and a good choice of cut-off parameters and values will make the 1,2 and 3 jet ratios compare well with the multiplicities of their underlying parton processes.

5.2.2 Jet Algorithms

The aim of jet algorithms is to find the number of jets in an event, and to reconstruct their energies and angles. Common to most of them is the principle of recombining 'pseudo-particles' until a certain cut-off condition has been satisfied. In practise the initial pseudo-particles will be the four-vectors of the calorimeter cell energies. We shall always exclude the cells associated with the 'electron' for the jet analysis. A number of such algorithms exist, and we shall briefly describe three appropriate ones for ZEUS:

- The **JADE** algorithm [77] is a Lorentz invariant algorithm (i.e. the recombination criteria is based on a Lorentz invariant quantity), and it aims to minimise the invariant mass of particles with respect to each other. It constructs invariant masses between all pairs of pseudo-particles, and compares the smallest such pair to a cut-off condition. If the condition is satisfied, the two particles are recombined into one pseudo-particle, and the process is continued until the cut-off condition no longer holds. At this point the remaining pseudo-particles define the four-vectors and number of jets in the event. The invariant mass squared is defined to be

$$m_{ij}^2 = 2E_iE_j(1 - \cos\theta_{ij}),$$

where E_i, E_j are the energies of the pseudo-particles i and j, and θ_{ij} is the polar angle between them. The cut-off condition,

$$m_{ij} < y_{cut} * Scale \qquad \text{for all } i,j \text{ pseudo-particles} \tag{5.4}$$

introduces an arbitrary, dimensionless cut-off parameter y_{cut}. Typically the scale can be

  - the total Centre of Mass (CMS) energy squared s (a popular choice in e^+e^- experiments),
  - the total visible energy squared $(E_{vis})^2$,
  - or the hadronic final state CMS energy W^2, which might be more appropriate for HERA [78].

  A number of modifications to this algorithm exist [79], and table 5.1 summarises the various recombination schemes.

- The **Durham** or 'k_t' algorithm is defined in a similar way to the JADE algorithm, replacing the invariant mass cut by a transverse momentum squared

Recombination Scheme	Implementation
E - scheme	The two pseudo-particle four-vectors p_i and p_j are simply added together. $p_k = p_i + p_j$
P - scheme	The recombined four-vector p_k is constructed such that it has zero invariant mass, according to $\vec{p_k} = \vec{p_i} + \vec{p_j}, E_k = \lvert\vec{p_k}\rvert$.
E0 - scheme	The four-vector p_k is constructed such that it has zero invariant mass, according to $E_k = E_i + E_j, \vec{p_k} = \frac{E_k}{\lvert\vec{p_i}+\vec{p_j}\rvert}(\vec{p_i} + \vec{p_j})$.
P0 - scheme	Similar to the P-scheme, only that the condition $y_{ij} < y_{cut} * Scale$ is reevaluated after each iteration (total energy will change due to the rescaling of E_k).

Table 5.1: JADE Recombination Schemes

cut

$$m_{ij}^2 = 2\min(E_i^2, E_j^2)(1 - \cos(\theta_{ij})) \qquad \text{for all } i,j \text{ pseudo-particles.}$$

This has advantages in the theoretical calculation of corrections to leading order processes [80].

- The **Cone** algorithm [81] uses a grid in pseudo rapidity $\eta = -\ln(\tan(\theta/2))$ and azimuth (ϕ) space. This metric is particularly useful at HERA[3], as η is invariant under longitudinal boost. The algorithm searches for deposits of energy within a cone of width $\Delta R = \sqrt{\Delta\eta^2 + \Delta\phi^2}$. The centre of the ZEUS calorimeter cells are the bin centres of the $\eta \times \phi$ space, with variable bin sizes.

  The cone algorithm - in contrast to Jade and Durham, which use invariant mass and p_T criteria respectively - relies on jet cluster finding, and hence on the *geometry* of the jet.

[3]For not too small pseudo rapidities η

5.2.3 Proton Remnant Treatment

The proton remnant (or beam jet) has a big effect on jet analysis at HERA and cannot be neglected. Particles from the remnant will leak out of the beam pipe into the calorimeter, leaving large energy deposits in cells in the forward region. These particles can be picked up by the clustering algorithms and will be recombined wrongly with other jets.

A possible cure to this problem is to introduce a pseudo-particle parallel to the beam, carrying the overall missing longitudinal momentum of the event. The algorithm will then reconstruct the proton remnant as an extra jet. Alternatively one can introduce a cut near the beam pipe, and only consider cells with polar angle $\theta_{cells} > \theta_{bpcut}$, excluding all the problematic cells. This however will also harm forwardly distributed jets. Such events can be excluded from the analysis by demanding that the reconstructed jets also lie outside the beam pipe region ($\theta_{jets} > \theta_{bpcut}$). The pseudo-particle approach was shown to be very effective in MC-studies [82] , however the beam pipe-cut approach is considered safer, as uncertainties in the simulation of the beam jet - such as size and fragmentation - will not effect the analysis [4]. Figure 5.3 shows a plot of the energy weighted θ-bins for the preselected exotics data (the sample is defined in the following section below) sample of 11394 events. The spike near $\theta = 0$ is attributed to the beam jet, and a cut at $\theta_{cells} > 0.2rad$ will safely remove most of it. The peak at $\theta = 3.0rad$ can be attributed to contributions from the electron.

Figure 5.4 shows the resulting jet multiplicities of the JADE (in this case, for example, the E-scheme,E_{vis} scale, $\theta_{bpcut} = 0.2rad$) algorithm as a function of the cut-off parameter y_{cut} for both a Deep Inelastic Scattering (DIS) Monte Carlo and ZEUS data. MC and data agree remarkably well, and it was concluded that the algorithm displayed a sensible behaviour.

[4] assuming that θ_{bpcut} is chosen large enough.

5.3 Data Taking and Simulation

The $\not{R}_p$ processes were simulated using the SUSANA [83] generator, and HERWIG [89] was used for the DIS NC background processes, with MRSD0 parton densities [85] in both cases. The CTD z-by-timing system, with a $4cm$ z-resolution, can only measure the charge of low p_T tracks. The p_T resolution was measured to be $\frac{\sigma(p_T)}{p_T} > 1$ for $p_T \geq 7\ GeV$, i.e. the error on the measurement of p_T of tracks above $p_T \geq 7\ GeV$ exceeded 100%. This meant that no discrimination between electrons and positrons was possible. The 'electron' ($e^{\pm}$) identification required a number of hits, or a reconstructed track to point to an electromagnetic calorimeter cluster with a shower profile characteristic to that of an electron [5]. The pointing track requirement was only applied if the polar angle of the electron cluster was within the geometrical acceptance of the CTD.

We now define the preselected exotics data sample, on which the analysis was performed. The trigger conditions of the ZEUS three level trigger over the period of data-taking in 1992 consisted of subtriggers constructed from sums over calorimeter cells [93]. Different thresholds were used in different calorimeter regions. In the FCAL, the electromagnetic thresholds were 20GeV close to the beam pipe, then 10GeV further away from the beam pipe, 2.5GeV in the BCAL, and finally only 1GeV in the RCAL. Subsequent selection criteria on the data reduced the sample to the 11394 events of the preselected exotics data sample. The selection criteria were:

- E-p_z >20GeV: For a description of the E-p_z quantity see chapter 1. For the $\not{R}_p$ SUSY events of interest, the majority of the final state particles are detected in the event, and the SUSY event topology lies at high values of E-p_z. Therefore an E-p_z >20GeV cut would not have harmed potential SUSY candidates.

- electron cut: The preselection required an electron to be found in the calorime-

[5] A number of electron finders were used in combination to yield higher identification efficiencies.

ter.

- Vertex cut: A vertex formed from one or more CTD tracks was demanded. If only one track was found in the event, the track was extrapolated back towards the interaction region, and the vertex was determined at the closest distance of approach of the track to the z-axis (the beam axis).

A number of cuts reduced the initial 11394 preselected exotics data sample to a SUSY search sample of 1578 - their effects on the data are shown in table 5.2. The $E_{LUMI} < 5\ GeV$ cut gets rid of photoproduction background with an electron in the LUMI detector. The |vtx| $< 75cm$ cut requires a vertex position at the interaction point. During 1992 HERA operated with nine colliding electron and proton bunches. The 'ep bunch' cut requires the event to come from a non-empty electron and proton bunch bucket, i.e. a genuine e-p collision. The $E - p_z$ cut intends to remove all remaining photoproduction and beam-gas background. The final θ_{jets} cut removes events with very forwardly distributed jets. The non-DIS backgrounds to the total SUSY search sample of 1578 events was estimated to be less than 2.7%. This was done by replacing the $E_{LUMI} < 5\ GeV$ cut with a $E_{LUMI} > 5\ GeV$ cut. The resulting 69 observed events, together with the assumption that the LUMI detector has a 25% efficiency for photoproduction electrons, permitted above estimate (see also [84] for a similar analysis). The 2.7% background would only be a problem if such events reconstructed as 3 jet events with high squark masses. The squark mass versus photino mass distribution of the 69 events was plotted and found to be below 50GeV (Figure 5.13).

Selection	$e^{\pm} + 3jets$
Preselection	11394
$E_{LUMI} < 5\ GeV$	9209
$\|\text{vtx}\| < 75cm$	8967
ep bunch	8961
$e^{\pm}$ found: $E_{e_{\pm}} > 5\ GeV$	3709
$30 < (E - p_z) < 60\ GeV$	2716
$\theta_{jets} > 0.2rad$	1578
SUSY Search Sample	1578

Table 5.2: Cuts for Final SUSY Candidate Sample

5.4 Event Reconstruction and Detection Efficiencies

In order to reconstruct process (5.2), the jet-finding algorithms described in section 5.2.2 were run on $\not{R}_p$MC events. Ideally the jet-finders should have reconstructed exactly three jets in the $\not{R}_p$events. Unfortunately it was found that the particular choice of the y_{cut} value (or $\triangle R$ for the cone algorithm), which gives a maximum number of 3 jet events, y_{cut}^{max}, depends on the mass of the generated squark and photino (see Figure 5.5). This behaviour was independent of the scale chosen (W^2 or E_{vis}), the algorithm used (Jade or Durham) or the recombination scheme (E,E0,P or P0). A similar result was obtained for the cone algorithm. Furthermore since the multiplicities of the events depend on the y_{cut} choice which in turn depends on the scale (W^2 or E_{vis}) and hence on absolute energy calibrations, it was decided to **constrain** the result of the jet-finders to 3 jets[6]. This was done by replacing the '$m_{ij} < y_{cut} * Scale$' cut-off condition of equation (5.4) with a '*Number of pseudo-particles* > 3'. Hence pseudo particles were recombined until only three remained, which were taken to be the jets. The choice of the algorithm thereafter made little difference to the quality of the jets, and the JADE (E-scheme,$\theta_{bpcut} = 0.2rad$) algorithm of section 5.2.2 in com-

[6]Plus an 'electron', which is reconstructed independently.

bination with the above constraint has been used throughout the analysis. Although this artificially and falsely constrains three jets in the majority of the DIS MC sample, it will be shown that the combination of effective masses of these reconstructed jets will have very different distributions to those resulting from $\not{R}_p$SUSY production.

By vectorially adding two four-vectors of any two jets (out of the three) and the four-vector of the $e^{\pm}$ one can reconstruct the $m_{\tilde{\gamma}}$, giving three possible values of $m_{\tilde{\gamma}}$ per event. By combining the resulting four-vector with the remaining jet, the value of $m_{\tilde{q}}$ can be determined. Figure 5.6 (a) shows the resulting $m_{\tilde{\gamma}}$ vs $m_{\tilde{q}}$ scatter plot for the DIS MC background events passing the cuts in table 5.2 (3 entries per event). Figure 5.6 (b) shows the same plot for the data. Figure 5.6 (c) and (d) show the reconstructed $m_{\tilde{\gamma}}$ and $m_{\tilde{q}}$ of the $\not{R}_p$MC events, generated at 50 and 120 *GeV* respectively. The shaded area in plot 5.6 (c) shows the 2 wrong combinations of jets discussed above.

The detection efficiency for $\not{R}_p$SUSY depends on the SUSY masses involved. Large squark masses will boost the event structure in the forward direction, whereas smaller photino masses will make the resulting decay products , the $e^{\pm}$ and the 2 jets, more collimated with respect to each other, and thus make $e^{\pm}$ identification and jet finding less efficient. 16 samples of 500 events each in four $m_{\tilde{\gamma}}$-bins and four $m_{\tilde{q}}$-bins have been generated with the SUSANA generator (section 5.3). Figure 5.7 shows the 1992 trigger efficiency of the samples, and Figure 5.8 summarises the detection efficiency after the trigger and the SUSY selection cuts (table 5.2). Note that the trigger efficiency is very high for the $\not{R}_p$samples, and 100% in nearly all cases. The detection efficiency however falls off at higher squark masses, as the events are more forwardly distributed, causing the electron identification and the jet-finding to become less efficient.

5.5 Results and Conclusions

Figure 5.6 (a) shows the DIS MC background to the SUSY signal well contained within a box of $m_{\tilde{q}}$ vs $m_{\tilde{\gamma}} = 80 \times 80\ GeV$. The data however have nine data points outside this area, corresponding to three events, and table 5.3 shows their $m_{\tilde{q}}$ and $m_{\tilde{\gamma}}$ values. All of these events have been scanned by eye, and show large energy depositions around the beam pipe; however none of them displays a clear 3 jet structure. Figure 5.9 shows a typical $\not{P}_T$ MC event for reference purposes, with a clear 3 jet structure. Figures 5.10, 5.11 and 5.12 show the 3 excluded events. All three events are presumed to be DIS NC events. In two of the three events the algorithm had misidentified electrons close to the beam-pipe. In the third event all three jets were very close to each other. We have therefore used the cut-sequence

- $\theta_{electron} > 0.2rad$
- (max(angles between jets))$> 0.35rad$

to exclude the three candidates.

Applying the same cuts to the SUSY events we obtain the overall efficiency of the SUSY samples (Figure 5.14). The upper two curves show the efficiencies before any mass cuts (to be compared with Figure 5.8). Note that the losses due to the '$\theta_{electron} > 0.2rad$' and '(max(angles between jets))$> 0.35rad$' cuts are negligible. The lower curves show the efficiencies after the box cut $m_{\tilde{q},\tilde{\gamma}} > 80$GeV. Note that the efficiency of the SUSY events close to $m_{\tilde{q}} = 80$GeV is low because the reconstructed squark masses generally lie below the generated squark masses (Figure 5.6d).

The conclusions to draw from the analysis is that no SUSY candidate with $m_{\tilde{q}} > 80\ GeV$ has been seen in the 1992 ZEUS autumn data. Folding in the efficiencies of Figure 5.7 and 5.14, and using Poisson statistics to give 2.3 signal events for a 90% confidence limit on no background, one can draw a discovery limit on the $m_{\tilde{q}}$ as a function of the coupling λ'. Figure 5.15 shows the 1992 limit - well below the CDF

Candidate	$m_{\tilde{q}}(GeV)$	$m_{\tilde{\gamma}_1}(GeV)$	$m_{\tilde{\gamma}_2}(GeV)$	$m_{\tilde{\gamma}_3}(GeV)$
A	85.8	78.3	75.7	40.5
B	91.8	78.2	72.7	51.9
C	80.6	75.8	74.7	39.5

Table 5.3: The 3 excluded candidates with $m_{\tilde{q}} > 80\ GeV$.

and CC universality limits of table 4.4. Note that for simplicity limits on λ'_{12i} have been omitted (the index 2 refers to the second quark generation).

Figure 5.15 also shows the discovery limit on process 5.1B from the 1992 ZEUS data taken from [75]. Although this limit is better than the limit from process 5.1C at a luminosity of 26.6 nb^{-1}, it will eventually become inferior as larger luminosities allow probing of smaller and smaller couplings λ'_{1jk} [7], and hence the cross-sections of process 5.1B become small compared to the cross-sections of process 5.1C.

This is demonstrated in Figure 5.15, where we have tried to estimate the potential discovery reaches for both processes for a luminosity of 10 pb^{-1}. For the projected limits on process 5.1B we have assumed a 100% trigger and detection efficiency of the SUSY signal. For the projected limits on process 5.1C we have folded in the efficiencies of Figure 5.8, and only considered photino decays to positrons[8]. Although we have overestimated the efficiencies of process 5.1B, the discovery reach of this process has now become inferior to that of process 5.1C.

The shaded area in Figure 5.15 shows just how big the potential improvement on previous limits can be for L=10pb^{-1}. SUSY could be discovered as a 3σ effect up to $m_{\tilde{q}}$ of 170 GeV, at λ'_{11i} as low as 0.03.

[7] Process 5.1B is suppressed by an order of λ' with respect to process 5.1C.

[8] The CTD-FADC readout will allow particle identification of high p_T positrons, and thus triggering on the e^+ will reduce backgrounds substantially.

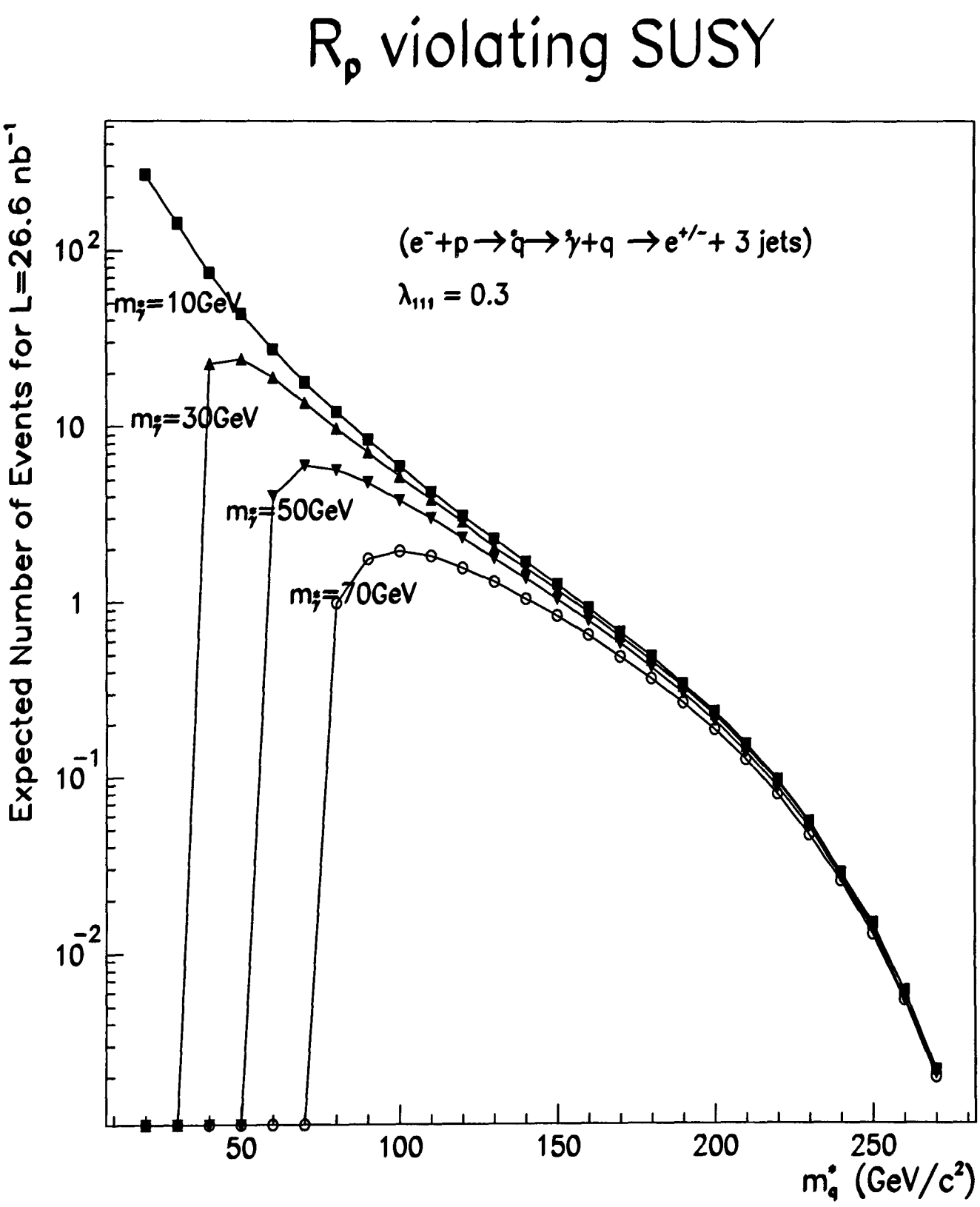


Figure 5.2: Expected number of events for L=26 nb^{-1} at the nominal electroweak coupling ($\lambda'_{111} = 0.3$).

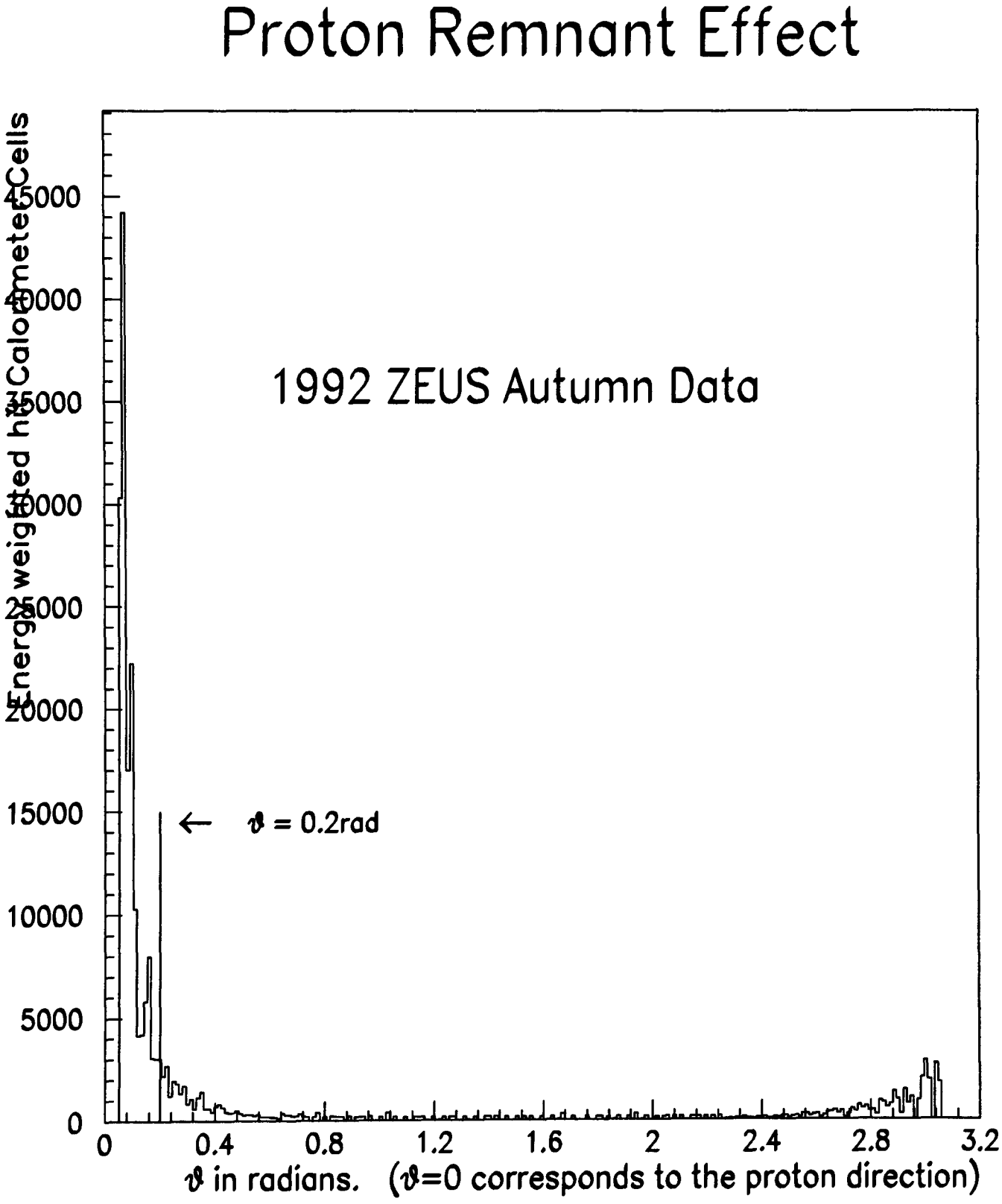


Figure 5.3: Energy weighted θ-bins of the hit Calorimeter Cells

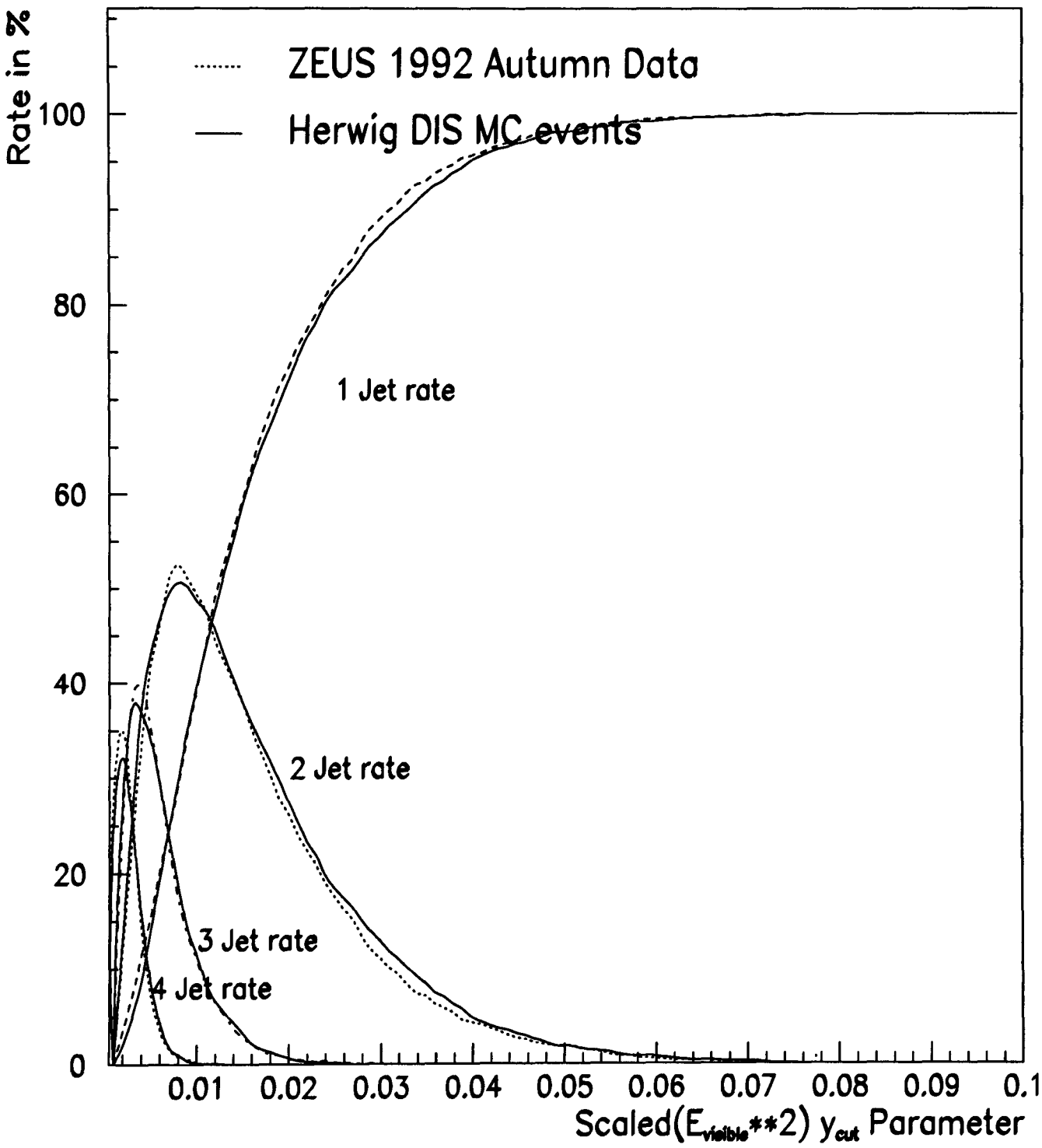


Figure 5.4: Scaled y_{cut} distribution of the JADE (E-scheme,E_{vis} scale, $\theta_{bpcut} = 0.2rad$) algorithm. It shows the dependence of the n-jet rates on the y_{cut} parameter.

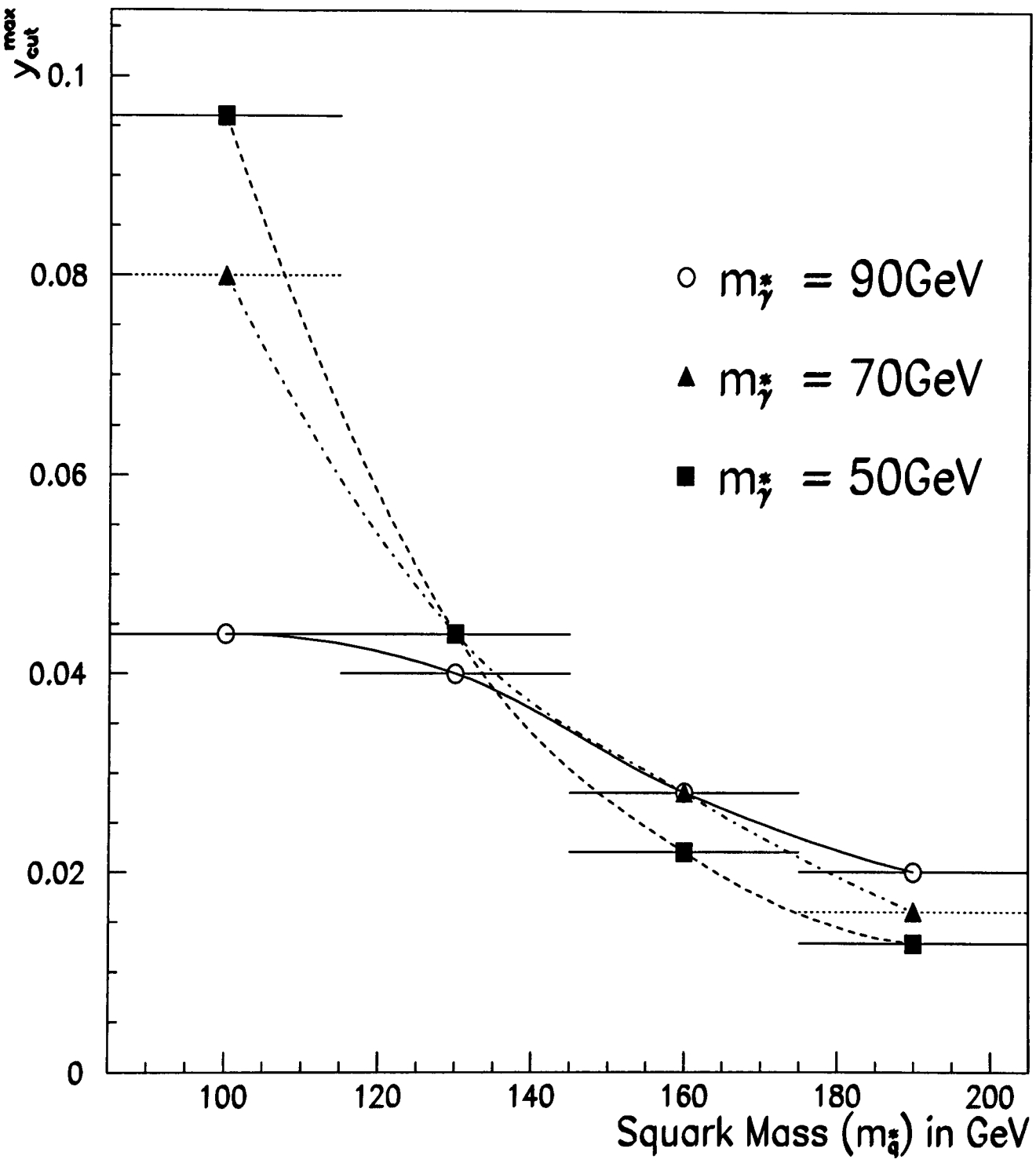


Figure 5.5: The dependence of y_{cut}^{max} on $m_{\tilde{\gamma}}$ and $m_{\tilde{q}}$. y_{cut}^{max} is the cut-off value which gives the maximum 3-jet rate.

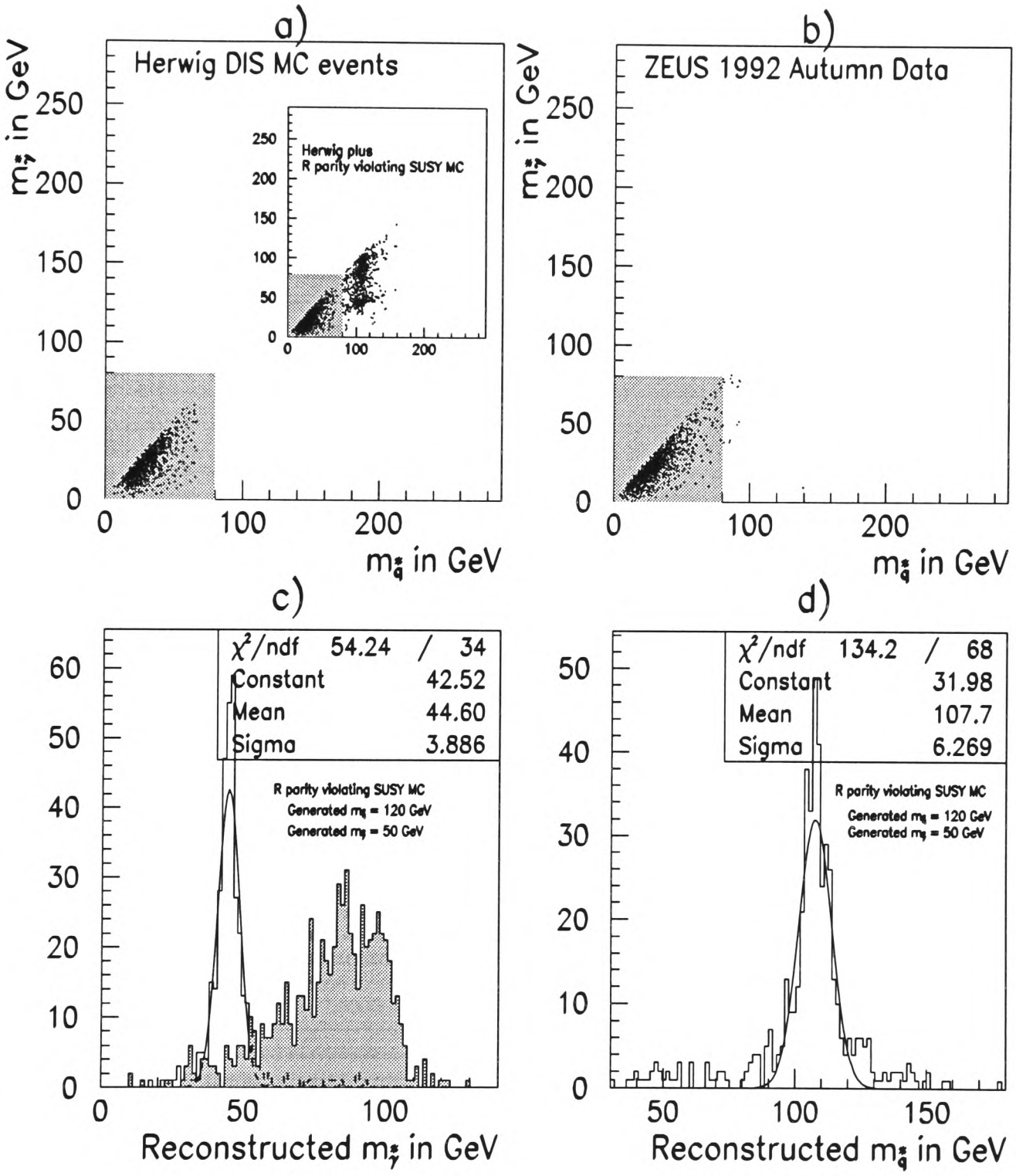


Figure 5.6: Figure (a): The $m_{\tilde{\gamma}}$ vs $m_{\tilde{q}}$ combinations (3 entries per event), reconstructed from the 3 jets of the DIS MC sample. All events were constrained to have a 3 jet multiplicity. The sample is equivalent to a luminosity of 26 nb^{-1}. The upper right-hand corner shows the same plot together with a SUSY MC mass peak at $m_{\tilde{q}} = 120\ GeV, m_{\tilde{\gamma}} = 50\ GeV$. Figure (b): $m_{\tilde{\gamma}}$ vs $m_{\tilde{q}}$ for the 1992 ZEUS autumn data sample (L=26 nb^{-1}). Figure (c): Reconstructed $m_{\tilde{\gamma}}$ of $\not{R}_p$ MC events. The shaded area shows the two wrong combinations of jets. Figure (d): Reconstructed $m_{\tilde{q}}$ of $\not{R}_p$ MC events.

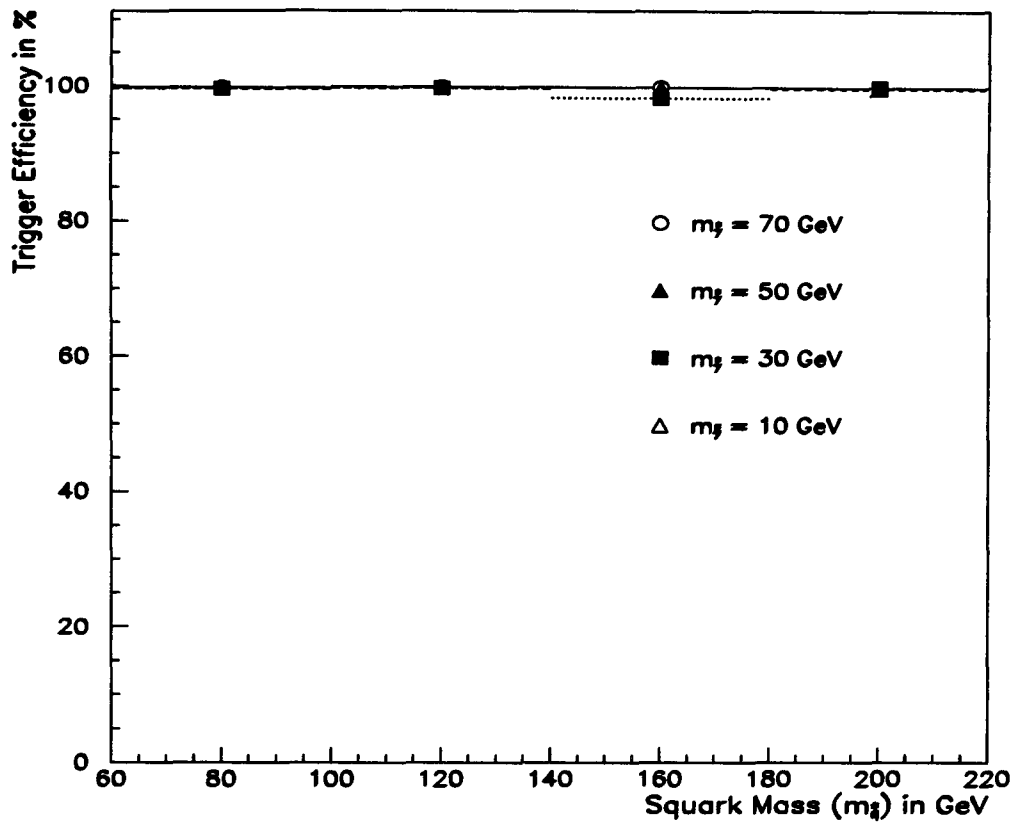


Figure 5.7: 1992 trigger efficiency of $\not{R}_p$-SUSY

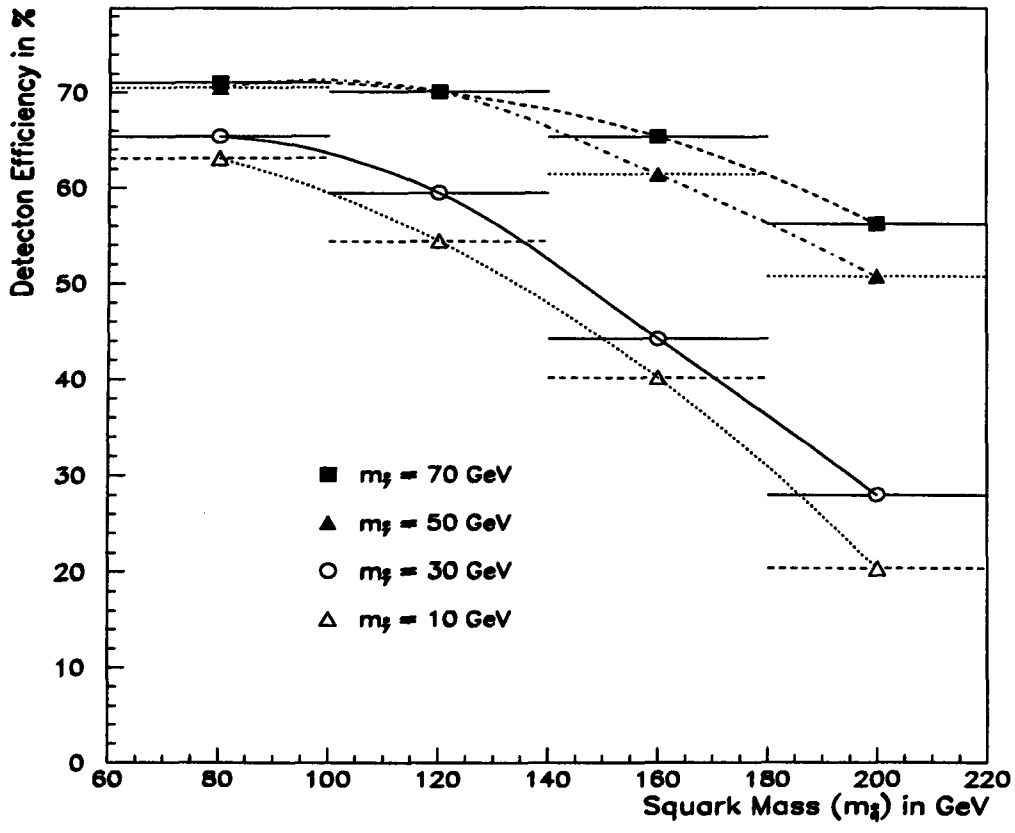


Figure 5.8: Detection efficiency of $\not{R}_p$ SUSY after trigger and offline cuts of table 5.2.

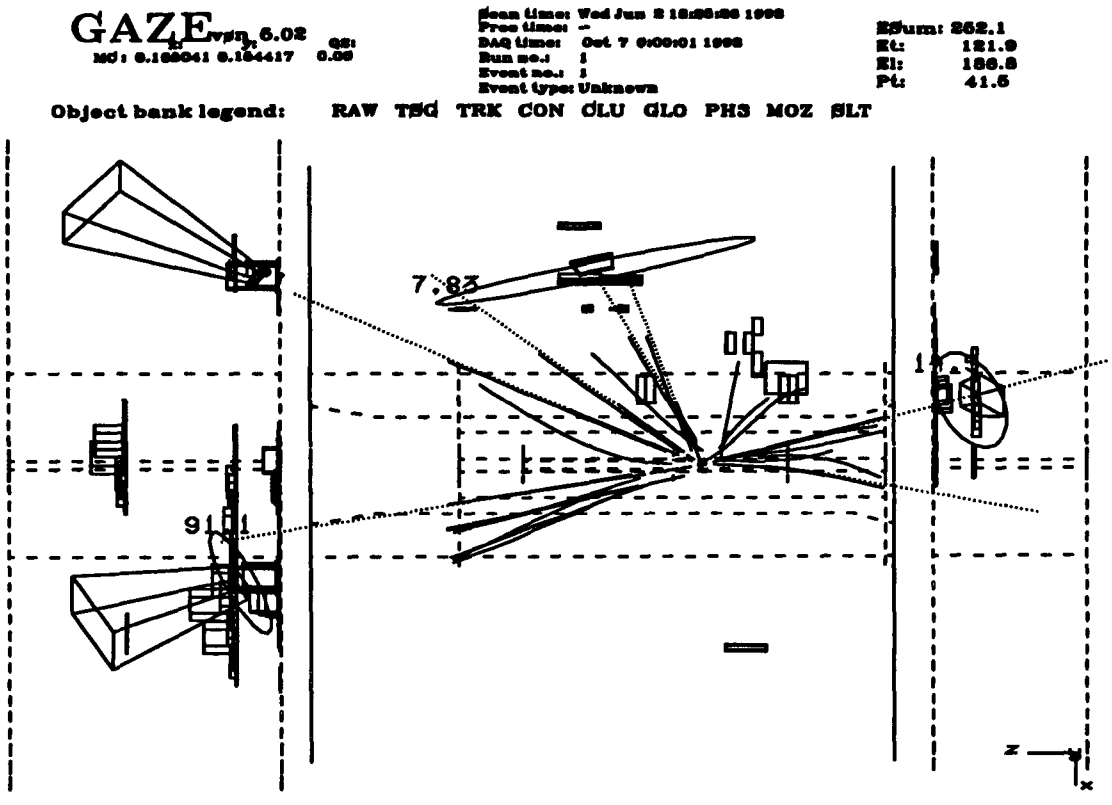


Figure 5.9: $\not{R}_p$ MC event (m_{squark} =120 GeV, $m_{\tilde{\gamma}}$ =50 GeV). The 3 jets (at 91.1, 7.83 and 14.5 GeV) and the $e^{\pm}$ (at 113 GeV) are well resolved and clearly visible.

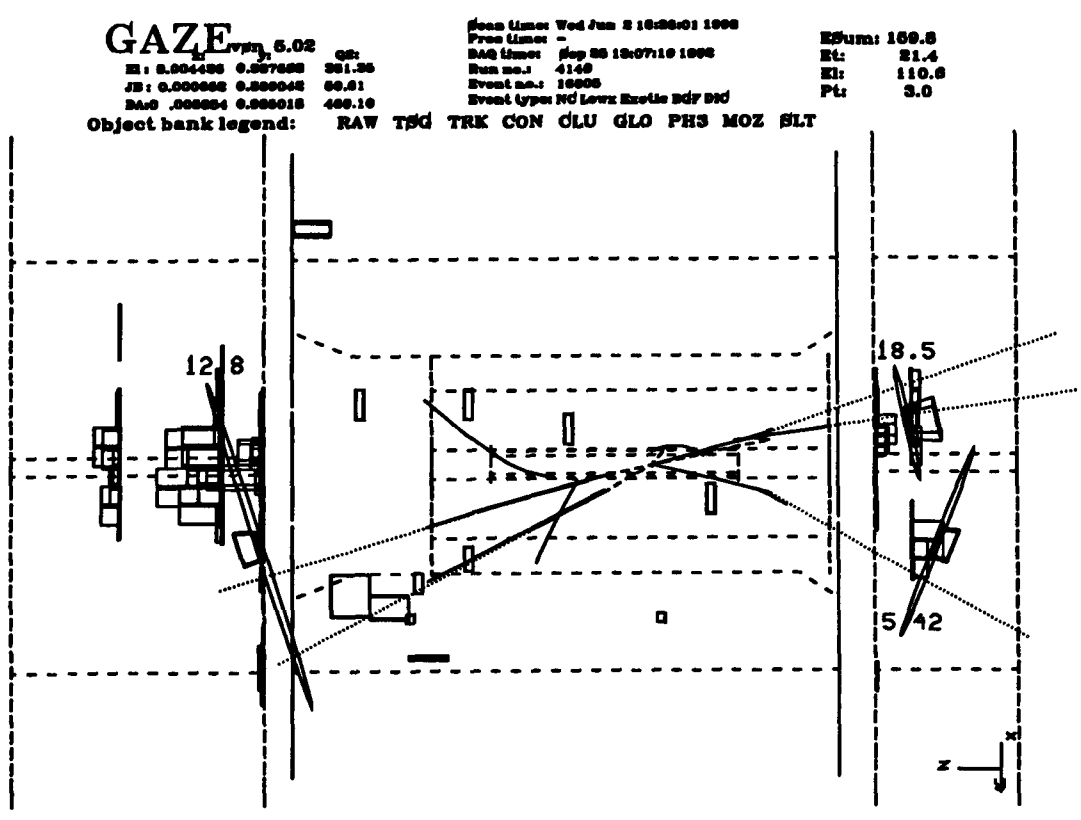


Figure 5.10: ZEUS 92 Autumn Data - Candidate 'A'. A lot of activity around the beam pipe 'fakes' the 12.8 GeV jet. The electron finder also found a high energetic $e^{\pm}$ at 64 GeV close to the beam pipe (not shown). The event is presumed to be a DIS NC event, in which the 'true' electron is near the FCAL/BCAL boundary.

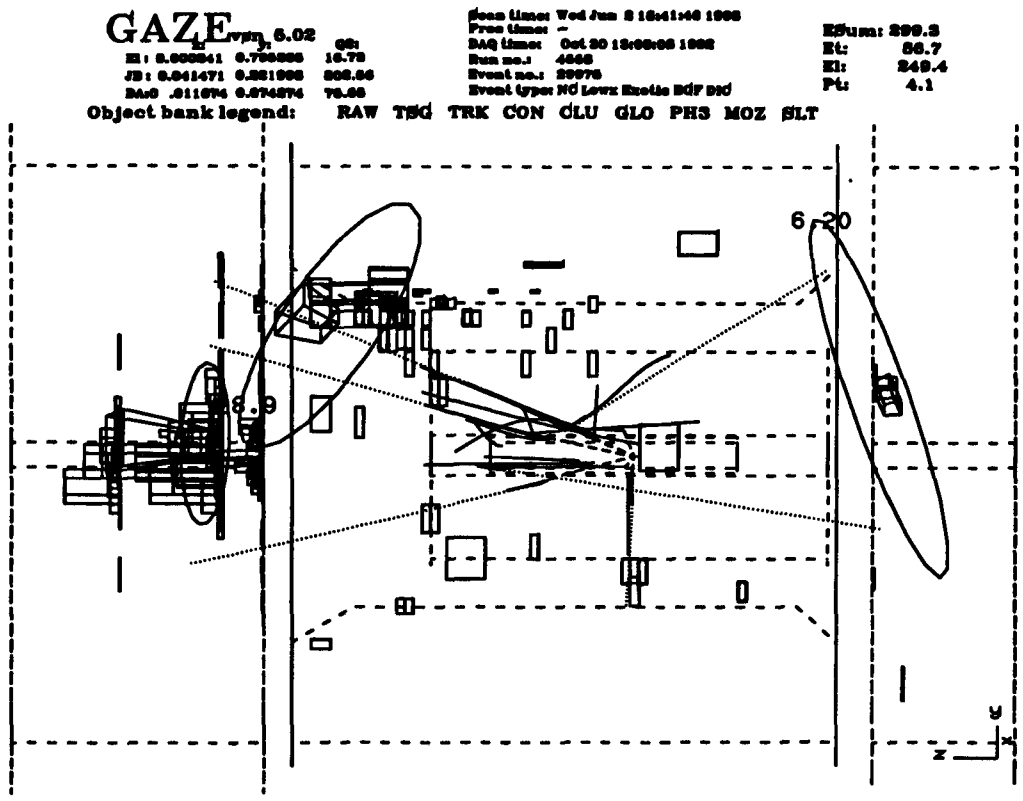


Figure 5.11: ZEUS 92 Autumn Data - Candidate 'B'. The found electron is again around the beam pipe, which shows a large activity due to proton remnant effects. The 'true' DIS electron in the rear direction is falsely reconstructed as a jet (the 6.20GeV jet).

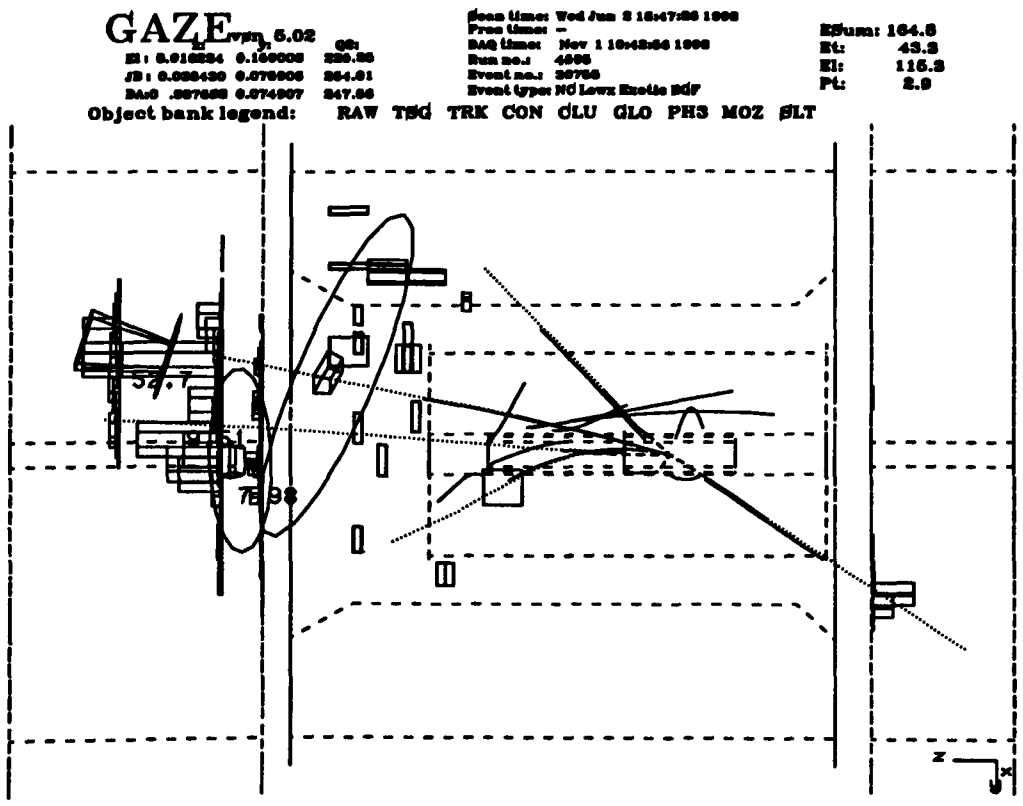


Figure 5.12: ZEUS 92 Autumn Data - Candidate 'C'. Although the DIS electron is correctly identified, there is no clear 3 jet structure in the event.

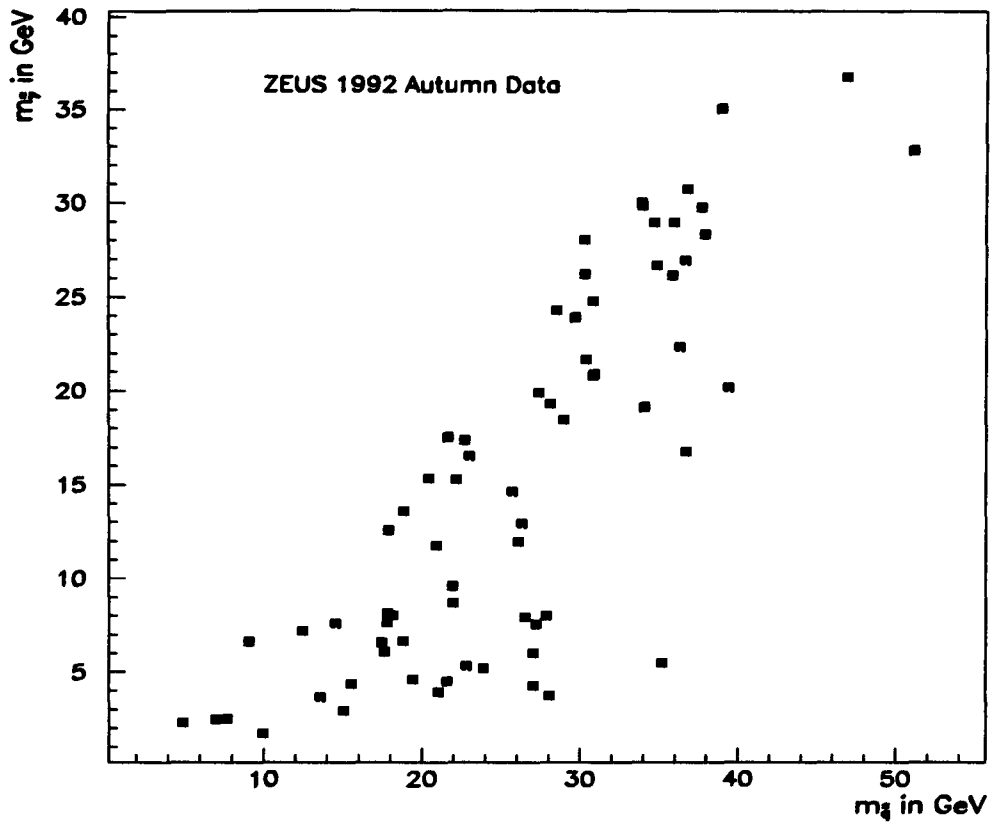


Figure 5.13: The $m_{\tilde{\gamma}}$ vs $m_{\tilde{q}}$ of backgrounds to Deep Inelastic Scattering events after the offline cuts of table 5.2.

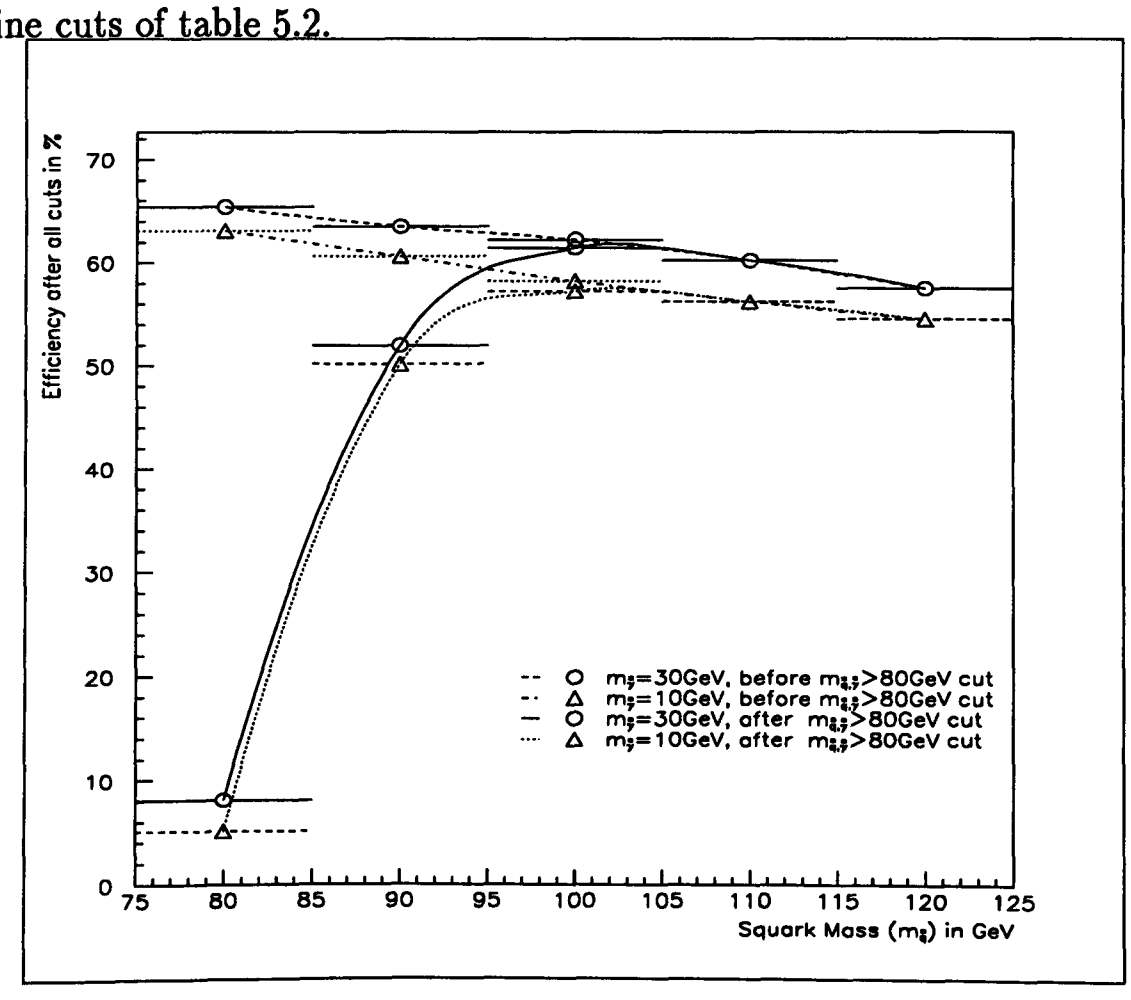


Figure 5.14: Overall efficiency of $\not{R}_p$ SUSY after the cuts of table 5.2 and the cuts '$\theta_{electron} > 0.2rad$' and '(max(angles between jets))$> 0.35rad$'.

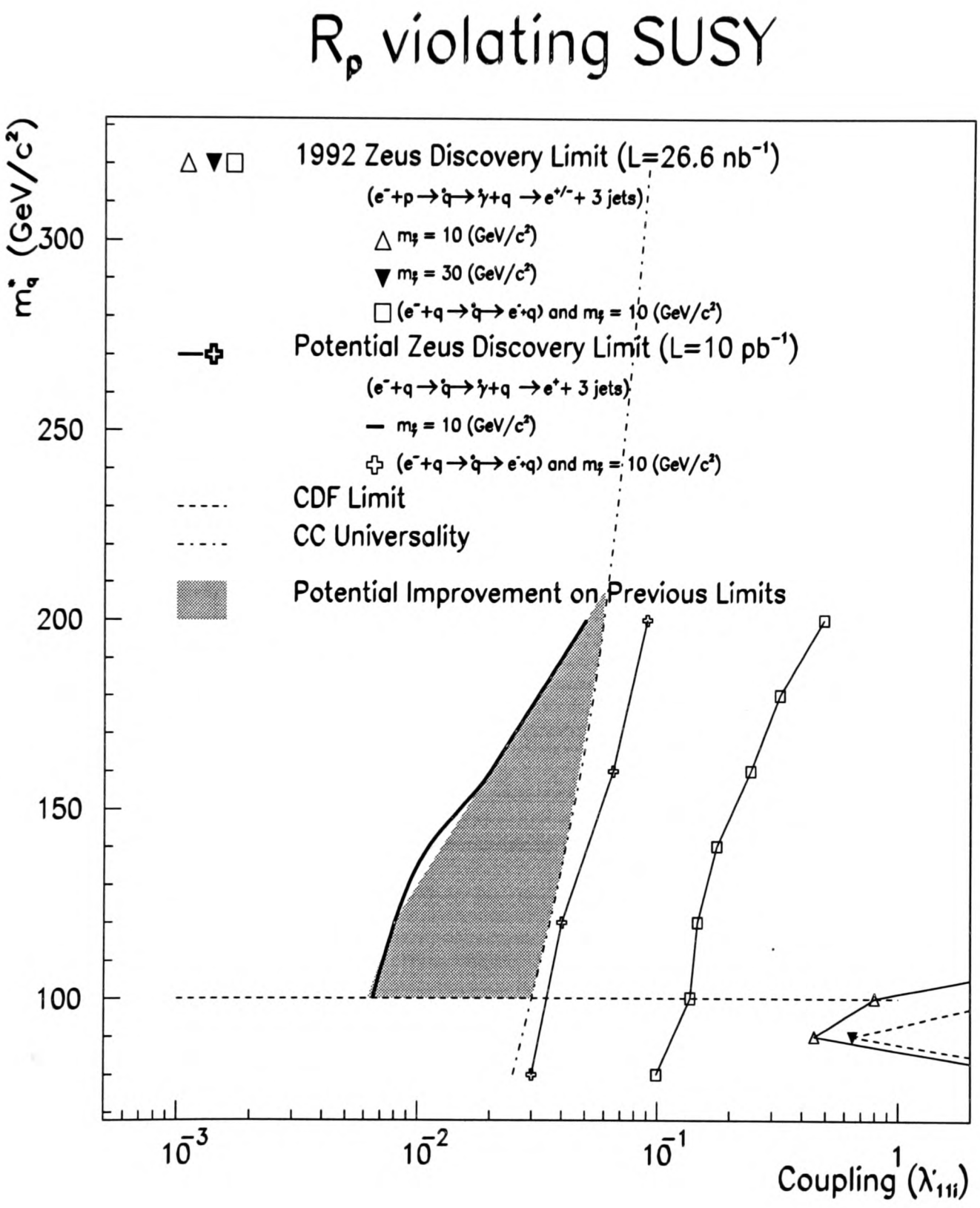


Figure 5.15: Discovery Limits (90% CL) on $m_{\tilde{q}}$ as a function of the R_p coupling constant λ'_{11i}. The regions to the right hand side of the lines are excluded. The limits which can be set from the search on the 1992 data are: (1) limits from process (5.1C) - the triangles. (2) limits from process (5.1B) - the squares. The hatched region shows potential discovery limits for a projected luminosity of $10pb^{-1}$ from process (5.1C). The condition that the lifetime of the photino is too large to decay within the beam-pipe (~10cm of the beam-line) translates to a value of the coupling $\lambda' \leq 1.6 \cdot 10^{-3}$.

Chapter 6

Tau-Signals for Supersymmetry at HERA

This chapter is based on reference [98].

6.1 Overview

In this chapter we further focus on R-parity violating SUSY signals at HERA. A Monte Carlo study is presented and the discovery potential of $R\!\!\!/_p$SUSY with the ZEUS detector is investigated. We consider the R-parity violating signals at HERA for the case of the MSSM production mechanisms: $e^- + q \to \tilde{e} + \tilde{q}$ and $e^- + q \to \tilde{\nu} + \tilde{q}'$. The supersymmetric particles will decay via the LSP to R-parity-even final states. For the final decay we focus on the lepton number violating couplings $L_i Q \bar{D}$. Since the production mechanism involves only gauge interactions we can probe very small Yukawa couplings $\lambda \gtrsim 3 \cdot 10^{-6}$, limited only by the decay length of the LSP. We assume the LSP to be the lightest neutralino and study its decays in detail. We find that the branching fraction (BF) to charged leptons strongly depends on the SUSY parameters: $10\% \leq BF(\tilde{\chi}^0 \to e_i^{\pm} + u_j + \bar{d}_k) \leq 95\%$, contrary to the naively expected 50%. These results significantly extend previous results by other authors [63, 64] and should be helpful for all future searches. The maximum SUSY mass reaches of the studied processes were found to be: $m(\tilde{e}, \tilde{\nu}) + m(\tilde{q}) \leq 170\,GeV (L_\tau Q \bar{D})$, and

$195\,GeV, 205\,GeV (L_\mu Q\bar{D}, L_e Q\bar{D})$. These are well above existing limits on $\not{R}_p$SUSY from previous experiments. We conclude that HERA offers a very promising discovery potential for $\not{R}_p$SUSY.

6.2 Introduction

HERA is particularly sensitive to the $LQ\bar{D}$ operator of Eq.(4.21) since it couples to both leptons and quarks. As already discussed in chapters 4 and 5, when including a substantial coupling λ'_{ijk} beyond those of the minimal supersymmetric standard model (MSSM) the phenomenology changes in two main respects: (1) resonant squark production is possible at substantial rates (this has been studied in the previous chapter), and (2) the lightest supersymmetric particle (LSP) is not stable and can decay in the detector.

In this chapter we fully exploit the second possibility. We consider the associate pair production of supersymmetric particles via supersymmetric gauge couplings

$$e^- + q \;\rightarrow\; \tilde{e}^- + \tilde{q}, \tag{6.1}$$

$$e^- + q \;\rightarrow\; \tilde{\nu} + \tilde{q}'. \tag{6.2}$$

This has been studied in detail in the context of conserved R_p, where the dominant signals are missing p_T [56, 73]. These studies have generally led to the conclusion that there is no discovery potential for supersymmetry at HERA beyond the existing TEVATRON limits (see section 4.5.1). One essential point of this chapter is that for $\not{R}_p$this is *not* the case. For $\not{R}_p$the scalar fermions (sfermions) subsequently cascade decay dominantly via the LSP [1] and the operator $L_iQ_j\bar{D}_k$ to

$$\tilde{f} \rightarrow f + \tilde{\chi}_1^0 \;\rightarrow\; f + (e_i^\pm + u_j + \bar{d}_k) \tag{6.3}$$

$$\tilde{f} \rightarrow f + \tilde{\chi}_1^0 \;\rightarrow\; f + (\nu_i + d_j + \bar{d}_k). \tag{6.4}$$

[1] The direct decay of the sfermions via the operator $LQ\bar{D}$ is strongly suppressed for the small values of λ' we are considering. For a detailed discussion see [61].

Here $e_i^{\pm}$ denotes a charged lepton of generation i, ν_i denotes a neutrino of generation i, u_j denotes a u-type quark of generation j [2], and $\bar{d}_k$ denotes a d-type quark of generation k (c.f. equation (4.21)). The main signal of interest for these events will then be a high p_T charged lepton.

In studying these signals we go beyond previous work [63, 64] on $\not{R}_p$supersymmetry (at HERA) in the following respects:

- Since the considered production mechanism is R_p conserving, the cross-section is independent of the Yukawa coupling. Thus it is possible to probe extremely small couplings, which are only limited by the requirement that the LSP decays within the detector [3], *i.e.* $\lambda \gtrsim 3 \cdot 10^{-6}$. Recall, the smallest Yukawa coupling in the SM, the electron-Higgs coupling, is just of this order.

- Since the lepton number violating coupling is not involved in the production cross-section, we are able to explore the full generation structure of the operator $L_iQ_j\bar{D}_k$. We must only require $j \neq 3$ since a top quark in the final state is kinematically prohibited. In particular we can also study the $L_\tau Q_j \bar{D}_k$ operator. This leads to a tau lepton in the final state. The bounds on the couplings involving tau lepton number violation are weak to non-existent (for existing world limits on $\not{R}_p$SUSY see table 4.4). We will show that HERA presently has the best discovery potential for the $L_\tau Q_j \bar{D}_k$ operator. Furthermore, based on the analogy with the SM, one might naively expect the higher generation Yukawa couplings to be the largest [58, 64], giving increased motivation to study the tau signals.

- We have considered a general neutralino as the LSP (as opposed to restricting the study to a photino). This has two main effects in $\not{R}_p$studies. (1) For the

[2] For example u_1 denotes a up-quark, u_2 a charm-quark and u_3 a top-quark.

[3] For smaller Yukawa couplings the LSP decays outside the detector, and the Minimal SUSY limits from missing p_T again become applicable.

operator $LQ\bar{D}$ the branching fraction for the LSP decay to charged leptons very strongly depends on the mixing parameters of the neutralino sector. We have found that in the region of parameter space where the photino component of the LSP is dominant, branching fractions of the LSP to charged leptons are large, i.e. $BF \sim 70\%$, reaching a maximum at 95%. In the region of a dominant Zino LSP, branching fractions to charged leptons are small, i.e. $BF \sim 15\%$, reaching a minimum at $\sim 10\%$. (2) In the region of a dominant Higgsino/Zino LSP and small LSP masses the decay rate (proportional the Yukawa coupling $(\lambda')^2$) can become so small that the LSP only decays within the detector for anomalously large $\not{R}_p$couplings. This severely limits the range of couplings to be probed.

- We have included the chargino current production mechanism (6.2). In R_p this is not very promising since it is difficult to distinguish from the SM charged current events (see also section 6.3). However, in $\not{R}_p$both the sneutrino and the squark decay via the LSP to predominantly visible final states which can be detected.

The clear disadvantage of employing the mechanisms (6.1), (6.2) is that the mass reach is severely restricted by the kinematic limit of HERA. This corresponds directly to the problem encountered in the context of the MSSM. However, since we are now considering the case where the LSP *decays*, the previous MSSM squark mass bounds derived mainly from searches for missing p_T signals (e.g. at CDF) must be reexamined.

In our analysis we shall make the following simplifying assumptions:

- We shall assume that the LSP is a neutralino. This is a non-trivial statement, as the LSP is not stable in $\not{R}_p$models and the bounds on relic densities of charged or colour charged particles [54] are not relevant. In some regions of the MSSM parameter space the LSP is a chargino. We do not study this possibility.

- Of the 27 operators $L_iQ_j\bar{D}_k$ we shall assume in turn that one operator domi-

nates, and the others are negligible. We point out that in the SM this is the case for the Yukawa couplings. We thus have 27 separate scenarios to consider; 18 for $j \neq 3$. However, there is no strict argument for this assumption. It does, however, greatly simplify the analysis; in particular the analysis of existing indirect bounds.

- We shall assume the slepton and squark masses to be degenerate. This assumption is made to simplify the SUSY model and its large parameter space.

- We shall assume that the branching fraction of the sfermion cascade decays to the LSP is 100%.

This chapter presents a Monte Carlo study of $\not{R}_p$SUSY production and is outlined as follows. In section 6.3 we review the work on the production mechanism (6.1), (6.2) which we consider. In Section 6.4 we present a detailed analysis of the LSP decays for the operator $LQ\bar{D}$. The associated background is discussed in Section 6.5. In Section 6.6 we perform appropriate cuts to extract $\not{R}_p$signals via Monte Carlo techniques. We present the results in Section 6.7 and conclude in Section 6.8.

6.3 Production Mechanism

The dominant R_p conserving SUSY production mechanisms at HERA are the Neutralino Current (NC) and Chargino Current (CC) processes of Figure 6.1. Here $\tilde{\nu}$, $\tilde{e}_{L,R}$ and $\tilde{q}'_{L,R}$ are the sneutrino, the left and right handed selectron and squark respectively. In the Minimal Supersymmetric Standard Model there are two pairs of charginos, $\chi^{\pm}_{1,2}$ and four neutralinos, $\chi^{0}_{1...4}$. Following the notation of [35], their masses and couplings depend on the parameters M' and M (the U(1) and SU(2) gaugino parameters), the Higgsino mass parameter μ, and $\tan(\beta) = \frac{v_1}{v_2}$, the ratio of the vacuum expectation values of the two Higgs doublets (gaugino mixing is also discussed in section 4.3.1). We shall throughout assume the GUT relation [52], also already introduced in chapter

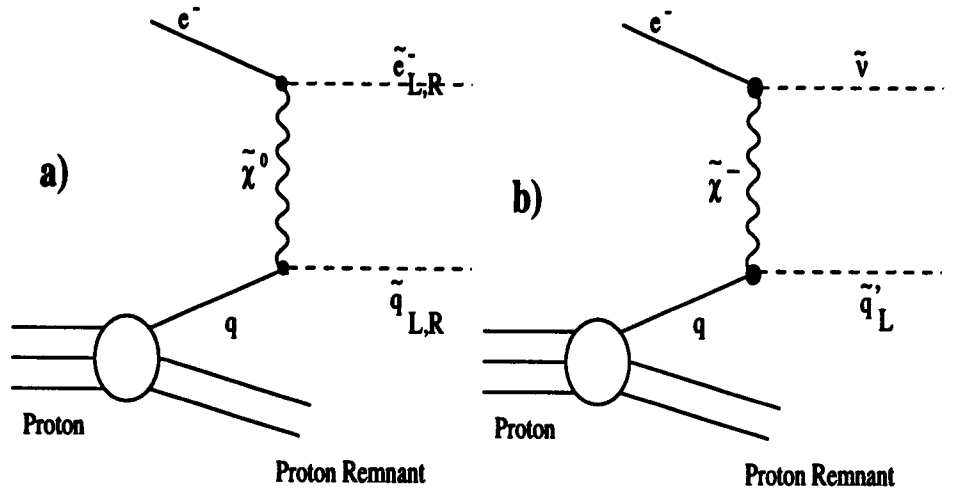


Figure 6.1: MSSM pair production at HERA: a) Neutralino Current, and b) Chargino Current SUSY production.

4,

$$M' = \frac{5}{3}\tan^2(\theta_W)M \tag{6.5}$$

where θ_W is the electroweak mixing angle. Gaugino mixing has been thoroughly discussed in the literature, and we refer to [35, 48, 49] for details.

Process 6.1 and 6.2 have been calculated by various authors [47, 50, 51]. As discussed in [56], the cross-sections exhibit a strong dependence on the sum of the two final state SUSY particle masses, $(m_{\tilde{e}}+m_{\tilde{q}})$ or $(m_{\tilde{\nu}}+m_{\tilde{q}})$. Furthermore they show some dependence on the gaugino mass parameter M', but are relatively insensitive to the parameters μ and $\tan(\beta)$. Figure 6.2 shows a contour plot of the SUSY cross-section $\sigma_{e+q\to\tilde{l}+\tilde{q}'}$ (where $\tilde{l}$ can be a selectron or a sneutrino) as a function of M' and $(m_{\tilde{l}}+m_{\tilde{q}})$. The hatched region indicates where the mass of the lightest neutralino becomes larger than $(m_{\tilde{l}}+m_{\tilde{q}})/2$, the masses of the scalars [4]. Since we have assumed the lightest neutralino to be the LSP, we do not consider this region of parameter space. Note that within the region of interest to HERA (scalar masses up to $\sim$ 200GeV), cross-section variations as a function of M' are within a factor of 2 for M'>10GeV. Figure 6.3 shows the number of expected events per two nominal years of HERA running

[4]Assuming $\tilde{e}$, $\tilde{\nu}$ and $\tilde{q}$ to be degenerate in mass.

at a luminosity of 200pb^{-1} for a number of values M' and their corresponding LSP masses.

The produced selectrons, sneutrinos and squarks subsequently cascade-decay into lighter SUSY particles via processes (6.6)-(6.8).

$$\tilde{e}^{-}_{L,R} \rightarrow e^{-} + \tilde{\chi}^{0}_{i} \tag{6.6}$$

$$\tilde{\nu} \rightarrow \nu + \tilde{\chi}^{0}_{i} \tag{6.7}$$

$$\tilde{q}_{L,R} \rightarrow q + \tilde{\chi}^{0}_{i} \tag{6.8}$$

Eventually only one type of SUSY particle remains, the LSP. In R-parity conserving models the LSP escapes detection, and the resulting SUSY signals are $e^{-} + 1jet + \not{p}_T$ for the NC case, and $1jet + \not{p}_T$ for the CC case. Initial studies [56, 73] have concluded that HERA's eventual discovery reach on selectron, sneutrino and squark production for R-parity conserving SUSY is $m_{\tilde{e}} + m_{\tilde{q}} < 200GeV$ and $m_{\tilde{\nu}} + m_{\tilde{q}} < 185GeV$ for a luminosity of 200pb^{-1}.

In the following sections we shall concentrate on the decay of the LSP via $\not{R}_p$ couplings. These are the first studies to date for MSSM pair production and $\not{R}_p$ LSP decays at HERA. We shall show that the discovery reach of the LQD operator is comparable to those of the R-parity conserving case.

6.4 LSP Decays

We shall now focus on the discussion of the LSP decays to τs via the $L_\tau Q_j \bar{D}_k$ operator[5]. We first turn to the branching fractions of the LSP to τs and τ-neutrinos. Detailed expressions of the $\not{R}_p$ LSP decay calculation can be found in [98]. Before discussing the results of the calculation in detail, we outline their general nature. We have found that the branching fraction of the LSP decay to τs and ν_τs strongly

[5]Throughout this chapter we will use the interchangeable notation $L_{e,\mu,\tau}Q_j\bar{D}_k$ and $L_{1,2,3}Q_j\bar{D}_k$.

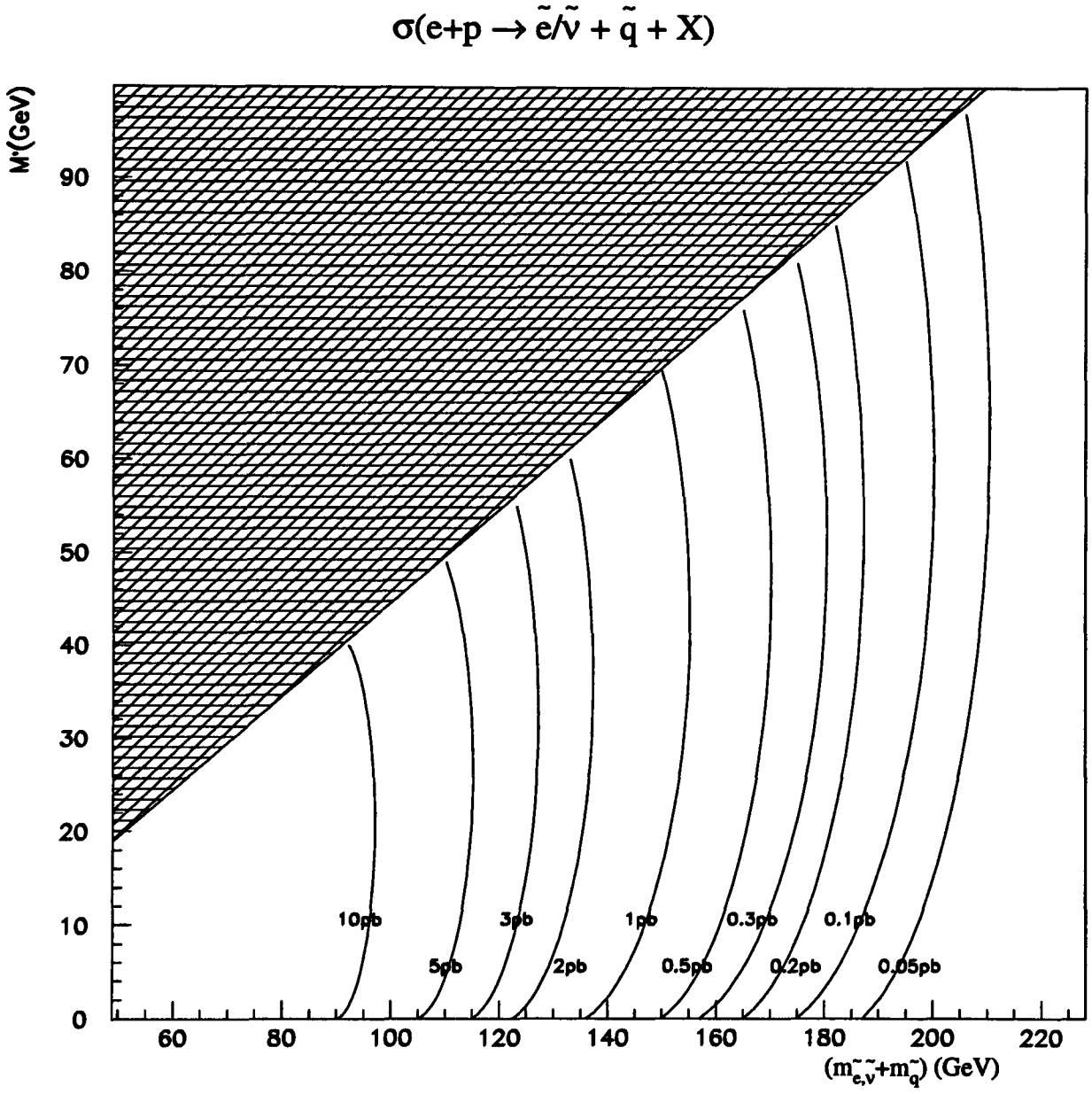


Figure 6.2: Contours of fixed SUSY cross-sections, $\sigma_{e+q\to\tilde{l}+\tilde{q}'}$, as a function of $(m_{\tilde{l}} + m_{\tilde{q}})$ and the gaugino parameter M' for fixed values of μ=-200GeV and $\tan(\beta)$=1. The hatched region indicates where $m_{\chi_1^0} > \frac{m_{\tilde{l}}+m_{\tilde{q}}}{2}$, e.g. where the mass of the lightest neutralino is greater than the mass of the scalars. We do not consider this region in parameter space.

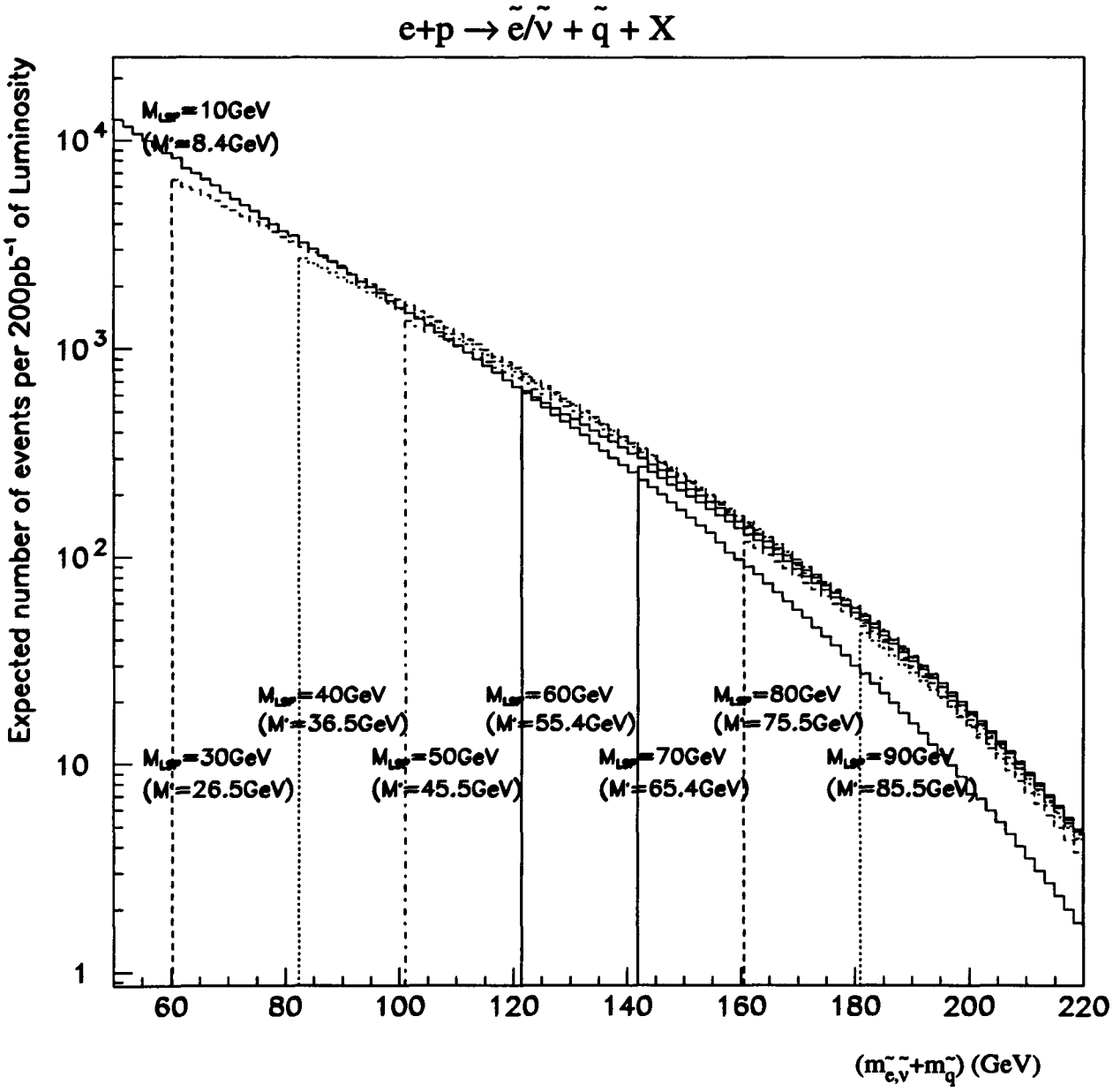


Figure 6.3: Expected number of events per 200pb^{-1} of luminosity as a function of $(m_{\tilde{l}}+m_{\tilde{q}})$ for a number of LSP masses (at fixed values of μ=-200GeV and tan(β)=1).

depends on the nature (i.e. the gaugino mixing parameters) of the LSP. The LSP decay is characterised by one of the following three distinctively different regions:

1. A region where the LSP predominantly decays to τs. Branching fractions of the LSP in this region are typically BF($\chi_1^0 \rightarrow \tau^{\pm} + 2jets$)$\sim$70%. Experimentally this region is the most interesting one, because the event topology contains an exotic lepton (the τ).

2. A region where the LSP predominantly decays to ν_τs. Branching fractions of the LSP in this region are typically BF($\chi_1^0 \rightarrow \nu_\tau + 2jets$)$\sim$85%. One can still look for the signature of decays of the LSP to charged leptons, but the branching fractions are much smaller ($\sim$15%).

3. A region in which Higgsino/Zino contributions to the LSP become dominant at small LSP masses. In this region, the decay rate of the LSP can become so small that the LSP only decays within the detector for anomalously large couplings λ'. We will not consider this region in the subsequent MC study.

We shall now discuss the results of the LSP calculation in detail: the neutralinos are admixtures of their weak eigenstates $\tilde{\gamma}$, $\tilde{Z}$, $\tilde{H}_1^0$ and $\tilde{H}_2^0$. If the LSP dominantly consists of the $\tilde{\gamma}$ component, branching fractions to $\tau^{\pm}$ are large, while a predominance of the $\tilde{Z}$ component makes $\chi_1^0 \rightarrow \nu_\tau + 2jets$ the preferred decay channel. If the LSP is more Higgsino-like, the scenario gets more complicated, as the branching fractions now also depend on both the vacuum expectation values of the SM Higgs', and the mass of the decay lepton.

The amount of mixing of $\tilde{\gamma}$, $\tilde{Z}$ and the two Higgsinos is determined by the SUSY parameters M', M, μ and tan(β). Assuming the GUT relation (6.5), we are left with the three 'free' parameters M', μ and tan(β). Figure 6.4 shows the resulting LSP decay regions as a function of the SUSY parameters. The white region indicates where $m_{\chi_1^0} > m_{\chi_1^{\pm}}$, the region where the mass of the lightest neutralino is greater

than the mass of the lightest chargino. Since we have assumed that the LSP is a neutralino, we do not consider this region in parameter space. The branching fraction BF($\chi_1^0 \to \tau^\pm + 2jets$) is less than 30% [6] in the light shaded area, and greater than 30% in the dark shaded regions. We have found that, over a wide range of parameter space, the branching fractions change abruptly when the nature of the LSP changes. This is demonstrated in Figure 6.4 by solid contours, where the $\tilde{\gamma}$, $\tilde{Z}$ and $\tilde{H}$ symbols on either side of the contours show which component's contribution dominates the LSP. Furthermore we have found that the branching fractions are fairly constant in a given branching region, and approximately BF($\chi_1^0 \to \tau^\pm + 2jets$)$\sim$ 70% in the dark regions, and BF($\chi_1^0 \to \tau^\pm + 2jets$)$\sim$ 15% in the light regions.

Although the above discussion was limited to the tau decays of the LSP, branching fractions to $e^\pm$ and $\mu^\pm$ (via the operators $L_e Q_j \bar{D}_k$ and $L_\mu Q_j \bar{D}_k$ respectively) are within a few percent of the tau results. The only noticeable difference enters in the Higgsino region, where the LSP lifetime is larger for decays to electrons and muons than for decays to taus.

Now we discuss the lifetime of the LSP. The size of the coupling of the $R\!\!\!/_p$ vertex $L_i Q_j \bar{D}_k$ depends on the Yukawa coupling strength λ'_{ijk}. The lifetime of the LSP is hence proportional to $\frac{1}{\lambda'^2_{ijk}}$. Therefore if λ' is very small, the LSP lifetime becomes too large, and the χ_1^0 will consequently decay outside the detector, giving again rise to the missing p_T signatures of the R_p conserving scenario.

In order to quantify such an effect, we have plotted the regions of parameter space (in black) in Figure 6.4 for which the LSP (at a value of $\lambda' = 0.03$) decays outside the detector[7]. These regions coincide with regions where the LSP is dominantly a

[6] We are interested in the pair production of sparticles via processes (6.1) and (6.2), and the produced selectron, sneutrino and squark will subsequently decay to a pair of LSPs (plus other decay products). The condition that BF($\chi_1^0 \to \tau^\pm + 2jets$)$<$ 30% corresponds to the condition that BF($2\chi_1^0 \to$ 1 or 2 $\tau^\pm$s + jets)$\lesssim$ 50%.

[7] We have used the arbitrary condition that the mean free path of the LSP is greater than 1 metre as the criteria for it to decay outside the detector.

mixture of Higgsino/Zino and the LSP mass is small. This is shown in Figure 6.5, which plots the LSP lifetime as a function of the Higgsino mass parameter μ.

The two peaks at $\mu \sim 0GeV$ and $\mu \sim 100GeV$ correspond to the region discussed above. The gap in the middle at $\mu \sim 50GeV$ corresponds to the region where the LSP is not a neutralino. Figure 6.4 also shows how far the black regions would extend (dashed lines) at the very small values of the coupling constant $\lambda' = 3 \times 10^{-6}$.

6.5 Signals and Backgrounds

In order to investigate the full phenomenological consequences of the LSP decay via the $L_i Q_j \bar{D}_k$ operator, we have used a R_p violating SUSY generator to simulate the SUSY production mechanism of Figures 6.1a and 6.1b and the subsequent $\not{R}_p$ LSP decays at the parton level. Throughout our analysis we have chosen to use the MRSD$^{-'}$ structure function set of reference [85] for the SUSY events and the background samples. We have generated the events at electron and proton beam energies of 26.6 GeV and 820 GeV respectively. The SUSY events and potential backgrounds to the SUSY signals were passed through a Monte Carlo detector simulation of the ZEUS experiment based on the GEANT program [86], and subsequently reconstructed using the ZEUS offline programs. We will now proceed to discuss the individual SUSY samples which we have used in our analysis, their signatures, and the potential backgrounds to each of the samples.

6.5.1 SUSY Signals

We have used the MSSM generator of appendix B to simulate the $\not{R}_p$ SUSY samples. In order to reduce the prohibitively large SUSY parameter space, we have made a number of simplifying assumptions:

- We have assumed sleptons (selectrons and sneutrinos) and the five squarks to be degenerate in mass. Throughout we shall denote the mass of the SUSY scalars

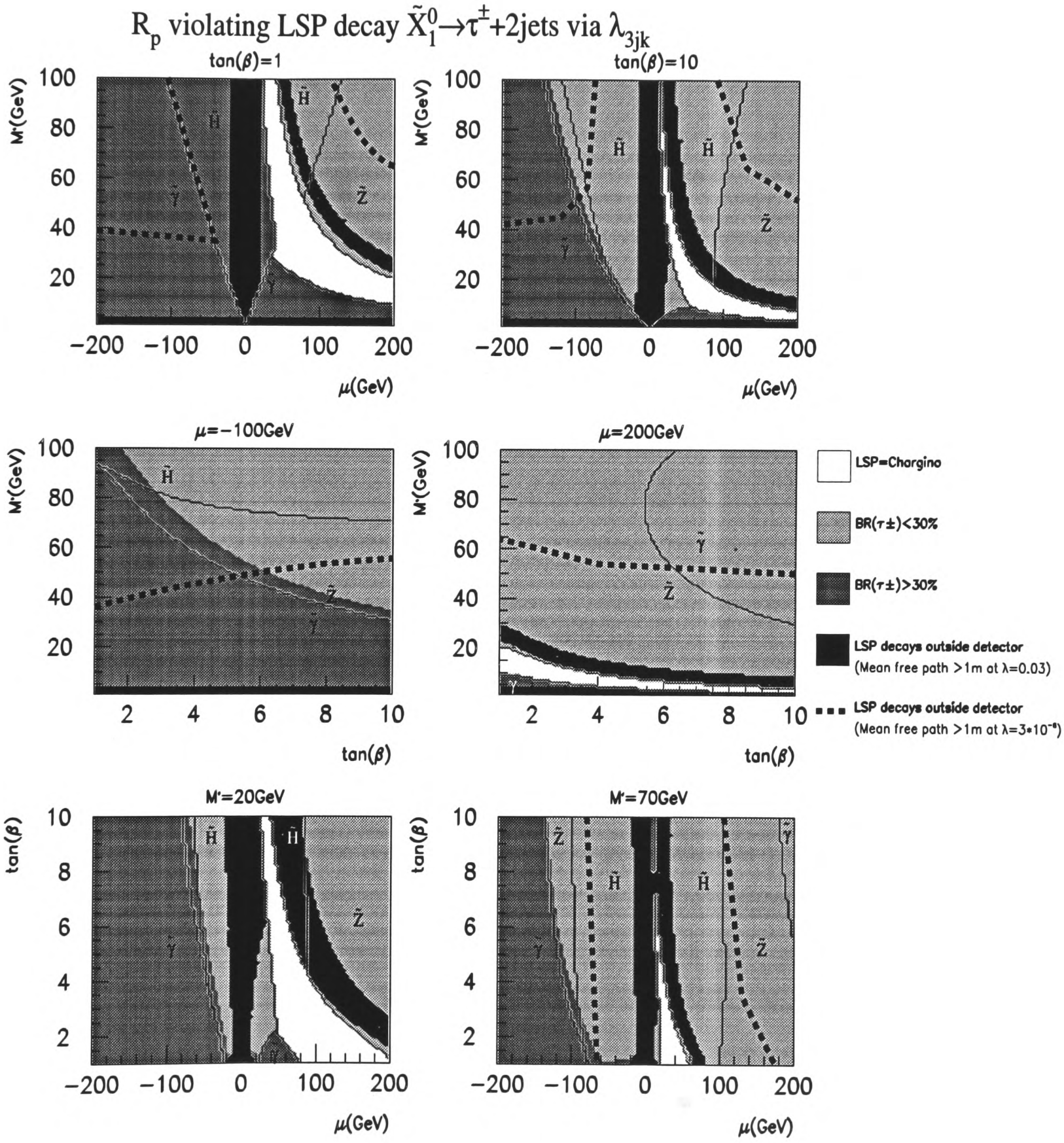


Figure 6.4: LSP decay $\chi_1^0 \to \tau^{\pm} + 2jets$ as a function of the gaugino parameters M', μ and tan(β).

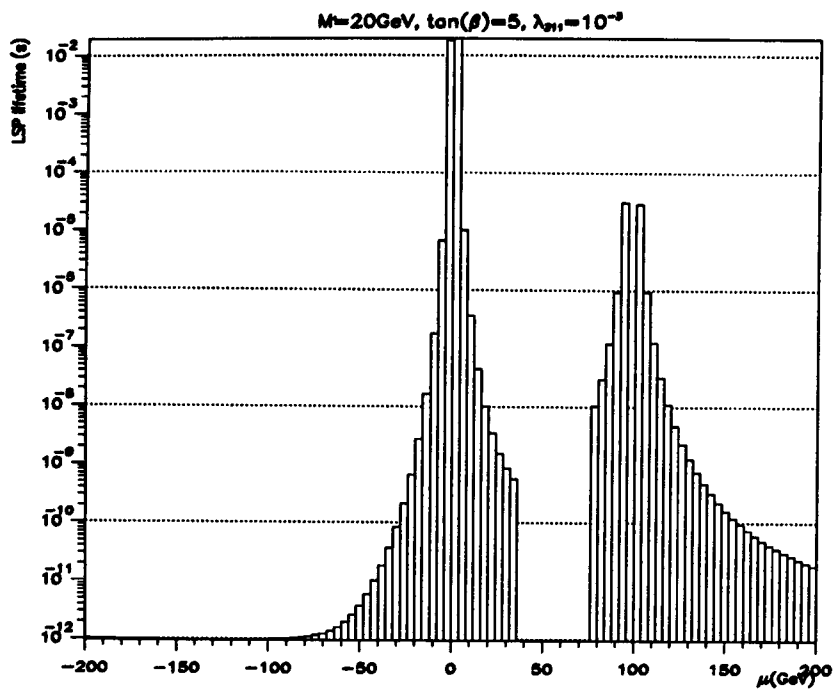


Figure 6.5: LSP lifetime as a function of the Higgsino mass parameter μ.

as $M_{SUSY}=(m_{\tilde{l}}+m_{\tilde{q}})/2=m_{\tilde{l}}=m_{\tilde{q}}$.

- We have assumed the lightest neutralino to be the LSP.

- We have only considered one set of gaugino mixing parameters (M'=40GeV, $\tan(\beta)$=1 and μ=-200GeV) in the region where the LSP predominantly decays to charged leptons, and one set of parameters (M'=55GeV, $\tan(\beta)$=4 and μ=+200GeV) in the region where the LSP predominantly decays to neutrinos. As discussed in sections 6.3 and 6.4, variations of the gaugino mixing parameters within a given LSP decay region have a relative small effect on the cross-section and LSP branching fractions (we have found that the combined changes in the cross-section and the branching fraction are within a factor of two). This is to be compared to the large changes in the cross-sections as a function of $(m_{\tilde{l}}+m_{\tilde{q}})$ which are approximately three orders of magnitudes over the SUSY mass scale of interest to HERA.

We now turn to the signatures of the SUSY events. From the production mechanisms of Figure 6.1a and 6.1b two sparticles, a slepton and a squark, are produced. The sleptons and squarks subsequently cascade-decay via processes (6.6)-(6.8) to neutralinos. Let us consider two specific examples of events in which the LSP decays via the $L_\tau Q\bar{D}$ operator (see also Figure 6.6):

$$e^- + q \to \tilde{e}^- + \tilde{q}' \to e^- + q' + 2\tilde{\chi}_i^0 \;\to\; e^- + q' + \tau + \nu_\tau + 4jets. \tag{6.9}$$

$$e^- + q \to \tilde{e}^- + \tilde{q}' \to e^- + q' + 2\tilde{\chi}_i^0 \;\to\; e^- + q' + 2\nu_\tau + 4jets. \tag{6.10}$$

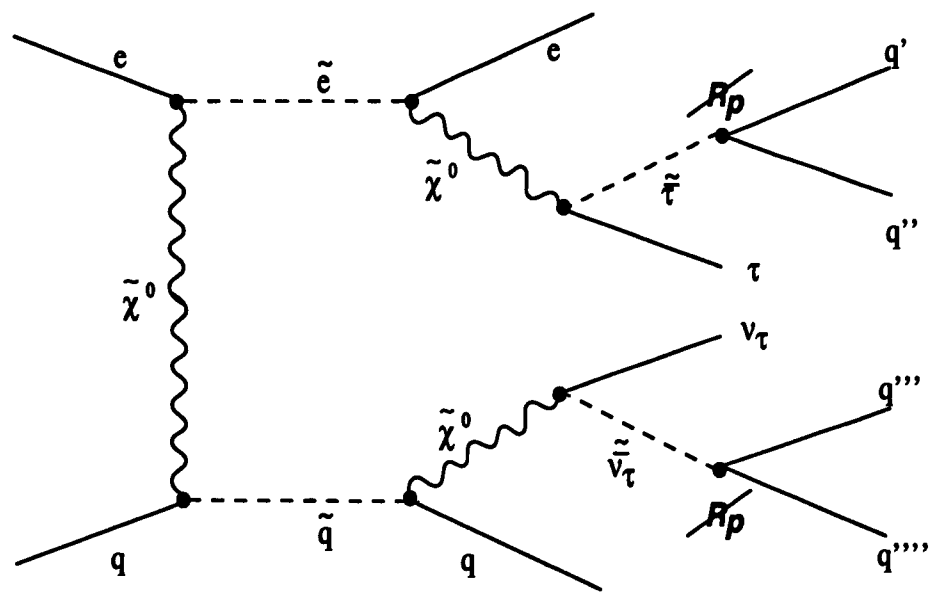
Processes (6.9) and (6.10) are both neutralino current (NC) processes. Note that the pair of sfermions will eventually cascade-decay to *two* LSPs. Process (6.9) has an 'exotic' charged lepton (the τ) in its final state. The τ can subsequently decay to a positron or a muon via

$$\tau^+ \;\to\; e^+\nu_e\bar{\nu}_\tau(\mathrm{BF} \sim 17.8\%) \tag{6.11}$$

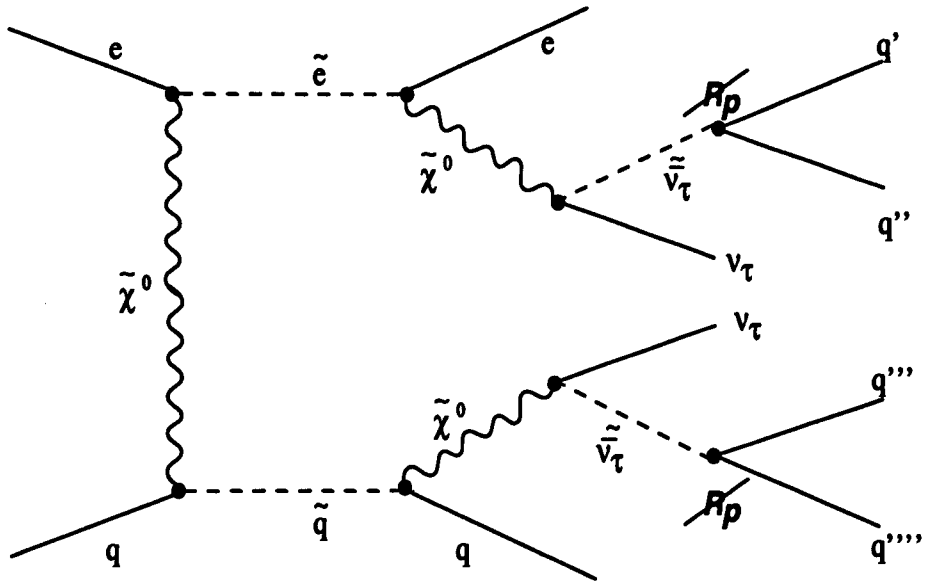
$$\tau^\pm \;\to\; \mu^\pm\nu_\mu\bar{\nu}_\tau(\mathrm{BF} \sim 17.8\%) \tag{6.12}$$

and the branching fractions of the decays are shown in brackets. Our overall signal for LSP decays via the $L_\tau Q\bar{D}$ is thus a positron or a muon and some jet activity in the detector. For the $L_e Q\bar{D}$ and the $L_\mu Q\bar{D}$ operator, our signals are one or more positrons or one or more muons respectively and some jet activity in the detector.

Having discussed the signals of interest, we now turn to the generated SUSY samples. We have generated samples of SUSY events for each of the three operators. The $L_e Q\bar{D}$ samples only contain events in which at least one of the two LSPs has decayed to a positron; the $L_\mu Q\bar{D}$ samples contain only events in which at least one of the LSPs has decayed to a muon; the $L_\tau Q\bar{D}$ samples contain only events in which at least one of the LSPs has decayed to a tau. Because the τ decays semileptonically to hadrons in the majority of cases, only a fraction of the $L_\tau Q\bar{D}$ samples contain a positron or a muon.



a)



b)

Figure 6.6: Examples of R_p conserving SUSY production and subsequent R_p violating LSP decays to: a) a tau and a tau-neutrino, and b) to two tau-neutrinos.

$R\!\!\!/_p$ Operator	M_{SUSY} (GeV)	SUSY M' (GeV)	parameters $\tan(\beta)$	μ (GeV)	Branch (%)	$\sigma_{TOT} \times BF$ (pb)	Ngen	Nexp
$L_eQ\bar{D}$	45	40	1	-200	0.80	6.72	940	1344
$L_eQ\bar{D}$	65	40	1	-200	0.80	1.71	500	342
$L_eQ\bar{D}$	80	40	1	-200	0.80	0.50	400	100
$L_eQ\bar{D}$	95	40	1	-200	0.80	0.11	100	22
$L_eQ\bar{D}$	105	40	1	-200	0.80	0.03	100	6
$L_\mu Q\bar{D}$	45	40	1	-200	0.80	10.10	1000	2020
$L_\mu Q\bar{D}$	65	40	1	-200	0.80	2.57	600	514
$L_\mu Q\bar{D}$	80	40	1	-200	0.80	0.75	400	150
$L_\mu Q\bar{D}$	95	40	1	-200	0.80	0.16	400	32
$L_\mu Q\bar{D}$	100	40	1	-200	0.80	0.09	200	18
$L_\tau Q\bar{D}$	45	40	1	-200	0.79	10.09	2000	2018
$L_\tau Q\bar{D}$	65	40	1	-200	0.79	2.56	1000	512
$L_\tau Q\bar{D}$	80	40	1	-200	0.79	0.75	1000	150
$L_\tau Q\bar{D}$	85	40	1	-200	0.79	0.46	400	92
$L_\tau Q\bar{D}$	90	40	1	-200	0.79	0.28	200	56

Table 6.1: Generated R_p violating SUSY samples. 'M_{SUSY}' is the mass of the scalars; 'M', $\tan(\beta)$, μ' are the gaugino mixing parameters; 'Branch' is the branching ratio of the LSP to a charged lepton $BF(\tilde{\chi}_i^0 \to l^\pm + 2jets)$; '$\sigma_{TOT} \times BF$' is the total cross-section of the sample; 'Ngen' is the number of events generated; 'Nexp' is the number of events expected per luminosity of 200pb^{-1}, two nominal years of HERA running.

For each type of operator, $L_eQ\bar{D}$, $L_\mu Q\bar{D}$ and $L_\tau Q\bar{D}$, we have generated MC samples at a number of SUSY masses M_{SUSY} ($=m_{\tilde{l}}=m_{\tilde{q}}$). The samples were generated at the gaugino parameters M'=40GeV, $\tan(\beta)$=1 and μ=-200GeV, which corresponds to a region where the LSP predominantly decays to charged leptons. The diagonalisation of the gaugino mass matrix produces a LSP with a mass of M_{LSP}=44GeV. Table 6.1 summarises the SUSY samples, their cross-sections and the expected number of events per luminosity of 200pb^{-1}.

6.5.2 Backgrounds

The most promising signature of the $\not{R}_p$ SUSY events is a positron or muon in the final state. Backgrounds to such a signature come from 'physics backgrounds', which produce at least one positron or muon directly, or from 'fake backgrounds', in which either detector effects fake positron or muon signals, or from positrons or muons produced during the fragmentation process from decays of secondary particles. The individual background samples are described below.

In anticipation of a cut in total transverse energy E_T in the following analysis, and in order to keep the number of events in our background samples down to a manageable size, we have applied a $Q^2 > 1000\text{GeV}^2$ cut to the deep inelastic scattering neutral current sample, and a $Q^2 > 500\text{GeV}^2$ cut to all other samples at the generator level. Kinematically this corresponds to a cut in total E_T, $E_T > 60\text{GeV}$, and $E_T > 45\text{GeV}$ respectively (see Figure 6.7). However, because a fraction of the transverse energy in each event will be missed in the detector and also carried off by neutrinos and hence will not be measured, the total visible (or reconstructed) transverse energy will be below the kinematically generated E_T of Figure 6.7. Also uranium calorimeter energy resolution effects will broaden the measured E_T spectrum, and hence smear events in E_T and shift them to higher/lower values of E_T. Even taking both effects into account, our generator cuts on Q^2 are well below our final cut of $E_T > 90\text{GeV}$ in the following analysis.

Physics Backgrounds

We have considered two types of physics backgrounds. The first one is heavy quark production via high Q^2 photon-gluon fusion [88]. The most dangerous case of photon-gluon fusion is expected to be $b\bar{b}$ production. The produced B^0 can decay semileptonically to a positron or a muon. We have also considered $c\bar{c}$ backgrounds, but note that these are generally less dangerous as their E_T distribution is much lower. The

Sample Name	Generator	Generated Q^2 range (GeV^2)	$\sigma_{TOT} \times BF(pb)$	Ngen	Nexp
$b\bar{b}$	HERWIG	500→87248	4.506	3395	901.2
$c\bar{c}$	HERWIG	500→87248	37.39	4105	7478
W (e^+, μ)	EPVEC	500→87248	0.219	400	43.8
NC	LEPTO	1000→87248	230.0	7149	46000
CC	LEPTO	500→87248	49.5	3541	9900

Table 6.2: Generated background samples.'$\sigma_{TOT} \times BF$' is the total cross-section of the sample; 'Ngen' is the number of events generated; 'Nexp' is the number of events expected per luminosity of 200pb^{-1}, two nominal years of HERA running.

HERWIG generator [89] was used to generate $b\bar{b}$ and $c\bar{c}$ events. Table 6.2 summarises all background samples, their cross-sections and the expected number of events per luminosity of 200pb^{-1}, nominally two years of HERA running.

The second background considered is W production [90] via the process

$$\gamma^* + q \rightarrow W + q', \tag{6.13}$$

where the virtual photon is radiated from the electron, and the W can decay to give a positron or a muon. Cross-sections are small compared to the photon-gluon fusion backgrounds. The EPVEC generator of reference [90] was used to generate the W sample. The sample only contains events in which the W decays to a positron or a muon.

'Fake Backgrounds'

Fake signals of positrons or muons in the ZEUS detector can be caused by a number of effects, and these include

- Misidentification of the curvature (and thus charge) of high p_T electrons in the tracking detector.

- Hadrons depositing energy in the uranium calorimeter with shower profile characteristics similar to that of a positron (misidentification of positrons in the calorimeter).

- Punch-through of high energetic charged hadrons through the uranium calorimeter will give rise to tracks in the muon chambers, and hence can lead to misidentified muons.

Furthermore, decays of secondary particles produced during fragmentation processes can lead to genuine positrons and muons. In order to investigate all the effects giving rise to fake backgrounds, we have generated deep inelastic neutral current (NC) and charged current (CC) events using the LEPTO program [91]. Table 6.2 summarises the two samples.

6.6 Analysis

6.6.1 Positron and Muon Identification

Positron and muon identification plays a key role in the extraction of the SUSY signals. The identification algorithms have to have a high purity in order not to contaminate the search sample with too much fake background. With this in mind, we have chosen the following methods for positron/muon identification:

Positron identification is achieved by first of all finding 'electrons'[8] in the uranium calorimeter, e.g. by finding shower profiles characteristic of those of 'electrons'. We require the cluster to have an energy above 5GeV. CTD tracks are then extrapolated from the drift chamber to the face of the electromagnetic calorimeter. If a track matches such an 'electron' cluster, and the curvature of the track is positive, then the cluster is identified as a positron.

[8]Electrons and positrons have the same characteristics in the calorimeter.

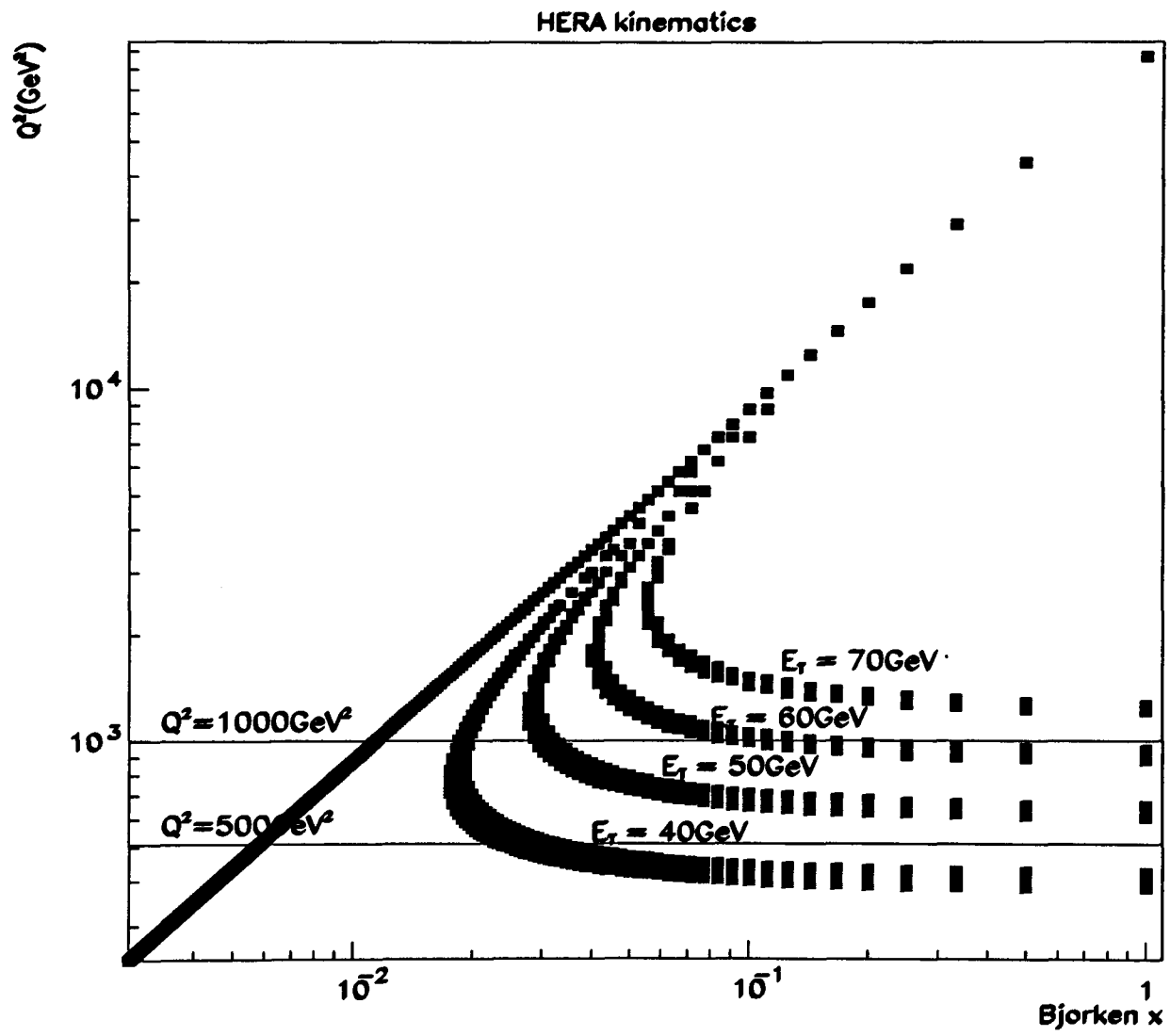


Figure 6.7: Contours of fixed total E_T in the x,Q^2 plane.

Muon identification is achieved by matching CTD tracks with track segments in the muon chambers. The track-matching employs the Kalman-fitting procedure of reference [92]. A global CTD-MUON (muon chamber) track identifies a muon. Note however that only high energetic muons can penetrate the uranium calorimeter before they reach the muon chambers. Requiring tracks in the muon chambers therefore implies an indirect muon momentum cut of p_μ >3-4GeV.

6.6.2 Cuts

Before we go on to discuss how the SUSY signals can be extracted from the background, we explain the cuts used in the subsequent analysis:

- **'e^+ found and μ found'**: positron and muon identification has been discussed in the previous section.

- **'30GeV<E-p_z < 60GeV'**: The kinematical quantity E-p_z is described in chapter 1. The above cut is very powerful in rejecting photoproduction events, in which the electron is not detected in the LUMI or BCAL [93] - it can be shown that E-p_z in such events is generally small, and in most cases below 30GeV. The cut is also very efficient in rejecting beam-gas events.

  In our study we have used the E-p_z cut to mainly reject charged current (CC) events and W events. In both types of backgrounds a considerable fraction of the energy is carried off by neutrinos, and hence will not be detected. As a result the E-p_z distribution of such events is shifted towards lower values.

- **'circularity > 0.1'**: One can define a 2-dimensional-like sphericity [94], circularity, which is defined in the range 0 <circularity< 1. The circularity (transverse sphericity) [95] is defined by

$$\text{circularity} = 2\lambda_2 \tag{6.14}$$

in terms of the smaller eigenvalue, λ_2, of the two dimensional sphericity tensor

$$S_{\alpha\beta} = \sum_i p_{i\alpha} p_{i\beta} / \sum_i {p_i}^2 \tag{6.15}$$

where α, β are Cartesian components, i runs over the number of particles (i.e. reconstructed calorimeter clusters) in the event, and p are the four-momenta of the particles. The thus defined circularity reflects the isotropy of the event. A circularity of 1 corresponds to a completely isotropic event. A three jet event, for example, with the three jets pointing in directions of $\phi = 0°$, $\phi = 120°$ and $\phi = 240°$ would be a good example of an event with a high value of circularity. A two jet event, for example, with a back-to-back jet configuration has a circularity of zero. We shall use this cut to distinguish between the SUSY events and backgrounds. As will be discussed below, the SUSY events are very isotropic, and thus have a high value of circularity.

- '$E_T > 90$GeV': E_T is the total transverse energy measured in the calorimeter. We also include the measurement of the muon track in the E_T if a muon was found.

6.6.3 Signal Extraction

We first examine the characteristics of the positrons and muons in the events. Figure 6.8a and 6.8b show the muon and positron p_T spectra for the SUSY samples at M_{SUSY}=80GeV, correctly normalised with respect to each other. Note that the muon and positron p_T spectrum of the $L_\tau Q\bar{D}$ sample is much softer than the $L_\mu Q\bar{D}$ and $L_e Q\bar{D}$ p_T spectra. This is because the τs have to decay via processes (6.11) and (6.12) to positrons and muons, and hence some of the energy of the e^+ or μ is shared with the associated neutrino.

Even though the p_T spectrum of the $L_\mu Q\bar{D}$ sample is slightly harder than the p_T spectrum of the considered backgrounds of section 6.5.2, we conclude that the

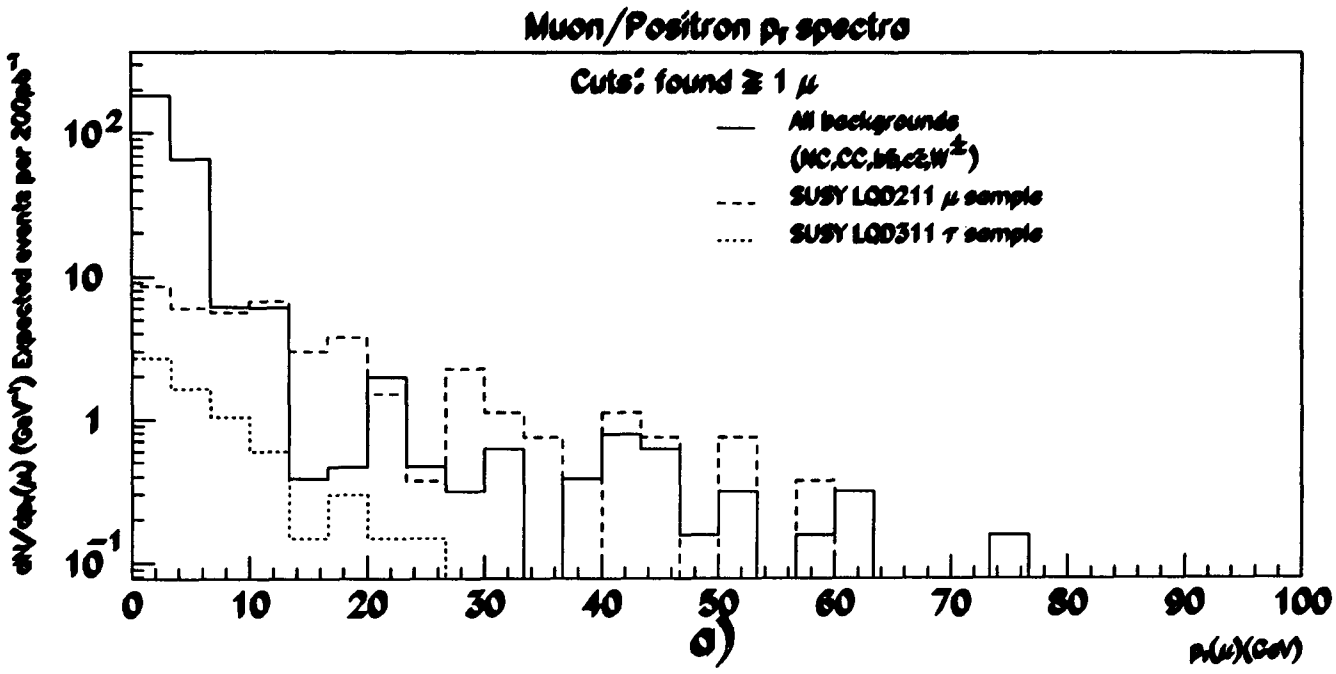


Figure 6.8: p_T distributions of a) muons and b) positrons for the SUSY events and the background samples. The SUSY samples were generated with the following parameters: M_{SUSY}=80GeV, M'=40GeV, $\mu = -200$GeV, $\tan(\beta)$ =1. No cuts were applied to the samples other than positron and muon identification. The distribution labelled 'All backgrounds' combines all the background samples (NC, CC, $b\bar{b}$, $c\bar{c}$, W) and normalises them with respect to their corresponding cross-sections.

positron or muon p_T variable is not a good discriminator between the SUSY signals and the background processes.

Next we consider the circularity of the events. Equation (6.9) gives a typical SUSY event topology, consisting of 5 jets, an exotic lepton, an electron, neutrinos and the proton remnant. Unfortunately not all of the jets are well resolved - most of the jets will generally be very soft. Jet finding algorithms can wrongly recombine the softer jets with harder jets, and the jet multiplicity of such events can therefore be reduced. We have run jet-finders on the MC samples, and have found that the jet multiplicity *can* be used to discriminate between the SUSY events and backgrounds. However, we have also found that the circularity variable is vastly superior to jet multiplicity. This can be explained as follows:

- The high number of jets result in a more isotropic event structure for the SUSY events. This makes the events more circular than their respective backgrounds.

- Soft jets can not be resolved by jet-finders, but they do contribute to the circularity of the event.

Figure 6.9a shows the circularity distributions of the individual backgrounds. In order to display the shape of the distributions with respect to each other, we have normalised the first bin of each sample to one. The NC, CC and W [9] circularity distributions fall off most rapidly, while the $b\bar{b}$ events have the highest circularity tail. This is because the NC events often have a back-to-back two 'jet' structure (the electron and the current jet). In the CC and W sample the isotropy is imbalanced by neutrinos, which are not detected.

Figure 6.9b shows the circularity of all combined backgrounds and the SUSY $L_\tau Q\bar{D}$ samples with M_{SUSY}=45GeV and M_{SUSY}=80GeV. We observe two facts:

[9]The CC and W distributions are not shown in Figure 6.9a.

- Because the circularity of the background falls off much more rapidly than the circularity of the SUSY events, a cut in circularity (at say 'circularity > 0.1') will be a good discriminator between the SUSY signal and backgrounds. We have for reference plotted the circularity of the signal and background events after a positron/muon cut normalised to a luminosity of 200pb^{-1} in Figure 6.10.

- Higher SUSY scalar masses have the effect of making the events more circular - as a result higher m_{SUSY} samples will be more efficient in passing the 'circularity > 0.1' cut.

Figure 6.11a shows the E_T distribution of the backgrounds with and without a circularity cut of 'circularity>0.1'. The cut reduces the background by a factor of 10 at E_T = 60GeV, and by a factor of 18 at E_T=140GeV [10]. A similar plot is shown for the SUSY $L_\tau Q\bar{D}$ samples with SUSY masses M_{SUSY}=45GeV and M_{SUSY}=80GeV. Again note that for the higher mass sample the efficiency of the number of events surviving the circularity cut at large values of E_T is higher than for the lower mass sample.

After applying the three cuts

- e^+ found or μ found
- 30GeV<E-p_z <60GeV
- circularity>0.1

to the MC background samples, we are left with (102.4 $\pm$ 20.9) events. Figure 6.12a shows their E_T distribution. The right-hand side of the E_T tail is dominated by $b\bar{b}$ and $c\bar{c}$ events. Note that due to the higher cross-section the $c\bar{c}$ sample is predominant in the E_T background distribution up to an E_T of 80GeV. The background events

[10]This is a desired effect because a subsequent cut in E_T can therefore be made less stringent, and thus increase the efficiency of the SUSY samples after all cuts.

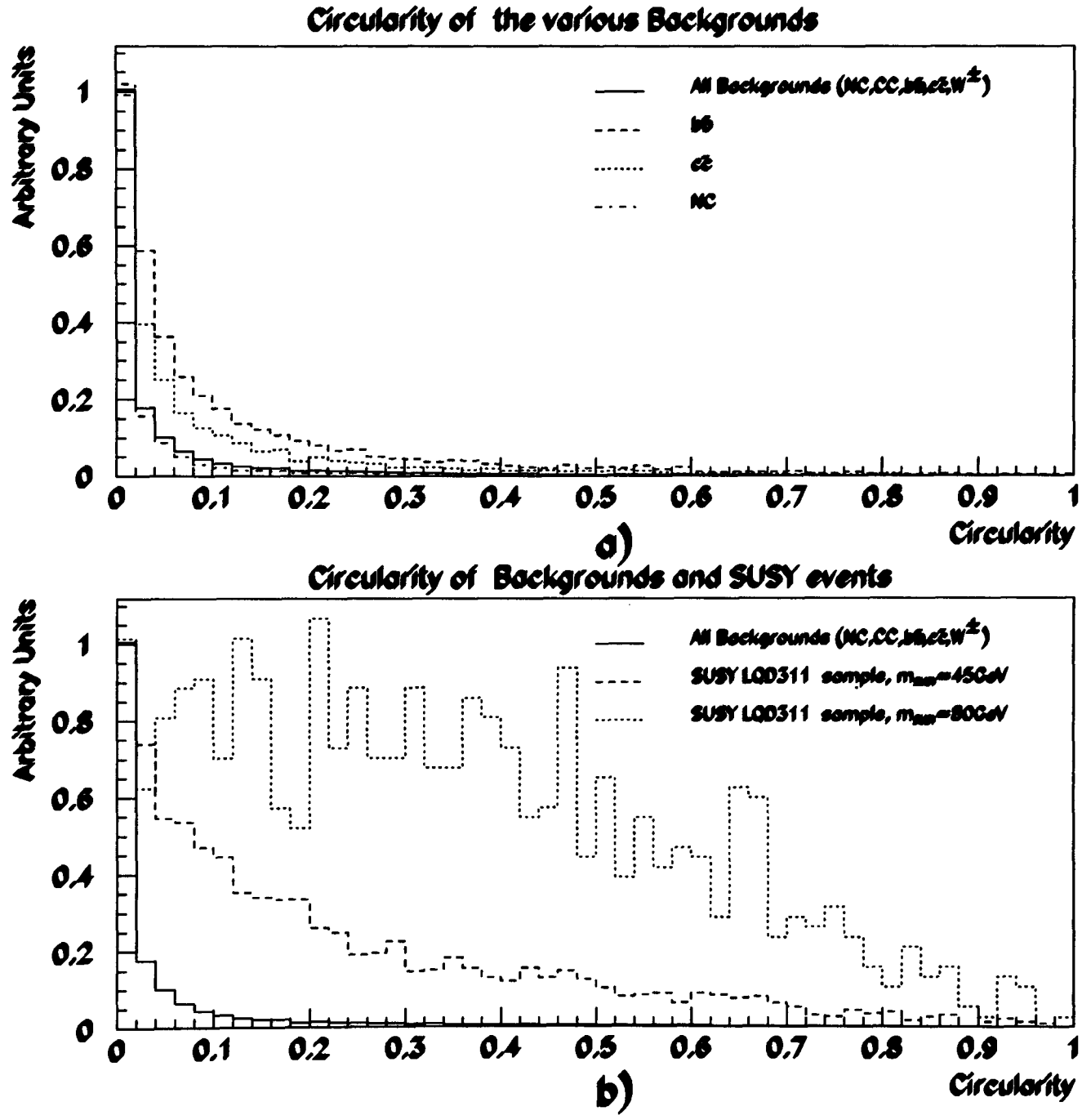


Figure 6.9: Circularity distributions of the SUSY events and backgrounds. The first circularity bin of each sample has been normalised to one in order to display the shape of the distributions with respect to each other.

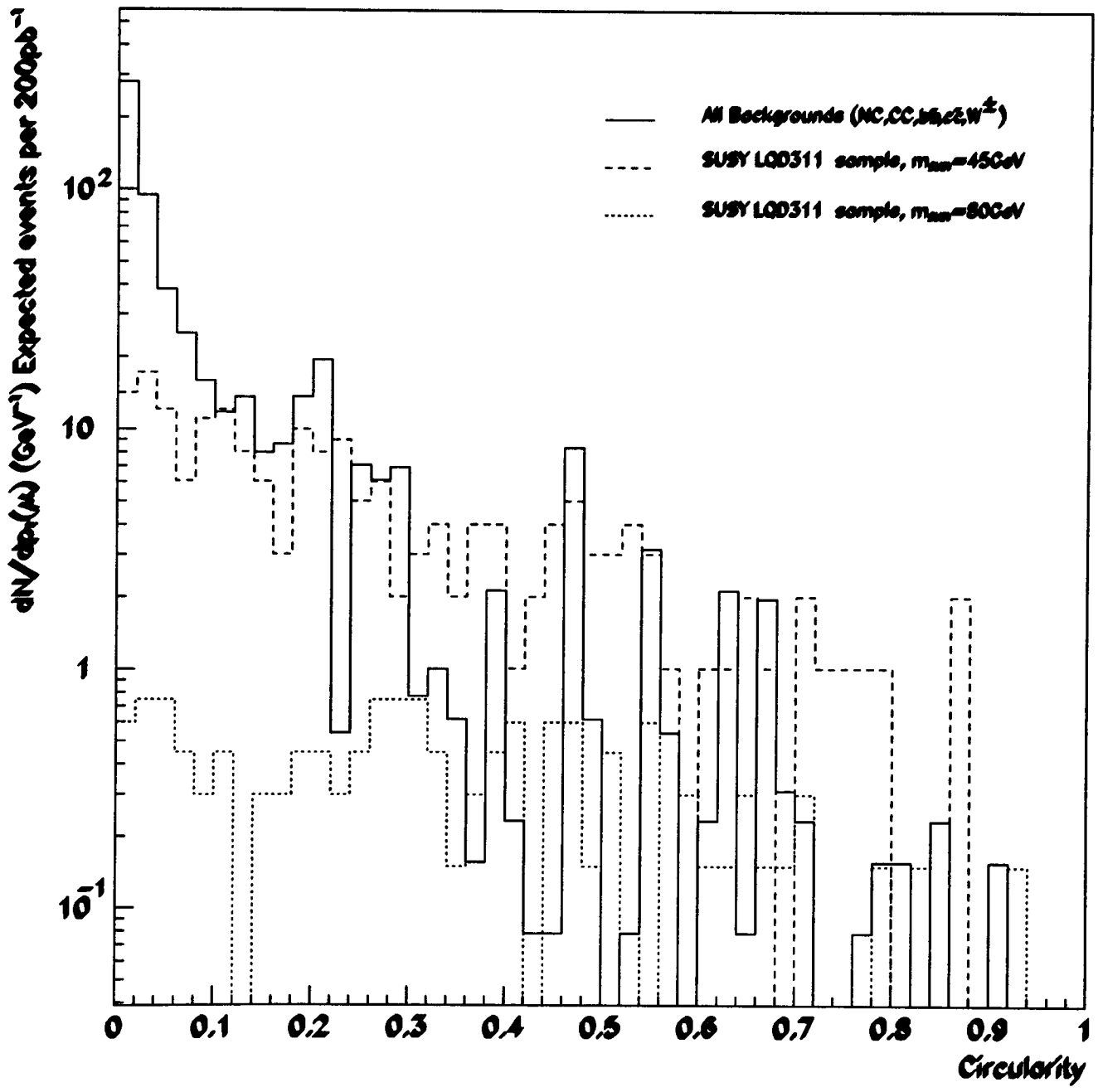


Figure 6.10: Circularity distributions of the SUSY events and backgrounds after the positron/muon cut. The distribution labelled 'All backgrounds' combines all the background samples (NC, CC, $b\bar{b}$, $c\bar{c}$, W) and normalises them with respect to their corresponding cross-sections.

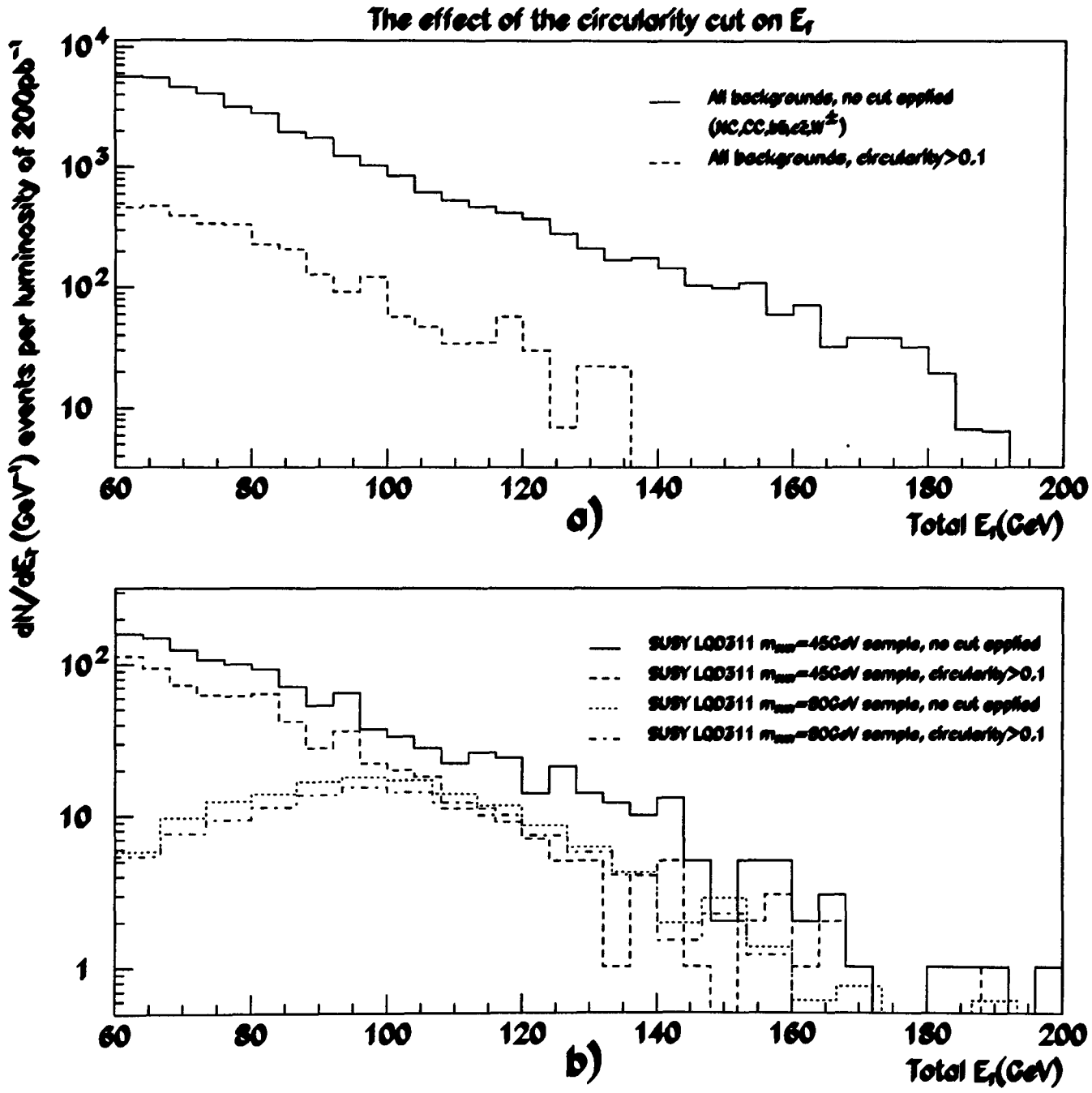


Figure 6.11: The effect of a circularity cut on the E_T distribution of a) the background processes, and b) the SUSY $L_\tau Q\bar{D}$ samples. The distribution labelled 'All backgrounds' combines all the background samples (NC, CC, $b\bar{b}$, $c\bar{c}$, W) and normalises them with respect to their corresponding cross-sections.

with E_T >80GeV are all $b\bar{b}$ events, which generally have a much harder E_T spectrum. We have chosen our final cut at E_T >90GeV. This includes (0.53 $\pm$ 0.31) $b\bar{b}$ events. Figure 6.12b shows for comparison the E_T distributions of the three SUSY samples $L_eQ\bar{D}$, $L_\mu Q\bar{D}$ and $L_\tau Q\bar{D}$ at high mass ranges.

6.6.4 Discovery Reaches

We now apply the four cuts discussed above to the rest of our MC samples. The only difference in the cut sequence applied to the $L_eQ\bar{D}$, the $L_\mu Q\bar{D}$ and the $L_\tau Q\bar{D}$ samples is the positron/muon cut. We demand

- One or more found positrons for the $L_eQ\bar{D}$ sample.
- One or more found muons for the $L_\mu Q\bar{D}$ sample.
- One or more found positrons or muons for the $L_\tau Q\bar{D}$ sample.

Tables 6.3, 6.4 and 6.5 show the effects of the cuts on the SUSY samples and the backgrounds. Figure 6.13a plots the efficiencies of the samples after cuts. Normalising the cross-sections of table 6.1 to an integrated luminosity of L=200pb^{-1}, and folding in the efficiencies of Figure 6.13a we obtain Figure 6.13b. We then use Poisson statistics to investigate the potential discovery limit of the $L_eQ\bar{D}$ operator at the 90% confidence level, and require 2.3 signal events and assume zero background. Above condition holds over the SUSY mass range 90GeV< $(m_{\tilde{l}} + m_{\tilde{q}})$ <205GeV for the $L_eQ\bar{D}$ operator and the chosen set of gaugino parameters (M'=40GeV, tan(β)=1 and μ=-200GeV). The lower mass point at $(m_{\tilde{l}} + m_{\tilde{q}})$ =90GeV corresponds to the current model-independent LEP bounds on sparticle masses > 45GeV. Using the same argument for the $L_\mu Q\bar{D}$ and the $L_\tau Q\bar{D}$ sample, but requiring 3.1 signal events and assuming 0.53 background events we can determine the approximate discovery reaches for the $L_\mu Q\bar{D}$ and the $L_\tau Q\bar{D}$ operators. Note that the gaugino parameters were chosen in a region where the LSP predominantly decays to charged leptons.

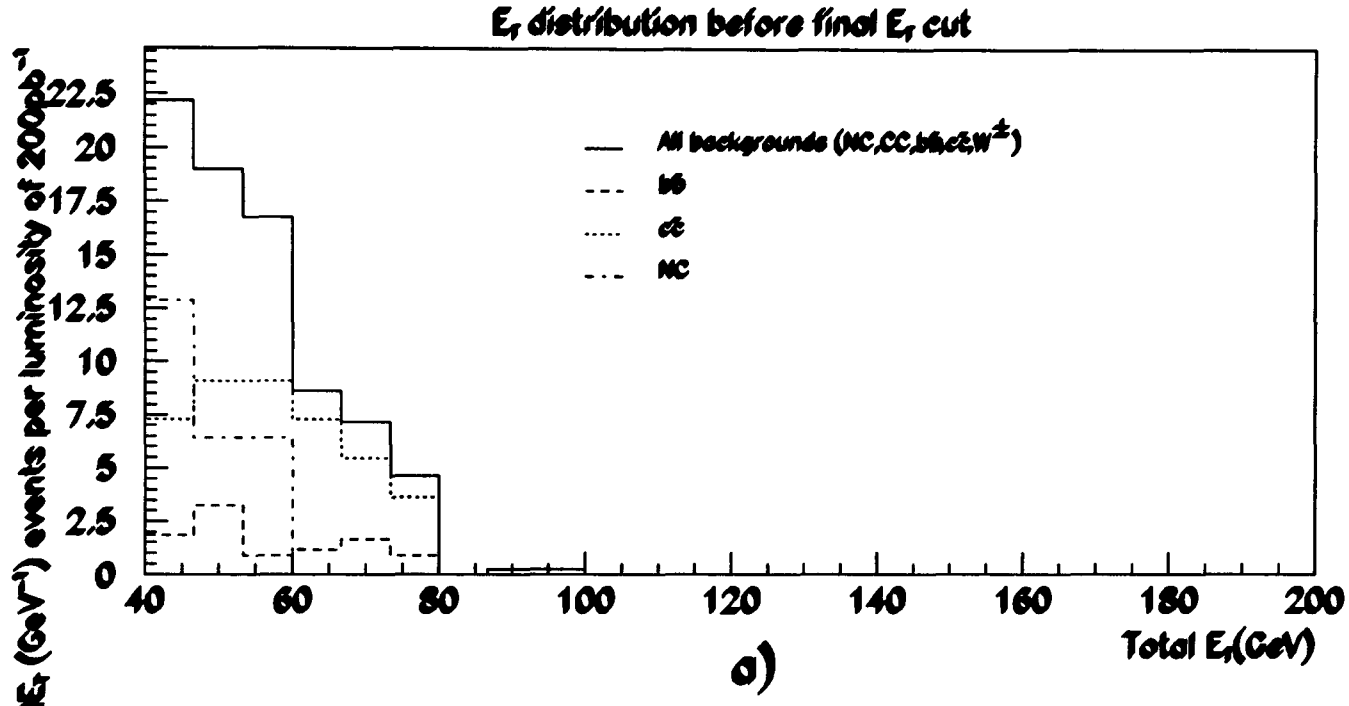


Figure 6.12: The E_T distributions of backgrounds and SUSY samples after the cut-sequence: '(e^+ found or μ found).and.(30GeV<E-p_z <60GeV).and.(circularity>0.1)'. An E_T cut at 90GeV will remove most of the background while keeping a high percentage of the SUSY sample. The distribution labelled 'All backgrounds' combines all the background samples (NC, CC, $b\bar{b}$, $c\bar{c}$, W) and normalises them with respect to their corresponding cross-sections.

cut	$b\bar{b}$	$c\bar{c}$	W	NC	CC
none	3395	4105	400	7149	3541
e^+ found	22	24	118	55	8
30GeV$< E - p_z <$ 60GeV	20	21	27	54	2
circularity > 0.1	4	7	9	5	0
$E_T >$ 90GeV	0	0	0	0	0
Exp. no. of evts	0	0	0	0	0

cut	$L_eQ\bar{D}_{45}$	$L_eQ\bar{D}_{65}$	$L_eQ\bar{D}_{80}$	$L_eQ\bar{D}_{95}$	$L_eQ\bar{D}_{105}$
none	940	500	400	100	100
e^+ found	423	230	177	38	44
30GeV$< E - p_z <$ 60GeV	385	201	151	35	36
circularity > 0.1	255	174	136	33	33
$E_T >$ 90GeV	67	124	124	32	32
Exp. no. of evts	95 ± 10	84.5 ± 6.5	31.0 ± 2.3	7.0 ± 1.0	1.9 ± 0.3

Table 6.3: The cut-sequence applied to the MC samples. Here '$L_eQ\bar{D}_{45}$' refers to the SUSY sample with M_{SUSY}=45GeV, and LSP decays via the $L_eQ\bar{D}$ operator. The last column, 'Exp. no. of evts', shows the expected number of events after cuts for a luminosity of 200pb^{-1}.

cut	$b\bar{b}$	$c\bar{c}$	W	NC	CC
none	3395	4105	400	7149	3541
μ found	126	71	65	29	11
30GeV$< E - p_z <$ 60GeV	114	59	24	20	3
circularity $>$ 0.1	42	18	3	2	0
$E_T >$ 90GeV	2	0	0	0	0
Exp. no. of evts	0.53 ± 0.31	0	0	0	0

cut	$L_\mu Q\bar{D}_{45}$	$L_\mu Q\bar{D}_{65}$	$L_\mu Q\bar{D}_{80}$	$L_\mu Q\bar{D}_{95}$	$L_\mu Q\bar{D}_{100}$
none	1000	600	400	400	200
μ found	395	191	114	119	50
30GeV$< E - p_z <$ 60GeV	330	157	92	102	44
circularity $>$ 0.1	177	131	78	88	31
$E_T >$ 90GeV	27	71	58	79	31
Exp. no. of evts	54 ± 10	60.7 ± 6.7	21.8 ± 2.7	6.3 ± 0.6	2.8 ± 0.5

Table 6.4: The cut-sequence applied to the MC samples. Here '$L_\mu Q\bar{D}_{45}$' refers to the SUSY sample with M_{SUSY}=45GeV, and LSP decays via the $L_\mu Q\bar{D}$ operator. The last column, 'Exp. no. of evts', shows the expected number of events after cuts for a luminosity of 200pb^{-1}.

cut	$b\bar{b}$	$c\bar{c}$	W	NC	CC
none	3395	4105	400	7149	3541
e^+ or μ found	148	95	183	84	19
30GeV$< E - p_z <$ 60GeV	134	80	51	74	5
circularity > 0.1	46	25	12	7	0
$E_T >$ 90GeV	2	0	0	0	0
Exp. no. of evts	0.53 ± 0.31	0	0	0	0

cut	$L_\tau Q\bar{D}_{45}$	$L_\tau Q\bar{D}_{65}$	$L_\tau Q\bar{D}_{80}$	$L_\tau Q\bar{D}_{85}$	$L_\tau Q\bar{D}_{90}$
none	2000	1000	1000	400	200
μ found	185	74	92	33	14
30GeV$< E - p_z <$ 60GeV	166	53	71	27	11
circularity > 0.1	105	40	58	21	8
$E_T >$ 90GeV	17	26	44	17	8
Exp. no. of evts	17.2 ± 4.2	13.4 ± 2.6	6.6 ± 0.9	3.9 ± 0.9	2.2 ± 0.8

Table 6.5: The cut-sequence applied to the MC samples. Here '$L_\tau Q\bar{D}_{45}$' refers to the SUSY sample with M_{SUSY}=45GeV, and LSP decays via the $L_\tau Q\bar{D}$ operator. The last column, 'Exp. no. of evts', shows the expected number of events after cuts for a luminosity of 200pb^{-1}.

$R\!\!\!/_p$ Operator	M_{SUSY} (GeV)	SUSY M' (GeV)	parameters $\tan(\beta)$	μ (GeV)	Branch (%)	$\sigma_{TOT} \times BF$ (pb)
$L_eQ\bar{D}$	45	55	4	+200	0.16	1.67
$L_eQ\bar{D}$	65	55	4	+200	0.16	0.43
$L_eQ\bar{D}$	80	55	4	+200	0.16	0.12
$L_eQ\bar{D}$	95	55	4	+200	0.16	0.03
$L_eQ\bar{D}$	105	55	4	+200	0.16	0.01
$L_\mu Q\bar{D}$	45	55	4	+200	0.16	3.12
$L_\mu Q\bar{D}$	65	55	4	+200	0.16	0.81
$L_\mu Q\bar{D}$	80	55	4	+200	0.16	0.24
$L_\mu Q\bar{D}$	95	55	4	+200	0.16	0.05
$L_\mu Q\bar{D}$	100	55	4	+200	0.16	0.03
$L_\tau Q\bar{D}$	45	55	4	+200	0.16	3.12
$L_\tau Q\bar{D}$	65	55	4	+200	0.16	0.81
$L_\tau Q\bar{D}$	80	55	4	+200	0.16	0.24
$L_\tau Q\bar{D}$	85	55	4	+200	0.16	0.15
$L_\tau Q\bar{D}$	90	55	4	+200	0.16	0.09

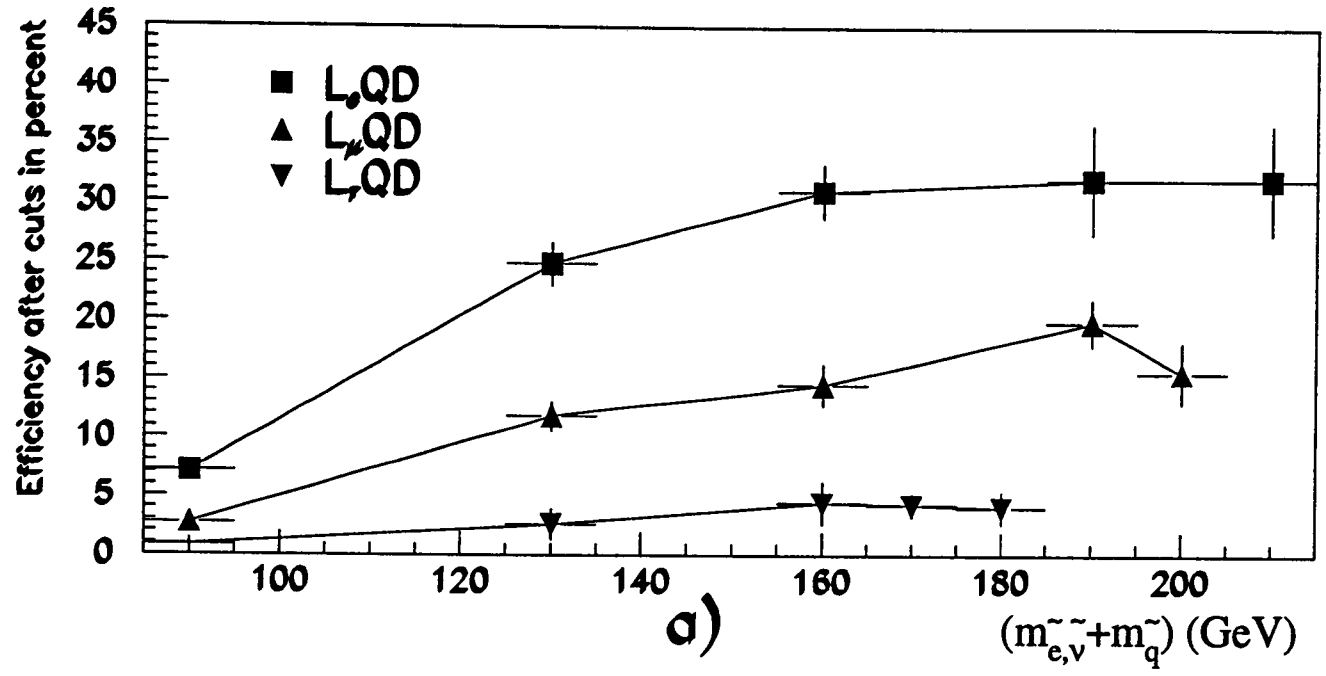
Table 6.6: Generated R_p violating SUSY samples in a region of gaugino parameter space where the LSP predominantly decays to neutrinos. 'M_{SUSY}' is the mass of the scalars; 'M', $\tan(\beta)$, μ' are the gaugino mixing parameters; 'Branch' is the branching ratio of the LSP to a charged lepton $BF(\tilde{\chi}_i^0 \rightarrow l^\pm + 2jets)$; '$\sigma_{TOT} \times BF$' is the total cross-section.

We have also investigated a region in parameter space where the LSP predominantly decays to neutrinos. Table 6.6 lists the SUSY cross-sections and LSP branching ratios in this region. Because the parameters M'=55GeV, $\tan(\beta)$=4 and μ=+200GeV produce a LSP with M_{LSP}=44GeV (the same LSP mass as the generated MC samples of table 6.1), we can use the efficiencies of table 6.13a to obtain the expected number of events after cuts of Figure 6.13c.

We now summarise the maximum discovery reaches for the three operators $L_eQ\bar{D}$, $L_\mu Q\bar{D}$ and $L_\tau Q\bar{D}$ in the two regions of gaugino parameter space:

$$m(\tilde{e},\tilde{\nu}) + m(\tilde{q}) \lesssim 205GeV \text{ for dominant } L_eQ\bar{D} \text{ LSP decays to } l^\pm \quad (6.16)$$

$$m(\tilde{e},\tilde{\nu}) + m(\tilde{q}) \lesssim 185GeV \text{ for dominant } L_eQ\bar{D} \text{ LSP decays to } \nu_{l^\pm} \quad (6.17)$$



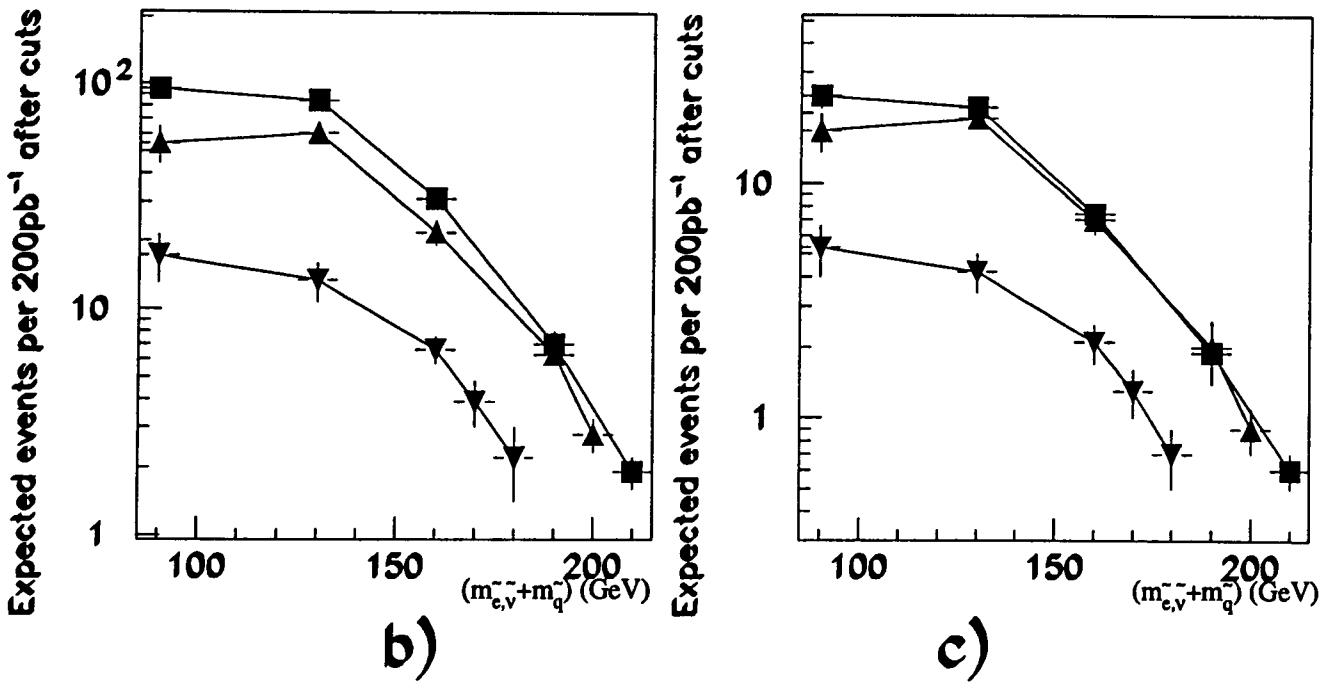


Figure 6.13: Figure a): The detection efficiencies of the $L_eQ\bar{D}$, $L_\mu Q\bar{D}$ and $L_\tau Q\bar{D}$ samples as a function of the SUSY masses $(m_{\tilde{l}} + m_{\tilde{q}})$ after cuts. Figure b) shows the number of expected signal events for an integrated luminosity of 200pb^{-1} in a region of gaugino mixing (M'=40GeV, tan(β)=1 and μ=-200GeV) where the LSP predominantly decays to charged leptons. Figure c) shows the number of expected signal events for an integrated luminosity of 200pb^{-1} in a region of gaugino mixing (M'=55GeV, tan(β)=4 and μ=+200GeV) where the LSP predominantly decays to neutrinos. The error bars in the plots reflect the statistical error due to the limited size of the MC samples.

$$m(\tilde{e},\tilde{\nu}) + m(\tilde{q}) \lesssim 195GeV \text{ for dominant } L_\mu Q\bar{D} \text{ LSP decays to } l^\pm \quad (6.18)$$

$$m(\tilde{e},\tilde{\nu}) + m(\tilde{q}) \lesssim 175GeV \text{ for dominant } L_\mu Q\bar{D} \text{ LSP decays to } \nu_{l^\pm} \quad (6.19)$$

$$m(\tilde{e},\tilde{\nu}) + m(\tilde{q}) \lesssim 170GeV \text{ for dominant } L_\tau Q\bar{D} \text{ LSP decays to } l^\pm \quad (6.20)$$

$$m(\tilde{e},\tilde{\nu}) + m(\tilde{q}) \lesssim 140GeV \text{ for dominant } L_\tau Q\bar{D} \text{ LSP decays to } \nu_{l^\pm} \quad (6.21)$$

Note that the potential limits (6.16)-(6.21) only hold for the assumptions we have made in section 6.5.1, and only for the particular choice of the gaugino mixing parameters, namely (M'=40GeV, tan(β)=1 and μ=-200GeV) for dominant LSP decays to $l^\pm$, and (M'=55GeV, tan(β)=4 and μ=+200GeV) for dominant LSP decays to $\nu_{l^\pm}$. We have also investigated the effect of smaller LSP masses on the detection efficiencies of the samples, but found that they were generally small: for a LSP mass of M_{LSP}=20GeV, the correction to the efficiencies of Figure 6.13a (at M_{LSP}=44GeV) were found to be $\lesssim$0.8 . Furthermore, because cross-section variations as a function of M', tan(β) and μ are relatively small (see section 6.3) and changes in the LSP branching fractions to charged leptons are fairly constant in a given characteristic region of the LSP (see section 6.4) we conclude that the discovery reaches of (6.16)-(6.21) are approximately valid over a wide range of gaugino mixing parameter space within a given characteristic region of the LSP.

6.7 Summary of Results

We have investigated decays of the LSP as a general neutralino via the $LQ\bar{D}$ operator. We have found that the results depend on the mixing parameters of the neutralinos. Three distinct regions in the parameter space characterise the LSP decay: (1) A region in which the photino component of the LSP is dominant. In this region branching fractions are high, typically $\sim$ 70%. (2) A region in which the zino component of the LSP is dominant. In this region branching fractions are low, and typically $\sim$ 15%. (3) A dominant Higgsino/Zino region at small LSP masses. In this region the decay

rate of the LSP can become so small that the LSP only decays within the detector for anomalously large couplings λ'.

Based on the above results, we have investigated the discovery reach of HERA on the $LQ\bar{D}$ operator using a full MC simulation of $\not{R}_p$SUSY events. We have considered the regions (1) and (2) in gaugino parameter space, and have found that $\not{R}_p$SUSY can be discovered at HERA up to a combined SUSY mass $m(\tilde{e},\tilde{\nu}) + m(\tilde{q})$ of

- 170GeV, 195GeV, 205GeV for $L_\tau Q\bar{D}$, $L_e Q\bar{D}$, $L_\mu Q\bar{D}$ and mixing scenario (1).
- 140GeV,175GeV,185GeV for $L_\tau Q\bar{D}$, $L_e Q\bar{D}$, $L_\mu Q\bar{D}$ and mixing scenario (2).

The potential limits will only hold for the stated LSP mixing scenario, and for the set of assumptions we have made on the SUSY model, namely that (a) the LSP is a neutralino, that (b) only one of the 27 operators $L_i Q_j \bar{D}_k$ is dominant, that (c) sleptons and squarks are degenerate in mass, and that (d) the branching fraction of sfermion cascade decays to the LSP is 100%.

These discovery reaches are well above current experimental bounds on $\not{R}_p$SUSY. The strongest current bounds on the $L_e Q\bar{D}$ and $L_\mu Q\bar{D}$ operators are [63]

$$m_{\tilde{q}} > 100 GeV. \tag{6.22}$$

This analysis assumed dilepton signals coming from the $\not{R}_p$decay of two LSPs. Our analysis does not rely on dilepton signals. As a consequence, the limits HERA will be able to set on the $LQ\bar{D}$ operator will be less dependent on the assumption of a dominant one operator scenario, and hence somewhat stronger.

6.8 Conclusions

HERA has been shown to be an ideal place to investigate $\not{R}_p$SUSY. The $LQ\bar{D}$ operator is particularly suitable to HERA, with discovery reaches on the combined SUSY scalar masses $m(\tilde{e},\tilde{\nu}) + m(\tilde{q})$ up to 205GeV. Furthermore it has been shown that one can

investigate tau-signals for supersymmetry at HERA, on which no direct experimental bounds to date exist.

Appendix A

Glossary

BAC : Backing Calorimeter.

BCN : The Bunch Crossing Number ranges from 0 to 219, and specifies the e-p bunch of the interaction.

BMUON : Barrel Muon detector.

BF : Branching Fraction.

CAL : Uranium scintillator Calorimeter.

CC - Charged Current events : Charged Current interactions are Deep Inelastic Scattering events with W exchange in the t-channel.

Cellpair : A cellpair is a pair of adjacent CTD drift cells.

Chargino - $\chi^{\pm}$: The supersymmetric partner of a SM charged gauge boson.

CMS : Centre of Mass System.

Cone algorithm : Jet finding algorithm. See for example [81].

CP - Cell Processor : The CTD First Level Trigger Cell Processor is a hardware module performing the task of segment finding.

CTD : Central Tracking Detector.

CTD-FLT - CTD First Level Trigger : A pipelined hardware trackfinding trigger providing information to the GFLT based on the measured event vertex and number of *pointing* tracks measured by the CTD z-by-timing readout.

CTDFLT test software : A program to perform a number of checks on the various

hardware components of the CTD-FLT.

DAQ : Data Aquisiton.

DESY laboratory : Deutsches Elektron Synchrotron laboratory.

DIS : Deep Inelastic Scattering.

DMA : Direct Memory Access.

DPM - Dual Port Memory : Are widely used as pipeline memories in the ZEUS trigger systems. The two ports of the DPMs allow concurrent access to the memory via two separate busses.

DSP : Digital Signal Processors, mounted on the CTD-FADC readout cards.

Durham algorithm : Jet finding algorithm. See for example [80].

ECL : Emitter Coupled Logic.

EVB - EVent Builder : Distributes the GSLT decision to all components and, in the case of a GSLT accept, collects component data and builds a complete event record. The EVB record gets sent on to the TLT.

FADC - Flash Analogue to Digital Converter readout : 104MHz Flash Analogue to Digital Converters are used in the CTD $r-\phi$ system to digitise the $r-\phi$ chamber pulses.

FC : Fast Clear. A component of the ZEUS First Level Trigger.

FDA : Functional Discriminant Analysis.

FDM - Final Decision Module : Hardware module of the RBOX. Performs the task of final event classification.

FLT - First Level Trigger : Component based hardware trigger, providing trigger information to the GFLT. Part of the ZEUS three level trigger system.

FLT number : First Level Trigger number, assigned to an event after a positive FLT trigger decision.

FMUON : Forward Muon detector.

FTD : Forward Tracking Detector.

GAL : Gate Array Logic.

Gaugino : The supersymmetric partner of a SM gauge boson.

GFLT - Global First Level Trigger : The first level of the three level ZEUS trigger system. Decisions are made based on the information provided by each of the local component FLTs.

Gluino : The supersymmetric partner of a SM gluon.

GSLT - Global Second Trigger : The second level of the three level ZEUS trigger system. Decisions are made based on the information provided by each of the local component SLTs.

GUT : Grand Unified Theory.

HCM - Hit Count Module : Hardware module of the RBOX. Performs the task of counting *potential* and *pointing* tracks.

HERA : Hadron Electron Ring Accelerator.

HERWIG : MC event generator. See for example [89].

Higgsino : The supersymmetric partner of the SM Higgs particle.

JADE algorithm : Jet finding algorithm. See for example [77].

LPS : Leading Proton Spectrometer.

LUMI : Luminosity Monitor.

LSP : The Lightest Supersymmetric Particle. Often assumed to be the lightest neutralino.

LTC - Local Timing Controller : Provides timing control to drive the front end CTD electronics. A single LTC is located in each of the z and $r-\phi$ electronics crates.

LUT : Look-up table.

MC : Monte Carlo. See Monaco.

MSSM - The Minimal Supersymmetric Standard Model : The minimal supersymmetric extension to the SM.

MTC - Master Timing Controller : Receives and fans out the GFLTB clock

and trigger information to each LTC. An $r-\phi$ MTC drives the $r-\phi$ LTCs and a separate z MTC drives the z LTCs.

NC - Neutral Current events : Neutral Current interactions are Deep Inelastic Scattering events with photon/Z exchange in the t-channel.

Neutralino - χ^0 : The supersymmetric partner of a SM neutral gauge boson.

Occam : Programming language designed specifically for the transputer facilitating both simulated and true parallel processing.

Photino - $\tilde{\gamma}$: The supersymmetric partner of a photon.

Pointing (r-z) Tracks : Tracks which originated from the e-p interaction vertex.

Potential (r-ϕ) Tracks : Valid tracks in $r-\phi$, which did no necessarily originate from the e-p interaction vertex.

PROM : Programmable Read Only Memory.

QCD : Quantum Chromo Dynamics.

QPM : Quark Parton Model.

RAL - Rutherford Appleton Laboratory : National Laboratory situated in the vicinity of Didcot.

RBOX - Region First Level Trigger Box : The RBOX is the final stage in the CTD-FLT. It consists of Hit Count Modules and a Final Decision Module.

RMUON : Rear Muon detector.

ROC - ReadOut Controller : Each z crate and $r-\phi$ crate contains a ROC containing transputers controlling the electronics readout and performing CTD SLT processing.

ROT - ReadOut Transputer : The ROT is mounted on the ROC.

R-parity (R_p) : A multiplicative discrete quantum number in supersymmetric models.

RTD : Rear Tracking Detector.

Sfermion : The supersymmetric partners of the SM fermions.

SL1, etc : CTD Superlayer 1, etc.

Slepton : The supersymmetric partners of the SM leptons.

SLT - Second Level Trigger : Transputer and component based software trigger, providing trigger information to the GSLT. Part of the ZEUS three level trigger system.

SM : Standard Model.

Sneutrino : The supersymmetric partner of a SM neutrino.

Sector Processor(SP) : Attempts to extrapolate segments found by the superlayer 1 CTD FLT cell processors out to superlayer 3 and superlayer 5. Classes found tracks into *any* tracks and *pointing* tracks.

Sparticle : The supersymmetric partner of a SM particle.

Squark : The supersymmetric partner of a SM quark.

SRAM : Static Random Access Memory.

SUSANA : MC event generator for $\not{R}_p$SUSY. See for example [83].

SUSY - Supersymmetry : A theory relating bosons with fermions and vice versa.

TAC : Time-to-Amplitude Converter.

TLT - Third Level Trigger : The third level of the three level ZEUS trigger system. The TLT has access to the complete event data from all components.

TRD : Transition Radiation Detector.

TTL : Transistor-Transistor Logic.

VETO : Veto Wall.

VXD : Vertex Detector.

ZEUS : Zero Experience with Uranium Scintillators. One of the three experiments at HERA.

Zino : The supersymmetric partner of the SM Z.

Appendix B

MSSM 1.0: A MC Generator for SUSY at HERA

This appendix is based on reference [87].

B.1 Abstract

We present a Monte Carlo generator for the minimal supersymmetric extension of the SM, the Minimal Supersymmetric Standard Model (MSSM). The generator has been integrated into ZDIS, the interface to the ZEUS offline environment. The two dominant SUSY production mechanisms at HERA, namely Neutralino Current (NC) selectron and squark production, and Chargino Current (CC) sneutrino and squark production (both at tree level) have been implemented using full gaugino mixing. The generator allows one to choose either an R-parity conserving model, in which the lightest supersymmetric particle (LSP) is stable; or alternatively one can choose an R-parity violating model, in which the LSP can decay via $\not{R}_p$-Yukawa couplings.

B.2 Introduction and Overview

The Minimal Supersymmetric SM (MSSM) has been extensively treated in the literature, and we refer to [96] for general reviews of the subject. Detailed references for cross-sections and gaugino mixings are quoted in the appropriate sections below.

The MSSM conserves R-parity (R_p), a discrete multiplicative symmetry. As a consequence, the lightest supersymmetric particle (LSP) is stable. Recently there has been much interest in the field of R-parity violating ($\not{R}_p$) models, in which the LSP can decay. The reader is referred to [57] for theoretical, [59] for cosmological and [61, 60] for phenomenological work on $\not{R}_p$ SUSY.

This appendix intends to describe the assumptions we have made on the SUSY models, and to explain the usage of the program. We do not give an introduction to the subject of Supersymmetry itself. If the reader is not familiar with SUSY and its complex parameter space, we strongly recommend that he or she consults above literature before running the program.

Section B.3 lists the implemented SUSY production processes included in the MSSM generator, and the subsequent cascade decays of the sparticles to the lightest supersymmetric particle (LSP). Section B.4 comments on the gaugino mixing, while section B.5 describes the R-parity violating decays of the LSP. Section B.6 summarises the assumptions the generator makes on the SUSY model, and section B.7 gives instructions on how to run the program. Section B.8 describes future plans for the generator, and Section B.9 lists the functionality of the various subroutines.

B.3 Physics Processes

The dominant R-parity conserving SUSY production mechanisms at HERA are the Neutralino Current (NC) process and the Chargino Current Process of Figure 4.2. The produced selectrons, sneutrinos and squarks subsequently cascade-decay into lighter SUSY particles, until eventually only one type of SUSY particle remains, the LSP. We assume throughout that the LSP is the lightest neutralino. Equations (4.15-4.19) show examples of such cascade-decays. We make the simplifying assumption that decays to neutralinos ($\tilde{\chi}_i^0$) and gluinos($\tilde{g}$) will dominate over branchings to charginos ($\tilde{\chi}_i^{\pm}$), and hence only cascade-decays such as 4.14, 4.16 or 4.18 are included in the

generator.

Neutralinos and gluinos are assumed to decay simply to the LSP and two jets. Of course, more involved cascade decays are possible and will be included at a later date. In addition the further simplifying assumption is made that, viewed in the rest frame of the heavier parent particle, the daughter LSP is also at rest with the two jets back to back. In this way the decays are kinematically consistent without requiring a full treatment involving the generation of detailed angular distributions.

Cross-section formulae are taken from [47] for the NC process, and from [51] for the CC process. Both calculations allow for polarisation of the initial electron.

B.4 Gaugino Mixing

For the supersymmetric partners of the electroweak bosons, mixing will occur between the weak interaction eigenstates (see table 4.1). For example the physical mass eigenstate χ_0^0 (the lightest neutralino) will in general be an admixture of $\tilde{\gamma}$, $\tilde{Z}^0$, $\tilde{H}_1^0$ and $\tilde{H}_2^0$. The amount of mixing is determined by the mass parameters M, M', μ and the ratio of the vacuum expectation values of the two neutral Higgs, $\tan(\beta)$. The same parameters also determine the chargino mixing. Detailed expressions for the neutralino and chargino diagonalisation matrices and mass eigenstates can be found in [47] and [48] respectively.

Given the parameters M, M', μ and $\tan(\beta)$, the generator calculates the neutralino and chargino mass eigenstates. The program also allows the user to optionally override the full gaugino mixing, and instead to make the pure photino weak interaction eigenstate the only neutralino, and hence the LSP. The photino scenario simplifies the model considerably (the four parameters M, M', μ and $\tan(\beta)$ are replaced by a single parameter, $m_{\tilde{\gamma}}$), and is provided for comparison of existing limits on $\not{R}_p$SUSY with future limits HERA might provide. Note that the option is not of much use for R-parity conserving models, as the exploration of the full SUSY parameter space

by other experiments at LEP and the Tevatron is already well advanced and beyond such a simple model. Furthermore this option can only be used if the user switches off the CC production channel, because this process does require the full gaugino parameters to calculate chargino mixings.

B.5 R-parity Violating Decays

Given the particle content of the SM, the most general gauge and supersymmetry invariant superpotential is given by [97]

$$W = W_{MSSM} + W_{\not R_p}, \tag{B.1}$$

where W_{MSSM} is the superpotential of the MSSM, and $W_{\not R_p}$ consists of the $\not R_p$ Yukawa couplings

$$W_{\not R_p} = [\lambda_{ijk} L_i L_j \bar{E}_k + \lambda'_{ijk} L_i Q_j \bar{D}_k + \lambda''_{ijk} \bar{U}_i \bar{D}_j \bar{D}_k]_F. \tag{B.2}$$

L and $\bar{E}$ are the left-handed lepton doublet and antilepton singlet, and Q and $\bar{U}, \bar{D}$ are the (left-handed) quark doublet and the u-type and d-type antiquark singlet chiral superfields respectively. $\lambda, \lambda', \lambda''$ are dimensionless Yukawa couplings and i, j, k are generation indices. Any of the three operators in equation (B.2) will enable the LSP to decay, and Figure 4.3a shows the generic diagram for neutralino decay.[1] Figures 4.3b-d show examples of specific decays via the $L_1 L_2 \bar{E}_3$ (4.3b), $L_1 Q_1 \bar{D}_1$ (4.3c) and $\bar{U}_1 \bar{D}_1 \bar{D}_1$ (4.3d) operators. The $\not R_p$ vertices are marked. Note that the intermediate sparticles superscribed by asterisks are virtual. The LSP decay is determined by the coupling strength λ, as well as the MSSM parameters. If λ is too small ($\leq 10^{-6}$ for typical MSSM parameter values), the LSP will decay outside the detector, and will again produce the missing p_T signature of the R_p conserving scheme.

[1] Throughout we assume that the LSP is the lightest neutralino.

We make the non-trivial assumption that only one of the three operators in equation (B.2) is non-zero, and only one particular coupling λ_{ijk} is non-vanishing. The user can choose the operator, coupling indices and coupling strength. The MSSM generator uses a full calculation of the LSP decay, and explicit formulae are given in [98]. [2]

B.6 Assumptions on the SUSY Model

Below we explicitly list all the assumption and simplifications we have made in our SUSY model:

- We work in the minimal supersymmetric extension of the SM, the MSSM, but consider both R-parity conserving and R-parity breaking scenarios.
- The LSP is assumed to be the lightest neutralino.
- In case of the R-parity violating scenario, we assume that only one $\not{R}_p$ Yukawa coupling is non-vanishing.
- We simplify our cascade-decays by assuming that sparticles will dominantly decay to neutralinos and gluinos. We do not include sparticle cascades to charginos. This assumption will hold for a wide range of the gaugino parameter space. However if the lightest chargino mass becomes roughly equal to the mass of the LSP, sizable contributions from chargino cascades will enter, and produce additional leptons.
- We do *not* include a full treatment of the angular distribution of the decay products of neutralino and gluino decays. Instead $\tilde{\chi}_i^0$ and $\tilde{g}$ decays are simulated using the simplifying assumption that, viewed in the rest frame of the heavier parent particle, the daughter LSP is also at rest with the two jets back to back.

[2] Only the $L_iQ_j\bar{D}_k$ operator is supported in version 1.0 of the MSSM generator, but we plan to include the $L_iL_j\bar{E}_k$ and $L_iQ_j\bar{D}_k$ operators in a future version.

- The NC production cross-section of [47] only uses photino and zino contributions to the neutralino exchange, and neglects the higgsino contributions.

- The LSP decay calculation only uses photino and zino contributions. Higgsino contributions are again neglected.

B.7 The MSSM Generator - Program Usage and Availability

B.7.1 Availability

The generator is supported on both the VAX and on DEC stations. The source code of the program can be found in the Zeus offline area on VXDESY, namely

ZRSOURCE:[PAM]MSSM10.CAR

and example scripts to build and run the program in the ZEUS environment can be found in

ZREXAM:[GENERATOR]ZDIS_MSSM_EXE.COM

ZREXAM:[GENERATOR]ZDIS_MSSM_RUN.COM

An example cards file (which specifies the program input parameters) is kept in

ZREXAM:[GENERATOR]ZDIS_MSSM.CARDS.

The /userb/morawitz/susy/mssm area contains:

/userb/morawitz/susy/mssm/mssm.cmz

/userb/morawitz/susy/mssm/zdis.cmz

/userb/morawitz/susy/mssm/zdis_mssm_link

/userb/morawitz/susy/mssm/zdis_mssm_run

/userb/morawitz/susy/mssm/zdis_mssm.cards

Compilation of the program is done in CMZ via KUMACS, namely

//MSSM/$KUMACS/MSSMEXE to build the libmssm.a object library, and

//ZDIS/$KUMACS/MSSMEXE to build the zdis_mssm executable.

The Program can also be run outside the ZEUS environment as a stand-alone application. An example program script can be found in the patch ANAL, and //MSSM/$KUMACS/ANALEXE will build this example, which loops over the SUSY parameter space and calculates cross-sections.

B.7.2 Program Input, The Cards File

Below we list the example the input cards file

ZREXAM:[GENERATOR]ZDIS_MSSM.CARDS :

```
*
* -Total number of events to process" Default = unlimitted
ZRLIMIT-NEVT   20
* -Time limit"                    Default = 20 sec
ZRLIMIT-TLFT 20.
*
* .. Choose the generator you want - allowed options are MSSM
*
ZDIS-GEN       MSSM
*
ZDIS-INSTITUT   Oxford
*
* Specify SUSY production processes:
MSSM-NCBRANCH 1
*    Neutralino Current Process
*    switch on/off (1/0) ep-¿selectron+squark
MSSM-CCBRANCH 1
*    Chargino   Current Process
*    switch on/off (1/0) ep-¿sneutrino+squark
* Specify initial beam momenta:
*              Component      Value (GeV)
MSSM-PROTON          1             0.0
MSSM-PROTON          2             0.0
MSSM-PROTON          3           820.0
MSSM-PROTON          4           820.0
*
MSSM-ELECTRON        1             0.0
MSSM-ELECTRON        2             0.0
MSSM-ELECTRON        3           -26.6
MSSM-ELECTRON        4            26.6
*
* - Secify electron beam polarization:
* -  POLAR = [N(R)-N(L)]/[N(R)+N(L)]
MSSM-POLAR          0.0
*
* - Specify kinematic region.
*      Minimum x
MSSM-LOWX                    0.01
*      Maximum x
MSSM-HIGHX                   0.99
*      Minimum Q2
MSSM-LOWQ2                    5.0
*      Maximum Q2
MSSM-HIGHQ2                87248.
*
*
* Specify whether initial state radiation should be included:
* If IRADCOR is 1 then initial state radiation via WWA is included.
* If IRADCOR is 0 then NO initial state radiation.
* NOTE: Radiative Corrections not yet implemented in MSSM V1.0...
MSSM-RADCOR       0
* ZMAX is the maximum allowed fraction of initial electron momentum of after
* emission of a photon; ie ZMAX=Pe(Max)/Pe(beam).  ZMAX acts as an
* infra red cutoff for the initial state radiative corrections.
MSSM-ZMAX         0.999
*
*
* SUSY squark masses
* LEFT-handed  U squark:
MSSM-MASS         1          50.0
*
* RIGHT-handed U squark:
MSSM-MASS         2          50.0
```

```
*
* LEFT-handed  D squark:
MSSM-MASS        3          50.0
*
* RIGHT-handed D squark:
MSSM-MASS        4          50.0
*
* LEFT-handed  C squark:
MSSM-MASS        5          50.0
*
* RIGHT-handed C squark:
MSSM-MASS        6          50.0
*
* LEFT-handed  S squark:
MSSM-MASS        7          50.0
*
* RIGHT-handed S squark:
MSSM-MASS        8          50.0
*
* LEFT-handed  B squark:
MSSM-MASS        9          50.0
*
* RIGHT-handed B squark:
MSSM-MASS        10         50.0
*
* LEFT-handed Selectron:
MSSM-MASS        11         50.0
*
* RIGHT-handed Selectron:
MSSM-MASS        12         50.0
*
* SNeutrino: (left handed, or what did you expect?)
MSSM-MASS        13         50.0
*
*
* Neutralino mass matrix "free" parameters
* The SUSY GUT preferred values are in the ratio:
*     M1:M2:M3 = 5/3G1^2:G2^2:G3^2 = 1:2:7
MSSM-TANB                 0.9
MSSM-MU                  80.0
MSSM-M1                  15.0
MSSM-M2                  30.0
*
* Gluino mass:
MSSM-MGLUINO             140.0
*
*    Number of samples in xsec integration (DIVONNE4 Parameters):
MSSM-SAMPLE              3000
MSSM-MAXNUM               5000
*
*
* PDFLIB parameters:
MSSM-PDFPAR  1  MODE
MSSM-PDFVAL  1  47.
*     for mrds-'
*
MSSM-PDFPAR  2  XMIN
MSSM-PDFVAL  2  0.01
*
MSSM-PDFPAR  3  XMAX
MSSM-PDFVAL  3  0.99
*
MSSM-PDFPAR  4  Q2MIN
MSSM-PDFVAL  4  5.
*
MSSM-PDFPAR  5  Q2MAX
MSSM-PDFVAL  5  87248.
*
* SUSY squark lr mixing angles (radians):
* NB: This is not yet used in the cross section...
*
* U squark:
MSSM-LRMIX       1          0.0
* D squark:
MSSM-LRMIX       2          0.0
* S squark:
MSSM-LRMIX       3          0.0
* C squark:
MSSM-LRMIX       4          0.0
* B squark:
MSSM-LRMIX       5          0.0
* selectron:
MSSM-LRMIX       6          0.0
*
*
* ******************************************************
*      Rparity Violating SUSY
```

```
* ******************************************************
*  Switch on Rparity breaking LSP decays :(0=off,1=on)
MSSM-RPARBRK  0
*
* Operator via which the LSP decays Rparity violating: 1=LLE,2=LQD,3=UUD
MSSM-OPERATOR   2
* Yukawa coupling strength lamda of the Rparity iolating vertex
MSSM-COUPLING   0.03
*  COUPLING L'iQ'jD'k  indeces ijk
MSSM-INDEXI       2
MSSM-INDEXJ       1
MSSM-INDEXK       1
*
*
* LQD decay selection:  l+ l- nul+ nul-
MSSM-LQDCHAN          1100
* and the lepton l' is defined by MSSM-INDEXI: 1=electron,2=muon,3=tau'
* The TOTAL SUSY cros-section is multiplied by the corresponding branching
* ratio.
*
*
* The photino mass. NOTE: For the assumption that the LSP is a pure photino,
* the parameter MSSM-MPHOTINO should be made equal to the mass of the photino.
* In this simplifying scenario the full M,M,mu,tanb gaugino mixing is switched '
* off, and only the NC process is allowed (since the CC process does require full
* gaugino mixing). Keep at 0 for normal running.
MSSM-MPHOTINO          0.0
*
* Switch on/off (1/0) verbose debug info
MSSM-DEBUG             0
*
*     Random number seed
MSSM-SEED              1017539615
*
* ----------
* ZGEN DATA CARDS
* ----------
*    TRGTDATE is the date/time which specifies the Detector status
*          of the MCarlo events. (e.g. controls selection of Geom. etc.)
ZGEN-TRGTDATE      (yyyymmdd) 19921001    (hhmmss) 000001
*
* ----------
* ZEUS I/O
* ----------
ZeusIO-OUFI            output
C
ZeusIO-OOPT      MEDIUM=DISK,DRIVER=FZ,FILFOR=EXCH
C
ZeusIO-ODFL        FMCEvent
C
*
* user cards : # of  event listings wanted
*
USERS-DISLIST    20
*
STOP
```

B.7.3 Program Output Listing

Below we give part of an example run listing produced by the MSSM generator. Note that particles labeled 'neutral10', 'neutral20', 'neutral30', 'neutral40' and 'gluino' in the JETSET listing correspond to the lightest, second lightest etc. neutralino and gluino respectively. The listing shows the χ_1^0 from the squark[3] decay at line 11, and a χ_2^0 from the sneutrino decay at line 6, which subsequently decays to produce a χ_1^0

[3]The listing does not show the sneutrino and squarks directly, nor the exchanged t-channel neutralinos and charginos.

at line 7. The R-parity violating Yukawa coupling λ'_{211} were set non-zero in this run, and hence the LSP at line 7 decays into a μ^+ and 2 jets (line 12-14), and the second LSP at line 11 decays into a μ^+ and 2 jets (line 15-17).

```
 o-------------------------------o
 |      Minimal SUSY Standard Model      |
 |   R-parity conserving and violating   |
 |      Monte Carlo Event Generator      |
 |                                       |
 |       MSSM version 1.0, 18.11.93      |
 |                                       |
 | Grahame Blair, Herbi Dreiner, Peter Morawitz |
 |   Oxford,     ETH Zuerich,    Oxford  |
 |                                       |
 o-------------------------------o
AREA =  0.41 RADCON=   0.03
  Beam momenta in GeV:
  Proton      0.00  0.00  820.00
  Electron    0.00  0.00  -26.60
  CMS energy  295.38
  Polarization  0.00

  Kinematic limits:
  Minimum value of x      =  0.0100
  Maximum value of x      =  0.9900
  Minimum value of Q2     =     5.
  Maximum value of Q2     =  87248.

 MSSM will run with the following parameters:
  LH U-squark mass        =  50.0000 GeV
  RH U-squark mass        =  50.0000 GeV
  LH D-squark mass        =  50.0000 GeV
  RH D-squark mass        =  50.0000 GeV
  LH C-squark mass        =  50.0000 GeV
  RH C-squark mass        =  50.0000 GeV
  LH S-squark mass        =  50.0000 GeV
  RH S-squark mass        =  50.0000 GeV
  LH B-squark mass        =  50.0000 GeV
  RH B-squark mass        =  50.0000 GeV
  LH selectron mass       =  50.0000 GeV
  RH selectron mass       =  50.0000 GeV
  (LH) sneutrino mass     =  50.0000 GeV

 and with the following squark lr mixing angles:
  U-squark lr mixing angle      =  0.0000 radians
  D-squark lr mixing angle      =  0.0000 radians
  C-squark lr mixing angle      =  0.0000 radians
  S-squark lr mixing angle      =  0.0000 radians
  B-squark lr mixing angle      =  0.0000 radians
  selectron lr mixing angle     =  0.0000 radians

 MSSM will run with the following neutralino mass matrix//parameters:
  Mu                  =  80.00 GeV
  Tan(Beta)           =   0.90 GeV
  M1                  =  15.00 GeV
  M2                  =  30.00 GeV

 Diagonlisation produces the following neutralino masses:
  LSP Mass    ("photino") =   18.70 GeV
  Neutralino 1 ("zino")   =   41.60 GeV
  Neutralino 2 ("higgsino")=  80.42 GeV
  Neutralino 3 ("higgsino")=  148.32 GeV

 Diagonlisation produces the following chargino masses:
  Lighter chargino    =  29.12 GeV
  Heavier chargino    =  139.44 GeV


***** PDFLIB Version: 3.10 Released on 920722 at 8.15 in the
CERN Program Library  W5051 *****
***** Library compiled on  930429 at  848 *****


 Branching ratios for LH SELECTRON:
        Branching ratio to gluino      = 0.000
        Branching ratio to LSP         = 0.977
        Branching ratio to Neutralino 1 = 0.023
        Branching ratio to Neutralino 2 = 0.000
        Branching ratio to Neutralino 3 = 0.000


 Branching ratios for RH SELECTRON:
```

Branching ratio to gluino = 0.000
Branching ratio to LSP = 0.966
Branching ratio to Neutralino 1 = 0.034
Branching ratio to Neutralino 2 = 0.000
Branching ratio to Neutralino 3 = 0.000

Branching ratios for LH U-SQUARK:
Branching ratio to gluino = 0.000
Branching ratio to LSP = 0.913
Branching ratio to Neutralino 1 = 0.087
Branching ratio to Neutralino 2 = 0.000
Branching ratio to Neutralino 3 = 0.000

Branching ratios for RH U-SQUARK:
Branching ratio to gluino = 0.000
Branching ratio to LSP = 0.966
Branching ratio to Neutralino 1 = 0.034
Branching ratio to Neutralino 2 = 0.000
Branching ratio to Neutralino 3 = 0.000

Branching ratios for LH D-SQUARK:
Branching ratio to gluino = 0.000
Branching ratio to LSP = 0.653
Branching ratio to Neutralino 1 = 0.347
Branching ratio to Neutralino 2 = 0.000
Branching ratio to Neutralino 3 = 0.000

Branching ratios for RH D-SQUARK:
Branching ratio to gluino = 0.000
Branching ratio to LSP = 0.966
Branching ratio to Neutralino 1 = 0.034
Branching ratio to Neutralino 2 = 0.000
Branching ratio to Neutralino 3 = 0.000

Branching ratios for LH C-SQUARK:
Branching ratio to gluino = 0.000
Branching ratio to LSP = 0.924
Branching ratio to Neutralino 1 = 0.076
Branching ratio to Neutralino 2 = 0.000
Branching ratio to Neutralino 3 = 0.000

Branching ratios for RH C-SQUARK:
Branching ratio to gluino = 0.000
Branching ratio to LSP = 0.970
Branching ratio to Neutralino 1 = 0.030
Branching ratio to Neutralino 2 = 0.000
Branching ratio to Neutralino 3 = 0.000

Branching ratios for LH S-SQUARK:
Branching ratio to gluino = 0.000
Branching ratio to LSP = 0.657
Branching ratio to Neutralino 1 = 0.343
Branching ratio to Neutralino 2 = 0.000
Branching ratio to Neutralino 3 = 0.000

Branching ratios for RH S-SQUARK:
Branching ratio to gluino = 0.000
Branching ratio to LSP = 0.966
Branching ratio to Neutralino 1 = 0.034
Branching ratio to Neutralino 2 = 0.000
Branching ratio to Neutralino 3 = 0.000

Branching ratios for LH B-SQUARK:
Branching ratio to gluino = 0.000
Branching ratio to LSP = 0.830
Branching ratio to Neutralino 1 = 0.170
Branching ratio to Neutralino 2 = 0.000
Branching ratio to Neutralino 3 = 0.000

```
Branching ratios for RH B-SQUARK:
        Branching ratio to gluino       = 0.000
        Branching ratio to LSP          = 0.986
        Branching ratio to Neutralino 1 = 0.014
        Branching ratio to Neutralino 2 = 0.000
        Branching ratio to Neutralino 3 = 0.000


Branching ratios for (LH) SNEUTRINO:
        Branching ratio to gluino       = 0.000
        Branching ratio to LSP          = 0.029
        Branching ratio to Neutralino 1 = 0.971
        Branching ratio to Neutralino 2 = 0.000
        Branching ratio to Neutralino 3 = 0.000


    ================================================
    Rparity violating neutralino decay calculated using:
       Decay Operator (1=LLE,2=LQD,3=UUD) = 2
       Only non-zero couling indeces(ijk) =211
       Coupling Strength Lambda          =0.030000
       Mass of Lightest SUSY Particle = 18.70
       XMIX1 coupling                 = 0.853027
       XMIX2 coupling                 = 0.516725
       and a pure photino corresponds to
           (...XMIX1 =  0.879824)
           (...XMIX2 =  0.475300)
       N11prime (coupling xLSP(1) of Bartels) = 0.996113
       N12prime (coupling xLSP(2) of Bartels) = 0.049183

            Decay selection to l+,l-,nul+,nul-  = 1100
    ================================================


    ================================================
    Result of Rparity LSP decay calculation:
       Total LSP width                  =  0.1229020E-07
       LSP lifetime                     =  0.6174274E-16
       Branching (%) of LSP-¿   mu(+/-) + X = 86.74
       Branching (%) of LSP-¿ nu'mu(+/-) + X = 13.26
    ================================================

    ------------------------------------------------
    NC Xsection ep-¿Selectron+Squark =    1.4887+/-   0.0008pb
    CC Xsection ep-¿Sneutrino+Squark =    1.2118+/-   0.0004pb
    Branching % of chosen LSP decay channel =  86.74
    Total Susy cross-section         =    2.3424+/-   0.0007pb
    NC Branching : CC Branching  (%) =  55.13 :  44.87
    ------------------------------------------------

              TIME =  44.28

¿¿¿MSSM Generated Event=     1 x=  0.326 Q2=  798.42 Zradiative=1.000000 Evt type(1=NC,2=CC)= 2


                        Event listing (summary)

 I  particle/jet KS     KF orig    p'x     p'y     p'z      E       m

 1  !e-!         21     11    0    0.000   0.000 -26.600  26.600   0.001
 2  !p+!         21   2212    0    0.000   0.000 820.000 820.001   0.938
 3  (ud'0)       13   2101    2    0.071   0.347 552.282 552.282   0.579
 4  gamma         1     22    1    0.000   0.000   0.000   0.000   0.000
 5  nu'e          1     12    1   27.135 -10.655   0.812  29.163   0.000
 6  (neutral20)  11     42    1   -7.078  14.055   6.668  44.973  41.599
 7  (neutral10)  11     41    6   -3.181   6.318   2.997  20.215  18.698
 8  (u)          13      2    6    3.381   0.173  -8.224   8.894   0.006
 9  (u~)         13     -2    6   -7.277   7.564  11.895  15.864   0.006
10  (u)          13      2    2  -12.796   4.762  15.822  20.899   0.006
11  (neutral10)  11     41    2   -7.332  -8.509 217.815 218.905  18.698
12  mu+           1    -13    7   -6.262   1.937   4.664   8.046   0.106
13  (d)       A  12      1    7    2.967   2.064   4.388   5.685   0.010
14  (u~)      V  11     -2    7    0.114   2.317  -6.055   6.484   0.006
15  mu+           1    -13   11    1.116   0.873   2.389   2.779   0.106
16  (d)       A  12      1   11   -9.128  -8.976 117.467 118.162   0.010
17  (u~)      V  11     -2   11    0.680  -0.406  97.960  97.964   0.006
18  (ud'0)    A  12   2101    3    0.071   0.347 552.282 552.282   0.579
19  (u)       V  11      2   10  -12.796   4.762  15.822  20.899   0.006
20  (u)       A  12      2    8    3.381   0.173  -8.224   8.894   0.006
```

```
21 (u~)      V 11    -2    9  -7.277   7.564  11.895  15.864   0.006
22 (string)    11    92   13   3.081   4.380  -1.667  12.169  10.800
23 (rho-)      11  -213   22   1.342   0.549   2.062   2.662   0.856
24 (omega)      11   223   22   1.265   1.711   1.352   2.644   0.797
25 (rho0)      11   113   22   0.894  -0.083  -0.240   1.149   0.676
26 (pi0)       11   111   22  -0.915   1.405  -3.383   3.779   0.135
27 (rho0)      11   113   22   0.496   0.799  -1.457   1.936   0.859
28 (string)    11    92   16  -8.448  -9.382 215.427 216.126  11.923
29 (Lambda0)    11  3122   28  -5.791  -5.805  77.801  78.240   1.116
30 (K0)        11   311   28  -1.827  -1.659  20.849  21.000   0.498
31 n~0          1 -2112   28  -0.723  -0.625  20.598  20.641   0.940
32 pi-          1  -211   28   0.603  -0.352  27.352  27.361   0.140
33 (rho+)      11   213   28  -0.545  -0.501  12.733  12.780   0.807
34 pi-          1  -211   28  -0.236  -0.219   7.876   7.883   0.140
35 (pi0)       11   111   28   0.072  -0.221  48.218  48.219   0.135
36 (string)    11    92   18 -12.726   5.109 568.104 573.181  74.876
37 n0           1  2112   36   0.171   0.079 224.440 224.442   0.940
38 pi+          1   211   36  -0.248   0.082 184.601 184.601   0.140
39 (rho-)      11  -213   36   0.016   0.318 111.650 111.654   0.839
40 (rho+)      11   213   36   0.065  -0.364  13.450  13.478   0.776
41 (rho0)      11   113   36  -0.229   0.617   5.515   5.598   0.696
42 pi-          1  -211   36  -0.162  -0.227   1.513   1.544   0.140
43 (rho+)      11   213   36  -0.254   0.215   8.629   8.678   0.855
44 (omega)      11   223   36  -0.287  -0.654   1.741   2.043   0.796
45 (rho-)      11  -213   36  -4.579   2.776   8.342   9.931   0.608
46 (rho+)      11   213   36  -7.218   2.266   8.224  11.213   0.929
47 (string)    11    92   20  -3.896   7.737   3.671  24.758  22.900
48 (eta) 11 331 47 1.846 0.075 -4.291 4.769 0.957'
49 (rho+)      11   213   47   1.248  -0.216  -2.951   3.308   0.792
50 (rho-)      11  -213   47  -0.407  -0.115  -0.181   0.678   0.498
51 (rho+)      11   213   47   0.101   1.081   0.721   1.483   0.707
52 pi-          1  -211   47  -0.698   0.429   0.088   0.836   0.140
53 pi+          1   211   47  -1.161   1.352   2.370   2.968   0.140
54 (K*0)       11   313   47  -3.883   3.641   6.020   8.081   0.849
55 K-           1  -321   47  -0.943   1.489   1.896   2.635   0.494
56 pi-          1  -211   23   0.644   0.652   0.878   1.277   0.140
57 (pi0)       11   111   23   0.698  -0.104   1.184   1.385   0.135
58 pi+          1   211   24   0.675   0.564   0.469   1.006   0.140
59 pi-          1  -211   24   0.437   0.789   0.384   0.990   0.140
60 (pi0)       11   111   24   0.154   0.358   0.500   0.648   0.135
61 pi+          1   211   25   0.714  -0.054   0.102   0.737   0.140
62 pi-          1  -211   25   0.179  -0.029  -0.342   0.412   0.140
63 gamma        1    22   26  -0.710   1.074  -2.464   2.780   0.000
64 gamma        1    22   26  -0.205   0.332  -0.919   0.998   0.000
65 pi+          1   211   27   0.621   0.779  -1.426   1.745   0.140
66 pi-          1  -211   27  -0.124   0.020  -0.031   0.191   0.140
67 p+           1  2212   29  -4.896  -4.943  65.090  65.467   0.938
68 pi-          1  -211   29  -0.895  -0.862  12.712  12.773   0.140
69 (K'S0)      11   310   30  -1.827  -1.659  20.849  21.000   0.498
70 pi+          1   211   33  -0.497  -0.612   7.262   7.306   0.140
71 (pi0)       11   111   33  -0.048   0.111   5.472   5.475   0.135
72 gamma        1    22   35   0.107  -0.204  41.708  41.709   0.000
73 gamma        1    22   35  -0.035  -0.017   6.510   6.510   0.000
74 pi-          1  -211   39   0.233   0.059  13.210  13.213   0.140
75 (pi0)       11   111   39  -0.217   0.260  98.440  98.441   0.135
76 pi+          1   211   40   0.183   0.161   6.139   6.146   0.140
77 (pi0)       11   111   40  -0.118  -0.525   7.311   7.332   0.135
78 pi-          1  -211   41  -0.317   0.062   1.477   1.518   0.140
79 pi+          1   211   41   0.088   0.555   4.039   4.080   0.140
80 pi+          1   211   43  -0.535   0.090   6.257   6.282   0.140
81 (pi0)       11   111   43   0.281   0.124   2.372   2.396   0.135
82 pi+          1   211   44  -0.134  -0.301   0.945   1.010   0.140
83 pi-          1  -211   44   0.137  -0.030   0.186   0.272   0.140
84 (pi0)       11   111   44  -0.290  -0.323   0.610   0.761   0.135
85 pi-          1  -211   45  -3.708   2.185   7.028   8.242   0.140
86 (pi0)       11   111   45  -0.871   0.591   1.314   1.689   0.135
87 pi+          1   211   46  -1.417   0.793   1.940   2.534   0.140
88 (pi0)       11   111   46  -5.801   1.473   6.284   8.679   0.135
89 gamma        1    22   48   0.378  -0.008  -1.367   1.419   0.000
90 (rho0)      11   113   48   1.469   0.083  -2.924   3.351   0.717
91 pi+          1   211   49   0.121   0.181  -0.829   0.869   0.140
92 (pi0)       11   111   49   1.128  -0.397  -2.122   2.439   0.135
93 pi-          1  -211   50  -0.373  -0.019  -0.275   0.484   0.140
94 (pi0)       11   111   50  -0.034  -0.096   0.094   0.193   0.135
95 pi+          1   211   51   0.267   0.463   0.604   0.818   0.140
96 (pi0)       11   111   51  -0.165   0.618   0.117   0.664   0.135
97 K+           1   321   54  -3.493   3.051   5.089   6.903   0.494
98 pi-          1  -211   54  -0.390   0.591   0.932   1.178   0.140
99 gamma        1    22   57   0.229  -0.093   0.360   0.436   0.000
100 gamma       1    22   57   0.469  -0.010   0.825   0.949   0.000
101 gamma       1    22   60   0.094   0.255   0.434   0.512   0.000
102 gamma       1    22   60   0.059   0.102   0.066   0.135   0.000
103 pi+         1   211   69  -0.759  -0.524   6.545   6.611   0.140
104 pi-         1  -211   69  -1.069  -1.135  14.304  14.389   0.140
105 gamma       1    22   71  -0.064   0.136   4.716   4.718   0.000
106 gamma       1    22   71   0.016  -0.025   0.756   0.756   0.000
107 gamma       1    22   75  -0.034   0.143  38.919  38.920   0.000
```

108	gamma	1	22	75	-0.184	0.117	59.521	59.521	0.000
109	gamma	1	22	77	-0.015	-0.345	4.854	4.866	0.000
110	gamma	1	22	77	-0.103	-0.180	2.457	2.466	0.000
111	gamma	1	22	81	0.105	0.011	1.235	1.239	0.000
112	gamma	1	22	81	0.176	0.114	1.137	1.156	0.000
113	gamma	1	22	84	-0.153	-0.085	0.186	0.256	0.000
114	gamma	1	22	84	-0.137	-0.239	0.424	0.505	0.000
115	gamma	1	22	86	-0.099	0.022	0.106	0.146	0.000
116	gamma	1	22	86	-0.773	0.569	1.208	1.543	0.000
117	gamma	1	22	88	-5.791	1.467	6.264	8.656	0.000
118	gamma	1	22	88	-0.010	0.006	0.020	0.023	0.000
119	pi-	1	-211	90	0.483	-0.280	-1.102	1.243	0.140
120	pi+	1	211	90	0.985	0.363	-1.822	2.108	0.140
121	gamma	1	22	92	0.092	0.001	-0.130	0.159	0.000
122	gamma	1	22	92	1.036	-0.397	-1.992	2.280	0.000
123	gamma	1	22	94	0.016	0.007	0.075	0.077	0.000
124	gamma	1	22	94	-0.049	-0.103	0.018	0.116	0.000
125	gamma	1	22	96	-0.174	0.619	0.107	0.652	0.000
126	gamma	1	22	96	0.009	0.000	0.009	0.013	0.000
	sum:	1.00			0.000	0.000	793.400	866.222	347.646

B.8 Future Plans

We plan to include initial state radiative corrections, and implement the $L_iL_j\bar{E}_k$ and $\bar{U}_i\bar{D}_j\bar{D}_k$ R-parity violating Yukawa operators in a future version of the program.

B.9 Subroutines and Functions

Table B.1 below lists the main entry points of subroutines and functions, and provides short comments. The cross-section integration is carried out by the DIVON4 CERNLIB package.

Subroutine name	Comment
SSMINT	Initialise generator
SSMDIAG	Diagonalise neutralino and chargino mixing matrices
SSMBR	Calculate branching fractions of the cascade decays
SSMARR	Calculate cross-sections
SSMGEN	Generate event
SSMKIN	Calculate kinematics
SSMDK	Cascade-decays sparticle
SSMPEC	Add [roton remnant to event
SSMCDK	Perform a chain decay of heavier neuralinos to the LSP
SSMCHK	Check the starting parameters
SSMPHOTINOLSP	Make the pure photino the LSP
MYRANGEN	Generate x and Q2
MYINTGRL	Fast and dirty integration
MSSM_NCDFUN	NC cross-section
MSSM_NCDFUN	CC cross-section
BRANCH	Calculate branching fraction of sparticle decay
LSPINT	Rparity violating LSP decay calculation initialisation
LSPDEC	Decay LSP R-parity violating
LSPDKM	Decay LSP R-parity violating, called by LSPDEC
LSPBCH	Calculate LSP branchings and width
LSPDKL	Calculate LSP decay length
LSPDFUN	The Matrix element
SSMRNI	Initialise MSSM in ZEUS environment
SSMCRD	Read in input cards file
SSMFMC	Write event to output

Table B.1: MSSM Subroutine/Function listing.

Bibliography

[1] The ZEUS Detector Technical Proposal, ZEUS Collaboration, 1986.

The ZEUS Detector Status Report, ZEUS Collaboration, 1989.

The ZEUS Detector Status Report, ZEUS Collaboration, 1993.

[2] The H1 Detector Technical Proposal, H1 Collaboration, 1986.

[3] M.Dueren and K.Rith, 'Polarized Electron Nucleon Scattering at HERA - The HERMES Experiment', Proceedings of the HERA Workshop, Vol.1, Nov.1991, DESY.

[4] F. Halzen and A.Martin, 'Quarks and Leptons', Wiley 1984.

I.Aitchison and A.Hey, 'Gauge Theories in Particle Physics', Adam Hilger 1989.

[5] M.Diemoz et al., Phys.Rep. 130(1986)294;

T. Sloan et al, Phys. Rep. 162(1988)45.

[6] ZEUS Collaboration, M.Derrick et al., Phys.Lett. B293(1992)465.

[7] H1 Collaboration, T.Ahmed et al., Phys.Lett. B299(1993)374.

[8] ZEUS UK collaboration, Nucl. Instr. and Meth. A283(1989)466

[9] D.H.Saxon, Nucl. Instr. and Meth. A265(1988)20.

[10] D.G.Cussans et al., Nucl. Instr. and Meth. A315(1992)397.

[11] N.Harnew et al., Nucl. Instr. and Meth. A283(1989)781.

[12] 'Digitisation effects in the CTD FADC System'; H.Fawcett, Zeus-Note 93-011.

[13] T.Khatri, D.Phil. Thesis, University of Oxford(1993).

[14] W.H.Smith et al., 'The ZEUS Trigger System', ZEUS-Note-89-084 version 2.0 (1990).

[15] 'Monte Carlo Studies of the Level-2 Fast Clear Trigger'; B.Bylsma et al., AMZEUS83(1989).

[16] I.Silvester, D.Phil. Thesis, University of Oxford(1989).

[17] 'Trackfinding Algorithms and Vertex Position Measurement in the CTD First Level Trigger', G.P.Heath and I.M.Silvester, ZEUS-Note 89-119.

[18] 'Design of the CTD First Level Trigger Trackfinding Processors.', G.P.Heath et. al., ZEUS-Note 89-118.

[19] M.Lancaster, D.Phil. Thesis, University of Oxford(1992).

[20] INMOS Limited, 1Transputer Reference Manual', Prentice Hall, 1988.

[21] INMOS Limited, 'Occam 2 Reference Manual', Prentice Hall, 1988.

[22] 'A wirewrap LTC module', M.Postraneky (1990), UCL.

[23] 'The GFLT prototype board', K. Tokushuku, INS, Univ. of Tokyo.

[24] 'GFLT Design Document I', K. Tokushuku, ZEUS-Note 88-098

[25] 'The Cell Processor - user guide', R.Hasall, Rutherford Appleton Lab.

[26] 'The Sector Processor PCB V1.0', S.Madani, Rutherford Appleton Lab.

[27] S.Madani, Rutherford Appleton Lab., private communications.

[28] 'The Regional First Level Trigger Box: Simulation and Outline Hardware Design', T.L.Short and G.P.Heath, ZEUS-Note 91-027.

[29] 'Optimisation of the Tracking Detectors first level trigger using Functional Discriminant Analysis', F.F. Wilson.

[30] S.Wilson, D.Phil. Thesis, University of Bristol(1994), to be completed.

[31] M.Lancaster, private communications, DESY 1993.

[32] K.Tokushuku, Minutes of the ZEUS trigger meeting June 28, 1993.

[33] F.Wilson, Minutes of the ZEUS trigger meeting at DESY on June 28, 1993.

F.Wilson, Minutes of the ZEUS trigger meeting at DESY on December 14, 1993.

[34] See also [19, 33]

[35] H.E.Haber, G.L.Kane, Phys.Rep.117(1985)75

[36] R.J.Cashmore et al., Phys.Rep. 122, Nos.5&6(1985)275.

[37] 'Introduction to Supersymmetry and Supergravity'; P.West; World Scientific(1986).

[38] G.'t Hooft in 'Recent Developments in Gauge Theories', Plenum Press, New York(1981).

[39] M.E.Peskin, in: 'Proc.1981 Intern. Symp. on Lepton and Photon Interactions at High Energies', ed. W.Pfeil (Physikalisches Institut, Universitaet Bonn,1981) p.880.

[40] S.Weinberg, Phys.Rev.D13(1976)974 and D19(1979)1277;
L.Susskind, Phys.Rev.D20(1979)2619;
E.Farhi and L.Susskind, Phys.Rep.74(1981)277.

[41] S.Coleman, J.Mandula, Phys.Rev.159,n.5,(1967)159.

[42] J.Wess, B.Zumino, Phys.Lett.49B(1974)52;
J.Wess, B.Zumino, Nucl.Phys.B70(1974)39.

[43] R.Haag, J.T.Lopuszanski, M.Sohnius, Nucl.Phys.B88(1975)257.

[44] T.Inami, H.Nishino, S.Watamura, Phys.Lett.117B(1982)197.

[45] H.P.Nilles, Phys.Rep.110(1984)1.

[46] U.Amaldi, W. de Boer, P.H.Frampton, H.Fuerstenau, J.T.Liu, Phys.Lett.B281(1992)374;
U.Amaldi, W. de Boer, H.Fuerstenau, Phys.Lett.B260(1991)447.

[47] J.Bartels, W.Hollik, Z.Phys.C39(1988),433.

[48] A. Bartl, H. Fraas, W. Majerotto, B. Mösslacher; Z.Phys.C 55(1992)257.

[49] For reviews on the MSSM see [35, 36];
for MSSM calculations relevant to HERA see also:
S.K.Jones and C.H.Llewellyn Smith, Nucl.Phys.B217(1983)145.;
H.Komatsu, R.Rueckl, Nucl.Phys.B299(1988)407.;
and [50, 51, 47].

[50] A.Bartl, H.Fraas, W.Majerotto, Nucl.Phys.B297(1988)479.

[51] A.Bartl, H.Fraas, W.Majerotto, Z.Phys.C41(1988)475.

[52] J.Ellis, J.S.Hagelin, D.V.Nanopoulos, K.Tamvakis, Phys.Lett.125B(1983)275;
L.E.Ibanez, C.Lopez, Phys.Lett.126B(1983)54.

[53] J.Ellis, J.S.Hagelin, D.V.Nanopoulos, K.Olive, M.Srednicki, Nucl.Phys.B238(1984)453.

[54] P.F.Smith, J.R.J.Bennett, Nucl.Phys.B149(1979)525.

[55] 'Perturbative QCD Data are consistent with light Gluinos'; J.Ellis, D.V.Nanopoulos, D.A.Ross, CERN-TH.6824/93 (1993).

[56] 'The Minimal Supersymmetric Standard Model at HERA'; A.Bartl, M.Drees, W.Majerotto, B.Moesslacher; Proceedings of the HERA Workshop, Vol.2, Nov.1991, DESY.

[57] L.J. Hall and M. Suzuki, Nucl. Phys. B231 (1984) 419;
D. Brahm, L.J. Hall, Phys. Rev. D40 (1989) 2449;
see also [58].

[58] L.E.Ibanez, G.G.Ross, Nucl.Phys.B368(1992)3.

[59] H.Dreiner and G.G.Ross, Oxford Preprint OUTP-92-08P;
B.A.Campbell, S.Davidson, J.Ellis and K.Olive, Phys.Lett.B256(1991)457;
W.Fischler, G.Giudice, R.G.Leigh and S.Paban, Phys.Lett.B258(1991)45;
E.Roulet and D.Tommasini, Phys.Lett.B256(1991)218.

[60] H.Dreiner and R.J.N. Phillips, Nucl. Phys. B367(1991)591.

[61] J.Butterworth and H.Dreiner, Nucl.Phys.B397(1993)3.

[62] V.Barger, G.F.Giudice, T.Han, Phys.Rev.D40(1989)2987.

[63] D.P.Roy, Phys.Lett.B 283(1992)270.

[64] R.Godbole, P.Roy, X.Tata; Nucl.Phys. B401(1993)67.

[65] S.Dimopoulos, H.Georgi, Nucl.Phys.B193(1981)150;

S.Weinberg, Phys.Rev.D26(1982)287;

N.Sakai, T.Yanagida, Nucl.Phys.B197(1982)533.

[66] S.Weinberg, Phys.Rev.D26(1982)287;

N.Sakai, T.Yanagida, Nucl.Phys.B197(1982)83;

S.Dimopoulos, S.Raby, F.Wilczek, Phys.Lett.B112(1982)133.

[67] S.Dimopoulos, L.J.Hall, Phys.Lett.B207(1987)210.

[68] S.Dawson, Nucl.Phys.B261(1985)297.

[69] Aleph Collab.,Phys.Lett.236B(1990)86;

L3 Collab., Phys.Lett.233B(1989)530;

H.Baer, M.Drees, X.Tata, Phys.Rev.D41(1990)3414.

[70] L3 Collab.,Phys.Lett.B249(1990)341.

[71] A.Laasanen, Fermilab Preprint FERMILAB-CONF-91-236-E; Presented at Particles and Fields '91 Conf. (Vancouver, Canada, Aug.1991).

[72] M.Drees et. al., Phys.REv.D44(1991)725.

[73] H.Komatsu, R.Rueckl, Nucl.Phys.B299(1988)407.;

'SUSY detection within the MSSM at HERA',Y.Eisenberg, U.Karshon, A.Montag, G.D.Wolf, Proceedings of the HERA Workshop, Vol.2, Nov.1991, DESY.

[74] 'First Results on a Search for Supersymmetry via R-parity Violation', ZEUS-93-062, P.Morawitz.

[75] 'Limit on the d-Squark Mass in an R-Parity Violating SUSY Model', D.Gingrich, ZEUS-Note 93-048.

[76] 'Leptoquarks in Lepton-Quark Collisions', W.Buchmueller, R.Rueckl and D.Wyler, Phys.Lett.B 191(1987)442.

[77] 'Experimental Studies on Multijet Production in e^+e^- Annihilation at PETRA Energies', Jade Collaboration, Z.Phys.C 33C(1986)23.

[78] 'Jet reconstruction and jet properties at HERA', P.N.Burrows, G.Ingelman, E.Ros, Z.Phys.C 39C(1988)257.

[79] 'A study of the recombination scheme dependence of jet production rates and of $\alpha_s(M_{Z^0})$ in hadronic Z^0 decays', Opal Collaboration, Z.Phys.C 49(1991)375.

[80] 'New clustering algorithm for multijet cross sections in e^+e^- annihilation', S.Catani, Yu.L.Dokshitzer, M.Olsson, G.Turnock and B.R.Webber, Phys.Lett. 296B(1991)432.

[81] 'Status of the Uranium Calorimeter Reconstruction Software', P. de Jong, ZEUS-Note 92-019.

[82] 'The hadronic final state in ep scattering: global features and jet reconstruction', M.Fleischer, G.Ingelman, G.Knies, K.Meier, C.Pichler, A.Wegner, Proceedings of the HERA Workshop, Vol.1, Nov.1991.

[83] 'Monte Carlo Generator for R-parity Violating SUSY processes in Electron-Proton Collisions', J.Butterworth, RALT-148 and ZEUS-Note 91-113.

[84] 'Search for Leptoquarks with the Zeus Detector', ZEUS collaboration, Phys.Lett.B306(1993)173.

[85] A.Martin et al., RAL preprint RAL-92-021.

[86] R.Brun et al, CERN DD/EE/84-1.

[87] 'MSSM Version 1.0: A Monte Carlo Generator for Supersymmetry at HERA'; G.Blair, H.Dreiner and P.Morawitz; ZEUS-Note 93-121.

[88] A.Ali et al., Proceedings of the HERA Workshop, Vol.1, Nov.1991, DESY.

[89] G.Marchesini et al, Comp. Phys. Comm. 67(1992)465.

[90] U.Baur, J.A.M. Vermaseren and D.Zeppenfeld, Nucl.Phys. B375(1992)3;
U.Baur and D.Zeppenfeld, Nucl.Phys. B325(1989)253.

[91] G.Ingelman, Proceedings of the HERA Workshop, Vol.3, Nov.1991, DESY.

[92] 'The Global Track Reconstruction TGTRAK'; T. Shah et al.; RAL; in progress.

[93] ZEUS Collab., M.Derrick et al., Phys.Lett. B293(1992)465.

[94] MARK II, G.Hanson et al., Phys.Rev.Lett35(1975)1609.

[95] A.Ali et al.; Proceedings of the HERA Workshop, Vol.1, Oct.1987, DESY.

[96] For reviews see [36, 35, 45];
G.G.Ross, Grand unified theories (Benjamin/Cummings, 1985);
'Introduction to Supersymmetry and Supergravity'; P.West; World Scientific(1986)

[97] S.Weinberg, Phys.Rev.D26(1982)287;
N.Sakai, T.Yanagida, Nucl.Phys.B197(1982)83;

S.Dimopoulos, S.Raby, F.Wilczek, Phys.Lett.B112(1982)133.

[98] 'Tau-Signals for Supersymmetric Baryon Parity at HERA.',
ZEUS note in progress, ZEUS-94; H.Dreiner and P.Morawitz